UNIVERSITY OF CALIFORNIA
RIVERSIDE

# Mysteries of the Deep: A Multi-Scale Investigation of the Earth's Interior

A Dissertation submitted in partial satisfaction
of the requirements for the degree of

Doctor of Philosophy

in

Earth and Planetary Sciences

by

Andrew Joseph Birkey

June 2022

Dissertation Committee:
Dr. Heather A. Ford, Chairperson
Dr. Maryjo Brounce
Dr. Gareth Funning

The Dissertation of Andrew Joseph Birkey is approved:

_____

_____

_____

Committee Chairperson

University of California, Riverside

ACKNOWLEDGEMENTS

The text of this dissertation, in part, is a modified reprint of the material as it appears in The Journal of Geophysical Research – Solid Earth, 2021. The co-author Heather A. Ford listed in that publication directed and supervised the research which forms the basis for this dissertation. Additional co-authors for that publication include Page Dabney (who worked on result calculation) and Gillian Goldhagen (who provided technical expertise).

Funding for some of the work presented here comes from National Science Foundation grant EAR-1620386, the IRIS internship program, and the Shawn Biehler Scholarship.

Science is an iterative and collaborative process, and one that cannot be done in isolation. During my time as a graduate student, I have been extremely fortunate to have the constant and steadfast advice and support of my PhD advisor, Dr. Heather A. Ford. Without her, the work I have done would not be possible. Other mentors have also contributed to my growth as a scientist, including collaborators (Dr. Joseph Byrnes, Dr. Max Bezada, and Dr. Megan Anderson), my dissertation committee (Dr. Maryjo Brounce and Dr. Gareth Funning), and the faculty in the Earth and Planetary Sciences Department here at the University of California, Riverside. I thank all of them for their investment in me as a person and scientist.

Throughout my journey at UCR, I have encountered innumerable fellow graduate students in my department who have made the process not only endurable but pleasurable. They have fostered a sense of community within the department that has enabled me to achieve my best. Additionally, there are numerous undergraduate students who have worked in the Ford Lab, and their work has directly contributed to this dissertation. I thank both the graduate and undergraduate students I have been blessed to interact with over the past five years.

I was inspired to go to graduate school by the incredible faculty at my alma mater, the University of Illinois at Urbana-Champaign. In particular, I would like to thank my undergraduate research advisor (Dr. Patricia Gregg) as well as one of her graduate students who mentored me through a senior thesis (Dr. Haley Cabaniss). Their constant encouragement and enthusiasm about science motivates me to this day.

Finally, I would like to thank my family. My parents (Joe and Lou Ann Birkey) have supported me through my whole educational career and provide constant reminders of the need to work hard. I could not have finished this degree or any other without them. My sister Jessica Birkey (a newly minted Doctor of Audiology) has also been a constant source of support and encouragement.

ABSTRACT OF THE DISSERTATION

Mysteries of the Deep: A Multi-Scale Investigation of the Earth's Interior

by

Andrew Joseph Birkey

Doctor of Philosophy, Graduate Program in Earth and Planetary Sciences
University of California, Riverside, June 2022
Dr. Heather A. Ford, Chairperson

Earth's interior has increasingly been shown to be highly heterogeneous and complex. By utilizing four seismic different methods, we seek to better constrain this heterogeneity at multiple depth and areal scales. We begin with Sp receiver function analysis across the Australian continent, which uses direct seismic phases and those converted at boundaries to estimate velocity contrasts at boundaries below a seismometer. Then, using Ps receiver function analysis we expand beyond this to not only examine these velocity contrasts but also test for changes in seismic anisotropy across said boundaries. Next, we examine shear wave splitting both in Australia and at a smaller scale in the Wyoming Craton: this method relies on the fact that when a shear wave encounters anisotropic material, it is split into two orthogonal components, which can be retrieved at the receiver side. Finally, we cross correlate components of a single seismometer to estimate shallow subsurface velocity changes following the Ridgecrest earthquake sequence. Results from the Australian Sp receiver function analysis show a sharp, shallow seismic lithosphere-

asthenosphere boundary on the Phanerozoic east coast, with multiple mid-lithospheric discontinuities in the central cratonic portion. Our Ps receiver functions do not match well with simple models of seismic anisotropy changes across boundaries, but do exhibit characteristic backazimuthal variation: this implies more diffuse zones of seismic anisotropy. This is confirmed by our Australian shear wave splitting results, which show fast directions that often cannot be explained through plate-motion-induced shear alone and may require multiple layers of seismic anisotropy. Shear wave splitting in Wyoming also shows complexity in fast direction and delay time, but there appears to be a more systematic change in parameters moving into the Powder River Basin. Finally, velocity perturbations following the $M_w$ 7.1 Ridgecrest sequence generally recover within hours to days, suggesting a largely elastic response. Two stations do not show a recovery within the time period examined, implying a plastic response instead. All results bolster an argument for interior complexity mirroring Earth's surface.

## Table of Contents

## List of Figures

## List of Tables

## Introduction

This work examines the interior of our planet on multiple depth scales, moving from the base of tectonic plates, to the crust-mantle boundary, to the shallow subsurface. It also scales areally, starting with a continental, then regional, and finally fault-scale study. First, the structure of the Australian continent is discussed from multiple methods (in Chapters 1 and 2). Second, the eastern margin of the Wyoming Craton is analyzed (in Chapter 3). Third, changes in the subsurface following a large earthquake in California are explored (Chapter 4). To begin, we explain some basic definitions and concepts.

### *The lithosphere*

Earth's interior can be subdivided into concentric spheres, based on either changes in composition/chemistry or mode of deformation (referred to as rheology). The exterior rheological sphere is the lithosphere; this layer is brittle, moves coherently above the soft plastic asthenosphere below it, deforms in narrow zones at boundaries between pieces of lithosphere, and contains portions of two chemical layers (the outermost being the crust, the innermost being the mantle). In classic plate tectonic theory, the lithosphere corresponds to the rigid plate; indeed, some authors have referred to the portion of the Earth's interior that is directly involved surficial plate tectonics as the tectosphere (i.e., Jordan, 1975).

These layers are a consequence of chemical differentiation throughout Earth's history, as well as chemical and thermal recycling through plate tectonics. This has resulted in two

distinct types of lithosphere: oceanic and continental. Oceanic lithosphere forms through cooling of primary magma from the mantle at the Earth's surface: as material is pushed away from the mid-ocean ridge, it thickens with age following a half-space cooling model (Parsons and Sclater, 1977), but once oceanic lithosphere reaches an age of ~70 Myr, this model no longer holds and the lithosphere maintains a relatively constant thickness of 100 km (Stein and Stein, 1992). Additionally, oceanic lithosphere has a homogenous crust that thickens to a constant ~5-8 km (White et al., 1992). Continental lithosphere has a more complicated history: its exact origin is still debated, with some suggesting melting at the base of oceanic lithosphere due to plume interaction (e.g. Arndt et al., 2009; Griffin and O'Reilly, 2007), melting at mid-ocean ridges followed by underthrusting and imbrication (e.g. Canil, 2008; Pearson and Wittig, 2008; Simon et al., 2007; Su and Chen, 2018), island arc accretion with accompanying orogenic thickening (Keleman et al., 1998; Parman et al., 2004), and even impact from asteroids (e.g. Hansen, 2015).

One key component to the debate on formation of the continental lithosphere is the nature of Precambrian tectonics: there are several theories for the exact type of tectonic activity during the earliest portions of Earth's history, including distributed (Davies, 1992), heat-pipe (Kankanamge and Moore, 2016; Moore and Web, 2013), single-plate (Fischer and Gerya, 2016), and sluggish lid tectonics (Moyen and Van Hunen, 2012; O'Neill et al., 2007, 2015). For a review of these various types of tectonics and transitions between them, the reader is referred to Lenardic (2018). Additionally, the initiation of Earth's current tectonic regime (i.e., plate tectonics) is an active topic of debate. Onset of plate tectonics

may have occurred during the Hadean (e.g., Hopkins et al., 2008; Korenaga, 2021), Archean (e.g., Condie and Kröner, 2008), or the Neoproterozoic (e.g., Hamilton, 2011). Given that less than 5% of rocks preserved at the surface have ages older than 3.0 Ga (Goodwin, 1996), it is difficult to determine the onset of plate tectonics from the rock record alone. Interactions between tectonic mode and continental lithosphere formation may act as a feedback loop, with the initiation of plate tectonics corresponding to thickening of continental lithosphere (e.g., Beall et al., 2018).

Regardless of how continental lithospheric mantle originally formed, it seems clear that the crustal portion of the continental lithosphere formed (and continues to form today) through subduction zones that recycle and alter the original oceanic lithosphere. Petrologic evidence suggests that the extraction of the continental crust depleted the upper mantle, a process that strongly resembles processes in modern subduction zones (see Hawkesworth et al., 2010 and references therein). Because of its longer history and more complicated formation, continental lithosphere is able to achieve much greater thicknesses, sometimes up to 200 km or more, as evidenced by seismic tomography (e.g., Bedle et al., 2021; Yoshizawa, 2014; Yuan and Romanowicz, 2010). Its longer preservation time has also resulted in far more variable crustal composition (Rudnick et al., 2003) and thicknesses, ranging from ~20 km to 70 km in orogens (Laske et al., 2013).

Because of Earth's dynamic interior, oceanic lithosphere has a limited surface residence time: as it is pushed away from mid-ocean ridges where it originates, it is pulled toward

subduction zones. Thus, the oldest oceanic lithosphere is ~170 Myr old, except for a small portion of the Mediterranean where ~280 Myr old oceanic lithosphere can be found (Müller et al., 2008). Continental lithosphere can be billions of years old and may maintain distinct geochemical and geophysical signatures from its long history (the latter will be explored throughout the body of this work). However, not all regions of the Earth with ancient continental crust have an equally old lithospheric mantle: in some cases it is thought that deformation at the base of the plate due to subduction (Kusky et al., 2014), plume interaction (Lee et al., 2011), or rifting (Griffin et al., 2003) can remove portions of the lithospheric mantle and may cause compositional and structural changes. This has been suggested for the North China Craton (Kusky et al., 2014; Menzies et al., 1993; Wang et al., 2016), the Madagascar Craton (Tucker et al., 2014), and the Wyoming Craton (Humphreys et al., 2015).

While geochemistry and petrology can provide compositional information about the lithosphere, these observations are not made in situ and there can be complications with the use of xenoliths as geothermobarometers (Brey and Kohler, 1990). Seismology can be used to image the state of the lithosphere in situ, which can be combined with other datasets to provide information about its structure, temperature, and melt content (e.g., Debayle et al., 2020; Finger et al., 2022; Tesauro et al., 2020). Different methods can be used to image different portions of the solid Earth: seismic tomography, for instance, provides information about the bulk structure of a region, but generally has coarse vertical resolution due to its sensitivity to average velocities over the whole of a medium. Other methods (such

as those discussed here) can provide more localized information with somewhat improved resolution. Receiver functions, for instance, are very sensitive to sharp vertical changes in seismic velocity and are thus used to image boundaries within the Earth. Shear wave splitting is a path-integrated effect, but is the most obvious expression of deformation within the mantle. Filtering of tomographic results can improve vertical resolution, and result in the imaging of fine-scale shallow features (i.e., passive-image interferometry).

*The lithosphere-asthenosphere boundary*

Earth's most ubiquitous plate boundary is at the base of the plates, where the lithosphere transitions into the asthenosphere. One complication with studying the lithosphere is defining exactly where and how this transition occurs. A simplistic understanding of this boundary is that it is the segue from the rigid, coherently moving plate to the more plastic and convective mantle below it. Even this view, however, is not overly accurate in many regions throughout the world where the boundary may not be sharp or diffuse (Mancinelli et al., 2017). Often, it is thought of as a gradual transition from one to the other, and may even be referred to as the lithosphere-asthenosphere transition (Yoshizawa, 2014). The lithosphere and asthenosphere are often not fully decoupled, especially in older regions that have very thick, cold lithosphere (Debayle et al., 2005; Hoïnk et al., 2011; O'Neill et al., 2010).

Similar to this definition is a transition from the thermally conductive lithosphere, to the thermally convective asthenosphere (Sleep, 2005). Temperatures in the lithosphere

increase rapidly with depth; the sub-lithospheric mantle has more efficient heat transfer due to its convection, so temperatures increase far less quickly. This change in thermal modes is most obvious in younger or more tectonically active regions (i.e., oceans or active margins), where the geotherm is elevated. Older regions have a longer history of secular cooling, thus lower geotherms (Artemieva, 2008 and references therein). In the cratons, for instance, some regions are subadiabatic to 400 km depth or more (Boyd et al. 1993, 1997; Jordan, 1975; Lee and Rudnick, 1999).

One of the most commonly observed expressions of this boundary is a decrease in seismic wavespeeds below the seismically fast lithospheric lid. Tectonically active regions such as active margins and oceanic lithosphere have the most pronounced decrease, while tectonically quiescent regions such as cratons may have no decrease at all (Fischer et al., 2020; Rychert et al., 2020). However the specifics of this definition vary and include the depth to a negative velocity gradient (e.g., Debayle and Kennett, 2000), a specific velocity contour either in percent change (e.g., Gung et al., 2003) or absolute velocity (e.g., Li and Burke, 2006), or a change in the intensity or orientation of seismic anisotropy (e.g., Gaherty and Jordan, 1995). Throughout the body of this work, we will rely primarily on the seismic definition of the lithosphere.

While the upper mantle is peridotitic in composition, there can be slight variations in its depletion: the asthenosphere is mineralogically undepleted, while the lithosphere is mineralogically depleted. Cratonic lithosphere can have an olivine Mg# of 92 or higher,

compared to an olivine Mg# of 90 for younger continental regions and olivine Mg#88 for primitive mantle (Djomani et al., 2001) . This definition may not hold in all places, because the transition may be gradual or the lithosphere itself may be compositionally layered (e.g., in cratons).

The lithosphere is also far more electrically resistive than the asthenosphere below it. This may be due to the presence of partial melt within the asthenosphere, as well as an increase in the amount of hydration across the boundary (Lee, 2006; Sleep, 2005).

*Seismic results and the physical world*

It has long been assumed that conditions within the Earth (e.g., pressure, temperature, density) have a first-order effect on seismic velocities. Other potentially important parameters are grain size, water content, and the presence of melt. Laboratory experiments for instance have shown that an increase in temperature leads to a decrease in velocity, while an increase in pressure leads to an increase in velocity (Faul and Jackson, 2005). The heterogeneous thermal structure of the Earth however, leads to several complications. In most tectonic settings there is an observable low-velocity zone immediately below the lithosphere (between ~100 and 200 km depth) with a velocity decrease of 2-10% (Nettles and Dziewónski, 2008), often assumed to be associated with the transition from the lithosphere to the asthenosphere. Understanding the origin of the low-velocity zone is of paramount importance to finding ways to relate physical properties of the Earth to seismic velocities. In oceanic regions this low velocity zone may be explained entirely through

thermal causes and a gradual increase in grain size from the mm-scale in the uppermost mantle to the cm-scale near the low-velocity zone (Faul and Jackson, 2005). However, in continental regions the geotherm is much lower, and thus another explanation is needed for a transition from higher to lower velocities.

One possible explanation for this velocity drop is the presence of melt, water, or volatiles immediately below the base of the lithosphere. The effect that water has on seismic velocities is currently unsettled: some experiments have shown that olivine with 0.8 to 0.9 wt% water has a reduced bulk modulus of ~3.5% and a reduced shear modulus of 7.5% (Jacobsen et al., 2008). Other experimental data suggest that water itself may not play an important role in altering seismic velocities: rather, it is the oxygen fugacity that is important (Cline et al., 2018). Partial melt increasingly seems to play an important role not only in the presence of the low-velocity zone, but also in explaining magnetotelluric results. One study suggested that for 1% partial melt, Vp is reduced up to 3.6% and Vs is reduced up to 7.9% (Hammond and Humphreys, 2000); however, a more recent study determined that the presence of as little as 0.2% partial melt can reduce Vp by 2% and Vs by 5-8% (Chantel *et al.*, 2016). Seismology, petrology, and magnetotellurics all indicate that the presence of partial melt in the upper mantle is spatially heterogeneous, with the largest amount occurring at mid-ocean ridges and hotspots, while tectonically inactive regions such as cratons have very little or no partial melt at all (Debayle *et al.,* 2020; Selway *et al.*, 2019). This partial melt may also explain the viscosity contrast that exists between the

lithosphere and the asthenosphere (increased melt or fluid content serves to reduce viscosity), thus facilitating plate tectonics.

*Receiver functions*

There are sharp transitions in composition and seismic velocities at many boundaries between Earth's layers. If these transitions are sufficiently sharp (the crust-mantle boundary, for instance, has a 1 km/s velocity increase over 10 km or less; Jarchow and Thompson, 1989), they can produce conversions from a primary wave (P-wave) to a secondary wave (S-wave) or vice versa. Using direct and converted arrivals, the travel-time to the boundary and the seismic velocity contrast across it can be calculated. Local or global tomography models can be used to depth-migrate the receiver functions. This method has been used to image several first-order boundaries and velocity changes, including the lithosphere-asthenosphere boundary (imaged as a velocity decrease with depth), the crust-mantle boundary (known as the Mohorovičić discontinuity or Moho, observed as a velocity increase with depth), sharp velocity decreases with depth within the lithosphere above the lithosphere-asthenosphere boundary as estimated by tomography (known as mid-lithospheric discontinuities, and usually only observed in very old or very thick lithosphere), the base of the asthenosphere (a velocity increase with depth) and the mantle transition zone between 410 and 660 km (where changes in pressure result in new crystallographic structures and complex velocity changes).

By using one component of a seismogram as a reference for the source and receiver component of a seismic signal, the structural component can be found on another. This is

generally done through deconvolution of a parent phase (the direct arrival) from a daughter phase (the converted arrival). Because they share a common source and receiver, any signal left should be due to sharp seismic boundaries at depth that cause the parent phase to convert to the daughter phase. In this work, we examine the use of both P-to-S (Ps) and S-to-P (Sp) receiver functions: while both are sensitive to sharp boundaries, variations in the arrivals of the two phases mean they are often used to image different portions of the Earth's interior. Ps receiver functions are often used to image the crust and the Moho, but crustal reverberations arriving after the Moho conversion tend to obscure the mantle lithosphere and the lithosphere-asthenosphere boundary. Conversely, Sp receiver functions can be used for the mantle lithosphere because crustal reverberations arrive before the converted phase; this however (coupled with longer characteristic periods), makes them somewhat less useful for imaging the crust and Moho.

*Shear wave splitting*

Most seismic studies assume an isotropic velocity structure within the Earth. However, that is often not the case. The preferential alignment of crystals within the mantle, bodies of melt, or aligned cracks in the crust can all produce anisotropic (i.e., directionally dependent) seismic velocities and other material properties. One of the most prevalent minerals in the upper mantle is olivine: its crystal structure is highly anisotropic in terms of seismic velocities and hydrogen diffusivity (Simpson and Tommasi, 2005). Strong forces over very long periods of time (i.e., millions to billions of years) can preferentially align these crystals to produce macroscopic seismic anisotropy.

Seismic anisotropy can be measured through surface-wave tomography, receiver functions, and shear wave splitting (used in this work). When shear waves encounter an anisotropic medium, they are split into two orthogonal quasi-shear waves (one fast, one slow). As they propagate through the medium, they accrue a delay between components. This phenomenon is known as shear wave splitting. One major complication with this method is that it is a path-integrated effect: to reduce the contributions to shear wave splitting to only structure beneath the seismic receiver, core-converted phases such as SKS (an S-wave that converts to a P-wave at the core-mantle boundary, then back to an S-wave upon exiting the core) or SKKS (the same as SKS, but with a reflection at the core-mantle boundary). These phases have the benefit of a "reset" at the core-mantle boundary, thus reducing structure sampled to the upward path of the ray. Additionally, the second conversion at the core-mantle boundary results in only an SV-wave rather than coupled SV and SH-waves: without this, there would be four quasi-shear waves observed at the receiver which would significantly complicate the estimation of anisotropic parameters.

*Passive-image interferometry*

While much of this work focuses on deeper portions of the lithosphere, the shallowest portions of the crust can also be imaged through passive techniques. Ambient noise tomography is a relatively recent method that relies on noise in seismograms that are

generally filtered out to improve the signal from tectonic sources. By cross-correlating the signal between two seismic stations, one can approximate the Green's function between the two (Lobkis and Weaver, 2001). From this, the velocity structure along the path from one station to the other can be estimated. This is useful as it allows for the imaging of shallow structures without relying on earthquakes or active sources.

This has been further developed into passive-image interferometry, in which slight velocity changes can be interpreted (Sens-Schönfelder and Wegler, 2006; Snieder, 2004). In this work, we present results from a type of passive-image interferometry known as single-station cross-correlation, wherein the signal between multiple components of a seismogram is cross-correlated to estimate velocity changes (Hobiger et al., 2014).

*Cratons*

While large portions of the Earth's surface is covered by oceanic lithosphere, plate tectonics constantly recycles this material. The continents, however, can be less susceptible to this long-term deformation. Portions of the Earth's lithosphere that have existed for billions of years and have not undergone major deformation for at least the past billion are referred to as cratons. These regions provide a record of vast portions of the Earth's history. All continents have cratonic lithosphere in the form of either shields (regions exposed at the surface; e.g., the North Australian Craton, Superior Craton, or Amazonia craton) or platforms (regions that are not exposed and are covered by either sedimentary, igneous, or

metamorphic rock; e.g., The Siberian or North American platforms). Most cratons date to the Archean, but Proterozoic lithosphere is occasionally included as well.

Due to their long history, cratons have unique properties. They have far lower geothermal gradients than younger portions of the Earth, due primarily to secular cooling with age. They are also far thicker than other pieces of lithosphere: cratons can extend to more than 250 km in depth, while younger regions have much thinner lithosphere at 100 km or so. Their age has also given rise to repeated magmatism, leaving the mantle portion of cratons heavily mineralogically depleted and dehydrated. It has also resulted in a distinct composition that is generally not seen elsewhere, including a much higher than average mantle olivine Mg# as well as unique crustal rocks that are not produced today. These chemical differences have also left cratons with a different rheology: they are more viscous and less susceptible to deformation. This history of depletion and dehydration has left the cratons neutrally buoyant, with a decrease in density offsetting their exceptional thickness (known as the isopycnic hypothesis; e.g., Jordan, 1988). Altogether, this results in lithosphere that is far more stable than younger regions and does not actively deformed unless large-scale, dynamic processes create instability within the mantle.

Because cratons preserve billions of years of Earth's history, they provide information on the stabilization of our planet, the creation of continents, the initiation of plate tectonics (arguably Earth's most unique and important feature), and the overall evolution of the

planet physically and biologically (e.g., the emergence of continents has major ramifications for how/when life could evolve into more complex forms).

*Mid-lithospheric discontinuities*

In the last decade, it has become apparent that a ubiquitous feature of thick, ancient lithosphere is the presence of sharp decreases in velocity above the tomographically predicted depth of the lithosphere-asthenosphere boundary. These are referred to as mid-lithospheric discontinuities. Such discontinuities have mostly been observed in cratonic settings (e.g., Ford et al., 2010; Hopper and Fischer, 2015; Sodoudi et al., 2013), but they have also been seen in oceanic regions with particularly thick lithosphere (Tharimena et al., 2016). Mid-lithospheric discontinuities have been imaged primarily through receiver functions, but seismic daylight imaging (a form of reflectivity seismology) and magnetotelluric studies have also observed them (Selway, 2018; Sun and Kennett, 2017).

The cause and origin of these discontinuities is still an active area of debate: it seems most likely that they require the presence of hydrated minerals in what is nominally dry lithosphere. Amphibole and phlogopite are two commonly suggested minerals (Aulbach et al., 2017). However, it is not entirely clear how hydrated minerals are able to appear in the middle of the lithosphere, especially because cratons are assumed to be tectonically stable and inactive. One suggestion is that these mid-lithospheric discontinuities are the result of melt percolation beginning at the lithosphere-asthenosphere boundary and ending at some equilibrium depth around 70-100 km, though given the cool geotherms of most cratons this

is not a likely option (Aulbach et al., 2017). Another possibility is that these minerals are the result of ancient tectonic processes such as subduction, rifting, and orogenesis and they have remained in the lithosphere for hundreds of millions to billions of years (Wirth and Long, 2014). A third possibility is that mid-lithospheric discontinuities represent paleo-lithosphere-asthenosphere boundaries, with the lithosphere thickening as it ages and cools more (Aulbach et al., 2017). Finally, it is possible that mid-lithospheric discontinuities represent the top of a gradational region in the lithosphere known as the lithosphere-asthenosphere transition. This feature has been primarily observed through tomography in Australia (Yoshizawa and Kennett, 2015; Yoshizawa, 2014), and may correspond to changes in thermal and rheological structure at depth.

While first-order drops in seismic velocity internal to the continental lithosphere are not predicted by most reference models, there is clear evidence of a low-velocity zone beneath the oceanic lithosphere. The origin of this zone is debated, but some have suggested that it may be the result of elastically-accommodated grain boundary sliding (Karato, 2010). When a material is stressed, this may manifest as sliding at grain boundaries; under low-pressure systems this deformation occurs elastically (i.e., the strain is recoverable). At low temperatures, it is difficult to deform grain boundaries, but this process is eased at moderate temperatures (such as those found in the upper mantle). This deformation reduces the elastic constant, and thus reduces the seismic velocity. Such a phenomenon has more recently been linked to the presence of mid-lithospheric discontinuities (Karato et al., 2015; Karato and Park, 2019). However, this mechanism is still poorly constrained, with Karato

et al. (2015) estimating that the temperature at which this occurs is 900 ± 300□C, with the large error bars due to the unknown role of water and pressure. This is predicted to yield a velocity drop of 5%, which would correspond to the drop seen at mid-lithospheric discontinuities. However, if this critical temperature is at the high end of the given range, it is far warmer than most cratons at the depths where mid-lithospheric discontinuities have been observed. This mechanism cannot be ruled out as the cause of mid-lithospheric discontinuities, but further evidence is needed to both constrain the role of water and pressure.

In addition to sharp changes in seismic wavespeeds, several other changes occur at or near mid-lithospheric discontinuities. Magnetotellurics has imaged changes in conductivity in these ranges--which may be linked to hydrous minerals or graphite films (Selway et al., 2019). In some settings there is also a transition in the orientation or strength of seismic anisotropy, observed dominantly through seismic methods (e.g., Debayle et al., 2016; Wirth and Long, 2014; Yoshizawa and Kennett, 2015). The presence of anisotropy could potentially reduce shear wave speeds, but previous studies have indicated that it is not likely to be the sole cause of mid-lithospheric discontinuities in most cases (e.g., Selway et al., 2015). One of the major complications in studying these features is the dearth of xenoliths from these depths (both due to the depth of the discontinuities, but also the tectonic inactivity of cratons). Firmer constraints on fabric and composition from xenoliths are needed.

Consensus seems to be coalescing on hydrous minerals such as phlogopite or amphibole as the main cause of mid-lithospheric discontinuities (Aulbach et al., 2017; Rader et al., 2015; Saha et al., 2018; Selway et al., 2015), though it should be noted that none of these mechanisms are mutually exclusive. It is likely that various phenomena may be acting in concert to produce decreases in seismic velocity internal to the lithosphere. However, the ultimate cause of these phenomena is poorly constrained: most could be explained by either ancient or present activity, and both possibilities have implications for our understanding of the lithosphere, its evolution, and present-day geodynamics.

**References**


Almqvist, B. S., & Mainprice, D. (2017). Seismic properties and anisotropy of the continental crust: Predictions based on mineral texture and rock microstructure. *Reviews of Geophysics*, *55*(2), 367-433.

Arndt, N. T., Coltice, N., Helmstaedt, H., & Gregoire, M. (2009). Origin of Archean subcontinental lithospheric mantle: Some petrological constraints. *Lithos*, *109*(1-2), 61-71.

Artemieva, I. M. (2008). The continental lithosphere: Reconciling thermal, seismic, and petrologic data. *Lithos*, *109*(1-2), 23-46.

Aulbach, S., Massuyeau, M., & Gaillard, F. (2017). Origins of cratonic mantle discontinuities: A view from petrology, geochemistry and thermodynamic models. *Lithos*, *268*, 364-382.

Bedle, H., Lou, X., & Van der Lee, S. (2021). Continental Tectonics Inferred From High-Resolution Imaging of the Mantle Beneath the United States, Through the Combination of USArray Data Types. *Geochemistry, Geophysics, Geosystems*, *22*(10), e2021GC009674.

Boyd, F. R., Pearson, D. G., Nixon, P. H., & Mertzman, S. A. (1993). Low-calcium garnet harzburgites from southern Africa: their relations to craton structure and diamond crystallization. *Contributions to Mineralogy and Petrology*, *113*(3), 352-366.

Boyd, F. R., Pokhilenko, N. P., Pearson, D. G., Mertzman, S. A., Sobolev, N. V., & Finger, L. W. (1997). Composition of the Siberian cratonic mantle: evidence from Udachnaya peridotite xenoliths. *Contributions to Mineralogy and Petrology*, *128*(2), 228-246.

Brey, G. P., & Köhler, T. (1990). Geothermobarometry in four-phase lherzolites II. New thermobarometers, and practical assessment of existing thermobarometers. *Journal of Petrology*, *31*(6), 1353-1378.

Canil, D. (2008). Canada's craton: a bottoms-up view. *GSA TODAY*, *18*(6), 4.

Chantel, J., Manthilake, G., Andrault, D., Novella, D., Yu, T., & Wang, Y. (2016). Experimental evidence supports mantle partial melting in the asthenosphere. *Science advances*, *2*(5), e1600246.

Cline Ii, C. J., Faul, U. H., David, E. C., Berry, A. J., & Jackson, I. (2018). Redox-influenced seismic properties of upper-mantle olivine. *Nature*, *555*(7696), 355-358.

Condie, K. C., & Kröner, A. (2008). When did plate tectonics begin? Evidence from the geologic record. In *When did plate tectonics begin on planet Earth* (Vol. 440, pp. 281-294). Geological Society of America Special Papers.

Dannberg, J., Eilon, Z., Faul, U., Gassmöller, R., Moulik, P., & Myhill, R. (2017). The importance of grain size to mantle dynamics and seismological observations. *Geochemistry, Geophysics, Geosystems*, *18*(8), 3034-3061.

Davies, G. F. (1992). On the emergence of plate tectonics. *Geology*, *20*(11), 963-966.

Debayle, E., Bodin, T., Durand, S., & Ricard, Y. (2020). Seismic evidence for partial melt below tectonic plates. *Nature*, *586*(7830), 555-559.

Debayle, E., Dubuffet, F., & Durand, S. (2016). An automatically updated S-wave model of the upper mantle and the depth extent of azimuthal anisotropy. *Geophysical Research Letters*, *43*(2), 674-682.

Debayle, E., Kennett, B., & Priestley, K. (2005). Global azimuthal seismic anisotropy and the unique plate-motion deformation of Australia. *Nature*, *433*(7025), 509-512.

Djomani, Y. H. P., O'Reilly, S. Y., Griffin, W. L., & Morgan, P. (2001). The density structure of subcontinental lithosphere through time. *Earth and Planetary Science Letters*, *184*(3-4), 605-621.

Faul, U. H., & Jackson, I. (2005). The seismological signature of temperature and grain size variations in the upper mantle. *Earth and Planetary Science Letters*, *234*(1-2), 119-134.

Finger, N. P., Kaban, M. K., Tesauro, M., Mooney, W. D., & Thomas, M. (2022). A Thermo-Compositional Model of the African Cratonic Lithosphere. *Geochemistry, Geophysics, Geosystems*, *23*(3), e2021GC010296.

Fischer, K. M., Rychert, C. A., Dalton, C. A., Miller, M. S., Beghein, C., & Schutt, D. L. (2020). A comparison of oceanic and continental mantle lithosphere. *Physics of the Earth and Planetary Interiors*, *309*, 106600.

Fischer, R., & Gerya, T. (2016). Early Earth plume-lid tectonics: A high-resolution 3D numerical modelling approach. *Journal of Geodynamics*, *100*, 198-214.

Gaherty, J. B., & Jordan, T. H. (1995). Lehmann discontinuity as the base of an anisotropic layer beneath continents. *Science*, *268*(5216), 1468-1471.

Goodwin, A. M. (1996). *Principles of Precambrian geology*. Elsevier.

Griffin, W. L., O'Reilly, S. Y., Natapov, L. M., & Ryan, C. G. (2003). The evolution of lithospheric mantle beneath the Kalahari Craton and its margins. *Lithos*, *71*(2-4), 215-241.

Griffin, W. L., & O'Reilly, S. Y. (2007). Cratonic lithospheric mantle: is anything subducted?. *Episodes*, *30*(1), 43.

Gung, Y., Panning, M., & Romanowicz, B. (2003). Global anisotropy and the thickness of continents. *Nature*, *422*(6933), 707-711.

Hammond, W. C., & Humphreys, E. D. (2000). Upper mantle seismic wave velocity: Effects of realistic partial melt geometries. *Journal of Geophysical Research: Solid Earth*, *105*(B5), 10975-10986.

Hamilton, W. B. (2011). Plate tectonics began in Neoproterozoic time, and plumes from deep mantle have never operated. *Lithos*, *123*(1-4), 1-20.

Hansen, V. L. (2015). Impact origin of Archean cratons. *Lithosphere*, *7*(5), 563-578.

Hawkesworth, C. J., Dhuime, B., Pietranik, A. B., Cawood, P. A., Kemp, A. I., & Storey, C. D. (2010). The generation and evolution of the continental crust. *Journal of the Geological Society*, *167*(2), 229-248.

Hobiger, M., Wegler, U., Shiomi, K., & Nakahara, H. (2014). Single-station cross-correlation analysis of ambient seismic noise: application to stations in the surroundings of the 2008 Iwate-Miyagi Nairiku earthquake. *Geophysical Journal International*, *198*(1), 90-109.

Höink, T., Jellinek, A. M., & Lenardic, A. (2011). Viscous coupling at the lithosphere-asthenosphere boundary. *Geochemistry, Geophysics, Geosystems*, *12*(10).

Hopkins, M., Harrison, T. M., & Manning, C. E. (2008). Low heat flow inferred from> 4 Gyr zircons suggests Hadean plate boundary interactions. *Nature*, *456*(7221), 493-496.

Hopper, E., & Fischer, K. M. (2015). The meaning of midlithospheric discontinuities: A case study in the northern US craton. *Geochemistry, Geophysics, Geosystems*, *16*(12), 4057-4083.

Jarchow, C. M., & Thompson, G. A. (1989). The nature of the Mohorovicic discontinuity. *Annual Review of Earth and Planetary Sciences*, *17*(1), 475-506.

Kankanamge, D. G., & Moore, W. B. (2016). Heat transport in the Hadean mantle: From heat pipes to plates. *Geophysical Research Letters*, *43*(7), 3208-3214.

Kelemen, P. B., Hart, S. R., & Bernstein, S. (1998). Silica enrichment in the continental upper mantle via melt/rock reaction. *Earth and Planetary Science Letters*, *164*(1-2), 387-406.

Korenaga, J. (2021). Hadean geodynamics and the nature of early continental crust. *Precambrian Research*, *359*, 106178.

Kusky, T. M., Windley, B. F., Wang, L., Wang, Z., Li, X., & Zhu, P. (2014). Flat slab subduction, trench suction, and craton destruction: Comparison of the North China, Wyoming, and Brazilian cratons. *Tectonophysics*, *630*, 208-221.

Laske, G., Masters, G., Ma, Z., & Pasyanos, M. (2013, April). Update on CRUST1. 0—A 1-degree global model of Earth's crust. In *Geophys. res. abstr* (Vol. 15, p. 2658).

Lee, C.T. (2006). Geochemical/petrologic constraints on the origin of cratonic mantle. *GEOPHYSICAL MONOGRAPH-AMERICAN GEOPHYSICAL UNION*, *164*, 89.

Lee, C. T., & Rudnick, R. L. (1999). Compositionally stratified cratonic lithosphere: petrology and geochemistry of peridotite xenoliths from the Labait tuff cone, Tanzania. In *Proceedings of the 7th international Kimberlite conference* (pp. 503-521). Cape Town: Red Roof Design.

Lenardic, A. (2018). The diversity of tectonic modes and thoughts about transitions between them. *Philosophical Transactions of the Royal Society A: Mathematical, Physical and Engineering Sciences*, *376*(2132), 20170416.

Li, A., & Burke, K. (2006). Upper mantle structure of southern Africa from Rayleigh wave tomography. *Journal of Geophysical Research: Solid Earth*, *111*(B10).

Lobkis, O. I., & Weaver, R. L. (2001). On the emergence of the Green's function in the correlations of a diffuse field. *The Journal of the Acoustical Society of America*, *110*(6), 3011-3017.

Mancinelli, N. J., Fischer, K. M., & Dalton, C. A. (2017). How sharp is the cratonic lithosphere-asthenosphere transition?. *Geophysical Research Letters*, *44*(20), 10-189.

Menzies, M. A., Fan, W., & Zhang, M. (1993). Palaeozoic and Cenozoic lithoprobes and the loss of> 120 km of Archaean lithosphere, Sino-Korean craton, China. *Geological Society, London, Special Publications*, *76*(1), 71-81.

Moore, W. B., & Webb, A. A. G. (2013). Heat-pipe earth. *Nature*, *501*(7468), 501-505.

Moyen, J. F., & Van Hunen, J. (2012). Short-term episodicity of Archaean plate tectonics. *Geology*, *40*(5), 451-454.

Müller, R. D., Sdrolias, M., Gaina, C., & Roest, W. R. (2008). Age, spreading rates, and spreading asymmetry of the world's ocean crust. *Geochemistry, Geophysics, Geosystems*, *9*(4).

Munch, F. D., Khan, A., Tauzin, B., van Driel, M., & Giardini, D. (2020). Seismological evidence for thermo-chemical heterogeneity in Earth's continental mantle. *Earth and Planetary Science Letters*, *539*, 116240.

Nettles, M., & Dziewoński, A. M. (2008). Radially anisotropic shear velocity structure of the upper mantle globally and beneath North America. *Journal of Geophysical Research: Solid Earth*, *113*(B2).

O'Neill, C., Lenardic, A., & Condie, K. C. (2015). Earth's punctuated tectonic evolution: cause and effect. *Geological Society, London, Special Publications*, *389*(1), 17-40.

O'Neill, C., Lenardic, A., Moresi, L., Torsvik, T. H., & Lee, C. T. (2007). Episodic precambrian subduction. *Earth and Planetary Science Letters*, *262*(3-4), 552-562.

O'Neill, C. J., Kobussen, A., & Lenardic, A. (2010). The mechanics of continental lithosphere–asthenosphere coupling. *Lithos*, *120*(1-2), 55-62.

Parman, S. W., Grove, T. L., Dann, J. C., & De Wit, M. J. (2004). A subduction origin for komatiites and cratonic lithospheric mantle. *South African Journal of Geology*, *107*(1-2), 107-118.

Parsons, B., & Sclater, J. G. (1977). An analysis of the variation of ocean floor bathymetry and heat flow with age. *Journal of geophysical research*, *82*(5), 803-827.

Pearson, D. G., & Wittig, N. (2008). Formation of Archaean continental lithosphere and its diamonds: the root of the problem. *Journal of the Geological Society*, *165*(5), 895-914.

Rader, E., Emry, E., Schmerr, N., Frost, D., Cheng, C., Menard, J., ... & Geist, D. (2015). Characterization and petrological constraints of the midlithospheric discontinuity. *Geochemistry, Geophysics, Geosystems*, *16*(10), 3484-3504.

Rudnick, R. L., Gao, S., Holland, H. D., & Turekian, K. K. (2003). Composition of the continental crust. *The crust*, *3*, 1-64.

Rychert, C. A., Harmon, N., Constable, S., & Wang, S. (2020). The nature of the lithosphere-asthenosphere boundary. *Journal of Geophysical Research: Solid Earth*, *125*(10), e2018JB016463.

Rychert, C. A., & Shearer, P. M. (2009). A global view of the lithosphere-asthenosphere boundary. *Science*, *324*(5926), 495-498.

Saha, S., Dasgupta, R., & Tsuno, K. (2018). High pressure phase relations of a depleted peridotite fluxed by CO2-H2O-bearing siliceous melts and the origin of mid-lithospheric discontinuity. *Geochemistry, Geophysics, Geosystems*, *19*(3), 595-620.

Selway, K. (2018). Electrical discontinuities in the continental lithosphere imaged with magnetotellurics. *Lithospheric discontinuities*, 89-109.

Selway, K., & O'Donnell, J. P. (2019). A small, unextractable melt fraction as the cause for the low velocity zone. *Earth and Planetary Science Letters*, *517*, 117-124.

Selway, K., O'Donnell, J. P., & Özaydin, S. (2019). Upper mantle melt distribution from petrologically constrained magnetotellurics. *Geochemistry, Geophysics, Geosystems*, *20*(7), 3328-3346.

Sens-Schönfelder, C., & Wegler, U. (2006). Passive image interferometry and seasonal variations of seismic velocities at Merapi Volcano, Indonesia. *Geophysical research letters*, *33*(21).

Simon, N. S., Carlson, R. W., Pearson, D. G., & Davies, G. R. (2007). The origin and evolution of the Kaapvaal cratonic lithospheric mantle. *Journal of Petrology*, *48*(3), 589-625.

Simpson, F., & Tommasi, A. (2005). Hydrogen diffusivity and electrical anisotropy of a peridotite mantle. *Geophysical Journal International*, *160*(3), 1092-1102.

Sleep, N. H. (2005). Evolution of the continental lithosphere. *Annu. Rev. Earth Planet. Sci.*, *33*, 369-393.

Snieder, R. (2004). Extracting the Green's function from the correlation of coda waves: A derivation based on stationary phase. *Physical review E*, *69*(4), 046610.

Sodoudi, F., Yuan, X., Kind, R., Lebedev, S., Adam, J. M. C., Kästle, E., & Tilmann, F. (2013). Seismic evidence for stratification in composition and anisotropic fabric within the thick lithosphere of Kalahari Craton. *Geochemistry, Geophysics, Geosystems*, *14*(12), 5393-5412.

Stein, C. A., & Stein, S. (1992). A model for the global variation in oceanic depth and heat flow with lithospheric age. *Nature*, *359*(6391), 123-129.

Su, B., & Chen, Y. (2018). Making cratonic lithospheric mantle. *Journal of Geophysical Research: Solid Earth*, *123*(9), 7688-7706.

Sun, W., & Kennett, B. L. N. (2017). Mid-lithosphere discontinuities beneath the western and central North China Craton. *Geophysical Research Letters*, *44*(3), 1302-1310.

Tesauro, M., Kaban, M. K., & Aitken, A. R. (2020). Thermal and compositional anomalies of the Australian upper mantle from seismic and gravity data. *Geochemistry, Geophysics, Geosystems*, *21*(11), e2020GC009305.

Tharimena, S., Rychert, C. A., & Harmon, N. (2016). Seismic imaging of a mid-lithospheric discontinuity beneath Ontong Java Plateau. *Earth and Planetary Science Letters*, *450*, 62-70.

Tucker, R. D., Roig, J. Y., Moine, B., Delor, C., & Peters, S. G. (2014). A geological synthesis of the Precambrian shield in Madagascar. *Journal of African Earth Sciences*, *94*, 9-30.

Wang, X., Zhu, P., Kusky, T. M., Zhao, N., Li, X., & Wang, Z. (2015). Dynamic cause of marginal lithospheric thinning and implications for craton destruction: a comparison of the North China, Superior, and Yilgarn cratons. *Canadian Journal of Earth Sciences*, *53*(11), 1121-1141.

White, R. S., McKenzie, D., & O'Nions, R. K. (1992). Oceanic crustal thickness from seismic measurements and rare earth element inversions. *Journal of Geophysical Research: Solid Earth*, *97*(B13), 19683-19715.

Wirth, E. A., & Long, M. D. (2014). A contrast in anisotropy across mid-lithospheric discontinuities beneath the central United States—A relic of craton formation. *Geology*, *42*(10), 851-854.

Yoshizawa, K. (2014). Radially anisotropic 3-D shear wave structure of the Australian lithosphere and asthenosphere from multi-mode surface waves. *Physics of the Earth and Planetary Interiors*, *235*, 33-48.

Yoshizawa, K., & Kennett, B. L. N. (2015). The lithosphere-asthenosphere transition and radial anisotropy beneath the Australian continent. *Geophysical research letters*, *42*(10), 3839-3846.

Yuan, H., & Romanowicz, B. (2010). Lithospheric layering in the North American craton. *Nature*, *466*(7310), 1063-1068.

**The lithospheric architecture of Australia from seismic receiver functions**

Andrew Birkey[1,*], Heather A. Ford[1], Page Dabney[2], and Gillian Goldhagen[1]

[1]Department of Earth and Planetary Sciences, University of California – Riverside, Riverside, CA, USA.

[2]Department of Geosciences, Princeton University, Princeton, NJ, USA .

*Submitted with revisions to the Journal of Geophysical Research – Solid Earth*

*Corresponding author:

Department of Earth and Planetary Sciences, University of California – Riverside

900 University Avenue, Riverside, California, 92521

Email: abirk001@ucr.edu

**Abstract**

In the past decade mounting evidence has pointed to complex, layered structure within and at the base of the mantle lithosphere of tectonically quiescent continental interiors. Sometimes referred to as negative velocity gradients (NVGs) or mid-lithospheric discontinuities (MLDs), the origin of intra-lithospheric layering has prompted considerable discussion, particularly as to how they may result from continent formation and/or evolution. Previous Sp receiver function analysis in Australia found evidence for complex lithospheric layering beneath permanent stations located within the North, South and West Australian Cratons and characterized these as MLDs (Ford et al., 2010). This study provides an update. The Sp receiver function results are presented for 35 permanent broadband stations. We observe the lithosphere-asthenosphere boundary (LAB) on the eastern margin of the continent, at depths of 75-85 km. The cratonic core of Australia has discontinuities within the lithosphere, and no observable LAB. On the western margin of the continent we observe several stations with an ambiguous phase that may correspond to either an MLD or the LAB. We also observe multiple negative phases at most stations, suggesting a complex and heterogeneous lithosphere. Australian MLDs are likely linked to the presence of hydrous minerals in the mid-lithosphere and may result from ancient processes such as subduction, plume interaction, or melt infiltration from the paleo-LAB.

## 1. Introduction

### *1.1 Defining the lithosphere-asthenosphere boundary and mid-lithospheric discontinuities*

The lithosphere is the solid portion of the Earth that moves coherently over the convecting, plastic asthenosphere. Unlike the asthenosphere, the lithosphere is relatively rigid, due in large part to colder temperatures (Sleep, 2005), leading to faster seismic wavespeeds. The transition from the lithosphere to the asthenosphere is referred to as the lithosphere-asthenosphere boundary (LAB), a region of the Earth's interior of particular interest because it is a ubiquitous plate boundary, and because the interaction between the lithosphere and asthenosphere has major implications for understanding plate tectonics and the dynamics of the mantle.

Different methods estimate variable depths to this boundary due to differences in measurement resolution and properties being observed. For example, in the Kaapvaal craton (an ancient, thick, stable continental core) xenolith thermobarometry shows the lithosphere to be 195-215 km thick (Eaton et al., 2009), while magnetotelluric surveys suggest a thickness of ~230 km in the same region (Evans et al., 2011). In addition, there are differences in how the boundary is defined. Seismically, it is the velocity decrease from cold, fast lithosphere to warm, slow asthenosphere at 50 to >250 km (Fischer et al., 2010; Thybo, 2006). One common definition of the transition from lithosphere to asthenosphere is the point along a geotherm where temperature approach 90% of the value of the adiabatically-determined mantle potential temperature (~0.9 $T_M$) and heat transfer changes from dominantly conduction in the lithosphere to convection in the asthenosphere (Sleep

2005). In some regions, magnetotelluric inversions can be used to determine the boundary between lithosphere and asthenosphere: very old lithosphere tends to be highly resistive due to mineralogical depletion and dehydration during past melting events, while the asthenosphere below is generally more conductive (Baba et al., 2006; Eaton et al., 2009; Evans et al., 2005; Hirth et al., 2000). Dehydration and depletion couple with temperature to create a viscosity difference between layers: the cooler, dryer, more depleted lithosphere is more viscous than the hotter, wetter and more fertile asthenosphere (Hirth et al., 2000; Hirth & Kohlstedt, 1996; Karato & Jung, 1998; Lee et al., 2005; Lee 2006; Sleep 2005). This viscosity difference may correspond to a change in strength as well, going from the mechanically stronger lithosphere to a weaker asthenosphere (Lee et al., 2005). Because the lithosphere is more viscous than the asthenosphere, strain will be localized at the base of the lithosphere. Thus, the lithosphere-asthenosphere boundary may also represent a change in anisotropy as plate motions align olivine grains at the base of the lithosphere (Gaherty et al., 1999; Levin & Park, 2000; Yuan & Romanowicz, 2010).

While the seismic lithosphere-asthenosphere boundary is a relatively sharp, discrete change in oceanic and Phanerozoic continental lithosphere, that is not the case in older lithosphere, where the lithosphere-asthenosphere boundary is frequently characterized as being transitional, extending over tens of kilometers (Abt et al., 2010; Fischer et al., 2010; Ford et al., 2010; Rychert et al., 2020). Thus, some authors instead refer to it as the lithosphere-asthenosphere transition (LAT; Mancinelli et al., 2017; Yoshizawa, 2014; Yoshizawa & Kennett, 2015). In cratonic regions where the lithosphere is thick, this

transition occurs gradually over 60 km or more (Mancinelli et al., 2017). Both the depth of the lithosphere-asthenosphere boundary and the step-like nature of changes in seismic velocities across the boundary are well correlated with tectonic age. Global tomography models show that regions of old continental crust (i.e., cratons) have fast seismic velocities to depths greater than 150 km, whereas younger, more tectonically active regions transition to slower seismic velocities at shallower depths (Auer et al., 2014; Nettles & Dziewoński, 2008; Ritsema et al., 2011; Schaeffer & Lebedev, 2013). One promising avenue of investigation has been the use of Sp and Ps receiver functions to image the interface between lithosphere and asthenosphere. Receiver functions rely on conversions between P and S-waves at sharp seismic boundaries; a velocity increase with depth yields a "positive pulse", while a velocity decrease with depth yields a "negative pulse" (see **Figure 1.3**). This method has allowed for the high-resolution imaging of seismic discontinuities in the lithosphere including the Moho and the lithosphere-asthenosphere boundary. Rychert and Shearer (2009) used this technique to globally image the lithosphere-asthenosphere boundary, observing a negative boundary between 70 and 100 km. Other receiver function studies have observed the lithosphere-asthenosphere boundary in cratonic regions at depths of up to 250 km, and oftentimes no lithosphere-asthenosphere boundary is observed (Abt et al., 2010; Ford et al., 2010; Hopper & Fischer, 2015; Kennett et al., 2017; Shen et al., 2019; Sodoudi et al., 2013).

Regions of particularly thick lithosphere have been shown to possess velocity decreases of 5-7% at depths between 80 and 150 km, above the seismically-estimated lithosphere-

asthenosphere boundary in such regions (Carlson et al., 2005; Griffin et al., 2009; Schaeffer & Lebedev, 2013). These discontinuities are usually termed mid-lithospheric discontinuities (MLDs). Abt et al. (2010), Fischer et al. (2010), and Ford et al. (2010) first termed these discontinuities as mid-lithospheric discontinuities, but they had been observed previously (Chen, 2009; Dueker et al., 2001; Hales, 1969; Rychert & Shearer, 2009; Thybo, 2006; Wittlinger & Farra, 2007;) and have since been observed in numerous cratons (Bodin et al., 2013; Ford et al., 2016; Foster et al., 2014; Hansen et al., 2013; Hopper et al., 2014; Hopper & Fischer, 2015; Kennett et al., 2017; Kind et al., 2012; Kumar et al., 2012; Lekic and Fischer, 2014; Porritt et al., 2015; Selway et al., 2015; Shen et al., 2019; Sodoudi et al., 2013; Sun et al., 2018; Wölbern et al., 2012) and even in some regions of anomalously thick oceanic lithosphere (Tharimena et al., 2016). In some cases, these discontinuities are continuous across Precambrian terrane boundaries, but in others they vary within terranes and across boundaries. Some hypothesize that mid-lithospheric discontinuities may have formed as a result of cratonic thickening during the closure of ocean basins in the Precambrian, representing the scars of ancient and prolonged deformation within and at the base of the lithosphere (Cooper & Miller, 2014).

Despite mid-lithospheric discontinuities being nearly ubiquitous in cratons, there is much debate as to their origin. There is no evidence to suggest a phase transition occurring at the same depths (Carlson et al., 2005; Griffin et al., 2009). Mechanisms that have been invoked to explain them include partial melt (Kumar et al., 2012; Thybo, 2006), ancient solidified magma (Rader et al., 2015), partial melt in thermally perturbed cratons (Aulbach et al.,

2017a), elastically-accommodated grain boundary sliding (Karato, 2012), changes in olivine Mg# (Yuan & Romanowicz, 2010), hydrous minerals (Hopper & Fischer, 2015; Selway et al., 2015), or anisotropy (Rychert & Shearer, 2009; Wirth & Long, 2014). In **Section 4.3** we explore the potential mechanisms responsible for mid-lithospheric discontinuities in cratonic Australia.

*1.2 Continental tectonics and observed seismic structure*

Australian lithosphere preserves a long and complex tectonic history. The western two-thirds of the continent consists of Archean and Proterozoic cratons, while the eastern third is dominantly Phanerozoic-aged orogens (**Figure 1.1**). Precambrian Australia is generally divided into the West Australian Craton, the North Australian Craton, and the South Australian Craton. Most components of these composite cratons were formed by roughly 1.8 Ga and were sutured together by the Neoproterozoic as part of the supercontinent Rodinia (Betts et al., 2002; Cawood & Korsch, 2008). The amalgamation of these cratons can be observed seismically throughout central Australia as lower wavespeeds above 80 km, and anomalously strong radial anisotropy (Sun & Kennett, 2016; Wei et al., 2018; Yoshizawa, 2014; Yoshizawa & Kennett, 2015). In general, these cratons are thicker, colder, denser, and more depleted than the Phanerozoic east, with a gradational seismic lithosphere-asthenosphere boundary and mid-lithospheric discontinuities at depths between 70 and 90 km (Debayble & Kennett, 2000; Fichtner et al., 2010; Fishwick et al., 2005; Fishwick & Rawlinson, 2012; Fishwick & Reading, 2008; Ford et al., 2010; Tesauro et al., 2020; Yoshizawa, 2014; Yoshizawa & Kennett, 2015).

**West Australian Craton:** This composite craton is composed of the Yilgarn and Pilbara Cratons, which both locally preserve Archean crust in granite-greenstone belts (Barley et al., 1998; Betts et al., 2002; Myers et al., 1993). These cratons do not exceed ~800°C to 200 km depth and are highly depleted (olivine Mg# >90.5) with a strongly resistive cratonic root (Sun et al., 2018; Tesauro et al., 2020; Wang et al., 2014). Proterozoic orogens between the two cratons display a deepened, gradational Moho and complex upper crust; the cratons have a shallower, sharper Moho and simple crustal structure, with a thickened Moho (~40 km) in the Northern Yilgarn (Reading et al., 2007; Reading et al., 2012; Reading & Kennett, 2003). Additionally, the terranes of the West Australian Craton appear to have distinct crustal wavespeeds, implying that these were set properties before amalgamation (Reading et al., 2007). The seismic lithosphere-asthenosphere boundary in the West Australian Craton is likely very deep, with tomography estimating a potential depth of 100 to >250 km (Yoshizawa & Kennett, 2015). Previous receiver function studies have observed mid-lithospheric discontinuities at KMBL, MBWA, and NWAO between 70 and 85 km, with a potential lithosphere-asthenosphere boundary at NWAO at 164 km (Ford et al., 2010; Kumar et al., 2007).

**North Australian Craton:** This region is composed predominantly of Proterozoic basins rimmed by orogens (Betts et al., 2002; Cawood & Korsch, 2008; Myers et al., 1996). This region is typified by thick, depleted lithosphere (~200 km and olivine Mg# 90.5), with complex mid-lithospheric structure, and low attenuation (Kennett et al., 2017; Kennett &

Abdullah, 2011; Tesauro et al., 2020). There is a marked contrast between the eastern edge of the North Australian Craton and the Phanerozoic Thomson Orogen, with the former having thicker crust (Kennett & Liang, 2020). Earlier receiver function studies observed mid-lithospheric discontinuities at FITZ and WRAB at 81 km, and the lithosphere-asthenosphere boundary at 180 km (Ford et al., 2010; Kumar et al., 2007).

**South Australian Craton:** The South Australian Craton has Archean gneissic terranes in the Gawler Craton, rimmed by Proterozoic orogens and basins (Cawood & Korsch, 2008; Conor & Preiss, 2008; Daly et al., 1998). Unlike the other Australian cratons, the South Australian Craton has a higher temperature, thinner lithosphere with slower wavespeeds, and a less depleted mantle (olivine Mg# ~89.5); enrichment has been interpreted as due to the possible refertilization of the mantle during the Proterozoic, while the thinned lithosphere is more likely due to the detachment of the South Australian Craton from Antarctica (Rawlinson et al., 2016; Tesauro et al., 2020; Yoshizawa & Kennett, 2015). Despite these differences, there is still a marked change between the South Australian Craton and Phanerozoic lithosphere to its east, with a thinning of the Moho and seismic lithosphere to the east accompanied by changes in reflectivity (Liang & Kennett, 2020). Ford et al. (2010) observed a mid-lithospheric discontinuity at FORT at 79 km, while BBOO and STKA both had a visible lithosphere-asthenosphere boundary at 131 and 104 km respectively.

**Phanerozoic Australia:** Separating the Precambrian west and the Phanerozoic east is the Tasman Line: predominantly defined by surface geology, this line may be linked to the breakup of Rodinia (Direen & Crawford, 2003). There is a sharp transition in wavespeeds at depth between the east and west, but it is further to the east than most proposed models of the Tasman Line, suggesting a complex transition at depth between terranes of varying age (Kennett et al., 2004). Following the breakup of Rodinia, successive orogenic events accreted new lithosphere onto the cratonic core over a roughly 500 million-year time span (Betts et al., 2002). During the Cenozoic, Australia drifted north-northeast over a potential mantle plume, resulting in volcanic chains along the eastern margin that can be observed as lower seismic velocities and a shallower seismic lithosphere-asthenosphere boundary (Davies et al., 2015; Ford et al., 2010; Rawlinson et al., 2016; Wei et al., 2018). In contrast to most of the Precambrian west, eastern Australia has thinner, warmer lithosphere increasing stepwise to the west with a well-defined lithosphere-asthenosphere boundary between 70 and 100 km (Demidjuk et al., 2007; Fishwick et al., 2008; Ford et al., 2010).

## Data and Methods

### *2.1 Data and data preprocessing*

To begin the updated analysis of lithospheric structure of Australia, data were requested for 88 stations from five networks (AU, G, IU, II and S1). Data requests were limited to data archived at the Incorporated Research Institutions for Seismology (IRIS) Data Management Center (DMC). Data were also requested from network S1 (Seismometers in Schools): ultimately none of these stations produced Sp receiver functions of sufficient

quality to be included in the results section. Our final selection of 35 stations is an increase of 17 from Ford et al. (2010), with 10 years of additional data. On average, our Ps receiver functions had 950 events, while Sp receiver functions had 245 stations per event. There was an average increase of 238 events per station for Sp results, and a 1040 event increase for Ps results. To prepare the data for later analysis, seismograms were quality controlled to ensure continuity with no gaps or spikes, initially filtered from 0.01 to 9.9 Hz and rotated from north and east into radial and transverse components. Once completed, direct P and S phases were selected by automated algorithm, a procedure originally described in Abt et al. (2010). From there, the data were rotated again into the P-SV-SH coordinate system. This rotation minimizes the amount of parent phase energy on the daughter component. The method used in this study follows from Abt et al. (2010) with minor variations to account for multiple stations in close proximity using an array-based procedure as described in Lekic and Fischer (2014).

*2.2 The calculation of Sp and Ps receiver functions*

Sp receiver functions were bandpass-filtered to 0.03-0.5 Hz and limited to events occurring within an epicentral distance window of 55-75° and depths of less than 300 km—the direct S phase often arrives very close in time to other phases, and these constraints allow for the highest likelihood of isolating converted phases (Wilson et al., 2006). The deconvolution to generate the Sp receiver functions was performed using an extended-time multi-taper

cross correlation method (Helffrich, 2006), which builds upon the multi-taper method of Park and Levin (2000), with the added benefit of preserving the amplitude of phases at all depths within our study.

The receiver functions were stacked by station to enhance the signal-to-noise ratio of discontinuity phases. When binning per station, individual receiver functions were normalized relative to the amplitude of the parent phase; this allowed us to more directly compare amplitudes from different stations. An important step of this process was determining the statistical robustness of the resulting receiver function. To achieve this, a bootstrapping analysis was performed on the data. The published results are the mean of the receiver functions generated through the bootstrap analysis. The data set was also used to calculate two sigma uncertainties at each depth, allowing us to determine the uncertainties in receiver function phase depth and amplitude. In order to correct for variations in arrival time as a function of distance and to migrate the receiver functions to depth, the Australian Seismological Reference Model (AuSREM) was used (Kennett and Salmon, 2012). The AuSREM has a crustal component (Salmon et al., 2013) which includes Vp and Vs and was determined from earlier receiver function studies, seismic refraction, reflection, and tomography. A complete list of the references used to generate the crustal component of AuSREM can be found in Table 2 of Salmon et al. (2012). The mantle component of AuSREM (Kennett et al., 2012) provided values of Vp and Vs, gridded in 0.5° increments in latitude and longitude, and 25 km increments in depth from

75 km to 300 km. The model itself was generated using data from a variety of surface wave, body wave, and regional tomography models from the region.

It should be noted that a common concern of Sp receiver function analysis in the application of imaging mantle structure is the potential that the negative phase observed immediately beneath the Moho phase is a side lobe of the positive Moho phase. In Lekić and Fisher (2017) it was demonstrated that side lobes can become an issue in instances where Sp receiver functions are calculated using frequency domain methods such as extended-time multi-taper, which we use in this study. However, when the results are not bandwidth limited (e.g., the upper corner frequency limit extends beyond 0.125 Hz) and post-S arrivals are excluded (as we do here), this is not likely to be an issue. More qualitatively, we observe no correlation between the depths of the Moho and negative phases (**Figure 1.6**), as might be expected if the negative phase were a side lobe of the Moho phase (i.e., deeper Moho phase produces a side lobe with a deeper negative phase).

We also calculated Ps receiver functions. The Ps receiver functions were calculated in a method similar to that described above for Sp receiver functions. Exceptions to this are that the Ps receiver functions were filtered to 0.02-2 Hz and limited to epicentral distances of 35-80° with no hypocenter depth cut-off. Additionally, while the Sp receiver functions published in this study are flipped in time and polarity reversed, no such corrections are needed for Ps receiver functions. Due to potential interference from crustal reverberations the Ps receiver functions are not used to constrain potential mantle interfaces, which is the

focus of our study. However, we do include them in our results in order to demonstrate the robustness of inferred Moho depths from AuSREM (**Section 3.1**).

This study presents an updated catalog of Sp receiver function results from the earlier study by Ford et al. (2010). The methodology here is similar with minor variations. Both studies utilize the same data preparation, coordinate system (P-SVSH) rotation, and waveform windowing described in Abt et al. (2010). Both also employ the same epicentral distance and depth cut-offs. The biggest methodological differences are in the deconvolution methods and in the migration models used. In Ford et al. (2010) all waveforms were simultaneously deconvolved and migrated using a frequency domain, water-level stabilized deconvolution (Bostock, 1998). The migration model varied from station-to-station, using H-k stacking (Zhu & Kanamori, 2000) to determine the crustal velocities and applying a uniform mantle model of AK135 (Kennett, 1995) at all stations. In our updated study we individually deconvolve each waveform using an extended-time multi-taper cross correlation method (Helffrich, 2006) and later stack and migrate the receiver functions using the AuSREM velocity model. Because AuSREM is a local model, it provides us with better constraints for the Australian continent than utilizing H-k stacking for the crust and a global mantle model such as AK135. A final important distinction is that our study has more data, providing an extra decade of data compared to Ford et al. (2010), and allowed for the use of stations which previously only had a few years of data, increasing the number of stations analyzed for mantle structure from 14 to 34.

## Results

*3.1 Ps receiver function results*

As mentioned above, Ps receiver functions are not commonly used to image upper mantle discontinuities because of contamination from crustal reverberations. However, they are particularly sensitive to the Moho discontinuity and thus they are a useful independent constraint on Moho depths estimated from other methods, including Sp receiver functions. Throughout most of Australia, the Moho as estimated by Ps receiver functions falls between 35 and 45 km, with 7 stations recording a deeper Moho (**Figure 1.2**). In addition, the thickness of the crust seems to be in rough agreement with the age and local geology (i.e., particularly thick crust is seen in the cratons and Proterozoic orogens, with much thinner crust in the Phanerozoic east).

**Figure 1.2** shows both the misfit between the depth to Moho as predicted by AusMoho (Kennett et al., 2013; Salmon et al., 2012;) and the depth to Moho as determined from our Ps receiver functions. The AusMoho is a compilation of data from multiple seismic methods (i.e refraction and reflection studies, receiver functions, and tomography). The Moho was defined as the point below which compressional velocities are greater than 7.8 km/s and shear velocities are greater than 4.4 km/s; a grid was constructed for the continent using the weighted interpolation of data from different sources depending on the quality of the individual method (Kennett et al., 2013; Salmon et al., 2012). Most stations have a misfit of 4 km or less: this indicates that the AuSREM is robust and agrees well with our Ps results.

Most stations showed relatively good agreement between the depth of the Moho as estimated by Sp and Ps (see **Figure S1.1**). However, there were some noticeable outliers. At station CNB, Ps receiver functions predict a deeper Moho than Sp by almost 10 km; additionally, neither estimate falls within the error bars of the other. Station INKA had a similar noticeable discrepancy, with nearly 20 km between Moho estimates. Station CAN also has a large gap between the Ps estimate and the Sp estimate, with a much deeper Ps estimate. Station MUN and PSA00 have discrepancies between the Ps and Sp estimate, but in these cases the Ps estimate was shallower than the Sp estimate. At all other stations the estimates from the two methods fell within one another's error bars or were very close. When there are discrepancies between the two methods in the estimated depth to the Moho, we defer to the results of the Ps receiver functions because they are better able to resolve structure at Moho depths due to their higher frequency content. The Moho depths for both Ps and Sp are reported in **Table 1**.

*3.2 Quality control and phase picking of Sp receiver functions*

The Sp receiver functions were calculated for 88 stations across the Australian continent. However, limited data availability and/or quality ultimately restricted the total number of stations used in our subsequent analysis of mantle structure to 34 stations (**Figure 1.3**). The receiver function quality was rated as good, fair or poor. For a station to be rated fair or good more than 50 events were required, as stations with fewer events typically yielded receiver functions that are unstable (rapid, large amplitude oscillations). Other metrics used

in determining receiver function quality included the presence of a well-defined positive phase found at depths similar to the estimated Moho and relatively small error bars. **Figure S1.2** includes all of the Sp receiver functions calculated, including those which were rated as poor and not included in our analysis of lithospheric structure.

In this study, as in Ford et al. (2010), the criteria for the selection of a negative phase within a receiver function is a critical first step in determining the type of structure the negative phase(s) might represent. To begin, negative phases can only be selected if they fall between the positive phase inferred to be the Moho (magenta lines in **Figure S1.2**), and the depth corresponding to the base of the negative velocity gradient determined from the AuSREM, plus an additional 25 km to account for uncertainty in the negative velocity gradient depth. This uncertainty range has been chosen based on the interpolated model spacing from the mantle component of the AuSREM (Kennett et al., 2012). From there, we designate as many as two of the largest negative amplitude phases as significant, as taken from the mean amplitude of the single-binned Sp receiver function (**Figure 1.3** and **Figure S1.2**). The highest amplitude negative phase is designated "negative phase 1" in later discussion and selected for at every Good/Fair station. It is marked with a solid black, horizontal line at each station in **Figure 1.3**. If another negative phase of comparable amplitude is present, it is called the "negative phase 2", and is marked with a solid gray, horizontal line in **Figure 1.3**. Three things should be noted regarding these designations. First, we assume nothing about either phase in terms of their physical properties or what sort of boundary they represent. Both represent a decrease in velocity with increasing depth somewhere within the mantle. Both could be located within the potential lithosphere-

asthenosphere boundary depth range or both could be located at depths associated with the lithospheric mantle, or they could each represent a different structure. We endeavor to define boundaries associated with the negative phases in **Section 3.4**. Second, while negative phase 1 is typically shallower than negative phase 2, this is not universally true (see stations FORT and LCRK in **Figure 1.2** or **Table 1.1**). Third, the decision to select one versus two negative phases at a given station is subjective and varies from station to station. Not all stations have a second phase selected. In contrast to Ford et al. (2010), we have chosen to select more than one phase because many stations have multiple negative phases that are well-resolved. Our intention in selecting the two largest phases is to more completely describe the mantle structure present beneath Australia. The depth and amplitude of these negative phases, along with their associated uncertainties, are included in **Table 1.1**. In **Figure 1.3** and **Table 1.1** we also include information on up to two smaller negative phases (dashed gray lines). However, these negative phases are not directly compared to the AuSREM in later discussion (**Section 3.4**). We acknowledge that while it is possible to pick and analyze every negative phase that is statistically well-resolved (i.e., negative phase energy exceeding zero when including two sigma confidence limits), the goal of this study is to focus on the largest amplitude/most significant phases in order to place first order constraints on mantle structure beneath Australia.

*3.3 Negative phase depths across Australia from Sp receiver functions*

As described above, our analysis is restricted to up to the two highest amplitude, most robustly imaged negative phases present at each station labeled good or fair. The collectively averaged depth of these phases is 94 km and the median depth is 81 km, and the average depth to the largest negative phase (referred to earlier as negative phase 1) at each station is 83 km, with a median depth of 78 km. 88% of negative phase 1 phases fall within 15 km of the negative phase 1 average (83 km), while only 33% of all negative phases fall within the average of all negative phases (94 km). This observation indicates that while the largest negative phases (negative phase 1) tend to cluster at a single depth, negative phase 2 is significantly more distributed. This is also demonstrated in **Figure 1.4**.

There appears to be no systematic variation between negative phase depth and tectonic age in Australia although there does appear to be some consistency regionally. For example, in **Figure 1.5a** stations located within/near the Yilgarn Craton (i.e., MEEK, MORW, BLDU, MUN, NWAO and KMBL) have their negative phase 1 located within a very consistent depth range of 74-79 km. This is also demonstrated in profile DD' in **Figure 1.3**. This remarkable consistency within the Yilgarn is not observed everywhere elsewhere in Australia, as variations in depth in most regions tend to be greater than 5 km, although regional trends are still apparent, such as on the eastern margin of Australia (profile AA' in **Figure 1.3**).

The average amplitude of negative phase 1 is -0.006 and there appears to be no correlation between tectonic age and amplitude, although some weak correlations between regional location and amplitude may exist as sometimes, stations co-located near each other appear to have similar amplitudes **(Figure 1.5**). The average amplitude of negative phase 2 is -0.0036, which is roughly half the amplitude of the average of negative phase 1 amplitudes. In the following sections we carefully consider variations in the depth and amplitude of both negative phases as they compare to the previously published work of Ford et al. (2010) as well as how they relate to the mantle portion of the AuSREM.

*3.4 Comparison to previously published Sp receiver function results*

This study is an update to Ford et al. (2010), calculated using a similar method with slight variations to our own (see 2.2 for more information). Ford et al. (2010) used the negative velocity gradient inferred from surface wave tomography (Fischwick et al., 2008) to define the potential lithosphere-boundary range at each station. We use a similar definition, but utilize the AuSREM mantle velocity component (Kennett et al., 2012). Beyond differences in velocity model used, the process to determine whether the negative phase represents a conversion at the lithosphere-asthenosphere boundary or a discontinuity within the lithosphere (i.e., a mid-lithospheric discontinuity) is the same. At each station a 1D velocity profile is obtained from the AuSREM. The depth range of the negative velocity gradient is recorded at the location (see **Table 1.1**), as well as shown as a grey box in **Figure 1.3** and in **Figure S1.2**. The 1D profile for each station is shown in **Figure 1.9**. If negative phase 1 or 2 falls within the range of the negative velocity gradient, then it is interpreted to

potentially be a conversion at or within the lithosphere-asthenosphere boundary. If the negative phase is observed to be shallower than the negative velocity gradient, then it is interpreted to be a mid-lithospheric discontinuity. Due to the fact that we are picking the two largest negative phases at some stations, you will notice in **Table 1.1** that some stations have both a lithosphere-asthenosphere boundary phase as well as a mid-lithospheric discontinuity phase listed ("Both" in **Table 1.1**). If a negative phase falls on the cusp of the negative velocity gradient, but has overlapping error bars, we denote that it could be "Either", meaning that the interpretation is not clear. We report our results regionally, starting with the Tasmanides, then the North Australian Craton, South Australian Craton, and West Australian Craton.

**Phanerozoic Australia:** In eastern Australia at stations CTAO (within 1 km) and TOO (within 9 km) our results fall within error of the originally published work of Ford et al. (2010). At station YNG, the fit is slightly poorer, with a misfit of 11 km, however even then the error bars from the two studies do overlap. The same overlapping error is also true for station ARMA, however, upon closer inspection of receiver functions it has a small but well constrained pulse of negative phase energy next to the largest negative phase (**Figure 1.3**) that agrees within 1 km of the originally reported results of Ford et al. (2010). In Phanerozoic Australia, the stations ARMA, EIDS, TOO, YNG, RIV, CNB, CMSA, and CTAO all have negative phases that clearly fall within the negative velocity gradient inferred from the AuSREM. The negative phases at these stations are thought to represent a conversion at or within the lithosphere-asthenosphere boundary, in agreement with Ford

et al. (2010). At most of these stations, the negative velocity gradient falls within ±25 km the same range reported in Ford et al. (2010). Exceptions to this include stations CTAO and TOO, which had no reported negative velocity gradient in Ford et al. (2010) likely due to the fact that the gradient was shallower than what was resolvable. At station INKA (within the Thomson Orogen), there is no negative velocity gradient at lithospheric depths, and thus we interpret the negative phase at 61 km to be a mid-lithospheric discontinuity.

Ford et al. (2010) observed a distinct variation in amplitude correlated with depth at the stations where they found a lithosphere-asthenosphere boundary phase (mostly along the eastern margin of the continent). While we cannot directly compare our results (due to normalization and deconvolution differences), we can compare possible trends in our new results to the old ones. As discussed above, we observed relatively modest variations in amplitude between stations, and no correlation with tectonic age is seen (**Figure 1.5b,d**). Using best fitting models of the receiver function amplitude, locations of recent volcanism, and inferred topography of the lithosphere-asthenosphere boundary, Ford et al. (2010) postulated that either mantle melting influenced lithospheric thickness or that melt focused in regions of thinner lithosphere. In **Figure 1.7**, we plot our results including those at stations BBOO and STKA: though we do not observe the lithosphere-asthenosphere boundary at station BBOO, we want to compare the trend to Ford et al. (2010). We observe a weak correlation between negative phase depth and amplitude for stations YNG, ARMA, TOO and to a lesser degree for stations EIDS and CTAO (**Figure 1.7**). However, stations BBOO and STKA again prove problematic and when new stations from this study are

added, the correlation disappears completely (**Figure 1.7**). This discrepancy indicates that the apparent correlation observed in Ford et al. (2010) was the result of sampling bias and presents a clear argument for the densification of permanent networks to accurately describe lithospheric structure.

**North Australian Craton:** In the North Australian Craton, at stations FITZ and WRAB, the depth of the largest amplitude negative phase (negative phase 1) determined in this study falls within error of the depth determined for the largest amplitude negative phase in the Ford et al. (2010) study. At station FITZ, our results are within 5 km of the originally recorded negative phase depths of Ford et al. (2010). At station COEN there is a slight discrepancy, with our negative phase falling at 85 km versus 67 km in Ford et al. (2010), outside of uncertainties. The largest negative phase at station WRAB is located 10 km shallower than the negative phase reported in Ford et al. (2010), within the ±14 km of uncertainty. It is possible that the small changes in negative phase depth are due to the difference in velocity model used in the migration. Abt et al. (2010) migrated Sp receiver functions using AK135 as well as more regionally accurate Vp and Vs models and found that depths changed by no more than 6 km. It is likely that the newer values reported are more accurate since the original migration model used in Ford et al., (2010) was the globally averaged, 1D model AK135, whereas the AuSREM used in this study is specific to Australia. Another key difference between this study and Ford et al. (2010) is that we also report the negative phase depths for additional phases. This does not mean that those additional phases were not present in the original study. For example, in this study, at

station WRAB, the largest negative phase (negative phase 1) is located at a depth of 71 km, while a second significant negative phase (negative phase 2) is found at 91 km, and two additional negative phases are observed at 135 and 198 km. Upon comparison to the plotted Sp receiver function in Figure 6d (Ford et al., 2010), it is clear that an additional phase is located at ~140 km, which agrees with our observations. At stations FITZ, KDU, MTN, and WRAB we observe negative pulses that fall above the negative velocity gradient interpreted from the AuSREM; at stations MTN and WRAB we observe multiple mid-lithospheric discontinuities. However, at stations FITZ and KDU we observe a shallower mid-lithospheric discontinuity and a deeper negative phase that does correspond to the negative gradient in the AuSREM, thus we interpret these as the lithosphere-asthenosphere boundary. Station WRKA (which is not strictly within the North Australian Craton, but adjacent), also has these double negative phases interpreted as a mid-lithospheric discontinuity and the lithosphere-asthenosphere boundary. At station COEN, on the eastern edge of the North Australian Craton, our negative phase 1 fell within the depth range of the negative gradient and thus is likely the lithosphere-asthenosphere boundary.

**South Australian Craton:** Results at station FORT are in good agreement with Ford et al. (2010), with our negative phase 1 at 80 km and their largest phase at 79 km. As with their study, we interpret this energy to be a mid-lithospheric discontinuity. However, we do observe energy at greater depths that we interpret as the lithosphere-asthenosphere boundary. At station STKA we report negative phase energy at 83 (-6/+4) km (negative phase 1) and 137 (-23/+6) km (negative phase 2), whereas Ford et al. (2010) report a depth

of 104±9 km. At station BBOO negative energy is present at depths of 70 (-6/+5) km (negative phase 1) and 199 (-6/+5) km (negative phase 2), as well as a small amount of negative phase energy at 96 km and 251 km. In the study by Ford et al. (2010) the negative phase depth is reported to be at 131±9km and was interpreted as the lithosphere-asthenosphere boundary. However, there is no negative velocity gradient on the AuSREM profile, thus we have interpreted the largest negative phase to be a mid-lithospheric discontinuity. At station OOD (just to the north of the South Australian Craton), we also observed a negative phase within the lithosphere that we interpreted as a mid-lithospheric discontinuity. However, at stations LCRK and MULG we observed multiple negative phases within the negative velocity gradient of the AuSREM, which we interpreted as being multiple mid-lithospheric discontinuities. It should also be noted that station LCRK had the largest amplitude negative phase 1 depth of any station at 118 km. At station HTT, the negative phase at 85 km fell within the negative gradient of 50-175 km, thus this phase is the lithosphere-asthenosphere boundary. Station STKA (in the Curnamona Province) was reported by Ford et al. (2010) to have an lithosphere-asthenosphere boundary: this study found a negative conversion both within the lithosphere and within the negative velocity gradient, indicating the presence of a mid-lithospheric discontinuity and the lithosphere-asthenosphere boundary.

**West Australian Craton:** In the West Australian Craton, stations KMBL, MBWA, and NWAO have large amplitude negative phases at depths that are within error of those determined by Ford et al. (2010). At stations MBWA and NWAO, negative phases at both

stations are within ±5 km of those reported in Ford et al. (2010). However, the depth range of the negative velocity gradients at both stations have shifted to shallower depths, bringing the potential lithosphere-asthenosphere boundary depth range within error of the negative phases at both stations. At station NWAO negative phases 1 and 2 are interpreted to be the result of conversions within the lithosphere-asthenosphere boundary depth range, although the shallower phase has error bars that extended to lithospheric depths. While at station MBWA the shallower of the two phases falls within the lithosphere, its lower error bar extends into the negative velocity gradient. These results indicate that while the fundamental observations (depth of negative phases) have remained the same, the interpretation has changed as the result of a different velocity model. At station KMBL the largest amplitude negative phase is 6 km shallower than originally estimated, but well within the ±14 km of uncertainty in the originally reported study. This phase is interpreted to be a mid-lithospheric discontinuity. As at station MBWA, both negative phases at stations PSA00 and MUN were ambiguous and fell within error of the lithosphere-asthenosphere boundary depth range. At stations BLDU, MORW, and MEEK, the shallower of the two phases fell within the lithosphere, while the deeper phase was either within the AuSREM negative gradient or within error it. Thus, we interpreted the shallower phases here to be mid-lithospheric discontinuities and the deeper to be the lithosphere-asthenosphere boundary.

*3.5 Determining provenance of negative phases using the AuSREM velocity model*

We use the AuSREM both to migrate results (translating a time series into a depth series) and to determine if the scattered phase is from the lithosphere-asthenosphere boundary or a mid-lithospheric discontinuity. If a negative phase falls within depths corresponding to an overall velocity increase within the AuSREM, it seems unlikely that what we are observing is a conversion at or within the lithosphere-asthenosphere boundary, as the seismically this boundary is typically thought to be a region where velocities decrease. Instead, we assume that the negative phase falls within the lithospheric mantle and must represent a localized velocity decrease (i.e., a mid-lithospheric discontinuity), capable of generating a large enough conversion to be visible in Sp receiver function results, but insufficient in magnitude to be distinguished by lower resolution tomographic methods. The negative velocity gradients taken from the AuSREM are shown as gray boxes in **Figure 1.3** and **Figure S1.2**.

To aid in our discussion, the velocity profiles for the stations analyzed in this study are clustered according to profile shape. The station clusters are shown in **Figure 1.8** and are plotted on top of absolute Vs at a depth of 150 km (from AuSREM). In **Figure 1.9** the velocity profiles (and corresponding phase depths) for each cluster of stations are shown down to a depth of 300 km, including an average (in red). For the remainder of this section we review the key characteristics of each Vs profile cluster in terms of profile shape, relative geographic location, and whether negative phases within the cluster are typically mid-lithospheric discontinuities or the lithosphere-asthenosphere boundary.

Profiles in Vs Cluster 1 (shown in **Figure 1.9**) exhibit no high velocity lid. Negative velocity gradients are typically present from 50 to 150 km, with the greatest drop in velocity at depths of 50-100 km, consistent with a shallow lithosphere-asthenosphere boundary. Stations within Vs Cluster 1 are indicated in **Table 1.1** and **Figure 1.8** and are exclusively found on the continent's eastern margin or in one case, on Lord Howe Island, an ocean island station east of the continent. We note that while station COEN is west of the Tasman Line and on rock of Proterozoic age, it has a lithosphere-asthenosphere boundary phase indicating that the lithosphere in this region has been thinned or has properties more similar to lithosphere located east of the Tasman Line. In all cases, absolute velocities are low (< 4.5 km/s) at 150 km (**Figure 1.8**). Negative phase 1 and negative phase 2 for stations in Vs Cluster 1 are clearly separated, with the largest negative phases found between 70 and 85 km and the secondary negative phase found at between 101 and 153 km. Given that the depth range for the largest negative phases are within the same range as where the largest drop in velocity is found (50-100 km), we believe these negative phases originate from scattering at the lithosphere-asthenosphere boundary. This is in good agreement Ford et al. (2010), where eastern margin station receiver functions were thought to have negative phases originating from the lithosphere-asthenosphere boundary. The origin of the deeper negative phases is less clear. Since negative velocity gradients are present to 150 km at most stations, it is possible that the lithosphere-asthenosphere boundary should be thought of as more of a transition and both phases are part of a more complex, less continuous progression of lithospheric mantle to asthenosphere. Alternatively, the negative phases at

greater depths may be a boundary in melting within the asthenosphere. Electrical conductivity is often linked to the presence of melt, and there is a region of increased conductivity beneath Phanerozoic Australia between at least 92 and 172 km (Kennett et al., 2018; Wang et al., 2014). Additionally, electrical conductivity in the asthenosphere may be linked to the presence of small amounts of carbonate melt and Phanerozoic volcanism, decreasing seismic velocity (Aulbach et al., 2017a; Davies et al., 2015; Gaillard et al., 2008).

The key characteristic of velocity profiles in Vs Cluster 2 is that on average they have increasing velocities to 75 km and then decreasing velocities from 75 km to, on average, 175 km. This suggests a thin, high velocity lid, with a clear transition to a low velocity asthenosphere. The majority of the stations (all but one) are located in West Australian Craton. However, station CMSA, which is located within Phanerozoic Australia is an outlier in terms of location (but not with respect to the velocity profile cluster). The largest and second largest phases at stations within Vs Cluster 2 are not as clearly separated in Vs Cluster 1, however, the largest negative phases are typically located at shallower depths than the smaller amplitude negative phases. For the deeper, typically smaller phases, the depths commonly correspond to the depth range of the negative velocity gradient, suggesting they are the result of scattering within the potential lithosphere-asthenosphere boudnary depth range. Meanwhile, the average of the largest negative phases falls at a depth of 75km, which marks the transition to a negative velocity gradient. At roughly half of the stations, the error bars extend the phase picks down to the corresponding negative

velocity gradient for the given station, while for the other half, the phase picks fall within the high velocity lithosphere. Choosing to abide by our definition of potential lithosphere-asthenosphere boundary versus mid-lithospheric discontinuity phases, this means that roughly half of the largest negative phases in Vs Cluster 2 are lithospheric in origin (i.e., MLD) while the other half are the result of scattering from within the transition from lithosphere to asthenosphere.

The average shear velocity profiles for Vs Clusters 3 and 4 have increasing velocities to 125 km. Below 125 km, velocities decrease in both averaged profiles, however, the local minimum in the averaged profile for Vs Cluster 3 is observed at 225 km, while the local minimum in the averaged profile for Vs Cluster 4 is seen at 175 km. Generally, the absolute changes in velocity for Vs Cluster 3 are larger, both within the high velocity lid, as well within the region of negative velocity gradient. In Vs Cluster 4, the decrease in velocity within the negative velocity gradient is very small. Notably, the vast majority of the negative phases fall at depths above our defined potential lithosphere-asthenosphere boundary depth range indicating that at these stations the negative phases that we observed are predominately mid-lithospheric discontinuities. The stations in Vs Clusters 3 and 4 are listed in **Table 1.1**. In **Figure 1.8**, they are marked with the yellow and green inverted triangles and are located mostly in the North Australian Craton and South Australian Craton, with one in the West Australian Craton, and one slightly east of the Tasman Line. The stations are interspersed with stations labeled as belonging to Vs Clusters 5 and 6, which are marked as blue and cyan inverted triangles, respectively. The number of stations

clustered as 5 and 6 are distinct from Vs Clusters 3 and 4, due to the fact that the stations in Vs Clusters 5 and 6 have no apparent negative velocity gradient, which suggests there is no observed seismic transition from lithosphere-asthenosphere to at least 300 km, suggesting a very gradual change from one to the other. Therefore, all of the negative phases at stations in these two clusters are mid-lithospheric discontinuities.

## Discussion

### *4.1 The Importance of Additional Stations*

As mentioned in **Section 2.1**, this study has more stations and increased years of coverage from Ford et al., (2010), greatly improving the understanding of lithospheric complexity in Australia. However, coverage of the continent continues to expand, especially in more remote regions. More stations with smaller station spacing would allow for the calculation of common-conversion point stacks, a method used to image lithospheric layering in the North American cratons (Chen et al., 2018; Hopper et al., 2014; Hopper & Fischer, 2015; Hopper & Fischer, 2018; Kind et al., 2017). This is particularly important because we have detected the presence of multiple mid-lithospheric discontinuities at some stations (see **Figure 1.10**). Currently, we cannot say whether any of these structures are dipping as our receiver functions represent only the structure below the station/along the ray path. The presence of dipping surfaces may provide evidence as to the origin of the mid-lithospheric discontinuities, such as an ancient subduction zone setting as suggested by Hopper and Fischer (2015).

One important finding of Ford et al. (2010) was that at stations with an observable lithosphere-asthenosphere boundary there was a negative correlation between phase depth and amplitude (i.e., shallower phases had stronger amplitudes). The strongest, shallowest negative phases were observed in regions of recent volcanism. However, our study has found that with increased station coverage there does not seem to be a correlation (**Figure 1.7**). The previous negative correlation may have been an artifact of the limited station availability.

Additionally, Ford et al. (2010) did not report any observed lithosphere-asthenosphere boundary phases in western Australia. However, this study reports four stations in the West Australian Craton at which the negative phase is interpreted to be either a mid-lithospheric discontinuity or the lithosphere-asthenosphere boundary, and another three with both a mid-lithospheric discontinuity and the lithosphere-asthenosphere boundary; most of these stations fall within the Yilgarn and Pilbara cratons. These stations all belong to Vs Cluster 2 (which contains a clear negative velocity gradient at 75-175 km depth) and are distinctly different from the velocity gradients at many of the other cratonic stations in Australia (see Vs Clusters 3, 4, 5 and 6 in **Figure 1.9)**. The phases at these western stations all fall roughly between 70 and 90 km, corresponding to the upper bound placed on the lithosphere-asthenosphere transition (LAT) by Yoshizawa and Kennett (2015). It is possible that there is a strong impedance contrast at the top of the LAT (such as the base of the chemical boundary layer; Lee et al., 2005), but that the lithosphere extends well below that depth and may be more mechanically coupled to the asthenosphere. Tomography has shown that

the lithosphere in the southwestern portion of the Yilgarn craton may have been thinned (Kennett et al, 2013; Simons et al., 1999). However, the seven stations with observed and potential lithosphere-asthenosphere boundary span the entire Yilgarn craton, through the Capricorn Orogen, and into the Pilbara craton, suggesting that localized lithospheric thinning cannot entirely explain the negative phases. For most stations, though, it seems likely that we may be observing the top of the LAT.

*4.2 Comparisons to seismic reflectivity*

A number of recent studies (Gorbatov et al., 2013; Kennett, 2015; Kennett et al., 2016; Kennett & Furumura, 2016; Kennett & Sippl, 2018; Sun et al., 2018; Sun & Kennett, 2016) have focused on a seismic property related to receiver functions, seismic wave reflectivity. Like receiver functions, this method can provide information about depth to discontinuities and layers, but unlike receiver functions, the amplitude is not directly related to the impedance contrast between layers. These studies calculate P-wave reflectivity through a method known as seismic daylight imaging (SDI) and use a slightly higher and broader frequency band (0.5 – 4.0 Hz) than receiver functions (our Sp receiver functions are filtered at 0.03 – 0.5 Hz), useful for providing more detailed information on finer layering.

Multiple studies using this method have examined the structure of the Australian lithosphere in a way similar to receiver functions. Kennett (2015) first made use of this method to investigate lithosphere-asthenosphere reflectivity across Australia. That study used many of the same stations as this one but did not independently identify any phases

in the mid lithosphere. At stations ARMA, EIDS, STKA, TOO, and YNG the mid-lithospheric discontinuity as identified by Ford et al. (2010) was at the top of the tomographically-defined LAT of Yoshizawa and Kennett (2015) and corresponds to some change in the frequency or character of reflectivity (Kennett 2015; Kennett et al., 2017). Stations MBWA and CTA both had mid-lithospheric discontinuities that were at the base of a low frequency reflectivity packet, while station WRAB had a mid-lithospheric discontinuity within a higher frequency reflectivity packet. Sun et al. (2018) investigated reflectivity in the West Australian Craton, and additionally interpreted their own phases within the mid lithosphere. In general, they found a shallow mid-lithospheric discontinuity (~70-82 km), with the deepest phases in Proterozoic orogens. They reported a mid-lithospheric discontinuity at station MEEK at ~65 km (we report one at 79 km), at station KMBL at ~70 km (we report the most prominent phase at 79 km, but note another at 72 km), at station PSA00 at ~60 km (we report the most prominent negative phase at 67 km, but do report another at 61 km), and at station MBWA at ~70 km (we report one at 72 km). Sun et al. (2018) did note there was an 18-km discrepancy between the mid-lithospheric discontinuity they reported at station KMBL and that reported by Ford et al. (2010), which they explain as possibly being due to the presence of multiple mid-lithospheric discontinuities , a possibility we confirm with this study. A study focusing on central Australia found similar results, with a marked change in the frequency content of P-wave reflectivity profiles between 80 and 100 km (Kennett & Sippl, 2018). That study did not observe a clear, coherent mid-lithospheric phase in CCP stacks, but individual stations did show evidence of a possible discontinuity. Additionally, Kennett and Sippl (2018) did not

observe any strong negative phases that they could associate with the lithosphere-asthenosphere boundary, a finding mirrored by our own results.

Other recent work has used this same method and combined it with others to investigate the nature of the lithosphere from a slightly different perspective. Kennett and Furumura (2016) argued that the complex, high frequency coda observed for P and S-waves from local earthquakes were a result of complex and multiscale velocity variations within the lithosphere. They argue that in addition to the first order changes in seismic velocity (such as those we observe), there may also be variations at much finer scales on the order of kilometers to 10s of kilometers. The mid-lithospheric discontinuities may be a result of this fine-scale velocity variation. In reflection seismology, many reflectors arise due to such fine-scale variation, and the same effect may hold true for transmitted signals. The filtering of receiver functions may also have some effect on observations of mid-lithospheric discontinuities. Most Sp receiver functions are filtered at relatively low frequencies (>0.5 Hz), which in turn means less fine-scale variation in the results. This smoothing allows for velocity changes to be described in a few first order jumps, where in reality there may be more (Kennett et al., 2017). Multi-scale heterogeneity may have implications for other properties of the lithosphere-asthenosphere system: it is linked to anisotropy (Kennett & Furumura, 2016; Yoshizawa, 2014; Yoshizawa & Kennett, 2015), changes in olivine Mg# (Gaul et al., 2003; Kennett et al., 2017), and the top of the proposed LAT throughout Australia at ~70-100 km (Yoshizawa &Kennett, 2015). These properties are also linked to mid-lithospheric discontinuities.

We cannot rule out the possibility that the mid-lithospheric discontinuities we observe are due to multi-scale heterogeneity, however it should be noted that we do not currently have the observational data to support the idea that these variations in velocity at multiple scales exist everywhere. Additionally, while these variations may explain some of the observations we make regarding mid-lithospheric discontinuities, the argument for multi-scale heterogeneity relies on observations made in Australia. It may not explain mid-lithospheric discontinuities that occur elsewhere in the world.

*4.3 The Australian Mid-lithospheric Discontinuity and Lithospheric Layering*

We observed negative phases interpreted to be mid-lithospheric discontinuities at 17 stations, with four additional stations having ambiguous phases. These phases ranged in depth from 61 km to 118 km, with most falling between 70 and 90 km. Most of these stations are located within Central Australia, either in the North Australian Craton, or in the Proterozoic orogens to its south that suture it to the other Australian cratons. There are also mid-lithospheric discontinuity phases observed in the South Australian Craton, including the deepest observed at LCRK. Additionally, at 26 stations we observed a weaker negative phase either above or below the primary negative phase (i.e., the LAB or a mid-lithospheric discontinuity). This leads to the inference that there may be multiple mid-lithospheric discontinuities at some stations; in particular we see evidence for layering in cratonic settings.

The presence of multiple lithospheric layers has been well documented in other cratons. Hopper and Fischer (2015) identified several discontinuities in the North American craton below the Moho at varying depths. The shallowest negative phase (~70-90 km) was interpreted to result from frozen-in volatile-rich melt. Below that were dipping negative phases (85-200 km) that may be the result of the formation or stabilization of the ancient lithosphere. Additionally, most cratonic stations used in the study could not identify a clear negative phase associated with the lithosphere-asthenosphere boundary, a finding mirrored in our own results. Sodoudi et al. (2013) observed two mid-lithospheric discontinuities within the Kalahari craton, one at ~85 km depth that is most likely associated with a layer of anisotropy, and a second mid-lithospheric discontinuity between 150 and 200 km depth that seems to be linked to magmatic events and the base of the highly depleted cratonic lithosphere. In the stable western portion of the North China Craton, multiple mid-lithospheric discontinuities are observed which may be linked to the evolution of the craton and repeated melt infiltration throughout its history (Sun et al., 2020). Other studies have also indicated the presence of multiple phases beneath the Moho, both in cratonic and more active tectonic settings. Lekic and Fischer (2014) identified multiple negative phases in the oldest portions of the Northwestern US, with weaker amplitudes than those observed in the more tectonically active regions further to the west. This result is further strengthened by the presence of multiple mid-lithospheric discontinuities to the east of the Sevier thrust belt in the Western US, possibly explained by previous episodes of subduction (Ford et al., 2016; Hopper et al., 2014).

Just as Hopper and Fischer (2015) observed a consistent negative phase across terrane and age boundaries, we also observe a pervasive negative phase at almost every station between 70 and 100 km. Rychert and Shearer (2009) carried out a global Ps receiver function study and found a similar velocity drop in all settings at approximately the same depth range. The fact that almost all lithospheric types and tectonic settings seem to have this velocity drop has been used to argue for the presence of a global discontinuity at these depths. However, tomography seems to be insensitive to this boundary, as models often show fast, increasing velocities to at least 150 km and often deeper (Kennett et al., 2013; Schaeffer and Lebedev, 2013; Yoshizawa & Kennett, 2015). Other tomographic models have observed a velocity decrease at approximately the same depth as mid-lithospheric discontinuities inferred from receiver-function studies (Romanowicz, 2009; Yuan & Romanowicz, 2010). The one-dimensional shear velocity profiles from the AuSREM that we used to determine the provenance of negative phases lacked a negative velocity gradient at depths of less than 125 km for most stations in cratonic settings, except those in Vs Cluster 2 which lie on the western edge of the continent. Xenolith data also indicate the presence of ancient, mineralogically depleted lithosphere to depths of 150 km or more in cratonic settings, suggesting that at least in some instances the shallower discontinuity observed globally cannot be the lithosphere-asthenosphere boundary (Griffin et al., 1999; Jordan 1978, 1988; Lee, 2006). In the remainder of this section we explore whether mechanisms such as melting and/or thermal changes, anisotropy, or changes in composition can be invoked to explain the existence of mid-lithospheric discontinuities.

Partial melting followed by pooling of those melts within the lithosphere is one explanation for mid-lithospheric discontinuities, although under ambient cratonic conditions there is no reason to expect that the geotherm will cross any solidi. Between roughly 75 and 120 km depth there is a large high-temperature anomaly in central Australia of between ~900°C and ~1200°C (Kennett et al., 2018, Tesauro et al., 2020). The most likely cause of this large thermal anomaly is high crustal heat production, as observed in many Proterozoic terranes (>80 $mW/m^2$; McLaren et al., 2003). This corresponds with a region of increased conductivity at depths of 50-100 km in central Australia (Wang et al., 2014). Some of the mid-lithospheric discontinuities observed in central Australia (Station MULG has a mid-lithospheric discontinuity at 75 km, station WRAB has a mid-lithospheric discontinuity at 71 km, and station WRKA has a mid-lithospheric discontinuity at 74 km) may be explained by this thermal anomaly, but other stations in central Australia (stations OOD, INKA) have mid-lithospheric discontinuities either above or below this anomaly. Most of western and central Australia is relatively cold at mid-lithospheric depths (300°C to 500°C), indicating that a thermal anomaly is not able to explain the origin of mid-lithospheric discontinuities in these regions (Kennett et al., 2018; Tesauro et al., 2020).

Previous studies have linked the presence of mid-lithospheric discontinuities to anisotropy within the lithosphere (Bostock, 1998; Rychert & Shearer, 2009; Wirth & Long, 2014). In these cases, anisotropy is linked to past tectonic events such as the formation of cratons and accretion of island arcs. In Australia, a large body of evidence exists to suggest the presence of complex and possibly layered anisotropy within the Australian lithosphere

(Clitheroe & van Der Hilst, 1998; Debayle et al., 2005; Heintz & Kennett, 2005; Yoshizawa, 2014; Yoshizawa & Kennett, 2015). Thus, it is possible that the mid-lithospheric discontinuities we observed may be least partially due to anisotropy. Previous forward modeling of receiver functions and synthetic seismograms has relied on 10% anisotropy, though this is on the high end of what is expected to occur naturally (Ford et al., 2016; Levin & Park, 1997, 1998; Wirth & Long, 2014). However, these are simple estimates and the point at which anisotropy can produce a mid-lithospheric discontinuity may be slightly lower. The Australian lithosphere has strong anisotropy (~5%) down to at least 100 km, with moderate anisotropy (2-3%) below that, until asthenospheric depths where convection produces strong anisotropy again (Fouch & Rondenay, 2006; Yoshizawa, 2014; Yoshizawa & Kennett, 2015). There is no way to uniquely constrain anisotropy from this study, but analysis of the horizontal component of Ps receiver function can provide information about anisotropic boundaries. Forward modeling would help to constrain the needed amount of anisotropy to produce the conversions. If these boundaries occur at or near the same depth as the mid-lithospheric discontinuities, then they may be explained by anisotropy, but these phenomena need not be linked (Ford et al., 2016).

Compositional changes are also often invoked to explain mid-lithospheric discontinuities. One proxy for composition that is frequently used is known as the magnesium number (Mg#). This is defined as the amount of magnesium in a rock compared to the total magnesium and iron content in that rock (Mg# = Mg/(Mg+Fe) x 100). In peridotites, which are the dominant composition of the upper mantle, Mg# ranges from ~86-88 for the primary

composition and ~93-94 for more residual compositions such as those seen in cratonic settings. An increase in Mg# results in an increase in Vs (a roughly 2% increase between Mg# 88 and Mg#94), but causes no change in Vp; however, at standard temperature and pressure conditions Vp is weakly correlated with olivine abundance (Lee, 2003). Kennett et al. (2018) used a joint inversion of seismic and gravity data to produce a proxy for Mg#: their results show that while there are differences in the Mg# between the Phanerozoic east and the Precambrian west, there are not significant enough changes in Mg# with depth to explain the presence of mid-lithospheric discontinuities (though this model is relatively coarse). Another recent study using the same technique found no significant variations through the cratons to depths of 300 km, with values ranging from 91.6 to 89.6 (Tesauro et al., 2020). This relatively small variation is not expected to produce a major velocity change. Paired with the 2% change in Vs compared to the observed 5-7% needed to generate mid-lithospheric discontinuities, this makes it unlikely that changes in Mg# are the primary cause of most mid-lithospheric discontinuities observed in Australia.

One means of constraining changes in composition is from xenoliths originating from depths similar to that of the mid-lithospheric discontinuities, however there are limited xenolith suites in Australia. Since the mid-Cretaceous there has been volcanism on the eastern margin of Australia related to plate motion and plume events (Davies and Rawlinson, 2014; Sutherland et al., 2012), but there has been no recent volcanism in the cratons. The only xenoliths found in these areas are from much older volcanism and are only useful if the mid-lithospheric discontinuities are as old or older than the eruption. In

the Kimberley Block of the North Australian Craton, xenoliths show an enriched mantle with hydrous minerals such as phlogopite; thus metasomatism in the mantle may explain the velocity drop associated with mid-lithospheric discontinuities (Best, 1974; Edwards et al., 1992; Griffin et al., 1984; Konzett et al., 2013; McCulloch et al., 1983). Similarly, compatible element data from the Yilgarn Craton suggest that the mantle lithosphere was metasomatized before eruption around 2.025 Ga (Graham et al., 2004). Another study of xenolith compositions from the Yilgarn craton observed juvenile radiogenic isotopes and fluid-related trace element compositions, likely requiring the dehydration of a slab at 2.6-2.7 Ga (Choi et al., 2020). Saha et al. (2018) suggested that the presence of metasomatic minerals such as phlogopite or amphibole that formed during subduction or other melting events (even if ancient) may explain the seismic velocity decrease associated with mid-lithospheric discontinuities. If we observe metasomatic minerals in xenoliths that are ancient (in the case of Graham et al. (2004) the xenoliths are 2.025 Ga), it indicates that the conditions in the mid-lithosphere were conducive to the formation of zones of low velocity. If this is the case, then the mid-lithospheric discontinuities themselves may be as old if not older than the xenoliths.

Aulbach et al. (2017a) argue that the most likely explanation for mid-lithospheric discontinuities is the presence of hydrous minerals at depth. Their preferred mineral is phlogopite, which would create the observed seismic drop of ~5-7%. The origin of the phlogopite at mid-lithospheric depths is still under debate: one possibility is that the phlogopite forms as a direct result of subduction and the introduction of hydrous fluids into

the mantle (Konzett and Ulmer, 1999; Sato et al., 1997; Vilzeuf and Schmidt, 2001). However, other processes may have helped hydrate the lithospheric mantle, such as interaction with a mantle plume. There is evidence from multiple cratons for the presence of hydrous minerals dating to the Precambrian, including the Australian cratons (Aulbach et al., 2007; Best, 1974; Choi et al., 2020; Edwards et al., 1992; Giuliani et al., 2016; Graham et al., 2004; Hopp et al., 2008; Konzett et al., 2013; Priyatkina et al., 2014). In addition, there is evidence for dipping seismic discontinuities in several cratons (Bostock, 1998; Chen et al., 2009; Cook et al., 1999; Cooper & Miller, 2014; Hopper & Fischer, 2015; Snyder, 2008;) which has been linked to subduction in the Precambrian.

Alternatively, the presence of hydrous minerals may be linked to percolation of asthenospheric melt into the lithosphere, pooling around mid-lithospheric depths (Aulbach et al., 2017a; Rader et al., 2015). This may be linked to the presence of plumes or other thermal perturbations. Indeed, at least one mid-lithospheric discontinuity in the North Atlantic Craton seems linked to the intrusion of kimberlites in the Mesozoic (Aulbach et al., 2017b). There is at least one suspected plume event in the Proterozoic (the ~1.6 Ga Hiltalba event) that may explain some of the hydrous minerals in the South Australian Craton and North Australian Craton (Betts et al., 2002). Additionally, in the Mesozoic the western margin of Australia may have been affected by the Kerguelen Plume (Frey et al., 1996). This suggests that plumes cannot be ruled out as an origin for the hydrous minerals creating mid-lithospheric discontinuities. Plumes are often cited as a model to generate cratonic lithosphere, wherein melt generated near the lithosphere-asthenosphere boundary

may infiltrate and percolate to shallower depths (Lee et al., 2011). This model would also apply in subsequent interactions between craton and plumes, suggesting that repeated events of melt infiltration may leave behind hydrous minerals at mid-lithospheric depths. Furthermore, it is presently thought that the sharp lithosphere-asthenosphere boundary observed in oceanic and younger continental lithosphere is linked to the presence of a small amount of partial melt in the asthenosphere (Fischer et al, 2010; Rychert et al., 2020), suggesting that thinner cratonic lithosphere in the past may have been well situated for melt percolation even without a plume or subduction, especially given that the mantle is predicted to have been hotter in the Precambrian (Herzberg et al., 2010).

Elastically accommodated grain-boundary sliding has also been suggested as a mechanism to explain mid-lithospheric discontinuities (Karato, 2012; Karato et al., 2015). This mechanism requires at least a locally hydrated mantle and may thus be linked to the presence of metasomatic minerals at mid-lithospheric depths. However, it is predicted that grain-boundary sliding occurs at ~1000°C in olivine, yet most mid-lithospheric discontinuities are seen in regions with temperatures predicted to be 700° to 900°C (Selway et al. 2015 and references therein). Selway et al. (2015) carried out a calculation using velocity profiles determined from the geotherm of the Kaapvaal craton (Artemieva, 2009), with average composition for an Archean craton (Griffin et al., 2009), and found that this mechanism does not produce the predicted and observed velocity discontinuities seen at mid-lithospheric depths. It should be noted that the parameters involved in grain-boundary sliding are still poorly constrained and understood, and that this mechanism may operate

in concert with the presence of hydrous minerals in the mid-lithosphere to create mid-lithospheric discontinuities. However, it does not seem likely that grain-boundary sliding on its own can cause the ubiquitous and global mid-lithospheric discontinuities.

We have presented a case above that mid-lithospheric discontinuities observed in Australia cannot be uniquely explained by thermal causes, major changes in Mg# with depth, or anisotropy. In the case of the Australian mid-lithospheric discontinuities, we argue that the most likely cause is the presence of hydrous minerals precipitated sometime in the Archean or Proterozoic, which are linked to either plate tectonic processes, plume interaction, or frozen melt that originated from partial melting at a paleo-lithosphere-asthenosphere boundary. These events are not mutually exclusive and may have acted together to form mid-lithospheric discontinuities. Furthermore, it is likely that these would require multiple episodes of melt infiltration and prolonged interaction.

## *5. Conclusions*

We performed an updated continental Sp and Ps receiver function analysis in Australia. Our findings generally mirror those in Ford et al. (2010), with shallow, sharp negative phases in Phanerozoic Australia predicted to be the lithosphere-asthenosphere boundary, and no obvious lithosphere-asthenosphere boundary with discrete velocity drops in the mid-lithosphere in cratonic Australia. Stations throughout Australia have multiple negative phases, suggesting a complex and possibly layered cratonic lithosphere. However, we do

identify one cluster of stations in western Australia where both mid-lithospheric discontinuities and potential lithosphere-asthenosphere boundaries are observed.

We observe mid-lithospheric discontinuities at depths between 61 and 118 km. The most likely explanation for Australian mid-lithospheric discontinuities is the presence of hydrous minerals in the mantle. Xenoliths indicating hydrous minerals greater than 2 Ga in age suggest that mid-lithospheric discontinuities originated in the Precambrian, possibly from plate tectonic processes, plume interaction, or melt infiltration from the paleo-lithosphere-asthenosphere boundary.

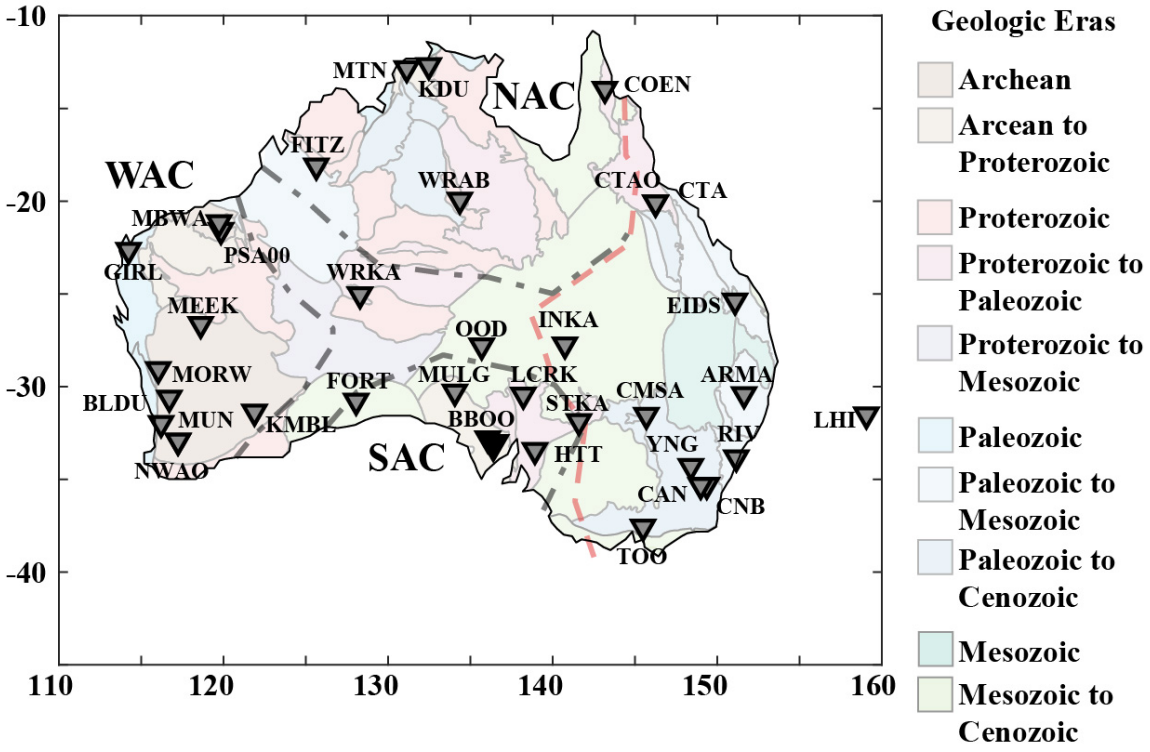


**Figure 1.1:** Map of significant geologic divisions of Australia, simplified from Fraser et al. (2007). Labelled are the West Australian Craton (WAC), the North Australian Craton (NAC), and the South Australian Craton (SAC). Inverted triangles are stations used in this study. Station names are shown in Figure 3.

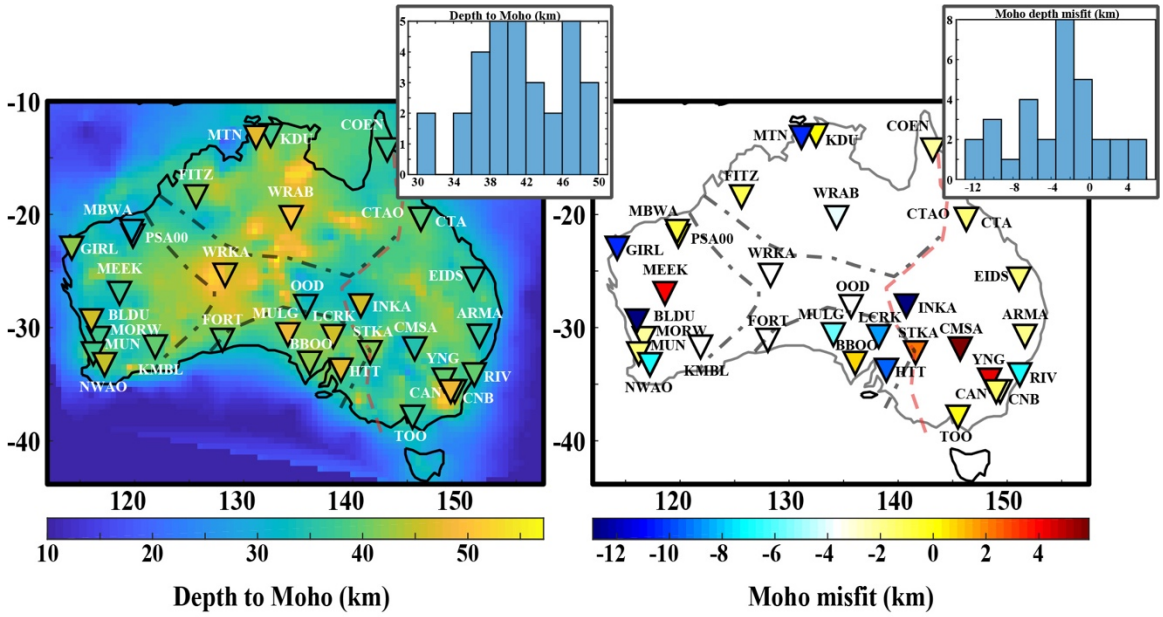


**Figure 1.2:** Depth to Moho as estimated from Ps receiver functions. (a) Depth in kilometers to Moho from our receiver functions plotted over the Moho depth as predicted by AuSREM (Kennett *et al.*, 2012; Salmon *et al.*, 2012). Inset shows histogram of Moho depth values (b) Misfit between our Moho pick and that estimated by AuSREM, in kilometers. Inset shows histogram of misfit values.

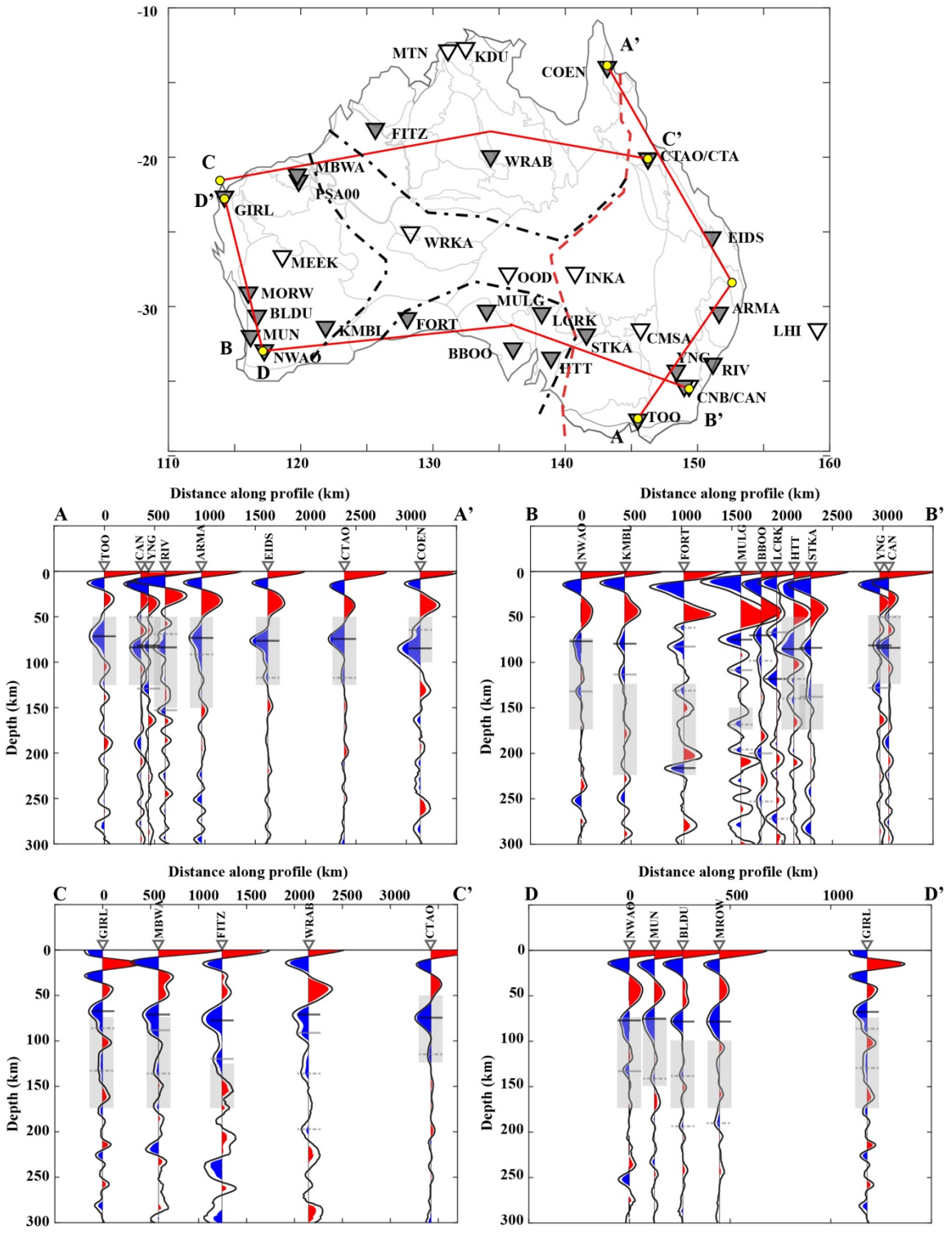
-10
-20
-30
110
120
130
140
150
160
MTN
KDU
COEN
A'
C'
CTAO/CTA
FITZ
WRAB
C
MBWA
PSA00
D'
GIRL
WRKA
EIDS
MEEK
OOD
INKA
MORW
BLDU
MULG
ARMA
MUN
KMBL
FORT
LORK
CMSA
LHI
B
NWAO
D
BBOO
STKA
YNG
HTT
RIV
CNB/CAN
TOO
B'
A
Distance along profile (km)
Depth (km)
TOO
CAN
YNG
RIV
ARMA
EIDS
CTAO
COEN
NWAO
KMBL
FORT
MULG
BBOO
LCRK
HTT
STKA
YNG
CAN
GIRL
MBWA
FITZ
WRAB
CTAO
NWAO
MUN
BLDU
MROW
GIRL

**Figure 1.3 (previous page):** (top) Map of the 34 good and fair stations (inverted triangles) used in this study. Gray filled in stations have receiver function results plotted in cross section. Remaining stations are shown in Supplementary Figure 2. Red lines show cross section locations. (middle and bottom rows) Cross sections A-A', B-B', C-C' and D-D'. Station stacked Sp receiver functions are plotted for individual stations along cross section lines. Red phases correspond to a velocity increase with depth, blue phases a velocity decrease with depth. The black line corresponding to the mean of the bootstrapped receiver functions is plotted, and only the statistically significant portions of the positive and negative phases are shown. Negative phase picks are plotted as black horizontal lines (negative phase 1), gray horizontal lines (negative phase 2) and other negative phases of potential interest are highlighted with dashed gray horizontal lines. Gray, semi-transparent boxes illustrate the depth range of the negative velocity gradient determined from the AuSREM velocity model.

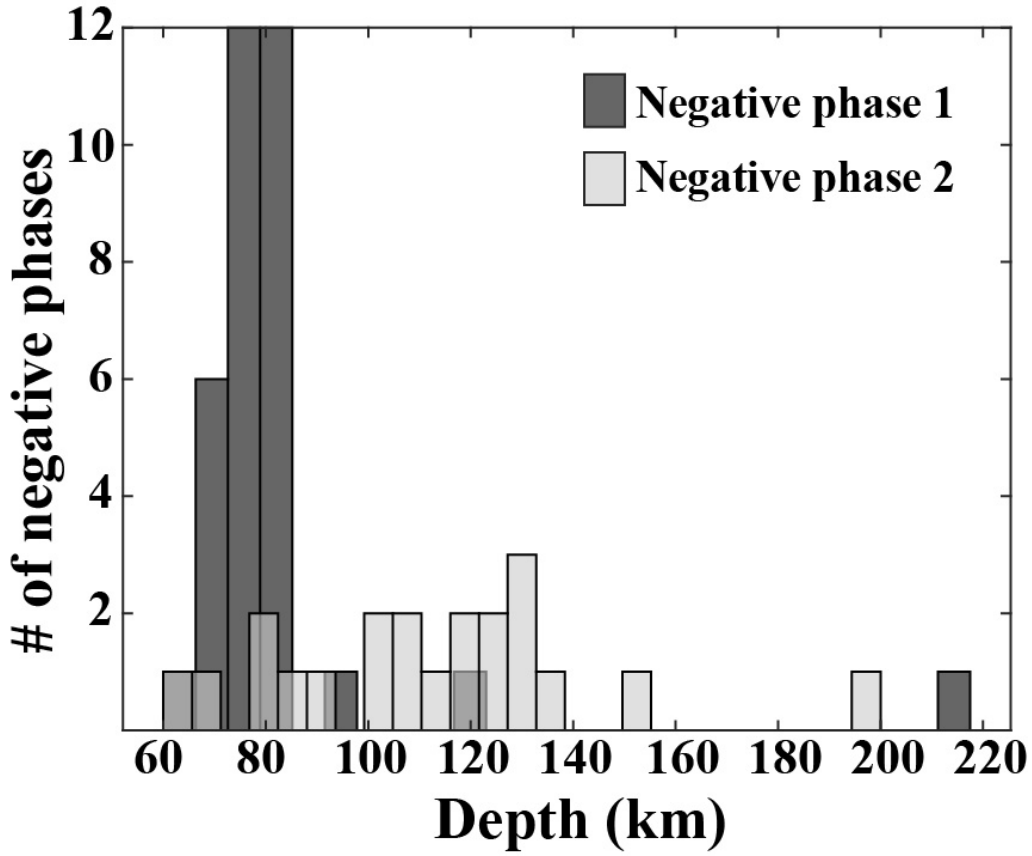


**Figure 1.4:** Histogram of depth distribution of negative phase 1 and negative phase 2 for all stations. Note that most of negative phase 1 picks fall between 60 and 120 km.

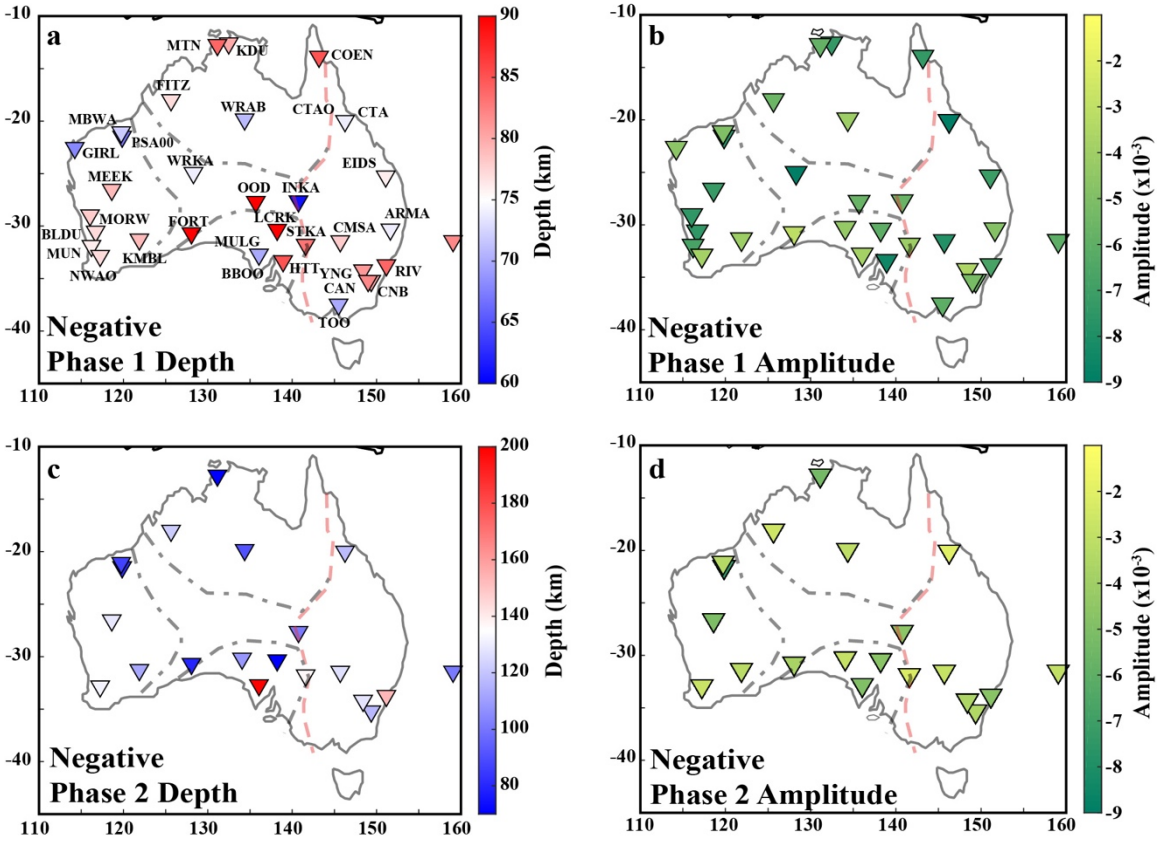


**Figure 1.5:** (a and c) Depth to (a) negative phase 1, and (c) negative phase 2, in kilometers. (b and d) Amplitude of (b) negative phase 1 and (d) negative phase 2.

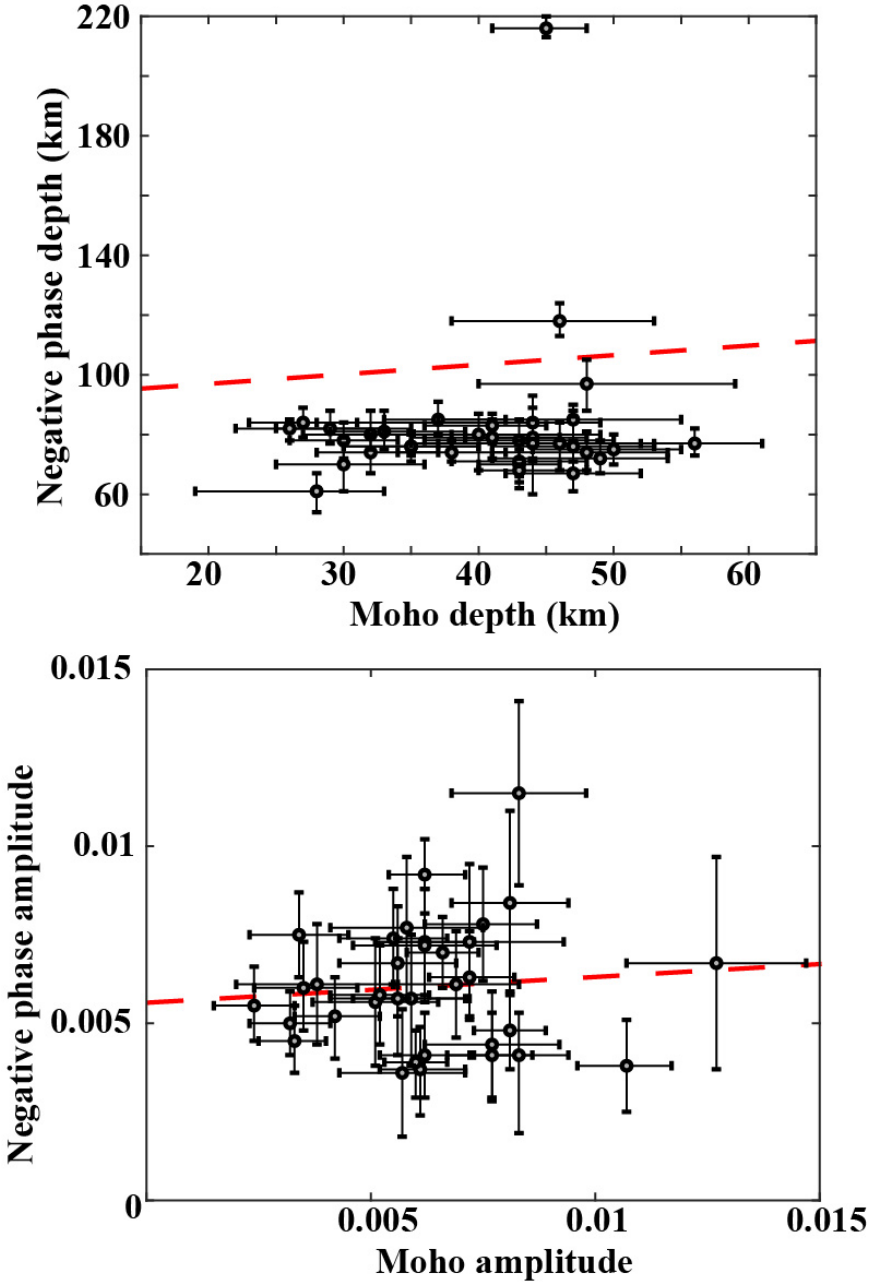


**Figure 1.6:** Scatter plots (including error bars) of relationship between negative phase depth and Moho depth and negative phase amplitude and Moho amplitude.

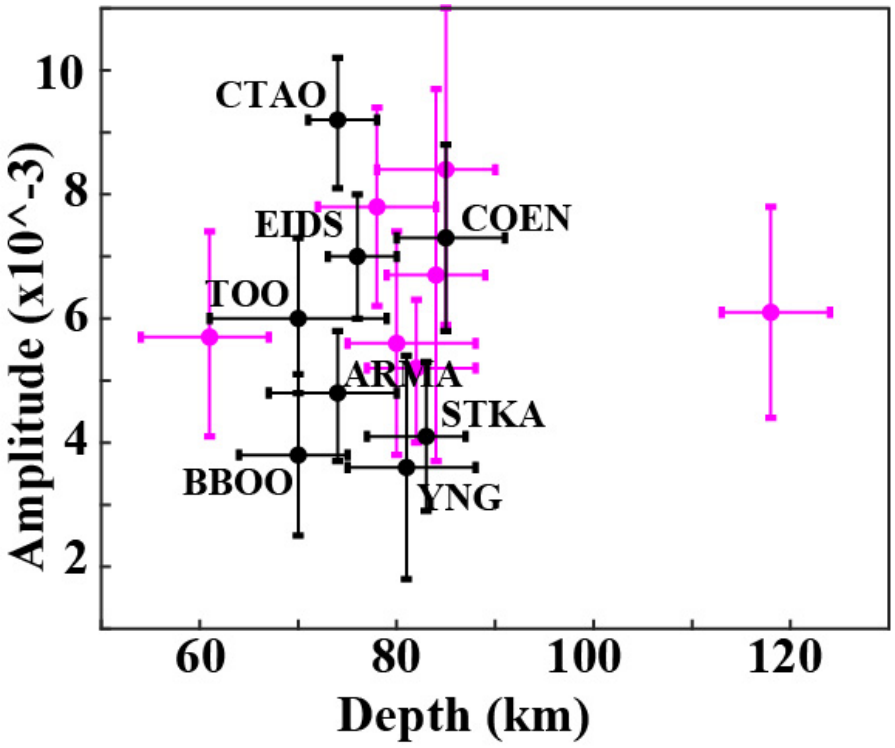


**Figure 1.7:** Plot of amplitude versus phase depth for stations in Phanerozoic Australia. Ford *et al.* (2010) posited a negative correlation between the two. However, with increased station coverage this does not appear to be the case. Black symbols correspond to Phanerozoic station results included in both the original (2010) study and this study. Magenta symbols are for stations new this study.

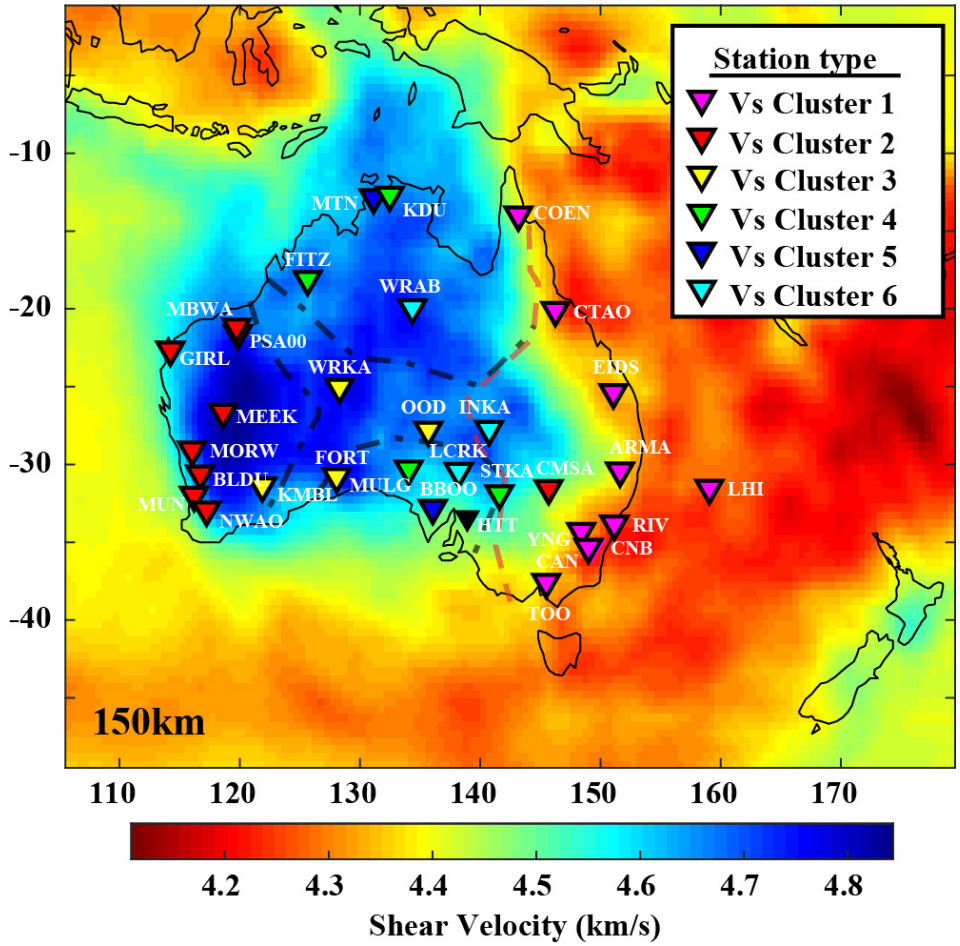


**Figure 1.8:** Base map is absolute shear velocity taken at 150 km from AuSREM. Stations are labeled by Vs cluster, see **Figure 9** and text for more information.

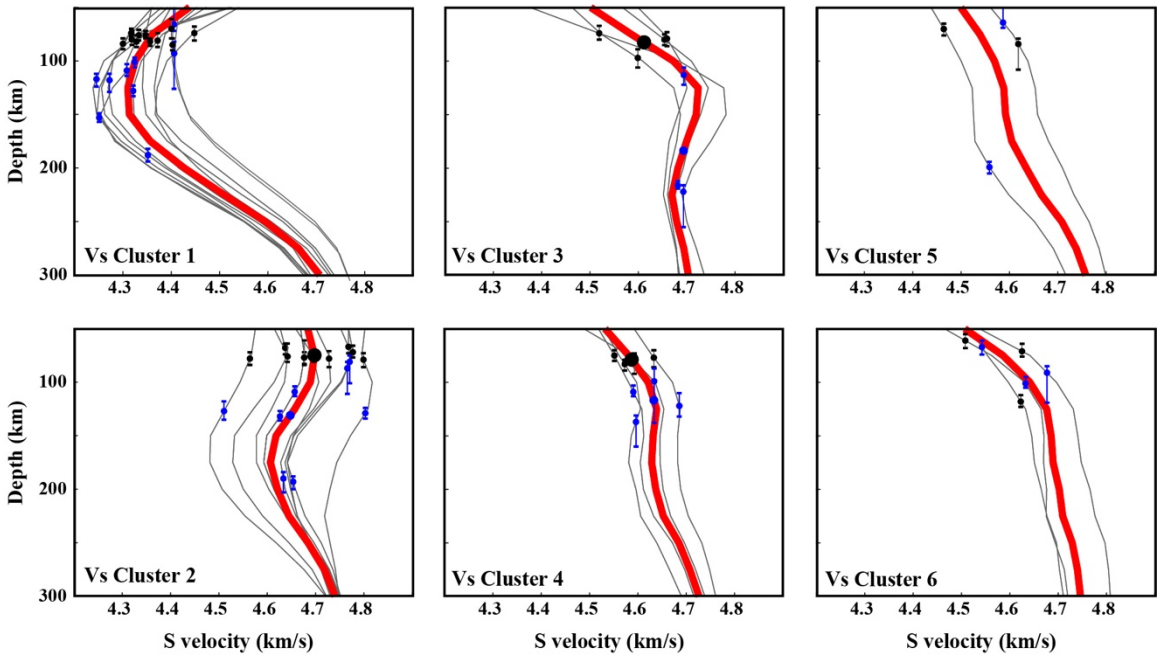


**Figure 1.9:** 1-D Velocity profiles from the mantle shear velocity component of AuSREM. Red lines are the average velocity from that cluster of profiles. Small black dots with error bars are negative phase 1 depths, and small blue dots are negative phase 2 depths. See **Figure 8** for geographic distribution of Vs clusters.

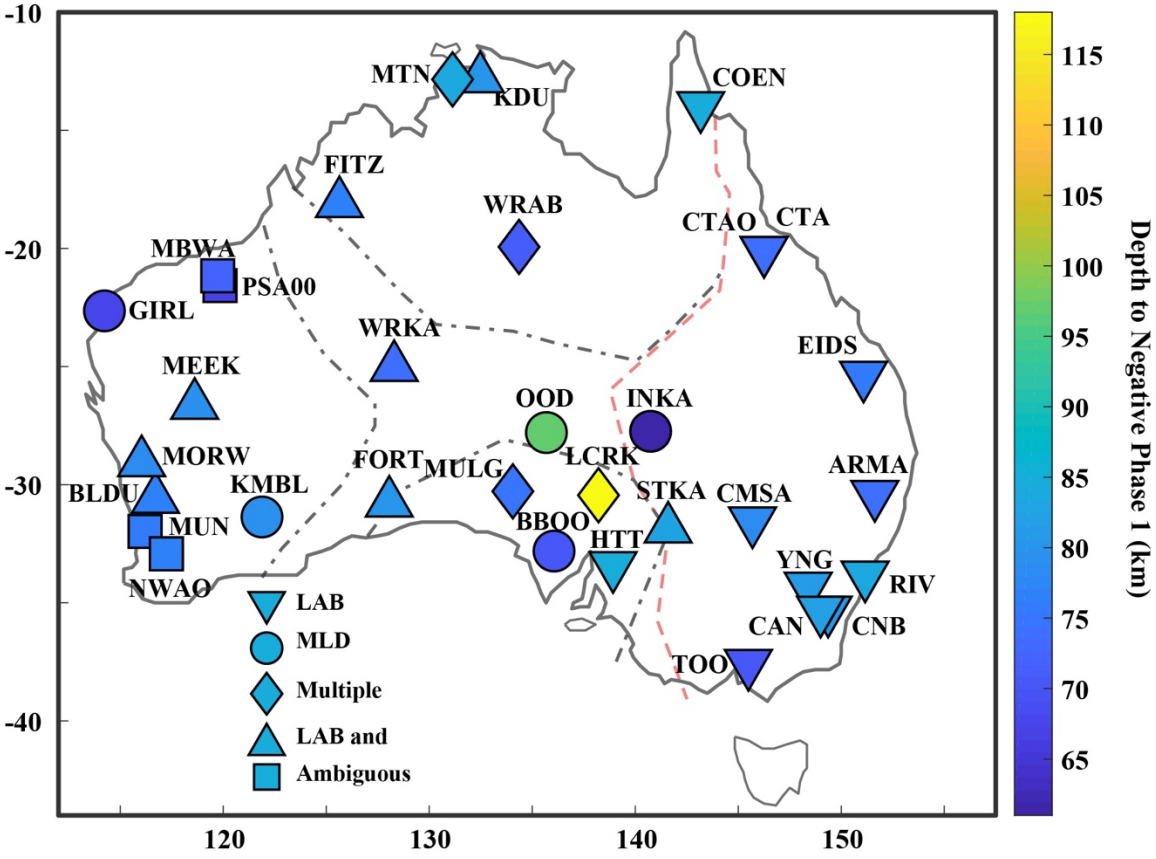


**Figure 1.10.** Depth to negative Phase 1 (km) and its interpretation. Stations plotted as inverted triangles only had an LAB, those as circles only had an MLD, diamond stations had multiple MLDs, normal triangles had both the LAB and MLD (labeled MLD/both in Table 2), and squares had phases that could be either the LAB or an MLD (labeled Either/Both in Table 2). LAB, lithosphere–asthenosphere boundary; MLD, midlithospheric discontinuity.

| Network | Station | Latitude | Longitude | Index | Total Time | # of Waveforms | Moho - Sp (km) | Moho - Ps (km) | Rank (P/F/G) | Vs Profile cluster |
|---|---|---|---|---|---|---|---|---|---|---|
| AU | ARMA | -30.418 | 151.629 | 1 | 15 | 339 | 32 | 36 | G | 1 |
| AU | BBOO | -32.810 | 136.059 | 2 | 15 | 275 | 43 | 42 | G | 5 |
| AU | BLDU | -30.615 | 116.709 | 3 | 16 | 330 | 39/56 | 38 | G/F | 2 |
| AU | CMSA | -31.538 | 145.692 | 4 | 18 | 240 | 30 | 35 | G | 2 |
| AU | CNB | -35.315 | 149.363 | 5 | 16 | 217 | 32 | 41 | G | 1 |
| AU | COEN | -13.957 | 143.175 | 6 | 16 | 225 | 37 | 37 | G | 1 |
| AU | CTA | -20.088 | 146.250 | 7 | 25 | 184 | 35 | 39 | G | 1 |
| AU | EIDS | -25.369 | 151.082 | 8 | 16 | 382 | 35 | 35 | G | 1 |
| AU | FITZ | -18.098 | 125.640 | 9 | 25 | 222 | 29/46 | 42 | F | 4 |
| AU | FORT | -30.779 | 128.059 | 10 | 27 | 229 | 46 | - | F | 3 |
| AU | GIRL | -22.643 | 114.234 | 11 | 24 | 245 | 43 | 42 | G | 2 |
| AU | HTT | -33.431 | 138.922 | 12 | 10 | 57 | 46 | 47 | G | 7 |
| AU | INKA | -27.741 | 140.746 | 13 | 6 | 70 | 28 | 46 | F | 6 |
| AU | KDU | -12.687 | 132.473 | 14 | 11 | 69 | 40 | 38 | G | 4 |
| AU | KMBL | -31.367 | 121.882 | 15 | 19 | 257 | 44 | 40 | G | 3 |
| AU | LCRK | -30.447 | 138.216 | 16 | 6 | 85 | 46 | 46 | G/F | 6 |
| AU | LHI | -31.520 | 159.061 | 17 | 12 | 232 | 25 | - | G | 1 |
| AU | MEEK | -26.638 | 118.615 | 18 | 16 | 205 | 41 | 37 | G | 2 |
| AU | MORW | -29.068 | 116.040 | 19 | 16 | 301 | 44 | 46 | G | 2 |
| AU | MTN | -12.844 | 131.133 | 20 | 13 | 124 | 33/45 | 47 | G/F | 5 |
| AU | MULG | -30.282 | 134.059 | 21 | 6 | 86 | 50 | 48 | G | 4 |
| AU | MUN | -31.978 | 116.208 | 22 | 18 | 279 | 47 | 38 | G | 2 |
| AU | NWAO | -32.928 | 117.239 | 23 | 25 | 155 | 40 | 45 | G | 2 |
| AU | OOD | -27.794 | 135.688 | 24 | 6 | 80 | 48 | - | G/F | 3 |
| AU | PSA00 | -21.573 | 119.846 | 25 | 8 | 177 | 28/47 | 30 | G | 2 |
| AU | RIV | -33.829 | 151.158 | 26 | 15 | 74 | 27 | 40 | G | 1 |
| AU | STKA | -31.876 | 141.596 | 27 | 25 | 302 | 41 | 41 | G | 4 |
| AU | TOO | -37.571 | 145.491 | 28 | 16 | 255 | 30 | 37 | G | 1 |
| AU | WRKA | -25.038 | 128.296 | 29 | 10 | 157 | 48 | - | G | 3 |
| AU | YNG | -34.298 | 148.396 | 30 | 20 | 288 | 33 | 40 | G | 1 |
| G | CAN | -35.319 | 148.996 | 31 | 32 | 523 | 29 | 48 | G | 1 |
| II | WRAB | -19.934 | 134.360 | 32 | 25 | 313 | 42 | 50 | G | 6 |
| IU | CTAO | -20.088 | 146.255 | 33 | 28 | 530 | 38 | 39 | G | 1 |
| IU | MBWA | -21.159 | 119.731 | 34 | 18 | 465 | 29/49 | 31 | F | 2 |
| IU | NWAO | -32.928 | 117.239 | 35 | 28 | 610 | 43 | 45 | G | 2 |

**Table 1.1a:** Results of Sp and Ps receiver function analysis

| Network | Station | Ford 2010 | Ford 2010 HVLid | Ford 2010 LAB/MLD | NVG | LAB/MLD | Negative Phase 1 | 2sigma (D) | 2sigma (D) | Amplitude | 2Sigma(A) | 2Sigma(A) |
|---|---|---|---|---|---|---|---|---|---|---|---|---|
| AU | ARMA | 93±16 | <150 | LAB | <150 | LAB | **74** | 67 | 80 | -0.0048 | -0.0058 | -0.0037 |
| AU | BBOO | 131±9 | 150–175 | LAB | Absent | MLD | **70** | 64 | 75 | -0.0038 | -0.0051 | -0.0025 |
| AU | BLDU | – | – | | 100-175 | MLD/Both | **77** | 73 | 82 | -0.0075 | -0.0087 | -0.0063 |
| AU | CMSA | | | | <175 | LAB | **78** | 72 | 84 | -0.0078 | -0.0094 | -0.0062 |
| AU | CNB | | | | <125 | LAB | **80** | 75 | 88 | -0.0056 | -0.0074 | -0.0038 |
| AU | COEN | 67±8 | Absent | LAB | <100 | LAB | **85** | 80 | 91 | -0.0073 | -0.0088 | -0.0058 |
| AU | CTA | | | | <125 | LAB | **76** | 71 | 81 | -0.0063 | -0.0076 | -0.0051 |
| AU | EIDS | 76±12 | <150 | LAB | <125 | LAB | **76** | 73 | 80 | -0.0070 | -0.0080 | -0.0060 |
| AU | FITZ | 81±8 | 125–225 | MLD | 125-175 | MLD/Both | **77** | 68 | 84 | -0.0055 | -0.0066 | -0.0045 |
| AU | FORT | 79±6 | 125–200 | MLD | 125-225 | MLD/Both | **80** | 75 | 85 | -0.0031 | -0.0044 | -0.0018 |
| AU | GIRL | | | | 75-175 | MLD | **68** | 62 | 72 | -0.0045 | -0.0055 | -0.0036 |
| AU | HTT | | | | 50-175? | LAB | **85** | 78 | 90 | -0.0084 | -0.0110 | -0.0059 |
| AU | INKA | | | | Absent | MLD | **61** | 54 | 67 | -0.0057 | -0.0074 | -0.0041 |
| AU | KDU | | | | 125-175 | MLD/Both | **80** | 68 | 87 | -0.0073 | -0.0945 | -0.0052 |
| AU | KMBL | 85±14 | 125–225 | MLD | 125-225 | MLD | **79** | 72 | 85 | -0.0041 | -0.0053 | -0.0042 |
| AU | LCRK | | | | Absent | MLD | **118** | 113 | 124 | -0.0061 | -0.0078 | -0.0044 |
| AU | LHI | | | | <150 | LAB | **82** | 78 | 85 | -0.0061 | -0.0076 | -0.0046 |
| AU | MEEK | | | | 100-225 | MLD/Both | **79** | 72 | 85 | -0.0072 | -0.0088 | -0.0056 |
| AU | MORW | | | | 100-175 | MLD/Both | **78** | 70 | 85 | -0.0074 | -0.0088 | -0.0061 |
| AU | MTN | | | | Absent | MLD | **84** | 60 | 89 | -0.0058 | -0.0072 | -0.0044 |
| AU | MULG | | | | 150-175 | MLD | **75** | 70 | 80 | -0.0044 | -0.0059 | -0.0028 |
| AU | MUN | – | – | | 75-150 | Either | **76** | 71 | 88 | -0.0067 | -0.0083 | -0.0052 |
| AU | NWAO | | | | 75-175 | Either/Both | **77** | 70 | 82 | -0.0052 | -0.0070 | -0.0033 |
| AU | OOD | | | | 150-225 | MLD | **97** | 88 | 105 | -0.0057 | -0.0075 | -0.0038 |
| AU | PSA00 | | | | 75-175 | Both | **67** | 61 | 86 | -0.0077 | -0.0097 | -0.0057 |
| AU | RIV | | | | <150 | LAB | **84** | 79 | 89 | -0.0067 | -0.0097 | -0.0037 |
| AU | STKA | 104±9 | 100–175 | LAB | 125-175 | MLD/Both | **83** | 77 | 87 | -0.0041 | -0.0053 | -0.0029 |
| AU | TOO | 61±11 | Absent | LAB | <125 | LAB | **70** | 61 | 79 | -0.0060 | -0.0073 | -0.0048 |
| AU | WRKA | | | | 150-225 | MLD/Both | **74** | 68 | 81 | -0.0115 | -0.0141 | -0.0089 |
| AU | YNG | 70±8 | <150 | LAB | <125 | LAB | **81** | 75 | 88 | -0.0036 | -0.0054 | -0.0018 |
| G | CAN | | | | <125 | LAB | **82** | 77 | 88 | -0.0052 | -0.0063 | -0.0040 |
| II | WRAB | 81±14 | 175–200 | MLD | Absent | MLD | **71** | 66 | 78 | -0.0041 | -0.0053 | -0.0029 |
| IU | CTAO | 73±6 | Absent | LAB | <125 | LAB | **74** | 71 | 78 | -0.0092 | -0.0102 | -0.0081 |
| IU | MBWA | 69±8 | 100–200 | MLD | 75-175 | Either/Both | **72** | 67 | 78 | -0.0050 | -0.0059 | -0.0041 |
| IU | NWAO | 81±8 | 100–175 | MLD | 75-175 | Either/Both | **77** | 71 | 93 | -0.0039 | -0.0048 | -0.0029 |

**Table 1.1b:** Results of Sp and Ps receiver function analysis

| Network | Station | Negative Phase 2 | 2sigma(D) | 2sigma(D) | Amplitude | 2Sigma(A) | 2Sigma(A) | Other (>0.001) | Other (>0.001) |
|---|---|---|---|---|---|---|---|---|---|
| AU | ARMA | **93** | 60 | 104 | -0.0025 | -0.0035 | -0.0016 | NaN | NaN |
| AU | BBOO | **199** | 193 | 204 | -0.0050 | -0.0034 | -0.0018 | 96 | NaN |
| AU | BLDU | **193** | 186 | 198 | -0.0024 | -0.0036 | -0.0012 | NaN | NaN |
| AU | CMSA | **127** | 119 | 136 | -0.0028 | -0.0039 | -0.0017 | 188 | NaN |
| AU | CNB | **117** | 110 | 122 | -0.0034 | -0.0050 | -0.0017 | NaN | NaN |
| AU | COEN | **66** | 60 | 103 | -0.0027 | -0.0039 | -0.0015 | 163 | NaN |
| AU | CTA | **109** | 104 | 115 | -0.0043 | -0.0057 | -0.0031 | NaN | NaN |
| AU | EIDS | **NaN** | NaN | NaN | NaN | NaN | NaN | NaN | NaN |
| AU | FITZ | **122** | 112 | 134 | -0.0026 | -0.0035 | -0.0016 | NaN | NaN |
| AU | FORT | **216** | 213 | 220 | -0.0037 | -0.0049 | -0.0024 | NaN | NaN |
| AU | GIRL | **NaN** | NaN | NaN | NaN | NaN | NaN | NaN | NaN |
| AU | HTT | **NaN** | NaN | NaN | NaN | NaN | NaN | NaN | NaN |
| AU | INKA | **101** | 97 | 107 | -0.0046 | -0.0061 | -0.0031 | 287 | NaN |
| AU | KDU | **99** | 60 | 111 | -0.0037 | -0.0063 | -0.0012 | NaN | NaN |
| AU | KMBL | **113** | 104 | 120 | -0.0032 | -0.0045 | -0.0195 | 249 | NaN |
| AU | LCRK | **67** | 60 | 73 | -0.0047 | -0.0069 | -0.0026 | 271 | NaN |
| AU | LHI | **101** | 96 | 105 | -0.0030 | -0.0044 | -0.0015 | 56 | 186 |
| AU | MEEK | **129** | 124 | 134 | -0.0051 | -0.0066 | -0.0036 | NaN | NaN |
| AU | MORW | **190** | 177 | 196 | -0.0028 | -0.0043 | -0.0012 | NaN | NaN |
| AU | MTN | **64** | 59 | 90 | -0.0053 | -0.0065 | -0.0040 | 170 | ***225*** |
| AU | MULG | **109** | 113 | 103 | -0.0028 | -0.0041 | -0.0015 | 169 | NaN |
| AU | MUN | **NaN** | NaN | NaN | NaN | NaN | NaN | NaN | NaN |
| AU | NWAO | **109** | 105 | 114 | -0.0030 | -0.0046 | -0.0014 | 186 | NaN |
| AU | OOD | **NaN** | NaN | NaN | NaN | NaN | NaN | NaN | NaN |
| AU | PSA00 | **81** | 61 | 87 | -0.0073 | -0.0091 | -0.0056 | 120 | 170 |
| AU | RIV | **153** | 149 | 157 | -0.0047 | -0.0072 | -0.0022 | 69 | NaN |
| AU | STKA | **137** | 114 | 143 | -0.0021 | -0.0032 | -0.0010 | NaN | NaN |
| AU | TOO | **NaN** | NaN | NaN | NaN | NaN | NaN | NaN | NaN |
| AU | WRKA | **222** | 189 | 228 | -0.0030 | -0.0050 | -0.0011 | NaN | NaN |
| AU | YNG | **128** | 123 | 133 | -0.0035 | -0.0048 | -0.0022 | NaN | NaN |
| G | CAN | **188** | 182 | 194 | -0.0029 | -0.0041 | -0.0017 | 50 | NaN |
| II | WRAB | **91** | 63 | 97 | -0.0030 | -0.0042 | -0.0019 | 135 | 198 |
| IU | CTAO | **118** | 107 | 124 | -0.0019 | -0.0027 | -0.0011 | NaN | NaN |
| IU | MBWA | **87** | 63 | 93 | -0.0033 | -0.0044 | -0.0023 | NaN | NaN |
| IU | NWAO | **132** | 128 | 137 | -0.0027 | -0.0037 | -0.0018 | NaN | NaN |

**Table 1.1c:** Results of Sp and Ps receiver function analysis

## References


Abt, D. L., Fischer, K. M., French, S. W., Ford, H. A., Yuan, H., & Romanowicz, B. (2010). North American lithospheric discontinuity structure imaged by Ps and Sp receiver functions. *Journal of Geophysical Research: Solid Earth*, *115*(B9).

Artemieva, I. M. (2009). The continental lithosphere: reconciling thermal, seismic, and petrologic data. *Lithos*, *109*(1-2), 23-46.

Auer, L., Boschi, L., Becker, T. W., Nissen-Meyer, T., & Giardini, D. (2014). Savani: A variable resolution whole-mantle model of anisotropic shear velocity variations based on multiple data sets. *Journal of Geophysical Research: Solid Earth*, *119*(4), 3006-3034.

Aulbach, S., Massuyeau, M., & Gaillard, F. (2017a). Origins of cratonic mantle discontinuities: A view from petrology, geochemistry and thermodynamic models. *Lithos*, *268*, 364-382.

Aulbach, S., Sun, J., Tappe, S., Höfer, H. E., & Gerdes, A. (2017b). Volatile-rich metasomatism in the cratonic mantle beneath SW Greenland: link to kimberlites and mid-lithospheric discontinuities. *Journal of Petrology*, *58*(12), 2311-2338.

Baba, K., Chave, A. D., Evans, R. L., Hirth, G., & Mackie, R. L. (2006). Mantle dynamics beneath the East Pacific Rise at 17 S: Insights from the Mantle Electromagnetic and Tomography (MELT) experiment. *Journal of Geophysical Research: Solid Earth*, *111*(B2).

Bagas, L. (2004). Proterozoic evolution and tectonic setting of the northwest Paterson Orogen, Western Australia. *Precambrian Research*, *128*(3-4), 475-496.

Barley, M. E., Loader, S. E., & McNaughton, N. J. (1998). 3430 to 3417 Ma calc-alkaline volcanism in the McPhee Dome and Kelly Belt, and growth of the eastern Pilbara Craton. *Precambrian Research*, *88*(1-4), 3-23.

Best, M. G. (1974). Mantle-derived amphibole within inclusions in alkalic-basaltic lavas. *Journal of Geophysical Research*, *79*(14), 2107-2113.

Betts, P. G., Giles, D., Lister, G. S., & Frick, L. R. (2002). Evolution of the Australian lithosphere. *Australian Journal of Earth Sciences*, *49*(4), 661-695.

Betts, P. G., & Giles, D. (2006). The 1800–1100 Ma tectonic evolution of Australia. *Precambrian Research*, *144*(1-2), 92-125.

Bodin, T., Yuan, H., & Romanowicz, B. (2014). Inversion of receiver functions without deconvolution—application to the Indian craton. *Geophysical Journal International*, *196*(2), 1025-1033.

Bostock, M. G. (1998). Mantle stratigraphy and evolution of the Slave province. *Journal of Geophysical Research: Solid Earth*, *103*(B9), 21183-21200.

Carlson, R. W., Pearson, D. G., & James, D. E. (2005). Physical, chemical, and chronological characteristics of continental mantle. *Reviews of Geophysics*, *43*(1).

Chen, L. (2009). Lithospheric structure variations between the eastern and central North China Craton from S-and P-receiver function migration. *Physics of the Earth and Planetary Interiors*, *173*(3-4), 216-227.

Choi, E., Fiorentini, M. L., Giuliani, A., Foley, S. F., Maas, R., & Taylor, W. R. (2020). Subduction-related petrogenesis of Late Archean calc-alkaline lamprophyres in the Yilgarn Craton (Western Australia). *Precambrian Research*, *338*, 105550.

Clitheroe, G., & Van Der Hilst, R. D. (1998). Complex anisotropy in the Australian lithosphere from shear-wave splitting in broad-band SKS records. *Structure and Evolution of the Australian Continent*, *26*, 73-78.

Conor, C. H., & Preiss, W. V. (2008). Understanding the 1720–1640 Ma Palaeoproterozoic Willyama Supergroup, Curnamona Province, Southeastern Australia: implications for tectonics, basin evolution and ore genesis. *Precambrian Research*, *166*(1-4), 297-317.

Cook, F. A., van der Velden, A. J., Hall, K. W., & Roberts, B. J. (1999). Frozen subduction in Canada's Northwest Territories: Lithoprobe deep lithospheric reflection profiling of the western Canadian Shield. *Tectonics*, *18*(1), 1-24.

Cooper, C. M., & Miller, M. S. (2014). Craton formation: Internal structure inherited from closing of the early oceans. *Lithosphere*, *6*(1), 35-42.

Daly, S. J. (1998). Tectonic evolution and exploration potential of the Gawler Craton, South Australia. *AGSO J. Aust. Geol. Geophys.*, *17*, 145-168.

Davies, D. R., & Rawlinson, N. (2014). On the origin of recent intraplate volcanism in Australia. *Geology*, *42*(12), 1031-1034.

Davies, D. R., Rawlinson, N., Iaffaldano, G., & Campbell, I. H. (2015). Lithospheric controls on magma composition along Earth's longest continental hotspot track. *Nature*, *525*(7570), 511-514.

Debayle, E., & Kennett, B. L. N. (2000). The Australian continental upper mantle: structure and deformation inferred from surface waves. *Journal of Geophysical Research: Solid Earth*, *105*(B11), 25423-25450.

Debayle, E., Kennett, B., & Priestley, K. (2005). Global azimuthal seismic anisotropy and the unique plate-motion deformation of Australia. *Nature*, *433*(7025), 509-512.

Demidjuk, Z., Turner, S., Sandiford, M., George, R., Foden, J., & Etheridge, M. (2007). U-series isotope and geodynamic constraints on mantle melting processes beneath the Newer Volcanic Province in South Australia. *Earth and Planetary Science Letters*, *261*(3-4), 517-533.

Direen, N. G., & Crawford, A. J. (2003). The Tasman Line: where is it, what is it, and is it Australia's Rodinian breakup boundary?. *Australian Journal of Earth Sciences*, *50*(4), 491-502.

Dueker, K., Yuan, H., & Zurek, B. (2001). Thick-structured Proterozoic lithosphere of the Rocky Mountain region. *Gsa Today*, *11*(12), 4-9.

Eaton, D. W., Darbyshire, F., Evans, R. L., Grütter, H., Jones, A. G., & Yuan, X. (2009). The elusive lithosphere–asthenosphere boundary (LAB) beneath cratons. *Lithos*, *109*(1-2), 1-22.

Edwards, D., Rock, N. M. S., Taylor, W. R., Griffin, B. J., & Ramsay, R. R. (1992). Mineralogy and petrology of the Aries diamondiferous kimberlite pipe, Central Kimberley Block, Western Australia. *Journal of Petrology*, *33*(5), 1157-1191.

Evans, R. L., Hirth, G., Baba, K., Forsyth, D., Chave, A., & Mackie, R. (2005). Geophysical evidence from the MELT area for compositional controls on oceanic plates. *Nature*, *437*(7056), 249-252.

Evans, R. L., Jones, A. G., Garcia, X., Muller, M., Hamilton, M., Evans, S., ... & Hutchins, D. (2011). Electrical lithosphere beneath the Kaapvaal craton, southern Africa. *Journal of Geophysical Research: Solid Earth*, *116*(B4).

Fischer, K. M., Ford, H. A., Abt, D. L., & Rychert, C. A. (2010). The lithosphere-asthenosphere boundary. *Annual Review of Earth and Planetary Sciences*, *38*, 551-575.

Fichtner, A., Kennett, B. L., Igel, H., & Bunge, H. P. (2010). Full waveform tomography for radially anisotropic structure: new insights into present and past states of the Australasian upper mantle. *Earth and Planetary Science Letters*, *290*(3-4), 270-280.

Fishwick, S., Kennett, B. L. N., & Reading, A. M. (2005). Contrasts in lithospheric structure within the Australian craton—insights from surface wave tomography. *Earth and Planetary Science Letters*, *231*(3-4), 163-176.

Fishwick, S., & Rawlinson, N. (2012). 3-D structure of the Australian lithosphere from evolving seismic datasets. *Australian Journal of Earth Sciences*, *59*(6), 809-826.

Fishwick, S., & Reading, A. M. (2008). Anomalous lithosphere beneath the Proterozoic of western and central Australia: a record of continental collision and intraplate deformation?. *Precambrian Research*, *166*(1-4), 111-121.

Ford, H. A., Fischer, K. M., Abt, D. L., Rychert, C. A., & Elkins-Tanton, L. T. (2010). The lithosphere–asthenosphere boundary and cratonic lithospheric layering beneath Australia from Sp wave imaging. *Earth and Planetary Science Letters*, *300*(3-4), 299-310.

Ford, H. A., Long, M. D., & Wirth, E. A. (2016). Midlithospheric discontinuities and complex anisotropic layering in the mantle lithosphere beneath the Wyoming and Superior Provinces. *Journal of Geophysical Research: Solid Earth*, *121*(9), 6675-6697.

Foster, K., Dueker, K., Schmandt, B., & Yuan, H. (2014). A sharp cratonic lithosphere–asthenosphere boundary beneath the American Midwest and its relation to mantle flow. *Earth and Planetary Science Letters*, *402*, 82-89.

Fouch, M. J., & Rondenay, S. (2006). Seismic anisotropy beneath stable continental interiors. *Physics of the Earth and Planetary Interiors*, *158*(2-4), 292-320.

Fraser, G. L., Huston, D., Gibson, G. M., Neumann, N. L., Maidment, D., Kositcin, N., ... & Cutten, H. (2007). *Geodynamic and Metallogenic Evolution of Proterozoic Australia from 1870-1550 Ma: A Discussion*. Geoscience Australia.

Frey, F. A., McNaughton, N. J., Nelson, D. R., deLaeter, J. R., & Duncan, R. A. (1996). Petrogenesis of the Bunbury Basalt, Western Australia: interaction between the Kerguelen plume and Gondwana lithosphere?. *Earth and Planetary Science Letters*, *144*(1-2), 163-183.

Gaherty, J. B., Kato, M., & Jordan, T. H. (1999). Seismological structure of the upper mantle: a regional comparison of seismic layering. *Physics of the Earth and Planetary Interiors*, *110*(1-2), 21-41.

Gaillard, F., Malki, M., Iacono-Marziano, G., Pichavant, M., & Scaillet, B. (2008). Carbonatite melts and electrical conductivity in the asthenosphere. *Science*, *322*(5906), 1363-1365.

Giuliani, A., Phillips, D., Kamenetsky, V. S., & Goemann, K. (2016). Constraints on kimberlite ascent mechanisms revealed by phlogopite compositions in kimberlites and mantle xenoliths. *Lithos*, *240*, 189-201.

Graham, S., Lambert, D., & Shee, S. (2004). The petrogenesis of carbonatite, melnoite and kimberlite from the Eastern Goldfields Province, Yilgarn Craton. *Lithos*, *76*(1-4), 519-533.

Griffin, W. L., Wass, S. Y., & Hollis, J. D. (1984). Ultramafic xenoliths from Bullenmerri and Gnotuk maars, Victoria, Australia: petrology of a sub-continental crust-mantle transition. *Journal of Petrology*, *25*(1), 53-87.

Griffin, W. L., O'reilly, S. Y., Afonso, J. C., & Begg, G. C. (2009). The composition and evolution of lithospheric mantle: a re-evaluation and its tectonic implications. *Journal of Petrology*, *50*(7), 1185-1204.

Hacker, B. R., Abers, G. A., & Peacock, S. M. (2003). Subduction factory 1. Theoretical mineralogy, densities, seismic wave speeds, and H2O contents. *Journal of Geophysical Research: Solid Earth*, *108*(B1).

Hales, A. L. (1969). A seismic discontinuity in the lithosphere. *Earth and Planetary Science Letters*, *7*(1), 44-46.

Hansen, S. E., Nyblade, A. A., Julia, J., Dirks, P. H., & Durrheim, R. J. (2009). Upper-mantle low-velocity zone structure beneath the Kaapvaal craton from S-wave receiver functions. *Geophysical Journal International*, *178*(2), 1021-1027.

Hansen, S. M., Dueker, K., & Schmandt, B. (2015). Thermal classification of lithospheric discontinuities beneath USArray. *Earth and Planetary Science Letters*, *431*, 36-47.

Heintz, M., & Kennett, B. L. (2005). Continental scale shear wave splitting analysis: investigation of seismic anisotropy underneath the Australian continent. *Earth and Planetary Science Letters*, *236*(1-2), 106-119.

Helffrich, G. (2006). Extended-time multitaper frequency domain cross-correlation receiver-function estimation. *Bulletin of the Seismological Society of America*, *96*(1), 344-347.

Herzberg, C., Condie, K., & Korenaga, J. (2010). Thermal history of the Earth and its petrological expression. *Earth and Planetary Science Letters*, *292*(1-2), 79-88.

Hirth, G., & Kohlstedt, D. L. (1996). Water in the oceanic upper mantle: implications for rheology, melt extraction and the evolution of the lithosphere. *Earth and Planetary Science Letters*, *144*(1-2), 93-108.

Hirth, G., Evans, R. L., & Chave, A. D. (2000). Comparison of continental and oceanic mantle electrical conductivity: Is the Archean lithosphere dry?. *Geochemistry, Geophysics, Geosystems*, *1*(12).

Hopp, J., Trieloff, M., Brey, G. P., Woodland, A. B., Simon, N. S. C., Wijbrans, J. R., ... & Reitter, E. (2008). 40Ar/39Ar-ages of phlogopite in mantle xenoliths from South African kimberlites: evidence for metasomatic mantle impregnation during the Kibaran orogenic cycle. *Lithos*, *106*(3-4), 351-364.

Hopper, E., Ford, H. A., Fischer, K. M., Lekic, V., & Fouch, M. J. (2014). The lithosphere–asthenosphere boundary and the tectonic and magmatic history of the northwestern United States. *Earth and Planetary Science Letters*, *402*, 69-81.

Hopper, E., & Fischer, K. M. (2015). The meaning of midlithospheric discontinuities: A case study in the northern US craton. *Geochemistry, Geophysics, Geosystems*, *16*(12), 4057-4083.

Jaques, A. L., O'Neill, H. S. C., Smith, C. B., Moon, J., & Chappell, B. W. (1990). Diamondiferous peridotite xenoliths from the Argyle (AK1) lamproite pipe, Western Australia. *Contributions to Mineralogy and Petrology*, *104*(3), 255-276.

Karato, S. I. (2012). On the origin of the asthenosphere. *Earth and Planetary Science Letters*, *321*, 95-103.

Karato, S. I., & Jung, H. (1998). Water, partial melting and the origin of the seismic low velocity and high attenuation zone in the upper mantle. *Earth and Planetary Science Letters*, *157*(3-4), 193-207.

Karato, S. I., Olugboji, T., & Park, J. (2015). Mechanisms and geologic significance of the mid-lithosphere discontinuity in the continents. *Nature Geoscience*, *8*(7), 509-514.

Kennett, B. L. N. (2015). Lithosphere–asthenosphere P-wave reflectivity across Australia. *Earth and Planetary Science Letters*, *431*, 225-235.

Kennett, B. L. N., & Abdullah, A. (2011). Seismic wave attenuation beneath the Australasian region. *Australian Journal of Earth Sciences*, *58*(3), 285-295.

Kennett, B., Chopping, R., & Blewett, R. (2018). *The Australian continent: A geophysical synthesis*. ANU Press.

Kennett, B. L., Fichtner, A., Fishwick, S., & Yoshizawa, K. (2013). Australian seismological reference model (AuSREM): mantle component. *Geophysical Journal International*, *192*(2), 871-887.

Kennett, B. L., Fishwick, S., Reading, A. M., & Rawlinson, N. (2004). Contrasts in mantle structure beneath Australia: relation to Tasman Lines?. *Australian Journal of Earth Sciences*, *51*(4), 563-569.

Kennett, B. L. N., & Furumura, T. (2016). Multiscale seismic heterogeneity in the continental lithosphere. *Geochemistry, Geophysics, Geosystems*, *17*(3), 791-809.

Kennett, B. L. N., & Liang, S. (2020). The transition from the Thomson Orogen to the North Australian Craton from seismic data. *Australian Journal of Earth Sciences*, 1-13.

Kennett, B. L. N., & Sippl, C. (2018). Lithospheric discontinuities in Central Australia. *Tectonophysics*, *744*, 10-22.

Kennett, B. L. N., Yoshizawa, K., & Furumura, T. (2017). Interactions of multi-scale heterogeneity in the lithosphere: Australia. *Tectonophysics*, *717*, 193-213.

Kind, R., Handy, M. R., Yuan, X., Meier, T., Kämpf, H., & Soomro, R. (2017). Detection of a new sub-lithospheric discontinuity in Central Europe with S-receiver functions. *Tectonophysics*, *700*, 19-31.

Kind, R., Yuan, X., & Kumar, P. (2012). Seismic receiver functions and the lithosphere–asthenosphere boundary. *Tectonophysics*, *536*, 25-43.

Konzett, J., & Ulmer, P. (1999). The stability of hydrous potassic phases in lherzolitic mantle—an experimental study to 9.5 GPa in simplified and natural bulk compositions. *Journal of Petrology*, *40*(4), 629-652.

Konzett, J., Wirth, R., Hauzenberger, C., & Whitehouse, M. (2013). Two episodes of fluid migration in the Kaapvaal Craton lithospheric mantle associated with Cretaceous kimberlite activity: evidence from a harzburgite containing a unique assemblage of metasomatic zirconium-phases. *Lithos*, *182,* 165-184.

Korsch, R. J., & Doublier, M. P. (2016). Major crustal boundaries of Australia, and their significance in mineral systems targeting. *Ore Geology Reviews*, *76*, 211-228.

Kumar, P., Kind, R., Yuan, X., & Mechie, J. (2012). USArray receiver function images of the lithosphere-asthenosphere boundary. *Seismological Research Letters*, *83*(3), 486-491.

Kumar, P., Yuan, X., Kumar, M. R., Kind, R., Li, X., & Chadha, R. K. (2007). The rapid drift of the Indian tectonic plate. *Nature*, *449*(7164), 894-897.

Lee, C. T. A. (2003). Compositional variation of density and seismic velocities in natural peridotites at STP conditions: Implications for seismic imaging of compositional heterogeneities in the upper mantle. *Journal of Geophysical Research: Solid Earth*, *108*(B9).

Lee, C.T.A. (2006). Geochemical/petrologic constraints on the origin of cratonic mantle. *Geophysical Monograph-American Geophysical Union*, *164*, 89.

Lee, C. T. A., Lenardic, A., Cooper, C. M., Niu, F., & Levander, A. (2005). The role of chemical boundary layers in regulating the thickness of continental and oceanic thermal boundary layers. *Earth and Planetary Science Letters*, *230*(3-4), 379-395.

Lee, C. T. A., Luffi, P., & Chin, E. J. (2011). Building and destroying continental mantle. *Annual Review of Earth and Planetary Sciences*, *39*, 59-90.

Lekić, V., & Fischer, K. M. (2014). Contrasting lithospheric signatures across the western United States revealed by Sp receiver functions. *Earth and Planetary Science Letters*, *402*, 90-98.

Lekić, V., & Fischer, K. M. (2017). Interpreting spatially stacked Sp receiver functions. *Geophysical Journal International*, *210*(2), 874-886.

Levin, V., & Park, J. (1997). P-SH conversions in a flat-layered medium with anisotropy of arbitrary orientation. *Geophysical Journal International*, *131*(2), 253-266.

Levin, V., & Park, J. (1998). P-SH conversions in layered media with hexagonally symmetric anisotropy: a cookbook. In *Geodynamics of Lithosphere & Earth's Mantle* (pp. 669-697). Birkhäuser, Basel.

Levin, V., & Park, J. (2000). Shear zones in the Proterozoic lithosphere of the Arabian Shield and the nature of the Hales discontinuity. *Tectonophysics*, *323*(3-4), 131-148.

Liang, S., & Kennett, B. L. (2020). Passive seismic imaging of a craton edge–Central Australia. *Tectonophysics*, *797*, 228662.

Liao, J., & Gerya, T. (2014). Influence of lithospheric mantle stratification on craton extension: Insight from two-dimensional thermo-mechanical modeling. *Tectonophysics*, *631*, 50-64.

Liu, L., Morgan, J. P., Xu, Y., & Menzies, M. (2018). Craton destruction 1: Cratonic keel delamination along a weak midlithospheric discontinuity layer. *Journal of Geophysical Research: Solid Earth*, *123*(11), 10-040.

Mancinelli, N. J., Fischer, K. M., & Dalton, C. A. (2017). How sharp is the cratonic lithosphere-asthenosphere transition?. *Geophysical Research Letters*, *44*(20), 10-189.

McBride, J. S., Lambert, D. D., Greig, A., & Nicholls, I. A. (1996). Multistage evolution of Australian subcontinental mantle: Re-Os isotopic constraints from Victorian mantle xenoliths. *Geology*, *24*(7), 631-634.

McCulloch, M. T., Jaques, A. L., Nelson, D. R., & Lewis, J. D. (1983). Nd and Sr isotopes in kimberlites and lamproites from Western Australia: an enriched mantle origin. *Nature*, *302*(5907), 400-403.

McLaren, S., Sandiford, M., Hand, M., Neumann, N., Wyborn, L., & Bastrakova, I. (2003). The hot southern continent: heat flow and heat production in Australian Proterozoic terranes. *Special Papers-geological Society of America*, 157-168.

Middleton, M. F., Wilde, S. A., Evans, B. A., Long, A., & Dentith, M. (1993). A preliminary interpretation of deep seismic reflection and other geophysical data from the Darling Fault Zone, Western Australia. *Exploration Geophysics*, *24*(4), 711-718.

Myers, J. S. (1993). Precambrian history of the West Australian craton and adjacent orogens. *Annual Review of Earth and Planetary Sciences*, *21*(1), 453-485.

Myers, J. S., Shaw, R. D., & Tyler, I. M. (1996). Tectonic evolution of proterozoic Australia. *Tectonics*, *15*(6), 1431-1446.

Nettles, M., & Dziewoński, A. M. (2008). Radially anisotropic shear velocity structure of the upper mantle globally and beneath North America. *Journal of Geophysical Research: Solid Earth*, *113*(B2).

Park, J., & Levin, V. (2000). Receiver functions from multiple-taper spectral correlation estimates. *Bulletin of the Seismological Society of America*, *90*(6), 1507-1520.

Porritt, R. W., Miller, M. S., & Darbyshire, F. A. (2015). Lithospheric architecture beneath H udson B ay. *Geochemistry, Geophysics, Geosystems*, *16*(7), 2262-2275.

Priyatkina, N., Khudoley, A. K., Ustinov, V. N., & Kullerud, K. (2014). 1.92 Ga kimberlitic rocks from Kimozero, NW Russia: Their geochemistry, tectonic setting and unusual field occurrence. *Precambrian Research*, *249*, 162-179.

Rader, E., Emry, E., Schmerr, N., Frost, D., Cheng, C., Menard, J., ... & Geist, D. (2015). Characterization and petrological constraints of the midlithospheric discontinuity. *Geochemistry, Geophysics, Geosystems*, *16*(10), 3484-3504.

Rawlinson, N., Pilia, S., Young, M., Salmon, M., & Yang, Y. (2016). Crust and upper mantle structure beneath southeast Australia from ambient noise and teleseismic tomography. *Tectonophysics*, *689*, 143-156.

Reading, A. M., & Kennett, B. L. N. (2003). Lithospheric structure of the Pilbara Craton, Capricorn Orogen and northern Yilgarn Craton, Western Australia, from teleseismic receiver functions. *Australian Journal of Earth Sciences*, *50*(3), 439-445.

Ritsema, J., Deuss, A. A., Van Heijst, H. J., & Woodhouse, J. H. (2011). S40RTS: a degree-40 shear-velocity model for the mantle from new Rayleigh wave dispersion, teleseismic traveltime and normal-mode splitting function measurements. *Geophysical Journal International*, *184*(3), 1223-1236.

Romanowicz, B. (2009). The thickness of tectonic plates. *Science*, *324*(5926), 474-476.

Rychert, C. A., Harmon, N., Constable, S., & Wang, S. (2020). The Nature of the Lithosphere-Asthenosphere Boundary. *Journal of Geophysical Research: Solid Earth*, *125*(10), e2018JB016463.

Rychert, C. A., & Shearer, P. M. (2009). A global view of the lithosphere-asthenosphere boundary. *Science*, *324*(5926), 495-498.

Saha, S., Dasgupta, R., & Tsuno, K. (2018). High pressure phase relations of a depleted peridotite fluxed by CO2-H2O-bearing siliceous melts and the origin of mid-lithospheric discontinuity. *Geochemistry, Geophysics, Geosystems*, *19*(3), 595-620.

Salmon, M., Kennett, B. L. N., Stern, T., & Aitken, A. R. A. (2013). The Moho in Australia and New Zealand. *Tectonophysics*, *609*, 288-298.

Sato, K., Katsura, T., & Ito, E. (1997). Phase relations of natural phlogopite with and without enstatite up to 8 GPa: implication for mantle metasomatism. *Earth and Planetary Science Letters*, *146*(3-4), 511-526.

Schaeffer, A. J., & Lebedev, S. (2013). Global shear speed structure of the upper mantle and transition zone. *Geophysical Journal International*, *194*(1), 417-449.

Selway, K., Ford, H., & Kelemen, P. (2015). The seismic mid-lithosphere discontinuity. *Earth and Planetary Science Letters*, *414*, 45-57.

Shen, X., Kim, Y., Song, T. R. A., & Lim, H. (2019). Data-oriented constraint on the interpretation of S receiver function and its application to observations of seismic discontinuities in the lithosphere–asthenosphere system. *Geophysical Journal International*, *219*(1), 496-513.

Simons, F. J., Zielhuis, A., & Van Der Hilst, R. D. (1999). The deep structure of the Australian continent from surface wave tomography. *Lithos*, *48*(1-4), 17-43.

Sippl, C. (2016). Moho geometry along a north–south passive seismic transect through Central Australia. *Tectonophysics*, *676*, 56-69.

Sleep, N. H. (2005). Evolution of the continental lithosphere. *Annual Review of Earth and Planetary Sciences*, *33*, 369-393.

Snyder, D. B. (2008). Stacked uppermost mantle layers within the Slave craton of NW Canada as defined by anisotropic seismic discontinuities. *Tectonics*, *27*(4).

Sodoudi, F., Yuan, X., Kind, R., Lebedev, S., Adam, J. M. C., Kästle, E., & Tilmann, F. (2013). Seismic evidence for stratification in composition and anisotropic fabric within the thick lithosphere of Kalahari Craton. *Geochemistry, Geophysics, Geosystems*, *14*(12), 5393-5412.

Sun, W., Fu, L. Y., Saygin, E., & Zhao, L. (2018). Insights into layering in the cratonic lithosphere beneath Western Australia. *Journal of Geophysical Research: Solid Earth*, *123*(2), 1405-1418.

Sun, W., & Kennett, B. L. N. (2016). Receiver structure from teleseisms: Autocorrelation and cross correlation. *Geophysical Research Letters*, *43*(12), 6234-6242.

Sun, W., Zhao, L., Yuan, H., & Fu, L. Y. (2020). Sharpness of the Midlithospheric Discontinuities and Craton Evolution in North China. *Journal of Geophysical Research: Solid Earth*, *125*(9), e2019JB018594.

Sutherland, F. L., Graham, I. T., Meffre, S., Zwingmann, H., & Pogson, R. E. (2012). Passive-margin prolonged volcanism, East Australian Plate: outbursts, progressions, plate controls and suggested causes. *Australian Journal of Earth Sciences*, *59*(7), 983-1005.

Tesauro, M., Kaban, M. K., & Aitken, A. R. (2020). Thermal and compositional anomalies of the Australian upper mantle from seismic and gravity data. *Geochemistry, Geophysics, Geosystems*, *21*(11).

Tharimena, S., Rychert, C. A., & Harmon, N. (2016). Seismic imaging of a mid-lithospheric discontinuity beneath Ontong Java Plateau. *Earth and Planetary Science Letters*, *450*, 62-70.

Thybo, H. (2006). The heterogeneous upper mantle low velocity zone. *Tectonophysics*, *416*(1-4), 53-79.

Till, C. B., Grove, T. L., & Withers, A. C. (2012). The beginnings of hydrous mantle wedge melting. *Contributions to Mineralogy and Petrology*, *163*(4), 669-688.

Vielzeuf, D., & Schmidt, M. W. (2001). Melting relations in hydrous systems revisited: application to metapelites, metagreywackes and metabasalts. *Contributions to Mineralogy and Petrology*, *141*(3), 251.

Wang, L., Hitchman, A. P., Ogawa, Y., Siripunvaraporn, W., Ichiki, M., & Fuji-ta, K. (2014). A 3-D conductivity model of the Australian continent using observatory and magnetometer array data. *Geophysical Journal International*, *198*(2), 1143-1158.

Wang, Z., Kusky, T. M., & Capitanio, F. A. (2016). Lithosphere thinning induced by slab penetration into a hydrous mantle transition zone. *Geophysical Research Letters*, *43*(22), 11-567.

Wang, Z., Kusky, T. M., & Capitanio, F. A. (2018). Water transportation ability of flat-lying slabs in the mantle transition zone and implications for craton destruction. *Tectonophysics*, *723*, 95-106.

Wang, Z., & Kusky, T. M. (2019). The importance of a weak mid-lithospheric layer on the evolution of the cratonic lithosphere. *Earth-science reviews*.

Wei, Z., Kennett, B. L., & Sun, W. (2018). Sn-wave velocity structure of the uppermost mantle beneath the Australian continent. *Geophysical Journal International*, *213*(3), 2071-2084.

Wirth, E. A., & Long, M. D. (2014). A contrast in anisotropy across mid-lithospheric discontinuities beneath the central United States—A relic of craton formation. *Geology*, *42*(10), 851-854.

Wittlinger, G., & Farra, V. (2007). Converted waves reveal a thick and layered tectosphere beneath the Kalahari super-craton. *Earth and Planetary Science Letters*, *254*(3-4), 404-415.

Wölbern, I., Rümpker, G., Link, K., & Sodoudi, F. (2012). Melt infiltration of the lower lithosphere beneath the Tanzania craton and the Albertine rift inferred from S receiver functions. *Geochemistry, Geophysics, Geosystems*, *13*(8).

Yoshizawa, K. (2014). Radially anisotropic 3-D shear wave structure of the Australian lithosphere and asthenosphere from multi-mode surface waves. *Physics of the Earth and Planetary Interiors*, *235*, 33-48.

Yoshizawa, K., & Kennett, B. L. N. (2015). The lithosphere-asthenosphere transition and radial anisotropy beneath the Australian continent. *Geophysical research letters*, *42*(10), 3839-3846.

Yuan, H., & Romanowicz, B. (2010). Lithospheric layering in the North American craton. *Nature*, *466*(7310), 1063-1068.

**Anisotropic Structure of the Australian Continent**

Andrew Birkey[1*] and Heather A. Ford[1]

[1]Department of Earth and Planetary Sciences, University of California – Riverside, Riverside, CA

*In preparation for Frontiers in Earth Science – Lithospheric Diversity: New Perspective on Structure, Composition, and Evolution*

*Corresponding author:

Department of Earth and Planetary Sciences, University of California – Riverside

900 University Avenue, Riverside, California, 92521

Email: abirk001@ucr.edu

**Abstract**

The Australian continent preserves some of the oldest lithosphere on the planet in the Yilgarn, Pilbara and Gawler Cratons. In this study we present shear wave splitting and Ps receiver function results at long running stations across the Australian continent. We use these results to constrain the anisotropic structure of Australia's cratons and younger Phanerozoic Orogens to better understand the deformational history of the continent. For shear wave splitting analysis, we utilize SKS and SKKS phases at 35 broadband stations. For Ps receiver function analysis, we utilize 14 stations. Our shear wave splitting analysis confirms the work of previous studies, which show that anisotropy in Australia cannot be explained by plate motion alone, nor do they follow the strike of major tectonic/geologic features at the surface. Shear wave splits at most stations show strong variations in both the orientation of the fast direction and delay time as a function of back azimuth, supporting the premise that Australian cratons have multiple layers of anisotropy. While shear wave splitting provides information about bulk properties, it is a path-integrated effect and thus has poor vertical resolution. We utilize Ps receiver functions to examine seismic boundaries at depth and observe significant variations in the amplitude and polarity of receiver functions with backazimuth at stations across Australia, indicating the presence of complex seismic anisotropy. These results confirm the presence of multiple layers of anisotropy within the thicker cratonic lithosphere to the west, as well as a complex signal in the Phanerozoic east. Such complex seismic anisotropy and seismic layering within the

lithosphere suggests that anisotropic fabrics may be preserved for billions of years and record ancient events linked to the formation, stabilization, and evolution of cratons in deep time.

## 1. Introduction

Earth's interior is commonly described as being divided into layers by one of two criteria: composition or rheology. The outermost rheological layer is the lithosphere, a rigid shell that translates coherently above the flowing asthenosphere and is composed of portions of two compositional layers, the crust and the mantle. In some instances, the lithosphere is considered to be that portion of the Earth which is engaged in plate tectonics and referred to as the tectosphere (Jordan, 1975). Increasing evidence suggests that the lithosphere is heterogeneous in many geophysical properties: this has been revealed through methods such as magnetotellurics (e.g., Bedrosian and Finn, 2021; Selway, 2018), tomography (e.g., Yoshizawa, 2014), attenuation (e.g., Kennett and Abdullah, 2011), reflectivity (e.g., Kennett et al., 2017), reflection (e.g., Worthington et al., 2015), refraction (Musacchio et al., 2004), shear wave splitting (e.g., Chen et al., 2018), and receiver functions (e.g., Hopper and Fischer, 2015). One of the key findings from some of these studies is that heterogeneity within the Earth's upper mantle is often expressed as anisotropy of material properties such as seismic wavespeeds (Debayle et al., 2016), strength (Vauchez et al., 1998), and electrical conductivity (Du Frane et al., 2005). In this study, we present results from two complementary techniques, shear wave splitting and receiver functions, to examine the internal structure of the Australian lithosphere, which has evolved over

billions of years of geologic history. We examine cratonic Australia (those regions that have been tectonically inactive for at least one billion years) as well as the younger, Phanerozoic eastern margin for evidence of preserved and inherited seismic lithospheric structure.

*1.1 Shear wave splitting background*

Seismic structures are sometimes assumed to be isotropic—that is, there are no variations with direction for material properties such as seismic velocities or strength. However, many of the Earth's constituent minerals have strongly anisotropic crystal forms that lead to variations in speed of light or seismic wave speeds according to the direction of propagation of energy through the crystal form. The observation of seismic anisotropy in Earth's lithosphere and asthenosphere thus requires the bulk alignment of crystal forms within the crust and/or mantle. In crustal depths, minerals such as quartz, mica, and amphibole have been shown to be seismically anisotropic (Brownlee et al., 2017). At upper mantle depths, the dominant mineral component is olivine, which is strongly anisotropic, exhibiting up to 22.3% single-crystal anisotropy for S-waves (Kumazawa and Anderson, 1969). In the crust, anisotropy may be expressed as either shape-preferred orientation (the alignment of fractures or magmatic bodies) or lattice-preferred orientation (the alignment of mineral crystals due to strain). In the mantle, the force of plate motion or convection may create lattice-preferred orientation, although shape-preferred orientation may also be present. While the mechanics behind the formation of LPO are complicated, in the upper

mantle they can usually be simplified to a case of dislocation glide where the shear in crystals mirror shear due to plate motion, and fast directions are parallel to flow (Karato et al., 2008).

One of the most used methods to image seismic anisotropy is known as shear wave splitting. A shear wave encountering an anisotropic medium will be split into two orthogonal quasi-shear waves (one fast, one slow). As the waves propagate through the medium, they accrue a delay time. Upon reaching a receiver, the delay time between the waves (a proxy for the strength of anisotropy or thickness of the layer) and the fast direction of the medium (or the alignment of mineral crystals) can be measured; see **Section 2.1** for more information on this methodology. This method has been used in several settings to measure the seismic anisotropy of crust and lithosphere, including subduction zones (Long and Silver, 2008), mid-ocean ridges (Conder, 2007), and tectonically quiescent regions such as cratons (Eakin et al., 2021).

*1.2 Ps receiver function background*

Earth's interior is composed of rocks with different material properties, such as velocity and density. Strong contrasts in such properties across layers can result in the conversion between a P-wave and an S-wave, or vice versa. These converted phases can be used in conjunction with the unconverted phase to deconvolve a structural component from the signal observed at a receiver. These are known as receiver functions, and have been used to image a number of lithologic and mineralogic boundaries within the Earth such as

sediment-basement contacts (Liu et al., 2018), deep crustal mineralogical/seismic structure (Hopper et al., 2017), the crust-mantle boundary (the Moho; Reading and Kennett, 2003), the lithosphere-asthenosphere boundary (Ford et al., 2010), seismic wave speed discontinuities internal to thick lithosphere (known as mid-lithospheric discontinuities; Wirth and Long, 2014), and the mantle transition zone (Ba et al., 2020).

In this study, we present results from Ps receiver functions across Australia. This method provides excellent vertical resolution of seismic boundaries and good lateral resolution. Because the direct and converted arrivals are time separated, Ps receiver functions are able to image the Moho well. Additionally, variations in the amplitude and polarity of transverse-component receiver functions with backazimuth can be used to detect changes in seismic wave speed anisotropy across boundaries (Levin and Park, 1997; Park and Levin, 2016; Schulte-Pelkum and Mahan, 2014). This method has been used to estimate seismic wave speed anisotropy in several settings, such as subduction zones (Wirth and Long, 2012), tectonically quiescent interiors (Chen et al., 2021b; Ford et al., 2016; Wirth and Long, 2014), and orogens (Long et al., 2017). However, Moho multiples can obscure arrivals from the uppermost mantle, making them less suitable for imaging the lithosphere-asthenosphere boundary in some instances (Bostock, 1997). Previous continent-wide receiver function studies of Australia provide independent constraints on both the seismic structure of the lithospheric mantle and the depth of lithosphere-asthenosphere boundary, but these studies have assumed a largely isotropic mantle (Birkey et al., 2021; Ford et al., 2010). Calculation of anisotropic Ps receiver functions will improve understanding of the

seismic structure and layering of the Australian continent, and provide a complementary dataset to shear wave splitting.

*1.3 Tectonic background*

The Australian continent has a long geologic history spanning the Archean to present. It can be divided into four broad regions (**Figure 2.1**). In the western two-thirds of the continent, there are three composite cratonic blocks: the West Australian Craton, composed of the Archean Pilbara and Yilgarn Cratons as well as Proterozoic Orogens and basins between them; the South Australian Craton, with the Archean Gawler Craton in the center, the Proterozoic Curnamona Craton along the eastern margin, and Proterozoic basins between; and the North Australian Craton, composed of the Proterozoic Kimberly Craton in the northwest, and Proterozoic basins and orogens throughout. The North Australian Craton and West Australian Craton were joined together around 1.8 Ga, evidence of which is preserved in the Rudall Complex and Arunta Inlier (Collins and Shaw, 1995; Li, 2000; Smithies and Bagas, 1997). Between 1.3 and 1.1 Ga, the South Australian Craton completed its final docking with the West Australian Craton and North Australian Craton during the Musgrave and Albany-Fraser Orogenies (Clarke et al., 1995; Myers et al., 1996). To the east are a series of Phanerozoic Orogens that were accreted to the cratonic core: the Cambrian Delamerian (Marshak and Flöttmann, 1996), the Cambrian to Late Permian Lachlan and Thomson (Foster and Gray, 2000; Murray and Kirkegaard, 1978), and the Carboniferous to Early Mesozoic New England Orogen (Coney et al., 1990).

*1.4 Previous geophysical studies*

Complex anisotropic structure of the Australian lithosphere has been indicated by previous shear wave splitting studies. Continental studies have indicated frequency dependent splitting, implying depth variation in anisotropic structure (Clitheroe and van der Hilst, 1998; Özalbey and Chen, 1999). A large percentage of nulls (results indicating no splitting or coming from backazimuths aligned with the fast or slow direction) have been calculated in both continental and local shear wave splitting studies (Chen et al., 2021; Heintz and Kennett, 2006; Eakin et al., 2021; Özalbey and Chen, 1999). Several studies have indicated potential correlation between fast directions and features observed at the surface or in the crust: at station WRAB (NAC), fast direction is consistent with Proterozoic faulting (Clitheroe and van der Hilst, 1998); splitting at KMBL in the Yilgarn Craton (WAC) roughly mirrors the trend of the Eastern Goldfields Terrane (Chen et al., 2021); results from the BILBY network near the North Australian Craton's Tenant Creek Inlier match its geometry (Eakin et al., 2021); and stations in eastern Australia have been shown to have fast directions that are subparallel to the structural trends of Phanerozoic fold belts or the Tasman Line—shown in **Figure 2.1** as a dashed red line (Bello et al., 2019; Clitheroe and van der Hilst, 1998; Heintz and Kennett, 2005). In general, fast directions across the continent have been shown not to mirror apparent plate motion, suggesting a contribution from fossil anisotropy within the lithosphere (Clitheroe and van der Hilst, 1998; Heintz and Kennett, 2005).

Tomographic studies have also been used to examine anisotropy within the Australian lithosphere and the asthenosphere beneath it. In general, azimuthal anisotropy is weaker above 150 km with complex patterns; below that depth, fast directions rotate to more N-S, mirroring plate motion (Debayle and Kennett, 2000; Debayle et al., 2005; Fishwick and Reading, 2008; Simons et al., 2002). While these models suggest broad trends such as shallower anisotropy roughly oriented E-W and deeper anisotropy oriented N-S, there are some variations. For instance, Fishwick and Reading (2008) find weak anisotropy within the center of Australia at 75 km, with stronger anisotropy around the edges; while most fast directions are oriented N-S by 250 km, their model suggests complex anisotropy within the WAC and SAC. Simons et al. (2002) constrain complex patterns that do not correlate to surface features down to at least 200 km, with a rotation to more N-S-oriented patterns by 300 km depth. Radial (or polarization) anisotropy has also suggested multilayered anisotropy, with complex changes through the lithosphere and into the asthenosphere (Debayle and Kennett, 2000; Yoshizawa and Kennett, 2015). As with azimuthal anisotropy, radial anisotropy is laterally heterogeneous throughout the continent. The strongest radial anisotropy is observed in Proterozoic suture zones of central Australia, with somewhat weaker radial anisotropy in the NAC and WAC (Yoshizawa and Kennett, 2015).

Anisotropic receiver function analysis of Australia has thus far been relatively limited. Chen et al. (2021b) calculated Ps receiver functions in the Yilgarn Craton, and found evidence for multiple layers of anisotropy. Ford et al. (2010) and Birkey et al. (2021)

utilized Sp receiver functions to examine the Australian lithosphere—while these analyses did not constrain anisotropy, they found evidence for midlithospheric discontinuities within cratonic Australia, which some have argued may be due to anisotropic layering (Rychert and Shearer, 2009; Wirth and Long, 2014).

## 2. Materials and methods

A total of 35 stations were used for shear wave splitting, including those from the Australian National Seismograph Network (AU, 32 stations), the Global Seismograph Network (IU and II), and the French Global Network of Seismological Broadband Stations (G, 1 station). Ps receiver functions used 14 total stations from the same networks; 11 from the AU network, and 1 each from the IU, II, and G networks. Data used in this study were accessed using the IRIS Data Management Center. They are free and publicly available.

### *2.1 Shear wave splitting*

We used core-refracted phases (i.e., SKS and SKKS) to calculate our shear wave splitting results. These have the benefit of a "reset" due to conversion from P-to-S at the core-mantle boundary; thus, the anisotropic signal observed at the surface is only due to receiver-side effects (assumed to be dominantly in the upper mantle, though this may not be the case). Phases used in our analysis were limited to 85° to 130° epicentral distance to avoid phase contamination, to events $M_w$ 5.5 and greater to maximize the signal-to-noise ratio, and no depth limits for the events were applied. Signals were filtered at multiple frequency bands

between 0.01 and 1.0 Hz as changes in splitting parameters with frequency bands have been linked to changes in anisotropy with depth (Eakin and Long, 2013).

Splits were calculated in an updated version of Splitlab (Deng et al., 2017; Wüstefeld et al., 2008), a free, publicly available MATLAB plugin. All splitting results shown in this paper are from the rotation correlation method (Bowman and Ando, 1987): this method takes the signal on both components, rotates them in 1° increments, and time shifts them in 0.1 sec increments. For each rotation and each time shift, the correlation between the two signals is calculated. The pair with the maximum correlation between the two signals represents the fast direction and delay time of the split. To check for the quality of splits, we also calculate splitting parameters using the minimum energy and eigenvalue methods (Silver and Chan, 1991). Fast directions between methods within 25° of one another and delay times within 0.4 seconds indicate a higher confidence in the quality of the split. Finally, splitting intensity is calculated to check whether the split is a null—a splitting intensity value close to 0 indicates a null value, and in cratons the absolute value tends to be smaller than in other regions. The signal-to-noise ratio was required to be above 5.0. Finally, the shape of the particle motion before and after correction for the preferred fast direction and delay time was examined: before correction particle motion should be elliptical, then rectilinear after correction.

*2.2 Ps receiver functions*

Events for Ps receiver function analysis were epicentrally limited to 30° to 95° with no depth limit. Stations with more than five years of data had a higher magnitude cutoff of 5.8 to maximize the signal-to-noise ratio, while stations with less than five years of data had a lower magnitude cutoff of 5.6 to maximize the number of waveforms available. Preprocessing of receiver functions included: cutting traces to identical length; detrending and demeaning waveforms; bandpass filtering from 0.02 to 2.0 Hz; visually sorting waveforms with clear P-wave arrivals; and manually picking P-wave arrivals in the Seismic Analysis Code (SAC). Waveforms were rotated into vertical, radial, and transverse components (with most Ps energy occurring on the radial component). Receiver functions were calculated with a 65 second data window. All backazimuths were calculated in 10° bins with a minimum of 2 events required per bin. Deconvolution of the daughter phase (Ps wave) was performed in the frequency domain using the multiple-taper spectral correlation method (Park and Levin, 2000). Once deconvolution was performed, receiver functions were migrated from the time domain to depth using the local tomography model AuSREM (Kennett et al., 2013; Kennett and Salmon, 2013; Salmon et al., 2013). We report receiver functions at 0.75 Hz--this frequency provides more clearly separated pulses than 0.5 Hz without introducing higher frequency noise (such as seen at 1.0 or 2.0 Hz).

## 3. Results

A total of 522 non-null splits were calculated, an average of 15 splits per station. Station AS31 had the most non-null splits with 63, while stations SDAN, STKA, and YAPP had

only one; station MBWA had zero non-null splits. Null results (i.e., nonsplitting) is evidence of no anisotropy, weak anisotropy, or alignment of the backazimuth of the wave with a fast or slow direction (Savage, 1999). There were a total of 409 nulls calculated, averaging 12 nulls per station. The maximum number of nulls was at station CAN (47), with one null at stations KDU, KNRA, NWAO, and STKA, and zero nulls at station KELC. Events for both splits and nulls were clustered around four backazimuths: 30° (199 results), 150° (206 results), 190° (189 results), and 300° (91 results). These correspond to the subduction zone along the northern Pacific plate, the subduction zone along the west coast of South America, the spreading center between the Antarctic and South American plates, and the Himalayan collision zone, respectively (**Figure 2.2**). We also calculated the ratio of splits to nulls for each station—station KNRA had a maximum ratio of 16, station SDAN had a minimum ratio of 0.25—and an average among all stations of 2.52. In total, 22 stations had a split-to-null ratio greater than or equal to one.

For Ps receiver functions, a total of 8,607 waveforms were used, an average of 615 waveforms per station. Station CAN used the most waveforms (1135) while station OOD used the fewest (308). The small number of events at station OOD is unsurprising: using the IRIS **M**odular **U**tility for **STA**tisical k**N**owledge **G**athering system (MUSTANG), probability density functions for seismic noise at the station indicate a large amount of noise above the Peterson New High Noise Model (Peterson, 1993). While station CAN is a similarly noisy station, it has been deployed since 1987 ensuring that there is a much longer period of time in which to find suitable events of high quality. Events for Ps come

primarily from backazimuths between 300° and 120°. In this range there are several plate boundaries, including those of the Australian plate, those along the western Pacific plate, and the complex boundary between the Indian, Eurasian, and Australian plates (**Figure 2.2**).

*3.1 Averaged splitting parameters*

Shear wave splitting results are often presented as averages. In **Figure 2.3** we display an arithmetic mean for the average fast direction and delay time at each station, plotted against tectonic terranes. Average fast directions at all stations trend either N-S or NE-SW, and there are few correlations between tectonic terranes inferred at the surface and average fast directions; however, there are slight variations between regions (**Figure S2.1**). Delay times tend to be around 0.6 sec (**Figure S2.2**), smaller than the average at stations globally but consistent with previous results in Australia (e.g., Heintz and Kennett, 2005). The minimum delay time occurs at station FORT (~0.4 sec) and the maximum delay time occurs at station MEEK (~0.9 sec). Station MEEK is in the North Australian Craton, while station FORT is along the perimeter. While other delay times are generally small across the Australian continent, the lithosphere is at least 200 km thick (Yoshizawa, 2014), suggesting that this long delay time may be due to multiple contributions within the lithosphere or a particularly thick layer of anisotropy.

In the same figure, we also plot average fast directions against plate motion from a hotspot frame of reference using HS3-NUVEL 1A (Gripp and Gordon, 2002). At 25 of the stations

analyzed, fast direction and plate motion disagree by more than 10°. One station (MBWA) had only nulls, and is therefore not included in this discussion. The remaining 9 stations with a fast direction within 10° of absolute plate motion are ARMA, BBOO CAN, CNB, INKA, MULG, RIV, WRKA, and YNG. The minimum difference is 0.273° at station ARMA with 44 splits, while the maximum is 65.65° at station GIRL with only 4 splits (which may explain the large misfit). Agreement between fast direction and plate motion is often assumed to be the case in tectonically quiescent regions, based on both splitting observations (e.g., Vinnik et al., 1992) and laboratory studies of olivine crystals (Karato et al., 2008). Stations ARMA, CAN, CNB, RIV, and YNG are along the eastern margin of the continent where the lithosphere is younger and thinner, and thus may be largely influenced by plate motion. The lithosphere in Australia has been shown to increase in a stepwise fashion to the west; while station INKA is on somewhat thicker lithosphere than those closer to the eastern coast, it is to the east of the Tasman Line, which is generally recognized to be the transition between cratonic Australia to the west and Phanerozoic Australia to the east. Station WRKA is within the Precambrian portion of the continent, with events coming from a wide range of backazimuths. Fast directions at station WRKA are clustered near -60° (7 splits) and 60° (8 splits), so the averaging of these two bins results in a near-zero fast direction. Stations BBOO and MULG are both firmly within cratonic lithosphere, but have clusters ~140° apart (near -70° and 70°), again resulting in a fast direction closer to zero. Interestingly, stations within the South Australian Craton (excluding station BBOO) have a systematic difference between absolute plate motion and fast direction (**Figure 2.3**). While 9 stations have average fast directions in good agreement

with plate motion, the averaging of splitting parameters smooths out significant backazimuthal variations (see **Section 3.2**). Therefore, the anisotropic fabric inferred from splitting may not be controlled solely by plate motion even at those stations where the agreement between average splitting direction and absolute plate motion are in good agreement.

### *3.2 Backazimuthal variation in splitting*

In settings with layered anisotropy, it is expected that fast direction and delay time will vary as a function of backazimuth. As seen in **Figure 2.4**, this is exactly what we found in Australia. In general, stations with longer deployment times have more data, but they also have more variation in splitting parameters with backazimuth (e.g., stations AS31 and CAN). It is clear that there is no obvious control on splitting parameters from tectonic terranes. Below, we examine the results of each region in the context of backazimuthal variations.

#### *3.2.1 Splitting in Phanerozoic Australia*

This region had the most stations (12) and the most non-null splits (190). Absolute plate motion varies somewhat from north to south and from east to west, but in general the Australian plate is moving to the north. Results are shown in **Figure 2.5**. For each region we calculate the absolute plate motion; in Phanerozoic Australia, the average absolute plate motion is oriented at -6.40°. While splitting parameters vary significantly by backazimuth, at a given backazimuth there is some consistency in results. We identified the five

backazimuths in this region with the most splits: 30°, 90°, 150°, 180°, and 300°. For each of these, we found the number of splits within ±10°, then averaged the fast direction and delay time. At 30° we found 18 splits, with an average fast direction of -6.88° and an average delay time of 0.59 sec; this is very close to the direction of absolute plate motion. There were 14 splits in the bin centered around 90°, with an average fast direction of 41.95° and an average delay time of 0.72 sec; for these splits, the average fast direction and average absolute plate motion vary by 48.35°. The 150° bin had the most splits (84), and an average fast direction of -23.25° (16.85° different from the average absolute plate motion) with an average delay time of 0.6 sec. With 31 splits, the 180° bin had an average fast direction of 16.30° and average delay time of 0.79 sec; the average fast direction in this bin varied from average absolute plate motion by 22.7°. Finally, the bin centered at 300° had 27 splits, an average fast direction of 8.97°, and an average delay time of 0.52 sec. This last bin had a 15.37° difference between fast direction and plate motion.

In **Figure S2.3**, we display splits for all stations according to backazimuth and inclination angle; we identify several trends across the region. While average fast directions for Phanerozoic Australia generally mirrored absolute plate motion, there was still some change with backazimuth. Notably, at most stations there was a clear NE-SW orientation at both 0° and 180°. Station ARMA had the most splits in this region, with consistency in fast direction at most backazimuths: most splits were oriented close to N-S, except for a handful near ~160° which were oriented closer to E-W. Station EIDS had more complexity in splitting, with most splits oriented NE-SW, but some oriented N-S; there was no

consistency in orientation by backazimuth. Finally, station COEN had a deviation from the general trend of stations in this region, with fast directions at 180° oriented NW-SE.

*3.2.2 Splitting in the North Australian Craton*

In the North Australian Craton, the average absolute plate motion is oriented at 1.17°, a slight eastward shift from Phanerozoic Australia. As with splits in Phanerozoic Australia, there is significant backazimuthal complexity in the North Australian Craton, with stations AS31 and MTN having the most splits and the most variability in fast directions and delay times (**Figure 2.6**). Within this region there were 8 stations and 180 splits. Four backazimuths were identified to have the most splits (30°, 150°, 195°, and 300°): as with Phanerozoic Australia, we found splits within ±10° of these and averaged fast directions and delay times. For the first bin (30°) there were 38 splits, an average fast direction of 35.56°, and an average delay time of 0.63 sec; the average fast direction and average absolute plate motion had a large disagreement here of 34.39°. At 150° we found 31 splits, with an average fast direction of -47.43 and an average delay time of 0.58 sec; this bin too had a significant disagreement between average fast direction and average absolute plate motion (48.60°). The bin centered at 195° had the most splits (62); the average fast direction was 58.54° (57.37° off from average absolute plate motion) with an average delay time of 0.61 sec. Our final bin (300°) had the least splits (21), an average fast direction of 10.69 and an average delay time of 0.72 sec; this bin had the smallest difference between absolute plate motion and average fast direction at 9.52°. In general, splits in the North Australian Craton do not agree with plate motion and vary as a function of back azimuth.

Other than a general disagreement between absolute plate motion and station-averaged fast directions, there were no noticeable key trends across the North Australian Craton. We show variations in splitting according to backazimuth and inclination angle at each station in **Figure S2.4**. Rather, most stations in this region exhibited considerable complexity in splitting parameters as a function of backazimuth. For instance, station AS31 had significant complexity: splits coming from just west of 180° backazimuth were oriented NE-SW, while those coming just east of 180° backazimuth were oriented NW-SE; for splits coming from backazimuths less than 90° or greater than 270°, the fast direction was oriented close to E-W. Station WRKA had similar behavior as AS31 for backazimuths close to 180°. At station WRAB, results were particularly complex and backazimuthally limited. Most splits come from close to 30°, with two dominant orientations: E-W and N-S. However, splits with a steeper incidence angle had the more N-S orientation. Station MTN was the least complex station in this region, with most splits oriented either N-S or NE-SW.

*3.2.3 Splitting in the South Australian Craton*

In the South Australian Craton, there are eight stations and compared to other areas in our study this region contained the fewest number of splits (72). Average absolute plate motion in the South Australian Craton was oriented at -0.82°. Four backazimuthal bins were identified: 30°, 150°, 180°, and 300°. Again, splits within ±10° of these backazimuths were identified, and an average fast direction and delay time was calculated. Regional

backazimuthal splits can be seen in **Figure 2.7**. At 30°, there were 10 splits, an average fast direction of 54.76° and 0.48 sec; the fast direction and absolute plate motion were 55.58° apart. The 150° had 15 splits, with an average fast direction of -44.51° (43.69° different from the average absolute plate motion) and an average delay time of 0.44 sec. For 180°, there were 21 splits; these had an average fast direction of 51.93° and an averaged delay time of 0.68 sec. In this bin, the average fast direction and the average absolute plate motion were 52.75° different. Finally, at the 300° bin, there were 19 splits, an average fast direction of 25.34°, and a delay time of 0.65 sec; this last bin had a difference of 26.16° between the average fast direction and absolute plate motion. While fast direction is variable at all backazimuths, those less than 180° have delay times roughly 0.2 sec smaller than those greater than 180°.

As seen in **Figure S2.5**, the most obvious trend in this region was a fast direction oriented NE-SW for splits coming from backazimuths just west of 180°. Station BBOO had the most complexity of fast directions in the South Australian Craton, ranging from E-W at ~315°, to NE-SW just west of 180°, and multiple fast directions just east of 180°. Station LCRK had the most consistency, with low delay times and fast directions oriented either NE-SW or E-W.

*3.2.4 Splitting in the West Australian Craton*

In the West Australian Craton, there were eight stations and 78 splits. Events were more backazimuthally limited here, and we identified only three backazimuths with more than

10 splits (30°, 135°, and 180°). As with all other regions, splits within ±10° of each backazimuth were found and splitting parameters were averaged. See **Figure 2.8** for results. The average absolute plate motion was 8.05°, the most eastward orientation for any of the regions. The bin centered at 30° had 46 splits; the average fast direction was 57.59° (49.54° off from the average absolute plate motion) and the average delay time was 0.66 sec. At 135°, there were 9 splits, with an average fast direction of 5.57° and an average delay time of 0.57 sec; this bin had a small misfit from the average absolute plate motion at 2.48°. Our last bin had 11 splits, an average fast direction of -8.76° and an average delay time of 0.49 sec. The difference between average fast direction and average absolute plate motion was 16.18° in this bin.

Several broad trends were observed across multiple stations in the West Australian Craton, displayed in **Figure S2.6**. At station KMBL, there was a rotation in fast direction from NE-SW close to 0° backazimuth to more E-W moving toward 90° backazimuth, then back to NE-SW at 180°. Station MEEK had a similar orientation for backazimuths just east of 0°, but had a rotation to NW-SE orientations just east of 180° backazimuths. Station MUN had significant complexity, with fast direction and delay time varying even for close backazimuths.

*3.3 Ps receiver functions*

We present results for nine Ps receiver functions across the Australian continent (**Figures 2.9-12**). Other receiver functions were of lower quality or had issues with data availability.

For instance, stations FORT and GIRL both had large amplitudes with frequent polarity flips, consistent with ringy data due to basinal reverberations (Zelt and Ellis, 1998); Ford et al., 2010 also observed shallow crustal reverberations that prevented them from interpreting upper mantle structure at station FORT. Receiver functions were binned by backazimuth, and both the radial (corresponding to SV energy) and the transverse (corresponding to SH energy) were calculated. Energy on the transverse component has been shown to be primarily due to the presence of isotropic dipping structures or anisotropic boundaries (Levin and Park, 1997; Park and Levin, 2016).

### *3.3.1 Crust and Moho structure*

The depth of the Moho is commonly mapped using Ps receiver functions, which we report below. We compare these results to those reported in the AuSREM (Kennett et al., 2011) and those calculated by Birkey et al. (2021), who used an automated receiver function method for both Sp and Ps receiver functions. With Ps receiver functions, the Moho can be identified by its positive polarity (indicating a velocity increase with depth, which is expected moving from the crust to the mantle). We identify the Moho depth using a single-station stacked receiver function, with the maximum amplitude positive pulse below the direct arrival located at or near zero. At stations ARMA, BBOO, EIDS, KMBL, MEEK, and WRAB, all three studies estimate the Moho depth within 10 km. At two stations (FITZ and OOD), our single-station stacks do not have a clear positive pulse we can associate with the Moho. At station QIS, our estimated Moho depth is within five km of the AuSREM estimate, but Birkey et al. (2021) did not include station QIS in their analysis. Previous

global observations have indicated that older continents tend to have thicker than average crust (Laske et al., 2013): this is generally confirmed by our receiver functions. There are some exceptions: we estimate the depth of the Moho to be 32 km at station MEEK and 35 km at station KMBL, despite both being within the West Australian Craton—though previous results do potentially indicate a thicker Moho (e.g., Birkey et al., 2021; Kennett et al., 2012). Phanerozoic Australia has a crustal thickness of less than 40 km (30 km at station ARMA and 31 km at station EIDS); the North Australian Craton has the thickest crust of any region in our results, with all stations having a thickness greater than 40 km; all stations within the West Australian Craton have a crustal thickness less than 40 km.

Two of the stations reported for Ps results were in Phanerozoic Australia—ARMA and EIDS (seen in **Figure 2.9**). At station ARMA, the positive pulse associated with the velocity increase across the Moho on the radial component is not consistent across all backazimuths, but rather is variable in shape and amplitude, and falls between 30 and 40 km. There is some positive and negative energy above the Moho, but most of the negative pulses at around 10 km depth (i.e., immediately below the direct arrival) are likely sidelobes given their timing and low amplitudes. Station EIDS has a slightly more consistent Moho pulse across backazimuths, with a clearer shape around 30 km. We observe both positive (e.g., between 160° and 190° backazimuth around 15 km) and negative energy (e.g., between 100° and 150° backazimuth around 20 km) above the Moho, potentially indicating sharp boundaries in velocity between different crustal layers.

In the North Australian Craton, we report results for three stations: FITZ, QIS, and WRAB (**Figure 2.10**). Station FITZ has the most variability in the shape and amplitude of the Moho pulse (which falls between 20 and 40 km), with some backazimuths having no clear positive pulse associated with the transition from crust to mantle. There is a significant amount of energy above the Moho at ~10 km, with large amplitude negative pulses between 60° and 120°, then again close to 270°: this indicates a lower-velocity layer above the Moho. Station QIS had a more consistent Moho pulse (ranging from 40 to 50 km), particularly between 280° and 350°, where the positive pulses fall roughly at the same depth (~50 km) and have similar amplitudes. There are complex switches between positive and negative pulses above the Moho; for instance, between 120° and 190° backazimuth where a negative pulse at ~10 km is followed by a positive pulse around 20 km, then another negative pulse ranging from 30 to 40 km depth. Station WRAB had the most consistency in the shape of its Moho pulse, with two distinct groups: one between 70° and 180° (at a depth of ~45 km), the other between 250° and 30° (where there appear to be two or more positive pulses connected to one another without one being larger than the others). There is a large amount of positive energy above the Moho, but little negative energy except at ~10 km where small negative pulses may represent sidelobes of the direct arrival.

The South Australian Craton had two stations with reported Ps results: BBOO and OOD (**Figure 2.11**). Station BBOO had a relatively consistent Moho pulse at all backazimuths around 40 km, and a secondary positive pulse above the Moho around 20 km (which in some cases was the same or greater amplitude than the deeper positive pulse). There was

little negative energy in the crustal portion of the receiver function. Station OOD had significantly more complex structure, with little consistency in the Moho pulse, and some backazimuths with unclear Moho arrivals. Between 150° and 170°, there are large amplitude negative pulses above the Moho at ~10 km. There are few other negative arrivals in the sub-Moho portion of the receiver function, but positive arrivals have complex shapes and amplitudes (e.g., between 90° and 160° backazimuth where a secondary positive pulse starts immediately below the direct arrival and increases its depth with increasing backazimuth).

Finally, in the West Australian Craton we report receiver functions for two stations: KMBL and MEEK (shown in **Figure 2.12**). Station KMBL has a clear, large, consistent amplitude positive pulse associated with the Moho at all backazimuths, generally around 35 km depth. There is a large amount of positive energy in the crustal portion of the receiver function (usually at ~15 km depth), with minimal negative arrivals. The positive Moho pulse at station MEEK is also generally consistent across backazimuths (between 30 and 35 km), with some variations in pulse shape and amplitude. Like station KMBL, there is significant positive energy at most backazimuths near 15 km depth but few negative arrivals.

Overall, our results show clear Moho arrivals, possible crustal structure such as sediment-basement contacts or low-velocity zones, and some polarity flips above the Moho. As polarity flips are indicative of either dipping layers or anisotropy, this suggests the presence

of one or both within the crust. However, we do not observe the two-lobe or four-lobe patterns predicted by modelling (Ford et al., 2016; Levin and Park, 1997; Park and Levin, 2016).

*3.3.2 Mantle structure*

As stated above, the presence of energy and polarity flips on the transverse component of receiver functions is often interpreted as being due to seismic anisotropy: our receiver functions do have significant energy below the Moho, but it is often difficult to interpret and does not follow predicted patterns of simple two-lobe or four-lobe polarity flips (e.g., Ford et al., 2016).

At station MEEK, we observe several possible polarity flips on the transverse component: first at roughly 80 km depth, then at 120 km depth, and finally at 180 km depth. Birkey et al. (2021) found two significant negative phases at station MEEK using Sp receiver functions: one at 80 km (interpreted to be a mid-lithospheric discontinuity) and one at 129 km (interpreted to be the lithosphere-asthenosphere boundary). All the Ps polarity flips appear to occur over 10s of kilometers, and thus may not be directly linked to negative phases observed in previous studies. At station KMBL there are several gaps in backazimuthal coverage: between 200° to 240° and between 250° and 300°. These gaps make observations of polarity flips more difficult, but there do appear to be flips at 80 km, 100 km, and 160 km. As with station MEEK, these are very gradual, with pulses that extend over 10s of kilometers in depth. Previous studies reported negative phases at 79 km and

113 km, both interpreted to be mid-lithospheric discontinuities (Birkey et al., 2021). Station WRAB has polarity flips at 60 km, 100 km, 140 km, and 180 km. Mid-lithospheric discontinuities were reported at 71, 91, 135, and 198 km (Birkey et al., 2021). We display receiver functions as rose diagrams for all 9 stations in **Figure 2.13**, ranging from 0 to 200 km depth. Significant complexity is present at most stations.

Our receiver functions indicate complex structure within the Australian lithosphere, as we see significant energy on transverse components with some polarity flips. However, our observed polarity flips are generally not consistent with predicted two-lobe or four-lobe patterns that a sharp boundary in seismic anisotropy would create (e.g., Ford et al., 2016; Levin and Park, 1997; Park and Levin, 2016). Due to the complexity of our results, we cannot easily generate comparative forward models, which would be necessary to infer orientations of seismic anisotropic layering in the mantle. Therefore, the summarizing result of our Ps receiver function analysis is that while anisotropic layering is present, it cannot provide us with unique insight into the orientation of such structures within the Australian lithosphere.

## 4. Discussion

### *4.1 Comparison of our results to previous shear wave splitting studies*

There have been numerous previous studies that examined the structure of the Australian continent in terms of seismic properties, including anisotropy, and other geophysical constraints (e.g., Debayle and Kennett, 2000; Fishwick and Reading, 2008; Ford et al.,

2010; Heintz and Kennett, 2005; Saygin and Kennett, 2012; Tesauro et al., 2020; Wang et al., 2014; Yoshizawa and Kennett, 2015). Seismic anisotropic studies have included continental and regional shear wave splitting analysis (Bello et al., 2019; Chen et al., 2021a; Clitheroe and Van der Hilst, 1998; Eakin et al., 2021; Heintz and Kennett, 2005; Heintz and Kennett, 2006; Özalbey and Chen, 1999) , and continental tomographic studies (Debayle, 1999; Debayle and Kennett, 2000; Debayle et al., 2005; Fishwick and Reading, 2008; Simons et al., 2002; Yoshizawa and Kennett, 2015). In this section we primarily focus on comparing our results to other shear wave splitting studies. In **Section 4.2**. we focus on comparing our results to constraints from tomography and in **Section 4.3**. we focus our comparison on other receiver function studies.

Eakin et al. (2021) examined shear wave splitting through central Australia, including three permanent stations that were also used in this study (stations AS31, MULG, and WRAB). That study found a significant number of null events (consistent with other studies of the Australian continent), average fast directions that paralleled topography, gravity, and magnetic trends with a transition from the Proterozoic orogens in central Australia into the North Australian Craton. They argue that their results indicate fossilized seismic anisotropy within the lithosphere, rather than from the asthenosphere (i.e., plate motion shear). Average splits from this study vary significantly from those reported in Eakin et al. (2021); however, their results are reported from the minimum energy method and included PKS phases as well, which may help to explain the discrepancies. The averages reported in Eakin et al. (2021) are also calculated using both non-null and null splits, whereas we only

use non-null splits for our averages. They report an average fast direction of 72° at AS31, while ours was 13.45°; however, we did have 14 splits between 62° and 82°. Beyond that there was a wide spread of fast directions. At station MULG, Eakin et al. (2021) found an average fast direction of 75°—ours was 40.73°, with five splits within 10° of their average. For station WRAB, we report an average fast direction of 19.65°, and 7 splits within 10° of the -17° reported by Eakin et al. (2021). While ray paths for PKS and SK(K)S phases are nearly identical in the upper mantle, different epicentral distance ranges are used for each phase to prevent phase contamination: this may result in differences in splitting parameters, especially if there are lower mantle contributions (see **Section 4.2**). Additionally, very few of the events analyzed were the same between Eakin et al. (2021) and this study. However, we did identify some events in common: six at station AS31, two at station MULG, and two at station WRAB (compared in **Table 2.2**). We compare their reported minimum energy splits to our rotation correlation splits and the values we obtained from the minimum energy method. Of the 10 splits in common, seven have comparable values (four at AS31, one at station MULG , and two at station WRAB).

A recent study of seismic anisotropy in the Yilgarn Craton (Chen et al., 2021a) used four of the same stations as used in this study (KMBL, MEEK, MORW, and MUN). We had two additional stations within the Yilgarn: BLDU and NWAO, both roughly in line with stations MORW and MUN along the western margin of the craton. Average fast directions reported in this study generally do not agree with Chen et al. (2021a), with the closest being KMBL: we report an average fast direction of 63.51° while they report 76°. Disagreement

between the two studies could be a result of variations in methodology or events chosen, or the phases used for splitting—Chen et al. (2021a) includes PKS, SKS, SKKS, and SKiKS phases, while this study has mostly SKS and SKKS phases. Average delay times are in closer agreement: our delay times range from 0.52 sec at station BLDU to 0.75 sec at stations KMBL and MEEK. Chen et al. (2021a) has a similar range, with 0.5 sec at station MUN (south of station BLDU) and 0.7 sec at station KMBL. Station MORW has roughly the same average delay time in both studies (0.63 sec v. 0.6 sec), and there are consistently lower delay times along the western margin of the craton. Both studies also suggest general disagreement between plate motion and average fast directions, though at stations BLDU and MUN our study has fast directions subparallel to both plate motion and the Mesoproterozoic Pinjarra Orogen along the western margin of the craton. Despite slight differences, the overall conclusion reached by Chen et al. (2021a) is supported by this study: seismic anisotropy is relatively weak but complex in the Yilgarn Craton, in stark contrast to the exceptionally fast plate motion with strong alignment of asthenospheric seismic anisotropy (Debayle et al., 2005).

Our results are not in good agreement with a previous study examining the structure of southeast Australia (Bello et al., 2019). Both studies indicate complex splitting parameters that often do not mirror plate motion. For all four stations used in both studies (CAN, CNB, TOO, and YNG), our average delay times were significantly lower (less than 1.0 sec at all stations), whereas Bello et al. (2019) estimate average delay times of greater than 1.0 sec. Additionally, fast directions are significantly different at all stations. Bello et al. (2019)

used a method similar to the eigenvalue method laid out in Silver and Chan (1991) and also deployed a weighted averaging scheme: this contrasts with our use of the rotation correlation method and no weighting in our averages, which may explain some of the differences.

The large differences between our results and those of the other studies indicates the need for a careful analysis of the methodological and data differences in shear wave splitting analysis, particularly in regions such as Australia where seismic anisotropy is vertically stratified and laterally complex. Such complexities are supported by our analysis, specifically in the backazimuthal variations, and echo the findings of previous studies (e.g., Clitheroe and van der Hilst, 1998; Heintz and Kennett, 2005). In the remaining sections, we compare our splitting results to constraints from receiver functions and tomography while acknowledging that more work on splitting is needed to shore up observational differences between studies.

*4.2 Constraining depth-dependent seismic anisotropy*

Shear wave splitting is a path-integrated effect from the core-mantle boundary to the surface, thus it cannot provide firm depth constraints without modeling. However, surface waves are sensitive to changes in seismic anisotropy with depth, thus tomography might help to provide depth constraints in our region of study. In **Figure 2.14** we plot our shear wave splitting results against an anisotropic tomographic model calculated using Rayleigh waves (Debayle et al., 2016). The increased depth resolution of surface waves relies on a

clear understanding of the relationship between dispersion and frequency (i.e., different frequencies are sensitive to different depths); however, it comes at a decreased lateral resolution. We include four depth slices (50, 100, 150, and 200 km) beginning just below the crust and extending well into the mantle lithosphere and even the asthenosphere in portions of the continent where the lithosphere is thought to be thinner. For each depth, there are several broad trends. At 50 km, there is a region in central Australia extending from the northwest to the southeast where modeled fast directions are oriented close to 90° surrounded by fast directions close to -90° (though these are the same in modulo); north of this, the northernmost North Australian Craton has fast directions ranging from 0° to 70°; finally, in southwestern Australia fast directions rotate from ~50° to 90° moving from northeast to southwest. At 100 km, there is a belt around the North Australian Craton which has fast directions changing from 70° in the west to 45° in the east; in the northernmost portion of the North Australian Craton fast directions become close to 0°; the remainder of the continent is broadly similar to 50 km depth. At 150 km, most modeled fast directions are greater than zero, except for a portion of southeastern Australia where fast directions range from -20° to -70°. Finally at 200 km, trends seen at 150 km continue, except for a small patch in the West Australian Craton with fast directions oriented at -16° surrounded by positive fast directions. Clear changes in fast direction can be seen between depths, particularly in cratonic Australia: such changes are likely to create complex splitting patterns, such as those seen in our results. Because shear wave splitting and surface waves are sensitive to different phenomena, a direct comparison is generally not possible and may be misleading. Ps receiver functions do have better depth resolution, but they resolve

boundaries rather than bulk properties: we more directly compare Debayle et al. (2016) to our receiver functions in **Section 4.3**.

For the 50 km depth slice, only two of the stations used in this study have an average fast direction within 10° of Debayle et al (2016): INKA and OOD. At 100 km, two stations (MEEK and OOD) have a misfit between average fast directions in this study and those predicted by Debayle et al. (2016), with two other stations slightly above that threshold (FITZ and KDU). Stations BBOO, FORT, MEEK, and WRAB all have a misfit of less than 10° between fast directions at 150 km. Finally, at 200 km six stations (EIDS, FORT, INKA, MEEK, STKA, and WRAB) have a misfit of less than 10°. Additionally, we averaged the fast directions from Debayle et al. (2016) for depths down to 150 km, which is the depth at which previous tomographic studies of the Australian continent have suggested a transition in seismic anisotropy (e.g., Fishwick et al., 2008). Only three of our stations (BLDU, MUN, and OOD) had a misfit of less than 10°: given that these are all within cratonic Australia, it may suggest that shear wave splitting observations at these stations are primarily due to fossilized seismic anisotropy within the lithosphere.

We also compare our shear wave splitting results against the model of Debayle et al. (2016) by calculating effective splitting parameters using MSAT (Walker and Wookey, 2012). For each station, we generate a four-layer model using the fast direction from Debayle et al. (2016) at the four depth slices shown in **Figure 2.14**. In general, effective splitting is not able to match the observed splitting parameters at individual stations. One station where

modeling and observations match well is FITZ, but results there are very backazimuthally limited and therefore this fit may be misleading. Other stations (like MTN) do have a systematic variation with backazimuth, similar to that observed by Eakin et al. (2021). However, our modeling approach relies on two key assumptions that may limit our comparison. First, we assume that each layer of seismic anisotropy used for the model is 50 km thick; however, the tomographic model from Debayle et al. (2016) has a finer resolution than this, suggesting that our assumptions may be an oversimplification. Second, we assume that the axis of seismic anisotropy is horizontal. If instead the axis is dipping, then effective fast direction and delay time would not maintain 90° periodicity but instead have more complexity in variation across backazimuths (see **Figure S2.7** for an example). While the direct comparison of our observed splitting results to the tomographically informed modeled splits does not provide new insight into our understanding of anisotropic structure of the Australian continent, the apparent discrepancies are not entirely unexpected; Eakin et al. (2021) produced a similar, two-layer model and argued that most models did not fit their results and were not strictly preferred over a one-layer model (wherein seismic anisotropy is present solely in the lithosphere).

One potential explanation for the observed discrepancies in the modeled versus calculated splitting results may come from seismic anisotropy in the lowermost mantle. Contributions to shear wave splitting are assumed to be predominantly within the upper mantle. However, previous studies have indicated the possibility of lowermost mantle seismic anisotropy as a contribution to Australian shear wave splitting results. Özalbey and Chen (1999) found

anomalous waveforms on transverse component seismograms that did not match the predicted shape for upper mantle shear wave splitting (the time-derivative of the radial component), arguing that these anomalous waveforms were likely due to the presence of heterogeneities within the lowermost mantle. More recent studies have also documented lowermost mantle contributions to shear wave splitting across the globe including Africa (Ford et al., 2015; Lynner and Long, 2014), Australia (Creasy et al., 2017), Eurasia (Long and Lynner, 2015); Iceland (Wolf et al., 2019), North America (Lutz et al., 2020). While these studies show a clear presence of seismic anisotropy within the lowermost mantle, results are often heterogeneous and indicate complex seismic anisotropy. Furthermore, constraints on both dominant slip systems and the mechanism of deformation responsible for development of fabric are poorly constrained. In **Figure S2.8**, we plot our splits at a depth of 2700 km against the GyPSuM tomography model for the same depth. Splitting parameters exhibit significant heterogeneity across the region, sampling the lowermost mantle over a region of roughly 60° of latitude and 50° of longitude. As such, it is possible that the lowermost mantle has some contribution to our observations of shear wave splitting. Furthermore, while different phases (i.e., SKS, SKKS, and PKS) have very similar paths in the upper mantle, paths diverge significantly in the lowermost mantle: thus, variations in studies may arise as a result of different phases used, especially if seismic anisotropy in the lowermost mantle has a significant contribution. Phases sampling the lowermost mantle coupled with complex upper mantle seismic anisotropy implies that our results are difficult to model or directly interpret without first concretely identifying contributions from each region, which is beyond the scope of the present study.

*4.3 Comparison of receiver functions to previous studies*

Our receiver functions indicate complex, heterogeneous structure at depth, with evidence of gradual polarity changes on the transverse component (suggesting the presence of seismic anisotropy). Chen et al. (2021b) examined four stations (KMBL, MEEK, MORW, and MUN) in the Yilgarn craton and performed a harmonic decomposition to constrain anisotropic structure; this method performs a linear regression to constrain polarity flips, and divides the receiver function into a combination of sine and cosine terms (Shiomi and Park, 2008). They report clear evidence for two layers of seismic anisotropy at three of these stations (KMBL, MORW, and MUN). At KMBL, Chen et al. (2021b) report three prominent phases potentially associated with dipping structure or seismic anisotropy: at 58, 87, 101 km; at MEEK, they report prominent phases at 74 and 94 km. While Chen et al. (2021b) utilized harmonic decomposition to analyze their receiver functions, rose diagrams can be used to provide a visual representation of similar trends such as seismic anisotropy or dipping layers (Ford et al., 2016; Park and Levin, 2016). In **Figure 2.15**, we plot rose diagrams for both stations at corresponding depths: 60, 90, and 100 km ±5 km for KMBL; 75 and 95 km ±5 km for MEEK. While there are polarity flips at station KMBL, these do not match simple two or four-lobed patterns. For station MEEK, polarity flips are much clearer, particularly at 75 km—this matches well with a two-lobed pattern; Chen et al. (2021b) report a dominant contribution to modelled energy from a two-lobed pattern.

Because receiver functions are sensitive to sharp boundaries, we utilize variations in fast directions with depth from Debayle et al. (2016) to isolate potential depths at which polarity

flips on the transverse component of receiver functions might be expected. At station ARMA, there is a single large change in modelled fast direction between 150 km (-89.94°) and 175 km (60.42°). We observe some evidence of a change in polarity at these depths, but these changes are subtle; additionally, this is beneath the predicted depth of the lithosphere-asthenosphere boundary along the eastern margin of the continent. Station BBOO also only has one large change in fast directions, between 70 km (-88.50°) and 90 km (-52.27°) according to Debayle et al. (2016). There are some slight changes in polarity between these two depths in our receiver function results, most consistent with a two-lobed pattern. At station EIDS, there are no large changes in tomographically inferred fast direction within lithospheric depth bounds; while our receiver function results for the station does have some polarity flips, these are not consistent and do not match predicted two-lobed or four-lobed behavior. Tomographically modeled fast directions for station FITZ show a continuous decrease from close to 90° near the surface to a more N-S orientation closer to plate motion at depth; polarity flips are isolated at station FITZ and do not indicate seismic anisotropy. At station KMBL, the model of Debayle et al. (2016) shows only one large jump in fast direction from -23.30° at 70 km to 35.70° at 90 km—our receiver functions for station KMBL do not show corresponding polarity flips. Station MEEK shows modelled fast directions that are roughly consistent at all depths, yet our receiver functions show a two-lobed polarity flip around 80 km. Between 100 km and 125 km, there is a shift in modelled fast direction (56.60° to 18.37°) at station OOD. The transverse component receiver function for station OOD does have complex changes in polarity between these two depths, but the pattern is not an obvious two or four-lobed one.

Finally, at station WRAB there is also a change in fast direction between 100 km (-57.80°) and 125 km (13.51°); however, while there are polarity flips on the receiver function, they are complex and do not match predicted patterns associated with seismic anisotropy. It is important to note that these comparisons are not direct ones: while receiver functions and surface wave tomography both provide good depth resolution, receiver functions are sensitive to sharp boundaries whereas tomography characterizes changes in volumetric properties. Thus, a lack of explicit agreement between the two methods does not indicate a lack of seismic anisotropy but rather a combination of gradually changing seismic anisotropy constrained by tomography, with fine scale layering of seismic anisotropy imaged by receiver functions.

*4.4 Implications for the nature of the Australian lithosphere*

Previous geophysical studies have made clear that the Australian continent has a complex lithospheric structure, with variations in the thickness of the lithosphere and its internal properties. Regional tomography models indicate some broad trends within the continent, such as thicker lithosphere with faster wavespeeds in cratonic Australia and thinner lithosphere with slower wavespeeds along the eastern margin (Kennett et al., 2012). Additionally, the lithosphere appears to increase in thickness in a stepwise fashion westward from the Phanerozoic eastern margin. While the lithosphere is generally thicker in the western two-thirds of the continent, there are still significant variations in the depth of the lithosphere-asthenosphere boundary determined from tomography (Kennett et al., 2012). Topography of the lithosphere-asthenosphere boundary may result in complex

mantle flow patterns and edge convection, which would produce its own anisotropic signature. Global models show the same broad features in Australia (such as 3D_2018Sv, the anisotropic component of which is displayed in **Figure 2.14**).

While the lithosphere-asthenosphere boundary is generally thought of as an immediate change, some studies have referred to it instead as the lithosphere-asthenosphere transition because (especially in cratons ) it is often not a sharp boundary (Mancinelli et al., 2017). One recent study (Yoshizawa and Kennett, 2015) utilized tomography to examine both the lithosphere-asthenosphere transition and radial seismic anisotropy within the Australian upper mantle. This transition occurs at different depths and has variable thickness across the continent: it is thickest and deepest in central Australia in the Proterozoic sutures between cratons; along the eastern margin of the continent the lithosphere-asthenosphere transition is shallower. Trends in radial seismic anisotropy are similar, with the strongest radial seismic anisotropy in the sutures between cratons, decreases in radial seismic anisotropy from the base of the crust to mid-lithospheric depths in the cratons, and strong radial seismic anisotropy in the asthenosphere along the eastern margin. Global models of azimuthal seismic anisotropy (e.g., Debayle et al., 2016) do show variations in seismic anisotropy with depth and across the continent, though these do not mirror major surficial boundaries.

As noted in **Section 3.3.2**, several of our Ps receiver functions had polarity flips that were roughly at the same depths as mid-lithospheric discontinuities reported previously (Birkey

et al., 2021; Ford et al., 2010). Mid-lithospheric discontinuities seem to be a near-ubiquitous feature of cratonic lithosphere, but their origin is still somewhat unclear. The most common explanations include the presence of current or solidified partial melt, hydrous minerals such as phlogopite, or seismic anisotropy. Birkey et al. (2021) argue that the most likely explanation for mid-lithospheric discontinuities in Australia is the presence of ancient hydrous minerals; however, they do not rule out the possibility that seismic anisotropy could contribute to the decrease in velocity associated with negative phases observed at mid-lithospheric depths. The polarity flips that we observe occur over 10s of km, which suggests either a thicker layer of seismic anisotropy or a more gradual transition from one fast direction orientation to another. Thus, seismic anisotropy seems likely to not be the main cause of observed mid-lithospheric discontinuities. However, it is clear from both this study and previous ones that the Australian lithosphere is anisotropic; such seismic anisotropy must be fossilized within the lithosphere, as it would be difficult to internally deform cratonic lithosphere in the present and produce a fabric. This argument is bolstered by the disagreement between absolute plate motion and the average fast direction of most cratonic stations (except for AS31, MORW, MUN, and WRKA; though an examination of individuals splits makes clear that these stations have significant backazimuthal variability that cannot be explained by plate motion).

In addition to the macroscopic alignment of intrinsically seismically anisotropic minerals, the layering of media with different material properties can also produce seismic anisotropy. Earthquakes originating from Australia have complex high-frequency body-

wave codas; Kennett et al. (2017) argue that this is due to multi-scale heterogeneity (i.e., layering occurs at multiple scales). Such heterogeneity could contribute to the complex splitting patterns that are observed in Australia, and could be linked to the formation and evolution of the lithosphere.

Simple interpretations of the seismic anisotropy present within the Australian lithosphere are not likely, and readers should be cautious of shear wave splitting results for two primary reasons. First, as noted in this study, there are discrepancies between various published shear wave splitting studies for Australia. While this could be partially attributed to methodology and phases used, it also underscores the complexity of seismic anisotropy in the region. Second, contributions to shear wave splitting from the lowermost mantle cannot be ruled out, implying that observed fast directions may be the result of splitting throughout the mantle. This second point is an emerging issue in the calculation of shear wave splitting globally.

## 5. Conclusions

We presented shear wave splitting and Ps receiver function results across the Australian continent. While average fast directions are similar to absolute plate motion, there are large variations in fast direction with backazimuth (a feature diagnostic of complex seismic anisotropy). Significant complexity exists in our results even at stations within Phanerozoic Australia, suggesting that in many cases multiple layers of seismic anisotropy may be required. This is further complicated by the potential for seismic anisotropy in the

lowermost mantle that affects the observed signal seen at the surface. Ps receiver functions display some changes in polarity on the transverse component, however these changes appear to occur over 10s of kilometers and thus do not indicate sharp changes in seismic anisotropy. Ultimately, while results warrant caution in interpretation, the ancient lithosphere of the Australian continent likely preserves anisotropic fabric related to its formation and evolution, with minimal contributions from present-day plate motion.

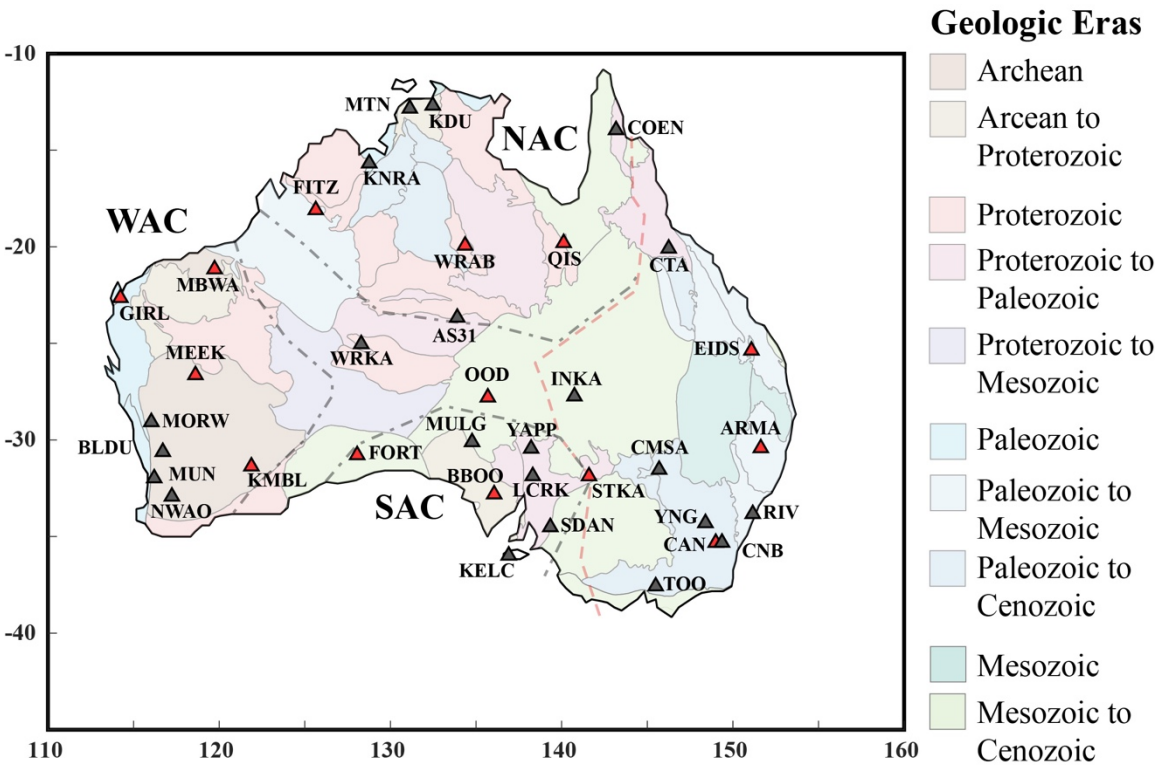


**Figure 2.1:** Map of stations used in this study. Red triangles indicate stations used in both shear wave splitting and receiver function analysis. Gray triangles indicates stations used only for shear wave splitting. Background shows significant geologic divisions of Australia, simplified from Fraser et al. (2007).

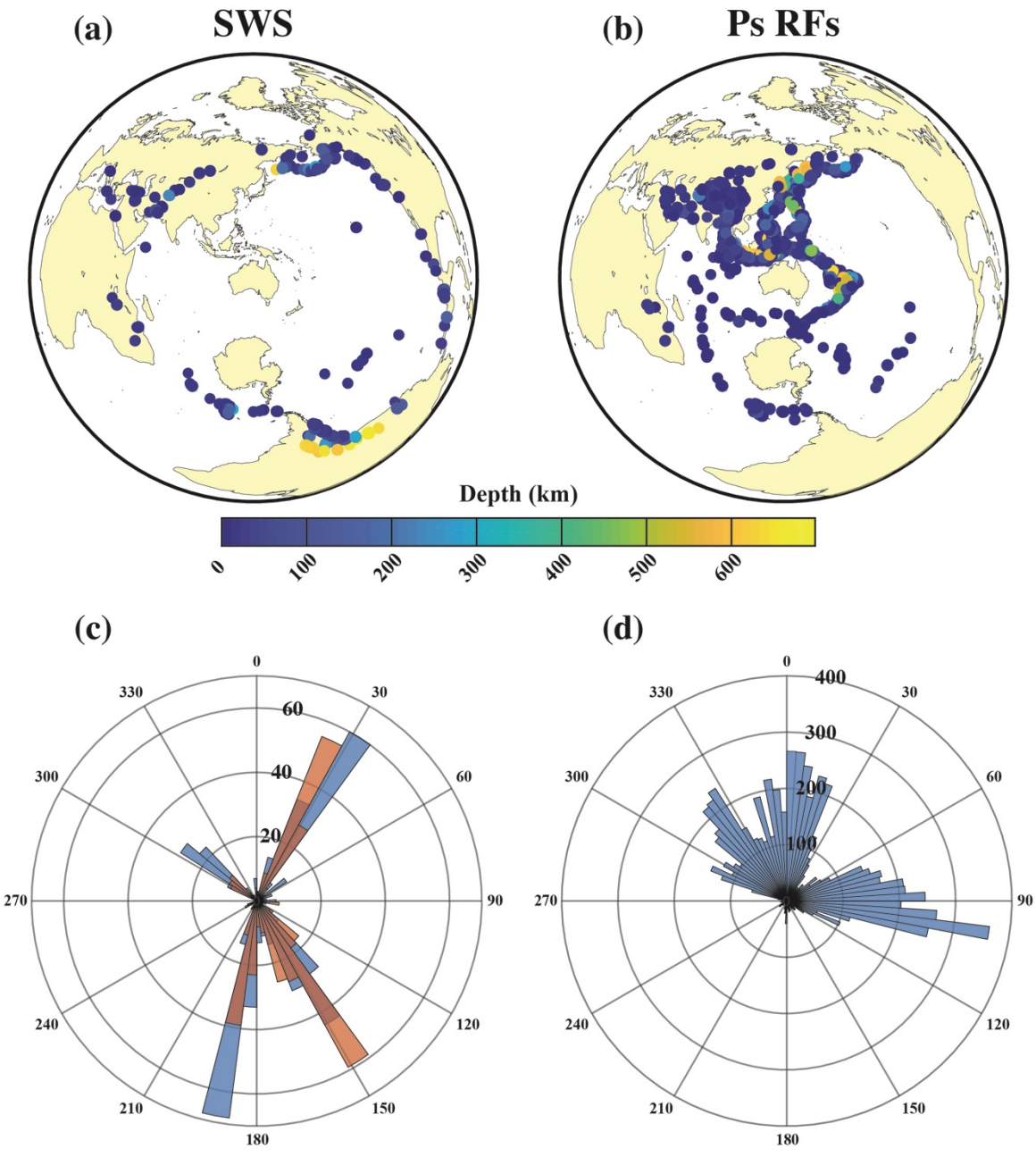


**Figure 2.2:** Event information for both methods used in this study. **(a)** Map of events used for shear wave splitting, color coded according to event depth. **(b)** Map of events used for receiver functions, color coded according to event depth. **(c)** Polar histogram of event distribution by backazimuth for shear wave splitting. Blue bins are splitting results, while orange bins are null results. **(d)** Polar histogram of event distribution by backazimuth for receiver functions.

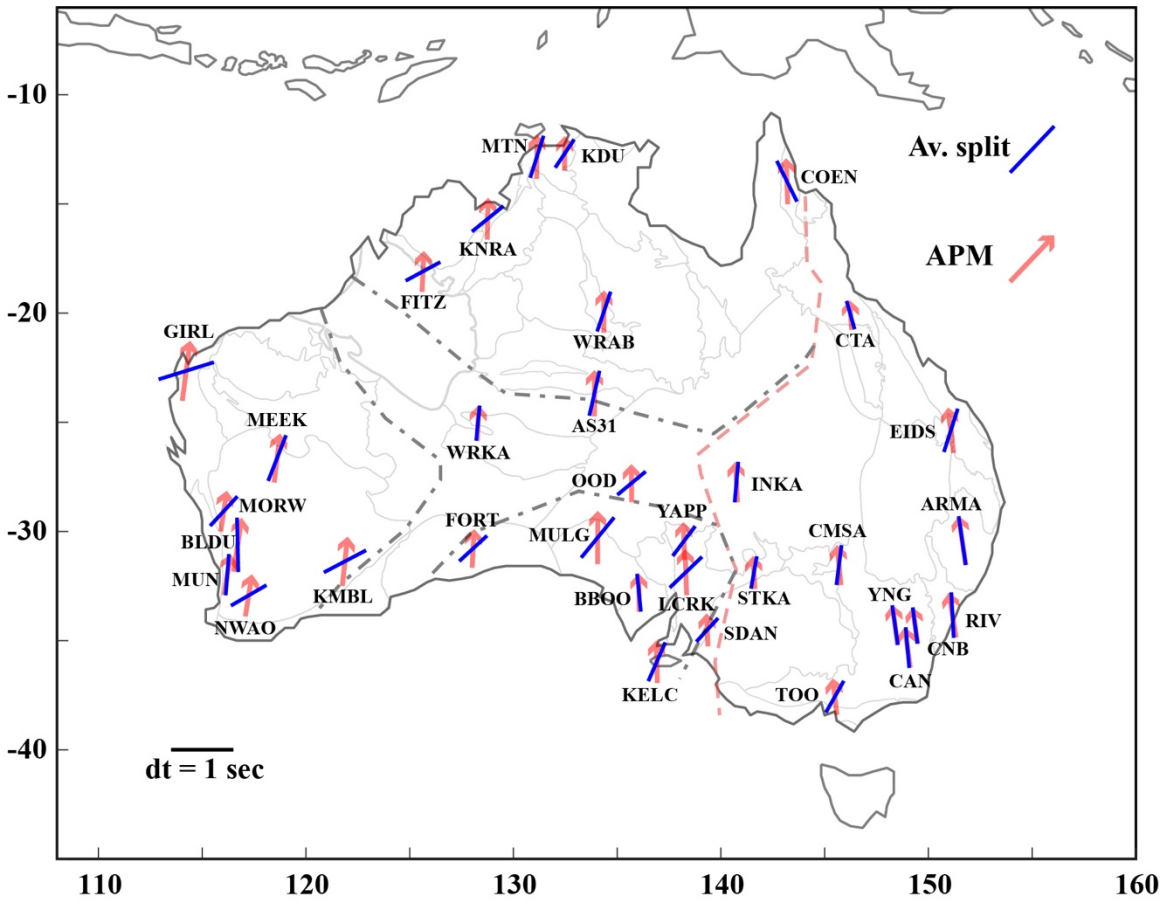


**Figure 2.3:** Average shear wave splitting parameters plotted against apparent plate motion from the HS3-NUVEL 1A model (Gripp and Gordon, 2002). An example split with a fast direction of 90° and a delay time of 1 second is shown in the lower left.

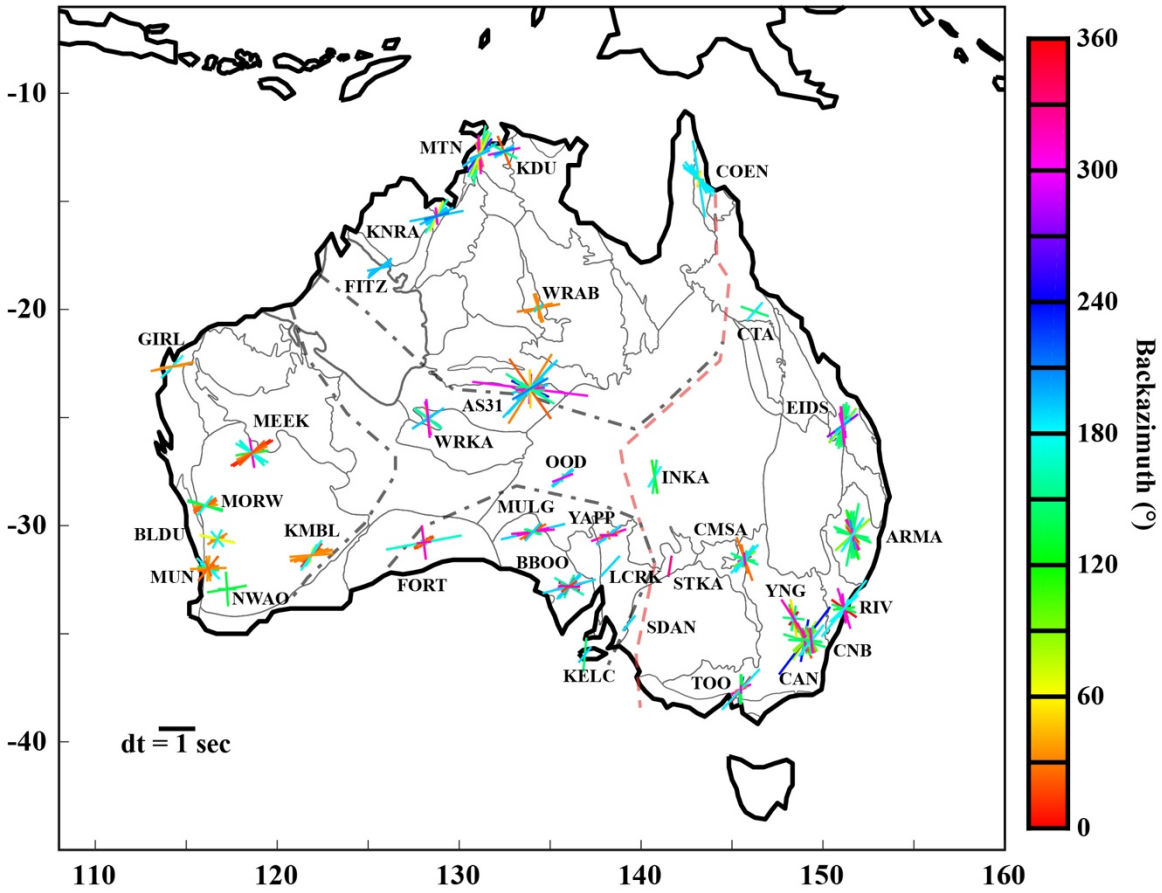


**Figure 2.4:** Splitting parameters color-coded by backazimuth of the event. An example split with a fast direction of 90° and a delay time of 1 second is shown in the lower left.

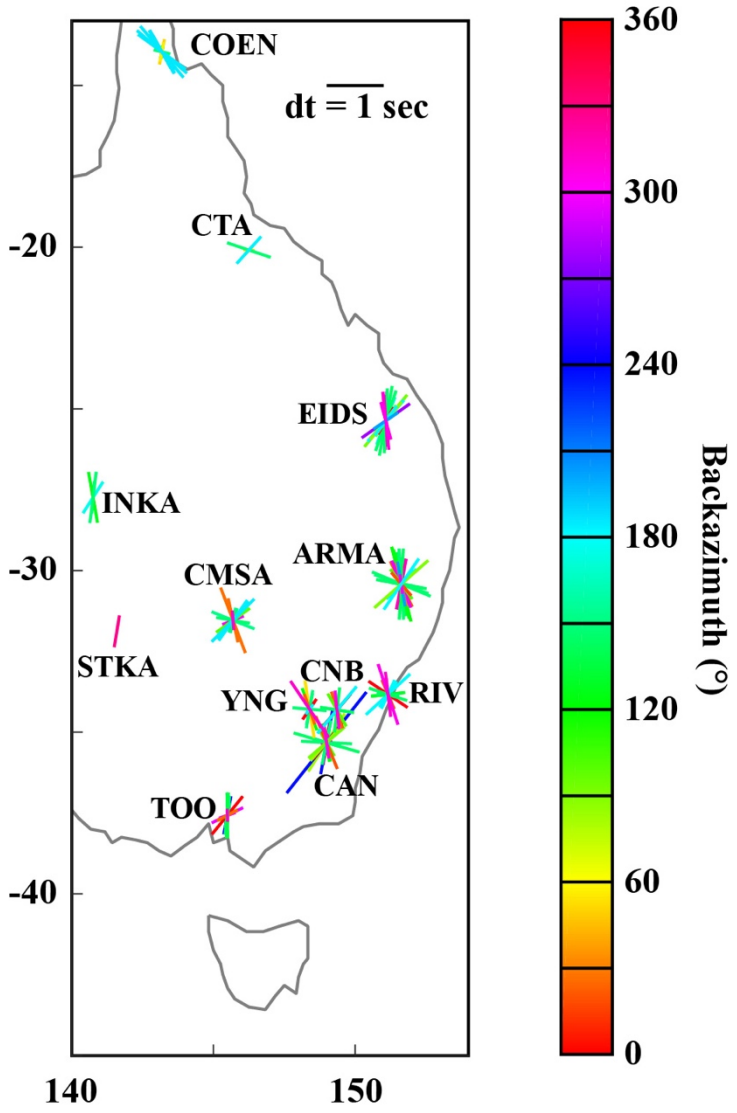


**Figure 2.5:** Splits from **Figure 4** zoomed in on Phanerozoic Australia. An example split with a fast direction of 90° and a delay time of 1 second is shown in the upper right.

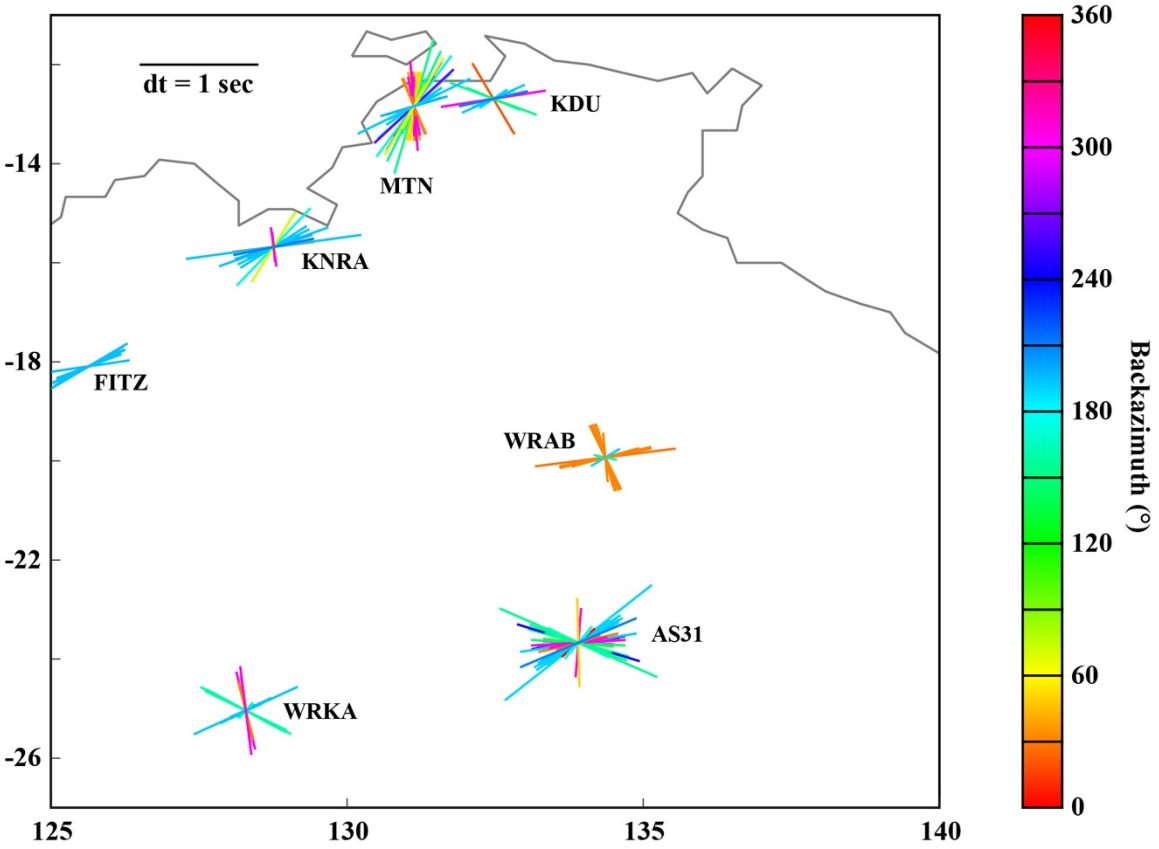


**Figure 2.6:** Splits from **Figure 4** zoomed in on the North Australian Craton (NAC). An example split with a fast direction of 90° and a delay time of 1 second is shown in the upper left.

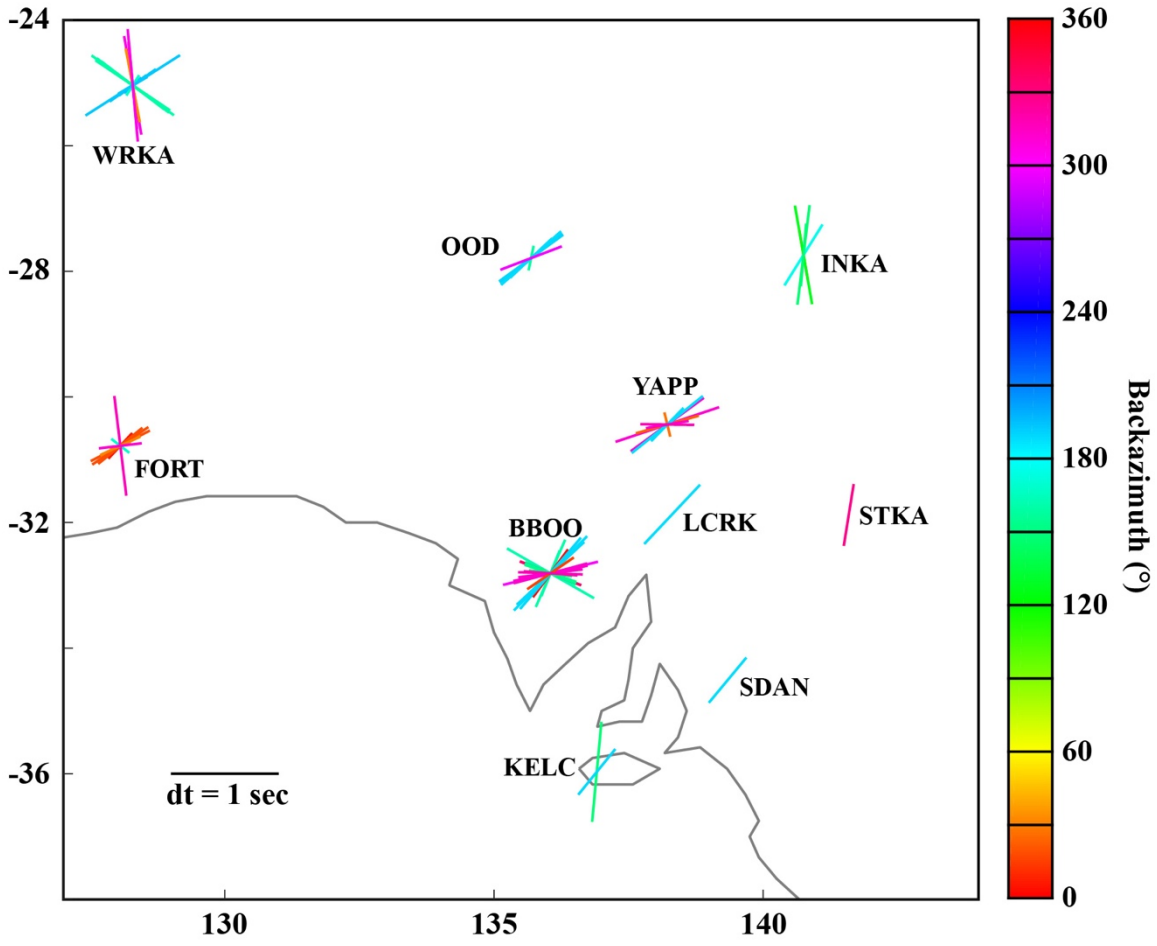


**Figure 2.7:** Splits from **Figure 4** zoomed in on the South Australian Craton (SAC). An example split with a fast direction of 90° and a delay time of 1 second is shown in the lower left.

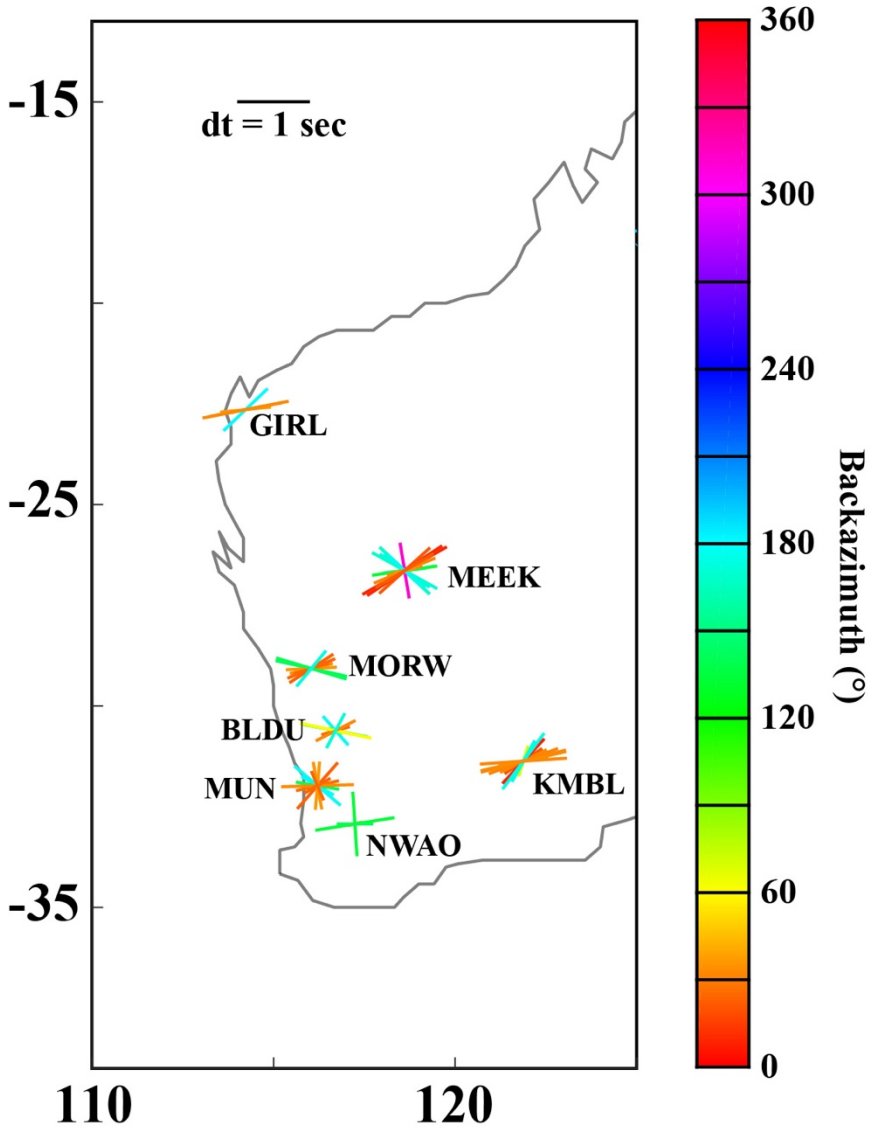


**Figure 2.8:** Splits from **Figure 2.4** zoomed in on the West Australian Craton (WAC). An example split with a fast direction of 90° and a delay time of 1 second is shown in the upper left.

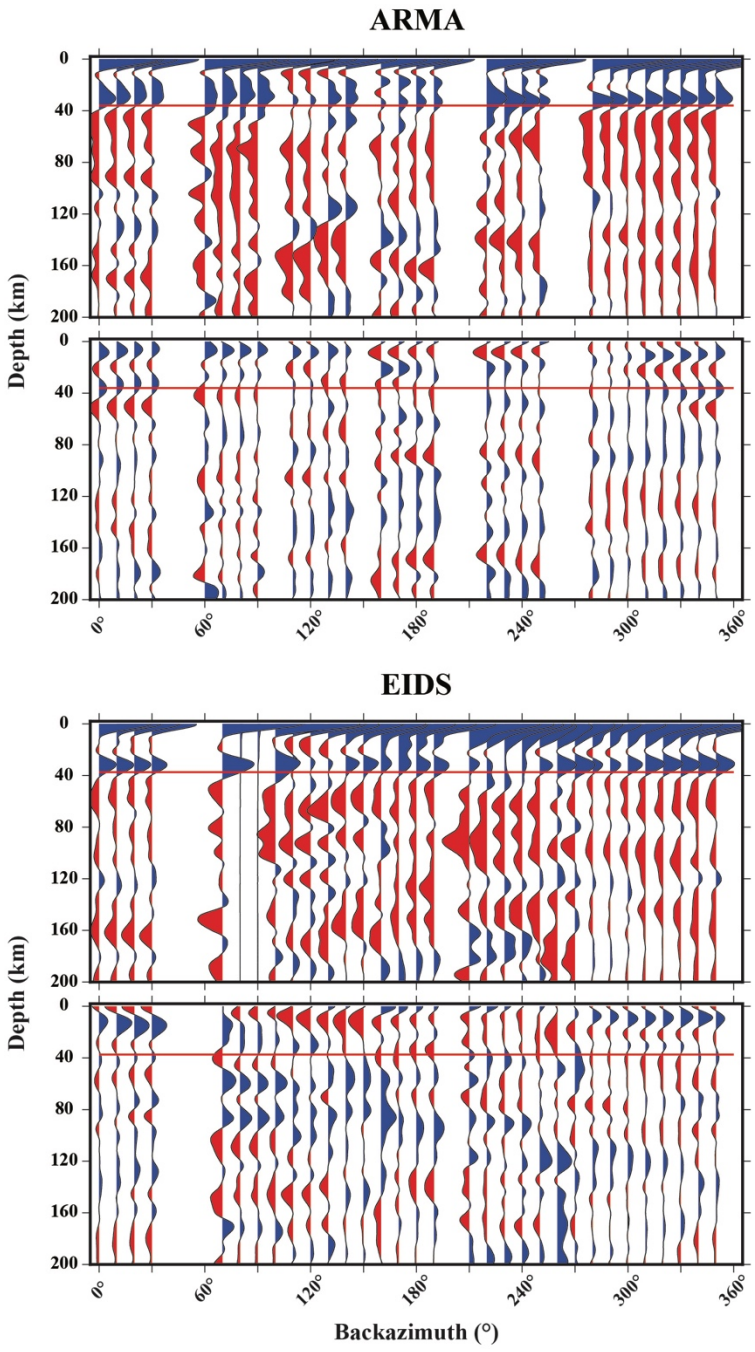


**Figure 2.9:** Backazimuthally-binned Ps receiver functions from Phanerozoic Australia.

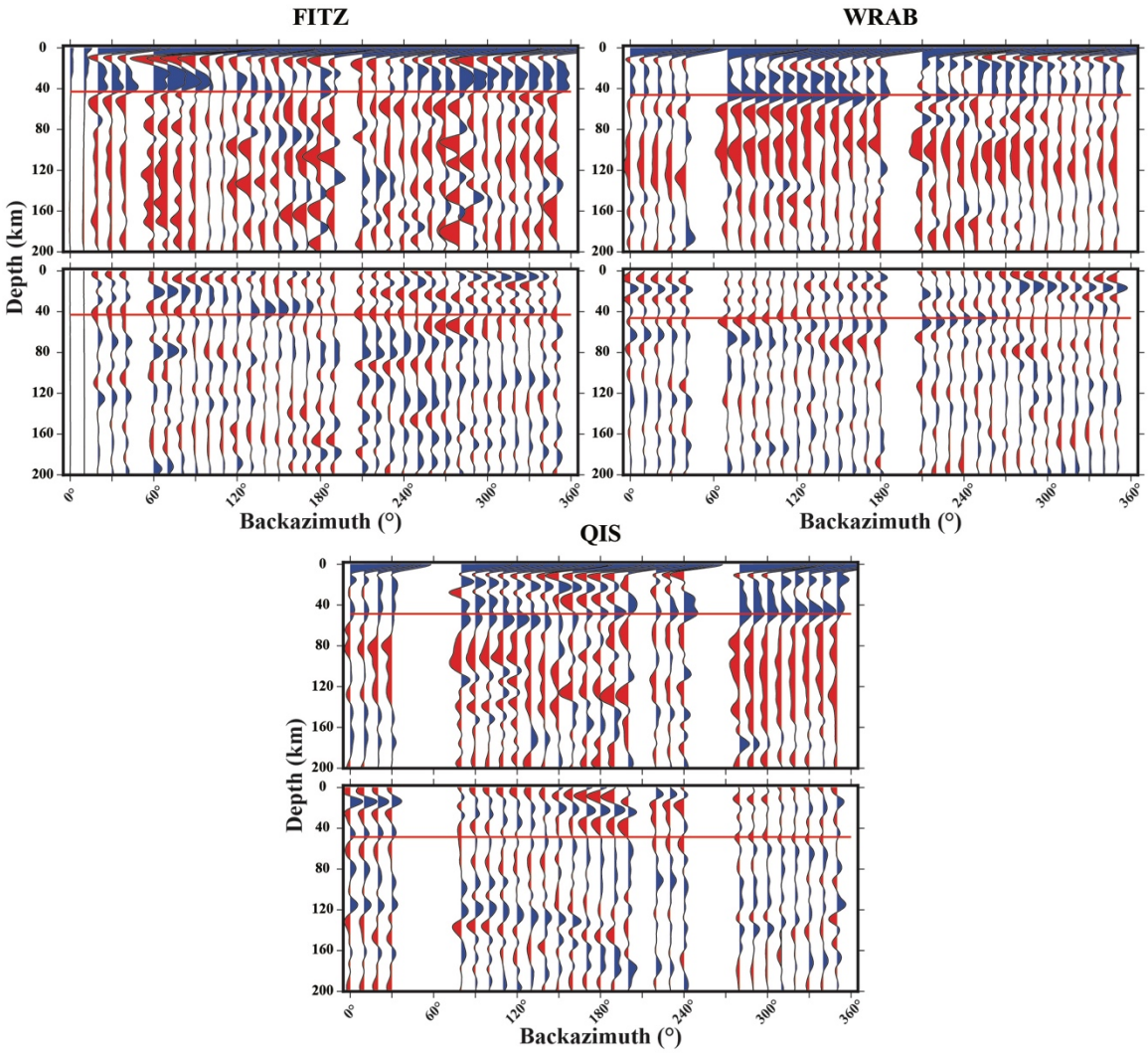


**Figure 2.10:** Backazimuthally-binned Ps receiver functions from the North Australian Craton (NAC).

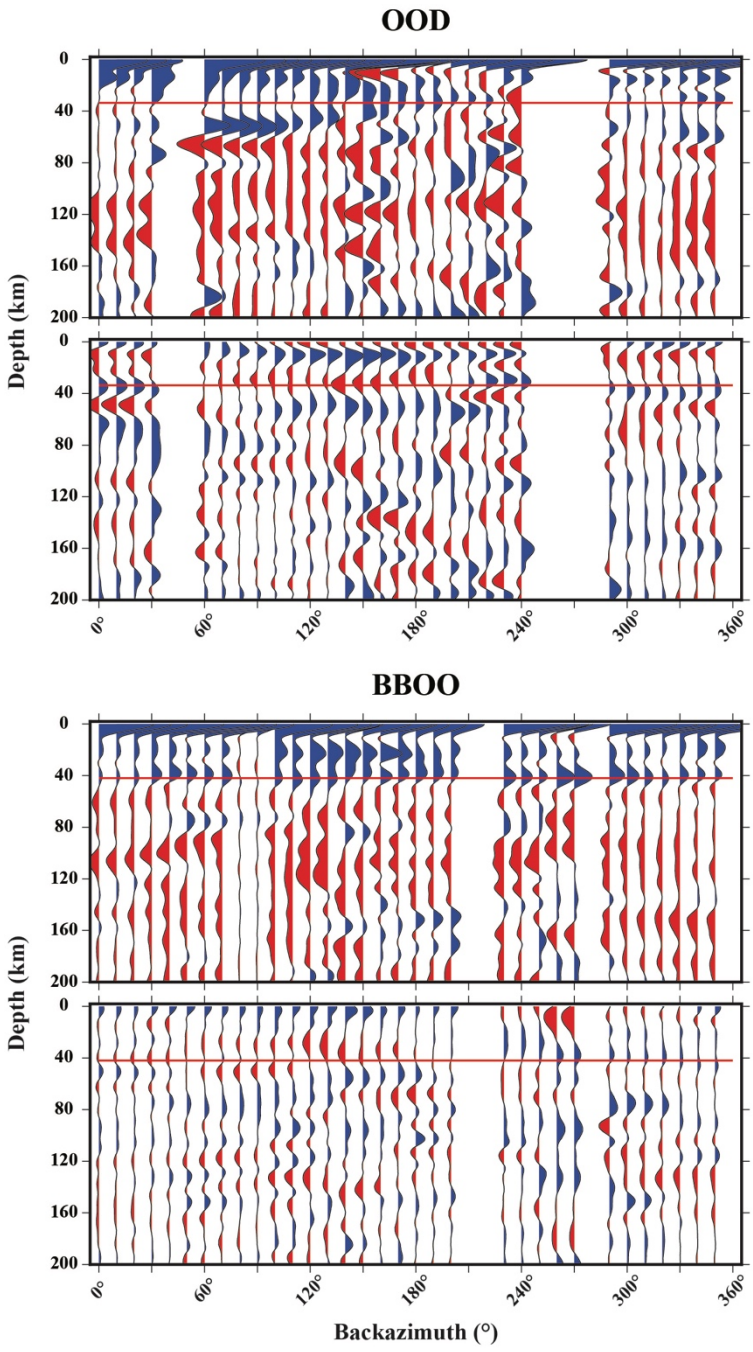


**Figure 2.11:** Backazimuthally-binned Ps receiver functions from the South Australian Craton (SAC).

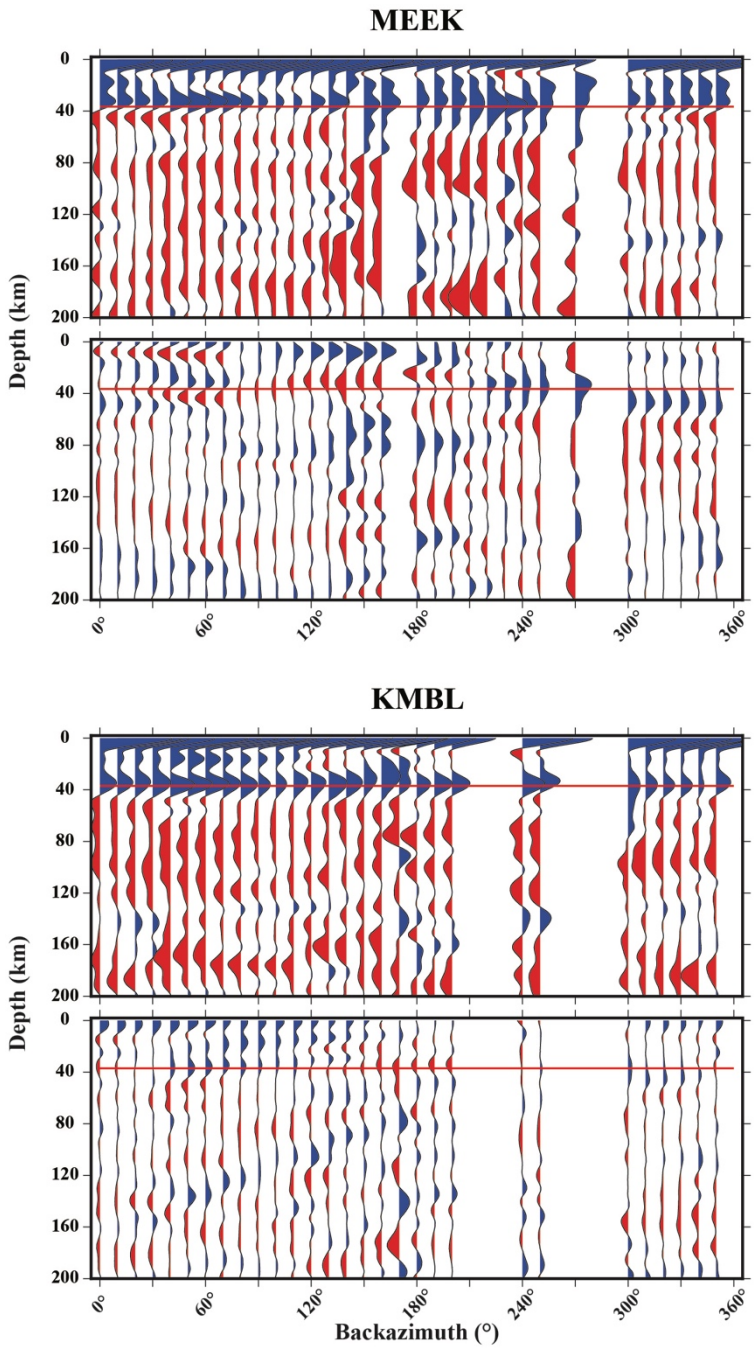


**Figure 2.12:** Backazimuthally-binned Ps receiver functions from the West Australian Craton (WAC).

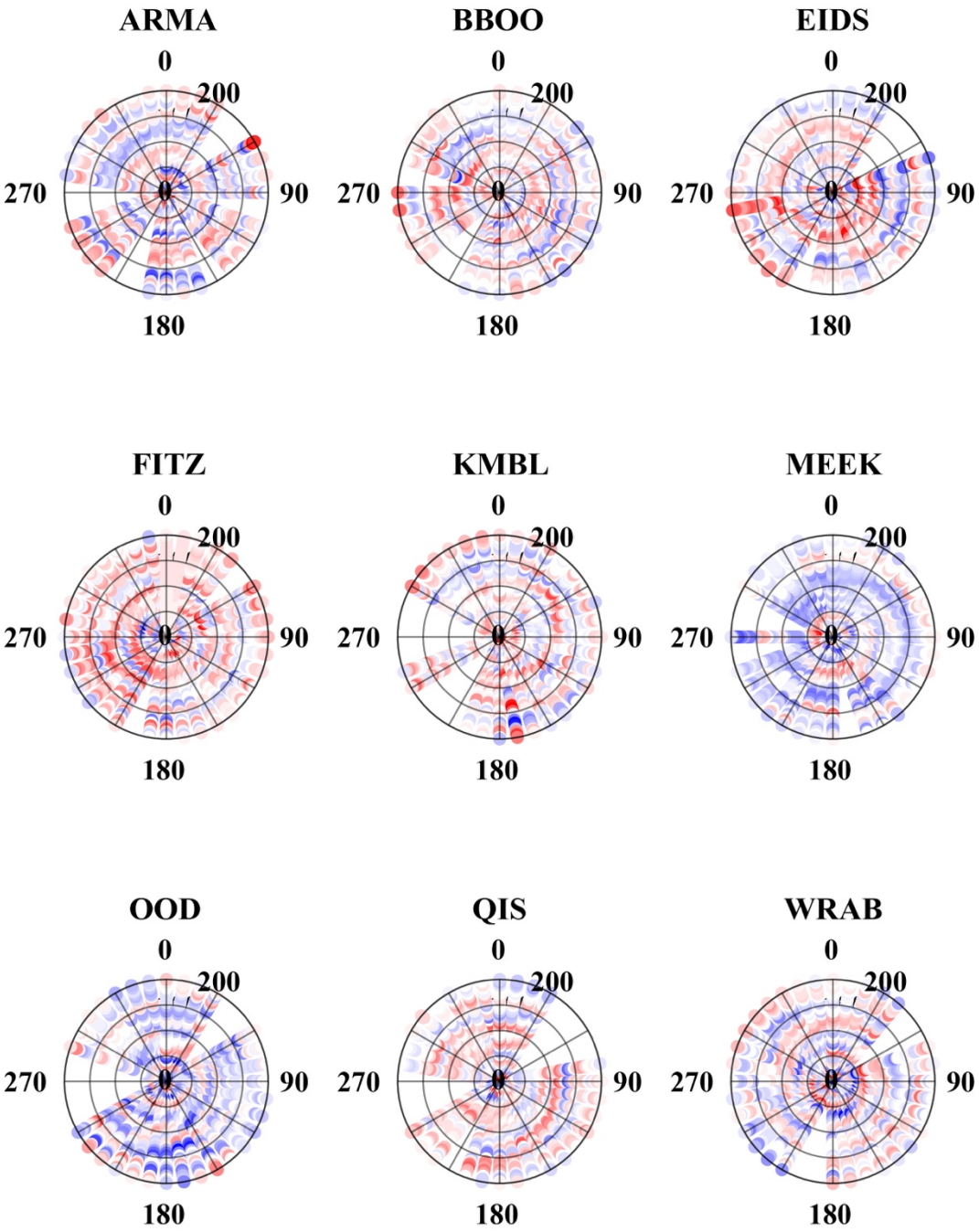


**Figure 2.13:** Rose diagrams of Ps receiver functions, showing backazimuth along the circumference of circles and the depth of the phase increasing from zero at the center. Each dot is color-coded according to the amplitude of the receiver function (blue indicates a positive phase, while red indicates a negative phase).

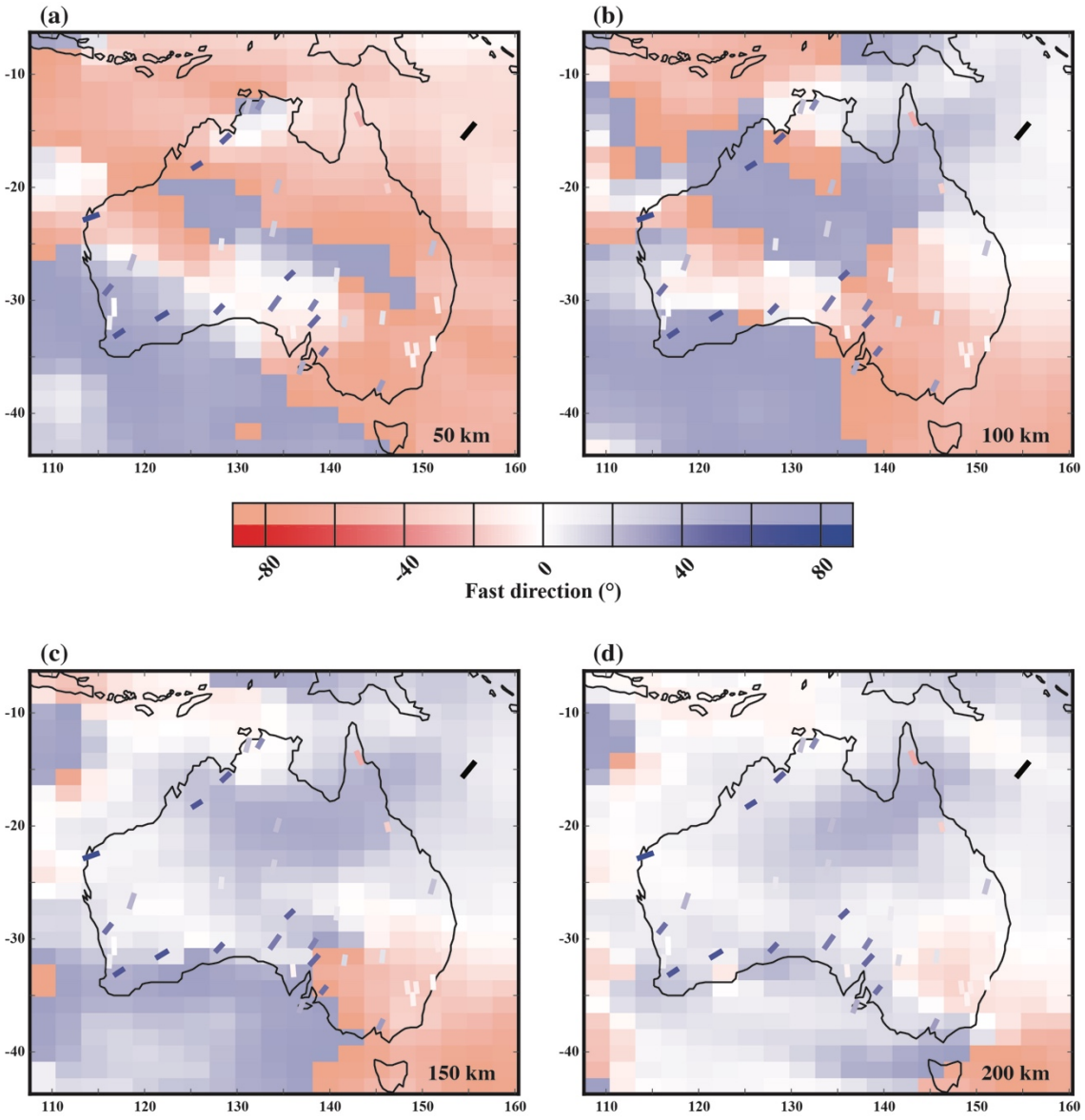


**Figure 2.14:** Average splitting parameters plotted against tomographically determined anisotropy from Debayle et al. (2016) for four depths.

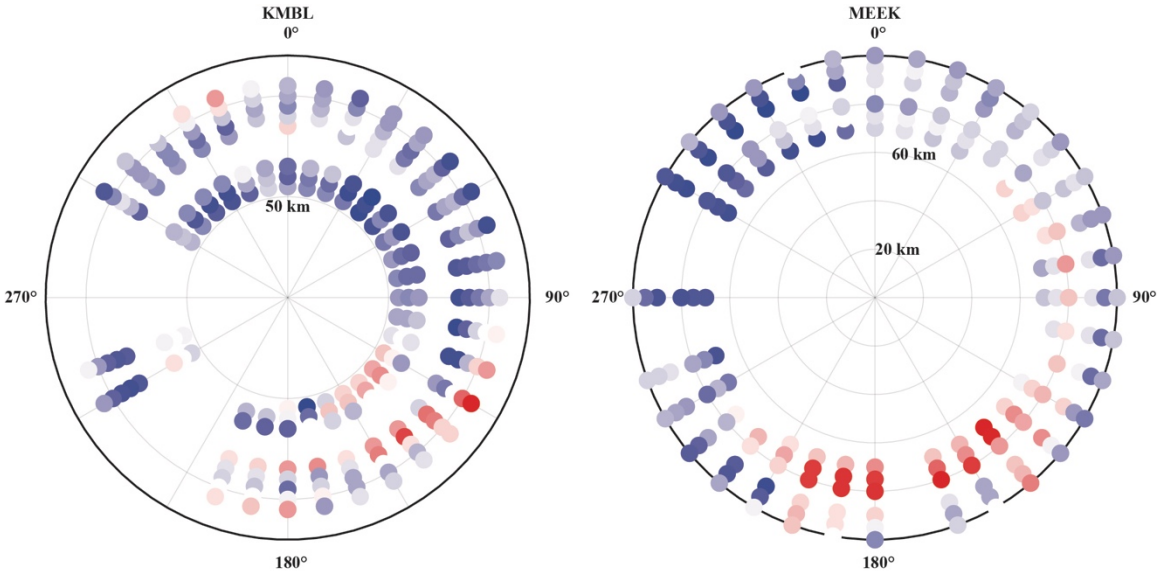


**Figure 2.15:** Rose diagrams of Ps receiver functions for stations used in Chen et al. (2021b) at the depths where their harmonic decomposition indicated polarity changes.

| Phanerozoic Australia | | | | North Australian Craton | | | | South Australian Craton | | | | West Australian Craton | | | |
|---|---|---|---|---|---|---|---|---|---|---|---|---|---|---|---|
| **Bin** | **Splits** | **Av. ϕ** | **Av. dt** | **Bin** | **Splits** | **Av. ϕ** | **Av. dt** | **Bin** | **Splits** | **Av. ϕ** | **Av. dt** | **Bin** | **Splits** | **Av. ϕ** | **Av. dt** |
| 30° | 18 | -6.88° | 0.59 s | 30° | 38 | 35.56° | 0.63 s | 30° | 10 | 54.76° | 0.48 s | 30° | 46 | 57.59° | 0.66 s |
| 90° | 14 | 41.95° | 0.72 s | 150° | 31 | -47.43° | 0.58 s | 150° | 15 | -44.61° | 0.44 s | 135° | 9 | 5.57° | 0.57 s |
| 150° | 84 | -23.25° | 0.60 s | 195° | 62 | 58.54° | 0.61 s | 180° | 21 | 51.93° | 0.68 s | 180° | 11 | -8.76° | 0.49 s |
| 180° | 31 | 16.30° | 0.79 s | 300° | 21 | 10.69° | 0.72 s | 300° | 19 | 25.34° | 0.65 s | | | | |
| 300° | 27 | 8.97° | 0.52 s | | | | | | | | | | | | |

**Table 2.1:** Bins with the most splits for each of the four regions. The number of splits, average fast direction (ϕ), and average delay time (dt) per bin are shown.

| AS31 | | | | | | |
|---|---|---|---|---|---|---|
| **Ev. lat** | **Ev. lon** | **Backazimuth** | **Phi (SC)** | **Phi (RC)** | **dt (SC)** | **dt (RC)** |
| -55.52° | -28.26° | 190.18° | 66.18° | | 0.55 s | |
| -55.50° | -28.30° | 190.20° | 88.20° | 51.20° | 1.10 s | 0.40 s |
| -56.20° | -26.89° | 190.72° | 60.72° | | 0.75 s | |
| -56.20° | -26.90° | 190.70° | 58.70° | 59.70° | 0.70 s | 0.70 s |
| -22.68° | 25.16° | 241.75° | -76.25° | | 1.30 s | |
| -22.70° | 25.20° | 241.70° | 87.70° | 80.70° | 0.70 s | 0.80 s |
| -36.12° | -101.02° | 137.53° | 71.53° | | 0.70 s | |
| -36.10° | -101.10° | 137.50° | -86.50° | -82.50° | 0.60 s | 0.60 s |
| -55.92° | -27.86° | 190.28° | 66.28° | | 0.55 s | |
| -55.90° | -27.90° | 190.30° | 68.30° | 59.30° | 0.70 s | 0.60 s |
| -60.21° | -26.53° | 189.66° | 81.66° | | 1.35 s | |
| -60.20° | -26.60° | 189.60° | 85.60° | 55.60° | 1.70 s | 0.70 s |
| **MULG** | | | | | | |
| **Ev. lat** | **Ev. lon** | **Backazimuth** | **Phi (SC)** | **Phi (RC)** | **dt (SC)** | **dt (RC)** |
| -56.20° | -26.89° | 190.52° | 80.52° | | 1.50 s | |
| -56.20° | -26.90° | 190.50° | 82.50° | 78.50° | 2.00 s | 1.80 s |
| -55.69° | -26.30° | 190.99° | 88.99° | | 2.35 s | |
| -55.70° | -26.20° | 191.00° | -89.00° | 46.00° | 3.60 s | 0.60 s |
| **WRAB** | | | | | | |
| **Ev. lat** | **Ev. lon** | **Backazimuth** | **Phi (SC)** | **Phi (RC)** | **dt (SC)** | **dt (RC)** |
| 59.03° | -155.12° | 29.44° | -24.56° | | 0.70 s | |
| 59.00° | -155.10° | 29.50° | -26.50° | -18.50° | 0.70 s | 0.70 s |
| 54.58° | -161.77° | 31.53° | -24.47° | | 1.05 s | |
| 54.50° | -161.70° | 31.60° | 5.60° | -22.40° | 1.10 s | 0.70 s |

**Table 2.2:** Comparison of splits calculated by both this study and Eakin et al. (2021). We display the fast direction ($\phi$) and delay time (dt) for both the minimum energy method (SC) and the rotation correlation method (RC).

## References


Ba, K., Gao, S. S., Liu, K. H., Kong, F., & Song, J. (2020). Receiver function imaging of the 410 and 660 km discontinuities beneath the Australian continent. *Geophysical Journal International*, *220*(3), 1481-1490.

Bello, M., Cornwell, D. G., Rawlinson, N., & Reading, A. M. (2019). Insights into the structure and dynamics of the upper mantle beneath Bass Strait, southeast Australia, using shear wave splitting. *Physics of the Earth and Planetary Interiors*, *289*, 45-62.

Birkey, A., Ford, H. A., Dabney, P., & Goldhagen, G. (2021). The lithospheric architecture of Australia from seismic receiver functions. *Journal of Geophysical Research: Solid Earth*, *126*(4), e2020JB020999.

Bostock, M. G. (1997). Anisotropic upper-mantle stratigraphy and architecture of the Slave craton. *Nature*, *390*(6658), 392-395.

Bostock, M. G. (1998). Mantle stratigraphy and evolution of the Slave province. *Journal of Geophysical Research: Solid Earth*, *103*(B9), 21183-21200.

Bowman, J. R., & Ando, M. (1987). Shear-wave splitting in the upper-mantle wedge above the Tonga subduction zone. *Geophysical Journal International*, *88*(1), 25-41.

Brownlee, S. J., Schulte-Pelkum, V., Raju, A., Mahan, K., Condit, C., & Orlandini, O. F. (2017). Characteristics of deep crustal seismic anisotropy from a compilation of rock elasticity tensors and their expression in receiver functions. *Tectonics*, *36*(9), 1835-1857.

Chen, X., Levin, V., & Yuan, H. (2021a). Small shear wave splitting delays suggest weak anisotropy in cratonic mantle lithosphere. *Geophysical Research Letters*, *48*(16), e2021GL093861.

Chen, X., Levin, V., Yuan, H., Klaser, M., & Li, Y. (2021). Seismic anisotropic layering in the Yilgarn and Superior cratonic lithosphere. *Journal of Geophysical Research: Solid Earth*, *126*(8), e2020JB021575.

Chen, X., Li, Y., & Levin, V. (2018). Shear wave splitting beneath eastern North American continent: evidence for a multilayered and laterally variable anisotropic structure. *Geochemistry, Geophysics, Geosystems*, *19*(8), 2857-2871.

Clarke, G. L., Sun, S. S., & White, R. W. (1995). Grenville-age belts and associated older terranes in Australia and Antarctica. *AGSO Journal of Australian Geology and Geophysics*, *16*(1), 25-40.

Clitheroe, G., & Van Der Hilst, R. D. (1998). Complex anisotropy in the Australian lithosphere from shear-wave splitting in broad-band SKS records. *Geodynamics Series*, *26*, 73.

Collins, W. J., & Shaw, R. D. (1995). Geochronological constraints on orogenic events in the Arunta Inlier: a review. *Precambrian Research*, *71*(1-4), 315-346.

Conder, J. A. (2007). Dynamically driven mantle flow and shear wave splitting asymmetry across the EPR, MELT area. *Geophysical Research Letters*, *34*(16).

Coney, P. J., Edwards, A., Hine, R., Morrison, F., & Windrim, D. (1990). The regional tectonics of the Tasman orogenic system, eastern Australia. *Journal of Structural Geology*, *12*(5-6), 519-543.

Creasy, N., Long, M. D., & Ford, H. A. (2017). Deformation in the lowermost mantle beneath Australia from observations and models of seismic anisotropy. *Journal of Geophysical Research: Solid Earth*, *122*(7), 5243-5267.

Debayle, E., Dubuffet, F., & Durand, S. (2016). An automatically updated S-wave model of the upper mantle and the depth extent of azimuthal anisotropy. *Geophysical Research Letters*, *43*(2), 674-682.

Deng, J., Long, M. D., Creasy, N., Wagner, L., Beck, S., Zandt, G., ... & Minaya, E. (2017). Lowermost mantle anisotropy near the eastern edge of the Pacific LLSVP: constraints from SKS–SKKS splitting intensity measurements. *Geophysical Journal International*, *210*(2), 774-786.

Du Frane, W. L., Roberts, J. J., Toffelmier, D. A., & Tyburczy, J. A. (2005). Anisotropy of electrical conductivity in dry olivine. *Geophysical research letters*, *32*(24).

Eakin, C. M., Flashman, C., & Agrawal, S. (2021). Seismic anisotropy beneath Central Australia: A record of ancient lithospheric deformation. *Tectonophysics*, *820*, 229123.

Ford, H. A., Fischer, K. M., Abt, D. L., Rychert, C. A., & Elkins-Tanton, L. T. (2010). The lithosphere–asthenosphere boundary and cratonic lithospheric layering beneath Australia from Sp wave imaging. *Earth and Planetary Science Letters*, *300*(3-4), 299-310.

Ford, H. A., Long, M. D., He, X., & Lynner, C. (2015). Lowermost mantle flow at the eastern edge of the African Large Low Shear Velocity Province. *Earth and Planetary Science Letters*, *420*, 12-22.

Ford, H. A., Long, M. D., & Wirth, E. A. (2016). Midlithospheric discontinuities and complex anisotropic layering in the mantle lithosphere beneath the Wyoming and Superior Provinces. *Journal of Geophysical Research: Solid Earth*, *121*(9), 6675-6697.

Foster, D. A., & Gray, D. R. (2000). Evolution and structure of the Lachlan Fold Belt (Orogen) of eastern Australia. *Annual Review of Earth and Planetary Sciences*, *28*(1), 47-80.

Gripp, A. E., & Gordon, R. G. (2002). Young tracks of hotspots and current plate velocities. *Geophysical Journal International*, *150*(2), 321-361.

Heintz, M., & Kennett, B. L. (2005). Continental scale shear wave splitting analysis: Investigation of seismic anisotropy underneath the Australian continent. *Earth and Planetary Science Letters*, *236*(1-2), 106-119.

Heintz, M., & Kennett, B. L. (2006). The apparently isotropic Australian upper mantle. *Geophysical Research Letters*, *33*(15).

Hopper, E., Fischer, K. M., Wagner, L. S., & Hawman, R. B. (2017). Reconstructing the end of the Appalachian orogeny. *Geology*, *45*(1), 15-18.

Kennett, B. L., Fichtner, A., Fishwick, S., & Yoshizawa, K. (2013). Australian seismological reference model (AuSREM): mantle component. *Geophysical Journal International*, *192*(2), 871-887.

Kennett, B. L. N., Salmon, M., Saygin, E., & Group, A. W. (2012). AusMoho: the variation of Moho depth in Australia. *Geophysical Journal International*, *187*(2), 946-958.

Kennett, B. L. N., & Salmon, M. (2012). AuSREM: Australian seismological reference model. *Australian Journal of Earth Sciences*, *59*(8), 1091-1103.

Kumazawa, M., & Anderson, O. L. (1969). Elastic moduli, pressure derivatives, and temperature derivatives of single-crystal olivine and single-crystal forsterite. *Journal of Geophysical Research*, *74*(25), 5961-5972.

Laske, G., Masters, G., Ma, Z., & Pasyanos, M. (2013, April). Update on CRUST1. 0—A 1-degree global model of Earth's crust. In *Geophys. res. abstr* (Vol. 15, p. 2658).

Levin, V., & Park, J. (1997). P-SH conversions in a flat-layered medium with anisotropy of arbitrary orientation. *Geophysical Journal International*, *131*(2), 253-266.

Li, Y., Levin, V., Elkington, S., & Hlavaty, J. (2019). Localized anisotropic domains beneath eastern North America. *Geochemistry, Geophysics, Geosystems*, *20*(11), 5499-5521.

Li, Z. X. (2000). Palaeomagnetic evidence for unification of the North and West Australian cratons by ca. 1.7 Ga: new results from the Kimberley Basin of northwestern Australia. *Geophysical Journal International*, *142*(1), 173-180.

Liu, G., Persaud, P., & Clayton, R. W. (2018). Structure of the northern Los Angeles basins revealed in teleseismic receiver functions from short-term nodal seismic arrays. *Seismological Research Letters*, *89*(5), 1680-1689.

Long, M. D., Ford, H. A., Abrahams, L., & Wirth, E. A. (2017). The seismic signature of lithospheric deformation beneath eastern North America due to Grenville and Appalachian orogenesis. *Lithosphere*, *9*(6), 987-1001.

Long, M. D., & Lynner, C. (2015). Seismic anisotropy in the lowermost mantle near the Perm Anomaly. *Geophysical Research Letters*, *42*(17), 7073-7080.

Long, M. D., & Silver, P. G. (2008). The subduction zone flow field from seismic anisotropy: A global view. *science*, *319*(5861), 315-318.

Lutz, K. A., Long, M. D., Creasy, N., & Deng, J. (2020). Seismic anisotropy in the lowermost mantle beneath North America from SKS-SKKS splitting intensity discrepancies. *Physics of the Earth and Planetary Interiors*, *305*, 106504.

Lynner, C., & Long, M. D. (2014). Lowermost mantle anisotropy and deformation along the boundary of the African LLSVP. *Geophysical Research Letters*, *41*(10), 3447-3454.

Mancinelli, N. J., Fischer, K. M., & Dalton, C. A. (2017). How sharp is the cratonic lithosphere-asthenosphere transition?. *Geophysical Research Letters*, *44*(20), 10-189.

Marshak, S., & Flöttmann, T. (1996). Structure and origin of the Fleurieu and Nackara Arcs in the Adelaide fold-thrust belt, South Australia: salient and recess development in the Delamerian Orogen. *Journal of Structural Geology*, *18*(7), 891-908.

Murray, C. G., & Kirkegaard, A. G. (1978). The Thomson Orogen of the Tasman orogenic zone. *Tectonophysics*, *48*(3-4), 299-325.

Musacchio, G., White, D. J., Asudeh, I., & Thomson, C. J. (2004). Lithospheric structure and composition of the Archean western Superior Province from seismic refraction/wide-angle reflection and gravity modeling. *Journal of Geophysical Research: Solid Earth*, *109*(B3).

Myers, J. S., Shaw, R. D., & Tyler, I. M. (1996). Tectonic evolution of proterozoic Australia. *Tectonics*, *15*(6), 1431-1446.

Özalaybey, S., & Chen, W. P. (1999). Frequency-dependent analysis of SKS/SKKS waveforms observed in Australia: evidence for null birefringence. *Physics of the earth and planetary interiors*, *114*(3-4), 197-210.

Park, J., & Levin, V. (2016). Anisotropic shear zones revealed by backazimuthal harmonics of teleseismic receiver functions. *Geophysical supplements to the monthly notices of the Royal Astronomical Society*, *207*(2), 1216-1243.

Reading, A. M., & Kennett, B. L. N. (2003). Lithospheric structure of the Pilbara Craton, Capricorn Orogen and northern Yilgarn Craton, Western Australia, from teleseismic receiver functions. *Australian Journal of Earth Sciences*, *50*(3), 439-445.

Salmon, M., Kennett, B. L. N., & Saygin, E. (2013). Australian seismological reference model (AuSREM): crustal component. *Geophysical Journal International*, *192*(1), 190-206.

Savage, M. K. (1999). Seismic anisotropy and mantle deformation: what have we learned from shear wave splitting?. *Reviews of Geophysics*, *37*(1), 65-106.

Shiomi, K., & Park, J. (2008). Structural features of the subducting slab beneath the Kii Peninsula, central Japan: Seismic evidence of slab segmentation, dehydration, and anisotropy. *Journal of Geophysical Research: Solid Earth*, *113*(B10).

Silver, P. G., & Chan, W. W. (1991). Shear wave splitting and subcontinental mantle deformation. *Journal of Geophysical Research: Solid Earth*, *96*(B10), 16429-16454.

Smithies, R. H., & Bagas, L. (1997). High pressure amphibolite-granulite facies metamorphism in the Paleoproterozoic Rudall Complex, central Western Australia. *Precambrian Research*, *83*(4), 243-265.

Tesauro, M., Kaban, M. K., & Aitken, A. R. (2020). Thermal and compositional anomalies of the Australian upper mantle from seismic and gravity data. *Geochemistry, Geophysics, Geosystems*, *21*(11), e2020GC009305.

Vauchez, A., Tommasi, A., & Barruol, G. (1998). Rheological heterogeneity, mechanical anisotropy and deformation of the continental lithosphere. *Tectonophysics*, *296*(1-2), 61-86.

Vinnik, L. P., Makeyeva, L. I., Milev, A., & Usenko, A. Y. (1992). Global patterns of azimuthal anisotropy and deformations in the continental mantle. *Geophysical Journal International*, *111*(3), 433-447.

Wang, L., Hitchman, A. P., Ogawa, Y., Siripunvaraporn, W., Ichiki, M., & Fuji-Ta, K. (2014). A 3-D conductivity model of the Australian continent using observatory and magnetometer array data. *Geophysical Journal International*, *198*(2), 1143-1158.

Wirth, E. A., & Long, M. D. (2012). Multiple layers of seismic anisotropy and a low-velocity region in the mantle wedge beneath Japan: Evidence from teleseismic receiver functions. *Geochemistry, Geophysics, Geosystems*, *13*(8).

Wirth, E. A., & Long, M. D. (2014). A contrast in anisotropy across mid-lithospheric discontinuities beneath the central United States—A relic of craton formation. *Geology*, *42*(10), 851-854.

Wolf, J., Creasy, N., Pisconti, A., Long, M. D., & Thomas, C. (2019). An investigation of seismic anisotropy in the lowermost mantle beneath Iceland. *Geophysical Journal International*, *219*(Supplement_1), S152-S166.

Wüstefeld, A., Bokelmann, G., Zaroli, C., & Barruol, G. (2008). SplitLab: A shear-wave splitting environment in Matlab. *Computers & Geosciences*, *34*(5), 515-528.

**Insight into the evolution of the eastern margin of the Wyoming Craton from complex, laterally shear wave splitting**

Andrew Birkey[1*], Heather A. Ford[1], Megan Anderson[2], Maximiliano J. Bezada[3], Joseph S. Byrnes[3,4] and Maxim Shapovalov[1]

[1]Department of Earth and Planetary Sciences, University of California – Riverside, Riverside, CA

[2]Washington Geological Survey

[3]Department of Earth & Environmental Sciences, University of Minnesota, Twin Cities, Minneapolis, MN

[4]School of Earth and Sustainability, Northern Arizona University, Flagstaff, AZ

*In preparation for Earth and Planetary Science Letters*

*Corresponding author:

Department of Earth and Planetary Sciences, University of California – Riverside

900 University Avenue, Riverside, California, 92521

Email: abirk001@ucr.edu

**Abstract**

Cratons (ancient continental cores) are often assumed to be static, homogeneous regions of high velocity: this has been challenged with the deployment of dense seismic arrays such as EarthScope's **T**ransportable **A**rray (TA), which has revealed complex structure throughout cratonic North America. In this study, we pair TA data with data from the **B**ighorn **A**rch **S**eismic **E**xperiment (BASE) and the **C**rust and lithosphere **I**nvestigation of the **E**asternmost expression of the **L**aramide **O**rogeny (CIELO) to provide unprecedented detail on the eastern margin of the Wyoming Craton. In this study we utilize shear wave splitting, a method that is often used to examine deformation and fabric within the Earth's crust and mantle. Our results show a clear change in seismic anisotropy within the Powder River Basin and backazimuthally dependent splitting, evidence of complex and multilayered seismic anisotropy. We argue that these results correspond to structure predating the Laramide Orogeny and indicate either a change at the eastern margin of the craton or a Neoarchean boundary preserved within the lithosphere.

## 1. Introduction

Situated in the center of the North American continent, the Wyoming Craton is an Archean to Proterozoic aged block of crust and lithospheric mantle that is divided into three main subregions (see **Figure 3.1**): in decreasing order of age, the Montana Metasedimentary Province in the northwest, the Beartooth-Bighorn Magmatic Zone across its middle, and the Southern Accreted Terranes in the southeast (Chamberlain et al., 2003). All three subregions were brought together as a distinct block of cratonic lithosphere by ~2.5 Ga

(Mueller and Frost, 2006). Following craton assembly and stabilization, interactions between the Wyoming craton and the other cratons of Laurentia is debated. There is general agreement that in Northern Laurentia, terminal collision between the Superior, Hearne-Rae, and Slave Cratons began earlier (~1.815 to 1.780 Ga) than in southern Laurentia, between the Wyoming and Superior Cratons (~1.750 to 1.700 Ga). However, it is unclear whether this represents one orogenic event (i.e., the Trans-Hudson Orogeny) or several discrete events, with some authors referring to the southern portion of the Trans-Hudson Orogeny as the Black Hills or Dakotan Orogeny (Chamberlain et al., 2002; Dahl et al., 1999; Killian et al., 2016). Furthermore, there is debate regarding the onset of terminal collision between the Wyoming and Superior cratons: some have argued based on geologic exposures and structural data that the suturing of the two cratons occurred ~1.750 Ga (Dahl et al., 2010; Hrcnir et al., 2017), while others have relied on the dating of dike swarms and paleomagnetic data to suggest that it occurred much later, at ~1.715 Ga (Chamberlain et al., 2017; Kilian et al., 2016). Regardless, by ~1.7 Ga Wyoming was sutured to other constituent cratons of the Laurentia core (i.e., the Hearne-Rae, Slave, and Superior Cratons). The suture with the Superior Craton via the Trans-Hudson Orogen represents the Wyoming Craton's eastern boundary. The Great Falls Tectonic Zone is to the north of the craton, and the boundary between the two is indicated by northeast trending magnetic data (Boerner et al., 1998) and a north-dipping reflector that may indicate relict subduction of oceanic lithosphere and the Proterozoic suturing of the Wyoming craton with the Medicine Hat Block and Hearne Craton to its north (Gorman et al., 2002). To the southeast of the Wyoming Craton is the Cheyenne Belt (geophysically characterized as a thick crustal root

with no accompanying surficial mountain range; Crosswhite and Humphreys, 2003), where Archean and Paleoproterozoic rocks of the craton abut younger Paleoproterozoic rocks of the Yavapai Province (Duebendorfer et al., 1987; Karlstrom and Houston, 1984).

The location of the eastern edge of the Wyoming Craton is still debated: some studies have suggested that the craton extends to the Black Hills, based primarily on the Archean age of rocks in both the Black Hills and uplifts throughout the Wyoming Craton (McCombs et al., 2004; Mueller and Frost, 2006) as well as the age of detrital zircons from the Black Hills (Dahl et al., 2010). However, there is an age difference of ~300 Myr between the Little Elk Granite in the Black Hills (McCombs et al., 2004) and Archean volcanic rocks in the Bighorn Mountains (Frost and Fanning, 2006). Others posit a more westerly craton boundary just to the east of the Bighorn Arch. This relies on a west-dipping reflector coupled with a magnetic contact to the east of the Bighorn Mountains (Worthington et al., 2015). Magnetotelluric studies image a region of high conductivity extending from northern Canada through the Cheyenne Belt, which has been referred to as the North American Central Plains Anomaly and is believed to be linked to the Trans-Hudson Orogen and the assembly of Laurentia (Bedrosian and Finn, 2021; Camfield and Gough, 1977). Since the Black Hills are to the west of this anomaly, their amalgamation to the Wyoming Craton likely predates the Trans-Hudson Orogeny.

Following the formation of Laurentia, the Wyoming Craton experienced a period of tectonic quiescence until ~80 Ma, when the flattening of the Farallon slab initiated the

Laramide Orogeny (Coney and Reynolds, 1977; Livacarri et al., 1981; Saleeby, 2003; Spasojevic et al., 2009). Cratons are assumed to be stable blocks of thick lithosphere resistant to deformation or destruction under certain circumstances (Cooper et al., 2004; Pollack, 1986), but the crust deformed in basement-cored uplifts during the Laramide across the Wyoming Craton (i.e., the Wind River Range, Granite Mountains, Owl Creek Mountains, the Bighorn Arch, Laramie Mountains, and the Black Hills). There have been many hypotheses for how such nominally strong lithosphere underwent this type of deformation. Some have suggested that Precambrian faults or other preexisting weaknesses within the crust were reactivated and allowed orogenesis deep within the continental interior (Allmendinger et al., 1982; Bader, 2019; Zhu et al., 2021). Other models for Laramide orogenesis include Moho-penetrating faults that define discrete blocks (Scheevel, 1983; McQueen and Beaumont, 1989), buckling of the upper crust accommodated by thickening of the lower crust (Egan and Urquhart, 1993), upper crustal buckling forced by crustal detachment (Erslev and Rogers, 1993), and buckling of the entire lithosphere (Tikoff and Maxson, 2001; Tikoff et al., 2022). Recent seismological examination of the shape of the Moho under the Bighorns arch via receiver function and deep crustal refraction analysis clearly disproves hypotheses involving Moho-penetrating faults or thickening under the range by pure shear thickening (Yeck et al., 2014; Worthington et al., 2015). However, mechanisms of crustal detachment and some component of lithospheric buckling still stand. The mechanisms by which these uplifts occurred has implications for the current state of the Wyoming Craton. For instance, if the lithosphere was heavily deformed during orogenesis through buckling or melting then the

craton may be currently engaged in ongoing deformation, destabilization, or delamination—similar to the North China Craton, which also saw subduction during the Mesozoic and potential destabilization (e.g., Huang et al., 2021; Kusky et al.,2014; Lei, 2012; Zhao et al., 2012; Zhu et al., 2012).

Regional and continental tomographic models reveal several broad trends in seismic wave behavior in the Wyoming Craton: first, the western Wyoming Craton is seismically slower where there is interaction with the Yellowstone Plume. Second, the central and eastern portions of the craton feature a high-velocity anomaly that extends below 200 km depth. Third, a swath of low velocities to the southeast of the Wyoming Craton occurs along the Cheyenne Belt (Bedle et al., 2021; Burdick et al., 2012; Dave and Li, 2016; Obrebski et al., 2011; Schmandt and Humphreys, 2010; Schmandt and Lin, 2014; Shen and Ritzwoller, 2016). Several models also estimate a velocity low beneath the Black Hills (Bedle et al., 2021; Burdick et al., 2012; Dave and Li, 2016; Schmandt and Lin, 2014; Shen and Ritzwoller, 2016) that extends to at least 100 km depth. Bedle et al. (2021), Burdick et al. (2012), Schmandt and Humphreys (2010), Schmandt and Lin (2014), and Shen and Ritzwoller (2016) observe a NE-SW trending high velocity region in the center of the craton, bound by velocity lows to the west and southeast, with a clear slowing of velocity to the east below 100 km depth. Several studies have suggested that this may represent a remnant of the Farallon Slab (Bedle et al., 2021; Schmandt and Humphreys, 2010; Schmandt and Lin, 2014). This hypothesis is further developed in Humphreys et al. (2015), who argue that because xenoliths from northern Wyoming indicate a warmer geotherm

than predicted for Archean lithosphere, this NE-SW trending high velocity block extending to ~300 km depth most likely indicates the emplacement of depleted oceanic mantle beneath the Wyoming Craton. Dave and Li (2016), however, argue that tomographic models show that the interaction of the Wyoming craton with the Yellowstone hotspot and flat-slab subduction initiated small-scale convection at the base of the lithosphere as opposed to the emplacement of depleted mantle beneath the craton. Both agree, though, that the lithospheric root of the Wyoming Craton has been severely deformed and modified since the Laramide Orogeny.

A recent attenuation study by Zhu et al. (2021) has confirmed the presence of a thick block of lithosphere beneath the central Wyoming Craton, with higher attenuation observed beneath mountain ranges than basins in the eastern portion of the craton. The magnitude of the signal requires thicker and less attenuating lithosphere beneath the Bighorn and Powder River Basins than the Bighorn Mountains and Black Hills. Furthermore, these variations in thickness provide a mechanism for localizing stress during the Laramide, as stronger blocks could resist deformation and transfer stress to weaker adjacent blocks. Zhu et al. (2021) refer to the high-velocity anomaly roughly coincident with the Powder River Basin as the Thunder Basin Block—we will utilize the same terminology here.

Key outstanding questions regarding the Wyoming Craton include the following: Where does the eastern edge of the craton lie? What is the physical state of the lithosphere in the Wyoming Craton? How does the current state of the lithosphere relate to the craton's

formation and evolution? In this study, we utilize shear wave splitting to provide new constraints on answers to these questions. Shear wave splitting has provided crucial insights into the state of both dynamic and static mantle throughout the world. For instance, in the tectonically active western United States, a characteristic pattern of swirling splitting results has been inferred to indicate either a lithospheric drip (West et al., 2009) or toroidal flow around the Gorda-Juan de Fuca slab (Zandt and Humphreys, 2008). Previous splitting results in this region indicate complex seismic anisotropy that generally does not mirror plate motion but rather exhibits a variety fast directions. In addition, smaller delay times within the craton that increase eastward into the Proterozoic orogens (Becker et al., 2012; Hongsresawat et al., 2015). However, to the west of the Wyoming craton (near the Yellowstone hot spot), splitting fast directions do parallel absolute plate motion but transition awy from it moving into the Archean lithosphere of the craton (Waite et al., 2005). Several studies and methods indicate that seismic anisotropy likely varies with depth across the region (Yuan and Romanowicz, 2010; Zhou et al., 2018). Preliminary shear wave splitting work focusing on the Bighorn Mountains found that fast directions do not generally align with plate motion but instead mirror crustal aeromagnetic anomalies, suggesting a coherence between crustal and mantle structures, hence an Archean origin to observed fabrics (Anderson et al., 2014). That study additionally observed a change in splitting parameters to the east of the Bighorn Mountains, a transition that corresponds with the more westerly boundary of the Wyoming craton posited in Worthington et al. (2015).

In this study we present shear wave splitting results from three networks. First, we use data from the **C**rust and lithosphere **I**nvestigation of the **E**asternmost expression of the **L**aramide **O**rogeny (CIELO), deployed from 2017 to 2019 (Ford et al., 2021). The goals of CIELO include characterizing the nature and location of the eastern margin of the Wyoming Craton, understanding the current physical state of the mantle lithosphere, and relating those observations to the mechanisms and style of Laramide Orogenesis. Second, the **B**ighorn **A**rch **S**eismic **E**xperiment (BASE) was deployed for a year and a half starting in 2010 (Sheehan, 2011). Similar to CIELO, the BASE aimed to understand the nature of the lithosphere beneath the Bighorn Mountains and the cause of basement-cored foreland uplifts of the Laramide Orogeny. Finally, we use data from the EarthScope **T**ransportable **A**rray (TA), which was deployed across the United States in two-year intervals and crossed our study area, to provide a more laterally complete view of splitting. Taken together, these results afford us a comprehensive view of seismic anisotropy beneath the eastern half of the Wyoming Craton.

## 2. Data and Methods

### *2.1 Data*

This study utilizes data from the Crust and Lithosphere Investigation of the Easternmost Expression of the Laramide Orogeny (CIELO), the Bighorn Arch Seismic Experiment (BASE), and the Transportable Array (TA) (see **Figure 3.2**). The CIELO experiment was a two-year (2017-2019), linear array deployment across the eastern portion of the Wyoming Craton, from the southern terminus of the Bighorn Mountains, through the

Powder River Basin, and ending to the east of the Black Hills (Ford et al., 2021). CIELO aimed to image the structure of the easternmost Wyoming Craton, examine its margin, and better understand the relationship between mantle lithosphere and Laramide orogenesis and deformation. It utilized 24 Nanometrics Meridian Compact Posthole seismometers. Ford et al. (2021) analyzed the quality of data at the stations, which we summarize here. Nineteen of the stations were misoriented within ±10° and five had misorienations ranging from 10.2° to 24.3° (deteremined via Latest Assessment of Seismic Station Observations—LASSO, IRIS Inc.); these misorientations were corrected in Splitlab (Deng et al., 2017; Wüstefeld et al., 2008). Ford et al. (2021) report the data quality for the CIELO array: overall, stations had high quality data, except in cases where anthropogenic noise was prevalent. They also reported preliminary Ps receiver functions, P-wave delay times, and shear wave splitting results (which we expand upon in this study).

The BASE was a twenty-month (2009-2010) experiment centered on the Bighorn Mountains, with stations to the west in the Bighorn Basin and the east in the Powder River Basin, with a goal of imaging the Moho of the Bighorn Arch and understanding the structural mechanism for uplift of foreland basement-cored arches. The broadband component of the BASE had 38 Guralp CMG-3 T Seismometers (see Yeck et al., 2014 for more details). Previous studies that have specifically examined the BASE data include receiver function analysis by Yeck et al. (2014), reflection and P-wave analysis by Worthington et al. (2015), and local seismicity analysis by O'Rourke et al. (2016). Here, we provide the previously calculated results of the BASE (Anderson et al., 2014) in

conjunction with new results from the CIELO experiment. It should be noted that the BASE and CIELO arrays overlap at the southern tip of the Bighorn Mountains and the westernmost portion of the Powder River Basin. Combined, the two experiments allow us to provide a more comprehensive view of lateral splitting variations than previous studies in the eastern half of the Wyoming Craton.

*2.2 Shear wave splitting methodology*

Anisotropy (i.e., directional dependence) results from the macroscopic alignment of intrinsically seismically anisotropic minerals. Shear waves passing through a seismically anisotropic medium are split into a fast and slow phase that become separated in time, with the time lag proportional to the strength of the seismic anisotropy; this is known as shear wave splitting, and is an unambiguous indication of seismic anisotropy (Savage, 1999; Silver and Chan, 1991).

Splitting parameters from different arrays were calculated separately by different groups with similar but not identical methodologies. All splits were calculated in an updated version of Splitlab (Wüstefeld et al., 2008; Deng et al., 2017) using the rotation correlation method (Bowman and Ando, 1987), which rotates two components in 1° increments and time shifts in 0.1 second increments; the cross correlation at each orientation and time is calculated, with the maximum correlation indicating the fast direction and delay time of that split. However, agreement between different methods is commonly used to check for the quality of the split, so the BASE and CIELO splits were also calculated using minimum

energy and eigenvalue methods (see Silver and Chan, 1991 for details). Agreement between the different methods, defined as a difference between the fast directions and delay times of less than 25° and 0.5 seconds, respectively, indicates a higher quality split and greater confidence in the estimated splitting parameters. Splits that do not agree between methods are reported here if other metrics listed below indicated they were stable results. Splits were only measured for recordings with a signal-to-noise ratio greater than 5.0. The particle motion before and after correction provides another useful metric: particle motion for SKS phases should be elliptical before correction and rectilinear after, so results that do not fit these criteria are of lower quality. Null splits— results with no evidence of splitting — were verified using the splitting intensity method (Chevrot, 2000), which has values near zero (< 0.1 in cratons) for null splits. SKS and SKKS phases were used: shear wave splitting is a path-integrated effect, and these phases convert from P-waves to S-waves at the core-mantle boundary, ensuring that any splitting is limited to the receiver-side path.

The BASE-affiliated researchers used events limited to Mw ≥ 5.75 and epicentral distances of 85° to 145° for the BASE and TA stations; for CIELO-affiliated researchers, events were limited to Mw ≥ 5.5 and epicentral distances of 90° to 130° for CIELO and TA stations with no restrictions on the depth of the event. Results for the BASE stations include 519 SKS phases, 109 SKKS phases, and 81 PKS phase. At CIELO stations, results include 275 SKS phases and 14 SKKS phases. TA stations had 716 SKS phases, 108 SKKS phases, and 58 PKS phases. The BASE-affiliated researchers calculated splits using five frequency

bands: a broad filter (0.02 to 1 Hz), a low filter (0.04 to 0.1 Hz), a medium filter (0.1 to 0.2 Hz), a high filter (0.2 to 0.5 Hz), and a very high filter (0.5 to 1 Hz). CIELO-affiliated researchers used seven frequency bands between 0.2 and 1.0 Hz to isolate the highest signal-to-noise ratio (0.02 to 0.1 Hz, 0.04 to 0.1 Hz, 0.02 to 0.2 Hz, 0.1 to 0.2 Hz, 0.08 to 0.3 Hz, 0.06 to 0.6 Hz, and 0.1 to 0.5 Hz). Frequency-dependent splitting can be used to estimate the presence of multiple layers of seismic anisotropy and changes in fabric with depth (Eakin and Long, 2013).

## 3. Results

### *3.1 Results overview and network comparisons*

There were 709 non-null splits found at the BASE stations, and 180 null splits. The CIELO stations had 296 non-null splits, and 241 null splits. The TA stations had the most non-null splits at 911 and 331 null splits; it should be noted that because 9 TA stations were used by both groups, there were 47 splits and 10 null splits from this network that were calculated twice. Frequency dependent splitting carried out by the BASE-affiliated researchers yielded 1175 non-null splits from the broad filter at both the BASE and TA stations, while only 242 non-null splits in total were found with the other four filters. Most of the splits calculated by CIELO-affiliated researchers at CIELO and TA stations fell into the lower range of frequencies (327 non-null splits were found at frequency bands below 0.5 Hz). Many splits and null splits have western backazimuths (180° to 360°) from subduction zones along the western boundary of the Pacific Plate (**Figure 3.3**). A mean of 20, 12, and 19 non-null splits were measured per station for the BASE, CIELO, and the

TA, respectively. The maximum number of splits for the BASE was at BH3E (50 splits), for CIELO it was at TB010 (37 splits), and for TA it was at I21A (71 splits). The BASE network had a minimum number of splits at BH4F and BHM1 (with 8 each), while the CIELO network had a minimum at TB028 (1 split), and the TA network had its minimum at I25A (5 splits).

In general, stations outside of the Powder River Basin have more non-null splits. In **Figure S3.3**, we show the percent of non-null splits for individual stations. The most obvious trend is that the southern Powder River Basin into the Black Hills has a lower percentage of non-null splits than elsewhere in the study region. One possible explanation for this is an increase in the amount of seismic noise: Ford et al. (2021) noted that using the USGS catalog, there were 428 mine blasts over the two-year period of the CIELO experiment (primarily in the eastern Powder River Basin, though the USGS had a cutoff of $M_L$ 2.5 so this may be an undercount). O'Rourke et al. (2016) used the BASE and TA data to find 1563 mine blasts in the region. The combination of basin structure and mining activity may increase the levels of ambient noise in the Powder River Basin.

We plot individual splitting measurements in **Figure 3.4** and color them according to backazimuth. A key observation of this study is the marked variations in fast direction and delay time with backazimuth. However, there is often good agreement in events coming from specific backazimuths at individual stations as well as regionally (see **Figures 3.8 and 3.9**). This collection of splits comes from independent analysis by the BASE and

CIELO-affiliated researchers, with differences both in the events utilized because of differences in the ranges of magnitudes and epicentral distances considered, and in the calculation of the splits because of differences in the frequency bands. To ensure that these differences do not have an impact on our understanding and interpretation of splitting in this region, we compared splits from the different groups in two ways. First, because 9 of the TA stations were used by both groups, we directly compare splitting parameters at those stations (**Figure 3.5**). Second, there were several groupings of stations that were in relatively close geographic proximity, so we compare splits across networks as well (**Figure 3.6**). A direct comparison of splits at TA stations indicates good agreement. For instance, both groups observed a change in splitting parameters with backazimuth at I21A (top row and third column of **Figure 3.5**): events coming from the southwest trend ~NW-SE, while those from the northwest rotate to a more E-W orientation. Splits measured at I22A, J20A, J21A, J22A, and J23A also feature a transition in the fast direction with backazimuth. Examining splits from different networks reveals similar consistency. For example, I21A, TB010, and BH3E all had a transition in fast direction from NW-SE at southwesterly backazimuths to more E-W fast direction at northwesterly backazimuths (**Figure 3.6**); they also had a rotation of fast direction to a more NE-SW orientation at events coming from close to 0° backazimuth. Overall, there is good agreement between different methodologies at TA stations and minor disagreement between results across networks. We conclude that the separate sets of splitting observations are consistent.

*3.2 Station Averages and backazimuthal variations*

Splits are often reported as station averages, which many researchers correlate with plate motion or geographic features within a region. In **Figure 3.7**, we show the arithmetic mean of the fast directions and delay times for all stations. If the only seismically anisotropic fabric in this region were that created by shearing at base of the lithosphere, then fast directions would mirror APM—in this region estimated to be N113W in a hotspot frame of reference (Gripp and Gordon, 2002). However, very few of these fast directions align with APM. We observe average fast directions in the east and west of the study area that trend northward with more variable direction in the center of the study region, particularly in the eastern Powder River Basin.

Such averaged splitting results obscure variations with backazimuth. However, complex, multilayered seismic ansitropy produces large and abrupt variations with backazimuth in both fast directions and splitting times (Levin et al., 1999) as is expected to be the case in older lithosphere or tectonically complex regions. Results from this study show strong variation with backazimuth (**Figure 3.4**), therefore we do not favor analysis based solely on station averages. We look for systematic variations in fast direction with backazimuth and then identify those backazimuthal bins that have the greatest number of splits, find the modal fast direction across the array, and examine the deviation of individual splits from the mathematical mode (see Section 3.4).

Although we find identify systematic variations of splitting parameters with backazimuth, clear trends are difficult to distinguish given the large amount of data (**Figure 3.4)**. To reduce the amount of data plotted in a single panel, we plot results from all stations in 90° bins from 0° to 360° (**Figure 3.8**). In the 0-90° bin, most splits across the array trend NE-SW, with some variation near the Bighorn Mountains (**Figure 3.8a**). From 90-180°, CIELO stations shift to a nearly W-E trend, while the BASE stations maintain a NE-SW trend (**Figure 3.8b**). This bin had the fewest splits from all networks, but the difference between the BASE and CIELO results may reflect a discontinuity in splitting parameters near a backazimuth of 150°. Splits from 180-270° trend NW-SE to the west of the Bighorn Mountains and east of the Black Hills and shift to N-S in the eastern Powder River Basin. Splits at stations north of the Bighorns have a noticeably smaller delay time and moderate heterogeneity for this bin. Finally, the bin with the most splits (270-360°) displays the most variability in fast direction and delay time.

**Figure 3.6** provides a more detailed view of backazimuthal variations for individual stations. For instance, at I22A splits in the 180° to 270° quadrant have a fast direction roughly NW-SE with small delay times, but splits in the 270° to 360° quadrant have a more variable fast direction and splitting times upwards of 1 second. Many of the splits coming from backazimuths close to 0° (such as at J21A, I21A, TB010, BH3E, I22A, and TB011) have fast directions that trend NE-SW with variable delay times; I21A, for example, shows uniform fast directions with delay times that vary significantly. Many stations have significant complexity in splitting parameters with backazimuth, exemplified by I21A:

while splits from 180° to 270° are generally oriented NW-SE, some are oriented E-W. Moving to the 270° to 360° quadrant, splits are highly variable in fast direction, ranging from NW-SE to E-W to NE-SW. TB010 and BH3E show a similar transition between fast directions from 270° to 360°, with fast directions changing quickly from NE-SW to more E-W.

*3.4 Deviation from backazimuthal modes*

As seen in **Figure 3.4**, most stations have a large variation in fast directions with backazimuth. We identified four distinct backazimuthal bins with data present: 130-170°, 220-270°, 290-330°, and 340-20°. Bins 220-270° and 290-330° have significantly more data than 130-170° or 340-20°. For each bin, we identified a modal fast direction for all splits. Splits from each of these bins were then plotted at their piercing point at 150 km (to separate splits and check for further geographic dependence), and were color coded according to how much their value deviated from the modal value for that bin (**Figure 3.10)**.

From 130° to 170° (**Figure 3.10a**), the modal fast direction is roughly 20°, which is 47° counterclockwise from apparent plate motion) with significant variation existing between the CIELO and the BASE stations. Given this pronounced difference we note that for both networks only one split within the corresponding backazimuth range is plotted for most stations and that these events vary in both backazimuth and epicentral distance, with events for the BASE coming from ~150° backazimuth and ~85° epicentral distance, while events

for CIELO come from ~140° backazimuth and ~120° epicentral distance. Therefore, fundamentally different ray paths sampled by the two networks most likely cause the variation, not a systematic difference between networks or analyses. In no other backazimuth range do we observe a systematic difference between CIELO and the BASE results, as shown in section 3.1 and **Figure 3.6**, which demonstrates that results for the BASE, CIELO and TA stations in geographic proximity generally agree well.

The modal fast direction from 220° to 270° is -60° (**Figure 3.10b**), which is approximately 60° from apparent plate motion. Of the 541 splits in this bin, 145 had a fast direction that deviated more than 15° from the modal fast direction. Splits that deviated the most from the mode are recorded in the eastern Powder River Basin, with a few to the west of the Bighorns. A similar deviation in splitting direction is observed in the 290-330° backazimuth bin (**Figure 3.10c**), where splits have an average fast direction of 90°, 23° clockwise from apparent plate motion. This bin also had the most splits, with 705. Of those, 207 had a deviation of 15° or more. As with the 220-270° bin, the splits with the largest deviations are within the Powder River Basin, east of the Bighorn Mountains in a NW-SE trending elongated region. In the 340-20° bin (**Figure 3.10d**) the modal fast direction is 50°—17° counterclockwise from apparent plate motion. 61 of 153 splits deviated 15° or more from the average fast direction, and do not display a clear geographical trend. This bin is the closest to APM.

## 4. Discussion

### *4.1 Comparison to other studies of seismic anisotropy in the region*

Our finding of complex seismic anisotropy within the Wyoming Craton agrees with multiple previous studies that observed similar complexity with coarser station spacing. Previous station-averaged splits show deviations of fast directions from plate motion direction in the eastern portion of the craton, suggesting multiple layers of seismic anisotropy in both the Trans-Hudson Orogen and Superior Craton (Hongsresawat et al., 2015). An aggregate study of seismic anisotropy also found a change in fast directions from the eastern Wyoming Craton to the Trans-Hudson Orogen, supporting the suggestion of multiple layers of both azimuthal and radial seismic anisotropy within the North American lithosphere more generally (Fouch and Rondenay, 2006). Anisotropic Ps receiver functions display clear evidence of multilayered seismic anisotropy in the Wyoming Craton, including within our study area at stations TA K22A and US RSSD (Ford et al., 2016). Multiple layers of azimuthal seismic anisotropy within the North American contient are supported by surface wave tomography, though in our study area this method predicts a smaller deviation from absolute plate motion than we observe (Yuan and Romanowicz, 2010). In the study most directly comparable to ours, station-averaged fast directions transition from more E-W in the Thunder Basin Block to NW-SE along the eastern margin of the Wyoming Craton, with a transition back to E-W in the Trans-Hudson Orogen (Yang et al., 2016). While we also observe changes in splitting parameters in the Thunder Basin Block, our station-averaged splits show a transition from fast directions oriented NNE outside of the Thunder Basin Block to NNW with more heterogeneity within it (**Figure**

**3.7**). Furthermore, Yang et al. (2016) used the minimum energy method: different methods for calculating shear wave splitting have been shown to yield different results (e.g., Vecsey et al., 2008).

It should be noted that shear wave splitting is a path-integrated observation: while it is assumed that the upper mantle is the primary contribution to seismic anisotropy in most continental regions, the crust (e.g., Kaneshima, 1990) and lowermost mantle (e.g., Lutz et al., 2020) can contribute as well. A Ps receiver function analysis with TA data across the continental U.S. found an abrupt transition in the signal of apparent, high-amplitude crustal seismic anisotropy (or possibly isotropic dipping structure) in the western U.S. to low values east of the Rocky Mountain Front (Schulte-Pelkum and Mahan, 2014). In our study area, this transition to low delay times is spatially complex because high delay times persist to the eastern edge of the Black Hills, suggesting that crustal seismic anisotropy may affect our shear wave splitting results, though an analysis of Ps receiver functions with the BASE and CIELO data is needed in order to fully test this possibility. Regarding the lower mantle, we did not have a sufficient number of SKS-SKKS pairs recorded for the same wave at the same receiver (which have divergent paths in the lowermost mantle) to determine whether there is a significant contribution to shear wave splitting from lowermost mantle depths (**Figure S3.4**). However, previous studies have determined the potential presence of seismic anisotropy within the D" layer beneath western North America (e.g., Lutz et al., 2020), suggesting that lower mantle seismic anisotropy should be considered more carefully in future work.

*4.2 Implications for the structure and evolution of the eastern Wyoming Craton*

A comparison of the fabrics of Precambrian rocks to the strike of Laramide orogens in Wyoming suggests that mechanical anisotropy within the crust and lithosphere may have guided the orientation of deformation during the Laramide (Bader, 2019). The best agreement between the structural and seismic data occurs in the Owl Creek Fault Zone, where basement fabrics exhibit a strike close to WNW-ESE. Average fast directions at stations in this region (TB009, J21A, and BH4C; **Figure 3.6**) all exhibit similar orientations, with excellent agreement for backazimuths of ~240° and a counterclockwise offset of the fast directions from the fabrics of only ~20° for backazimuths of ~300° (**Figure 3.6**). In contrast, the N-S oriented splits in the central Bighorns (see **Figure 3.7**) do not agree well with the orientations of any of the reported fabrics from Bader (2019), even though these orientations are highly variable in this region. There are several Proterozoic dikes throughout the Bighorn Mountains: these are generally oriented NE-SW in the southern Bighorn Mountains, and either NE-SW or NW-SE in the northern Bighorn Mountains (Bader, 2019). In the Bighorn Mountains, average fast directions for the BASE and TA stations are N-S, and so again do not agree well with the structural data. Station BH4D from the BASE has an average fast direction oriented more NE-SW, but is not close to any known dikes. Fabric orientations are not available in the Powder River Basin because thick sedimentary deposits cover the Precambrian rocks. We hypothesize that the seismic anisotropy responsible for the splitting in the Owl Creek fault zone is crustal and

related to mechanical anisotropy in the basement, but that the predominant patterns of splitting across the rest of the region reflect structures in the mantle.

One of the main purposes of this study is to utilize observations of seismic anisotropy to constrain the evolution of the eastern margin of the Wyoming Craton. Previous studies utilizing the BASE data (Worthington et al, 2015; Yeck et al., 2014) observed a clear transition in the structure of the crust coincident with the eastern edge of the of the Bighorn arch, roughly coincident with our observed change in average splitting parameters and the region with the most splits deviating from the mode (**Figures 3.7 and 3.9**). More specifically, Worthington et al. (2015) observed a west dipping reflection boundary and modeled a sharp magnetic contact immediately east of the Bighorn Arch, which they hypothesized represents a suture zone between the Wyoming Craton and Proterozoic orogens to the east. Building on this interpretation, Kilian et al. (2016) present a model in which the Black Hills represent an exotic block within the Black Hills/Dakotan Orogen, with the eastern boundary of the Wyoming Craton again sitting immediately east of the Bighorn Arch. However, in a comment in response to Kilian et al. (2016), Hrncir et al. (2017) argue that the Black Hills reliably record a maintained connection to the rest of the Wyoming Craton throughout the Proterozoic and that the suture zone imaged by Worthington et al. (2015) more likely corresponds to a suture of Neoarchean age. Such an explanation might help to reconcile the geophysical evidence of Worthington et al. (2015) while allowing for an interpretation in which the presence of the North American Central Plains Anomaly marks the remnants of oblique subduction zones formed during the Trans-

Hudson Orogen (Bedrosian and Finn, 2021). While our results cannot confirm or deny the presence of either a more westerly border to the Wyoming Craton or an ancient Neoarchean suture, the relatively good agreement between our results and others suggests that at least one of these features may explain our observations. However, one potential complexity that would need to be explained if either mechanism is favored is why the changes in splitting behavior are concentrated within the Powder River Basin (**Figure 3.10**), and do not extend further east beneath the Black Hills.

A recent attenuation study (Zhu et al., 2021) found variations in the attenuation of teleseismic *P* phases recorded within the eastern Wyoming Craton as part of the CIELO study: higher attenuation occurs in orogens (i.e., the Bighorn Mountains and Black Hills) and lower attenuation occurs in the corresponding basins (i.e., the Bighorn Basin and the Powder River Basin). The Powder River Basin only exhibits low attenuation in the eastern half that abuts the Black Hills. The transition within this basin is roughly coincident with the transition in splitting parameters that we observe here. A comparison with our shear wave splitting results between 290° and 330° backazimuth (**Figure 3.10c**) shows that the region of lower attenuation within the Powder River Basin roughly coincides with splits with the largest deviation from modal fast direction—which holds true for two backazimuthal bins (220°-270° and 290°-330°). Interestingly, in the Bighorn Basin (which has similarly low attenuation), our splits do not generally have a large deviation from modal fast direction. This is not due to differences in methodology (see Section 3.1), but instead

likely represents a robust change in the seismically anisotropic fabric moving from west of the Bighorn Mountains east into the Powder River Basin.

The extent which the Wyoming Craton may have recently experienced a weakening or strengthening mantle lithosphere is actively debated. One line of evidence possibly pointing to decratonization is evidence for currently delaminating lithosphere from regional two plane wave tomography (Dave and Li, 2016). Further, xenolith data from the northern part of the Wyoming Craton indicate that Eocene kimberlites sampled metasomatized mantle lithosphere, hypothesized to be a result of interaction with the Farallon slab during the Laramide Orogeny (Carlson et al., 2004). The path of the Farallon slab is predicted to be beneath the eastern portion of the Wyoming Craton by ~65 Ma (Humphreys et al., 2015)—providing a means to hydrate the crust and lithosphere along the eastern margin of the craton. In this scenario, the recent evolution of the Wyoming Craton reflects that of the North China Craton, which was destabilized during the Mesozoic by interaction with a subducting slab (e.g., Huang et al., 2021; Kusky et al., 2014; Lei, 2012; Zhao et al., 2012; Zhu et al., 2012).

Zhu et al., (2021), however, argue that the attenuation beneath the Powder River Basin is suggestive of thick, strong lithosphere—which could be either a remnant of or addition to the craton. Variations in lithospheric thickness between mountains and basins are the most likely explanation for the variations in attenuation, with thinner lithosphere located beneath the ranges and thicker lithosphere located beneath the basins, which is difficult to explain

with localized and rapidly convecting lithospheric drips as might be expected in a decratonization model. In the recratonization model, a layer of oceanic lithosphere beneath the Wyoming Craton was attached to the base of the Wyoming Craton beneath the Powder River Basin around ~70 Ma (Humphreys et al., 2015). Given that this allochthonous lithosphere would likely have its own seismically anisotropic fabric, this scenario could help explain the complex splitting we observe. Alternatively, the thickened, strong lithosphere could be original to the craton and is surrounded by thinned, weaker lithosphere. Given the dearth of tectonism in the region between the Trans-Hudson and Laramide Orogenies (Blackburn et al., 2012), the rheological contrast between orogens and basins may date back to the Proterozoic unless the subduction of the Farallon slab prior to the Laramide Orogeny weakened the locations of the future orogens. In either case, variations in lithospheric strength between thicker and thinner lithosphere in the region may have then led to the formation of the Black Hills and Bighorn Mountains (Zhu et al., 2021).

Our splitting results are more consistent with the recratonization than decratonization model. The pattern of splitting we observed does not exhibit either the delay time reduction attributed to lithospheric drips in previous studies (e.g., West et al., 2009) nor the radial pattern of fast directions that mirrors the pattern of mantle flow in some geodynamic simulations of dripping lithosphere (Elkins-Tanton, 2007). Regardless of the pattern in the fast direction, there is also no clear minimum in splitting times that would be expected to occur above the lithospheric drip. In the context of this study, the presence of thicker

lithosphere beneath the Powder River Basin may indicate the potential for more variable/complex seismic anisotropy due to lithospheric layering (Fouch and Rondenay, 2006; Levin and Park, 1999). Topography of the lithosphere-asthenosphere boundary may also help to explain changes in splitting parameters with backazimuth, as in this model different stations lie above lithospheric blocks with distinct histories and internal structures, similar to instances where different tectonic terranes are situated next to one another (e.g., Levin et al., 1999; Lopes et al., 2020). A layer of oceanic lithosphere beneath the Wyoming Craton (as in the model of Humphreys et al., 2015) with a distinct seismically anisotropic fabric could contribute to the complex splitting we observe. However, the predicted areal extent of the Shatsky Conjugate is far larger than the region of anomalous splits we identify in this study.

## 5. Conclusions

In this study, we generate shear wave splitting results from three separate temporary networks (BASE, CIELO, and TA), two of which are newly reported, in order to image variations in seismic anisotropy along the eastern margin of the Wyoming Craton at an unprecedented regional scale. Our results confirm the presence of complex, backazimuthally dependent splitting, indicating the presence of multiple layers of seismic anisotropy. While further work is needed to constrain the number and geometry of these layers, the findings appear to be robust given the agreement between results using different methods and data sets. Critically, our laterally dense station spacing allows us to constrain a clear change in splitting parameters within the Powder River Basin, with splits to the east

and west of the basin resembling one another. These changes in splitting are roughly coincident with other geophysical constraints from active source and potential field modeling (Worthington et al., 2015) and seismic attenuation analysis (Zhu et al., 2021), which indicate the presence of pronounced structural and rheologic variations within the eastern Wyoming Craton. While speculative, we argue that the variations in splitting may be the result of either a change in seismic anisotropy at the eastern margin of the Wyoming Craton (e.g., Worthington et al., 2015; Kilian et al., 2016), a change in seismic anisotropy at a Neoarchean-aged boundary within the Wyoming Craton (e.g., Hrncir et al., 2017), or is related to some other rheologic heterogeneity that pre-dates the Laramide Orogeny (Zhu et al., 2021). It is possible that our results reflect a combination of these scenarios. Most importantly, our results help to further demonstrate that the Wyoming Craton, and more specifically the eastern Wyoming Craton, is a seismically complex region with laterally varying structure.

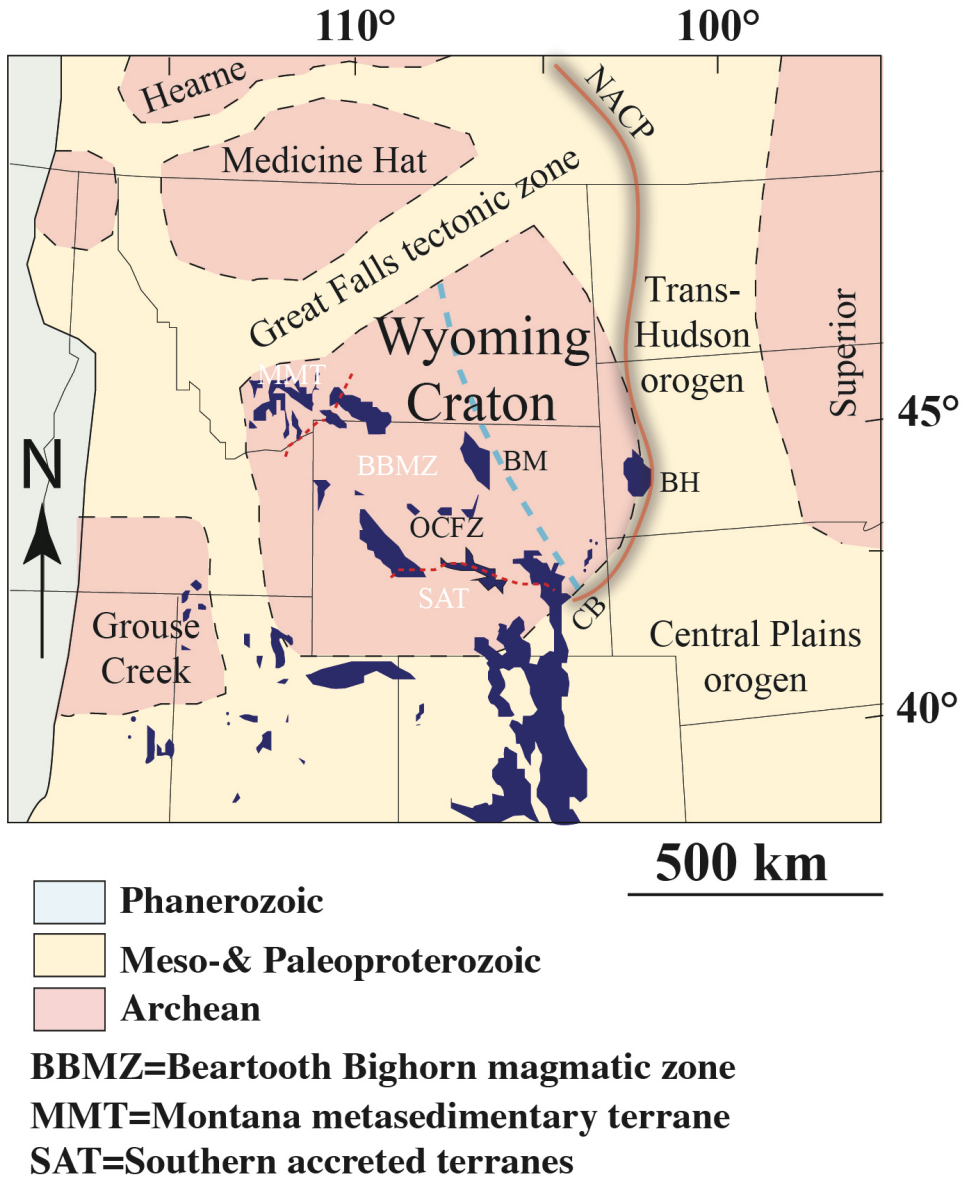


**Figure 3.1:** Map of major tectonic terranes within and surrounding our study area. Dark blue regions are basement-cored Laramide uplifts. Two potential boundaries for the Wyoming Craton are shown: the dashed cyan line is the more westerly boundary proposed by Worthington et al. (2016), while the black dashed line further to the east is from Foster et al. (2006). Modified from Bedle et al. (2021a). BH—Black Hills; BM—Bighorn Mountains; OCFZ—Owl Creek Fault Zone.

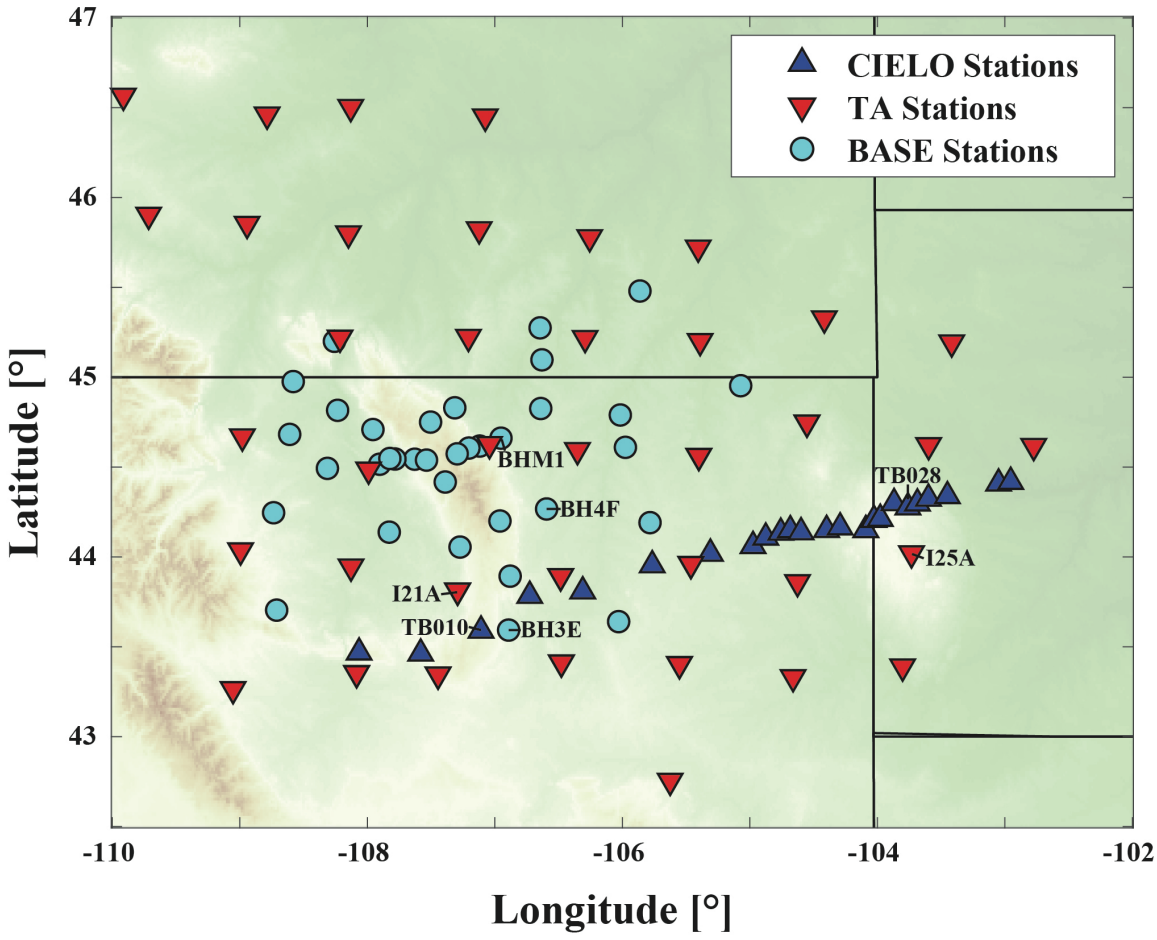


**Figure 3.2:** Map with all stations used in this study. Cyan circles are from the BASE deployment, blue triangles from the CIELO deployment, and red inverted triangles from the TA deployment.

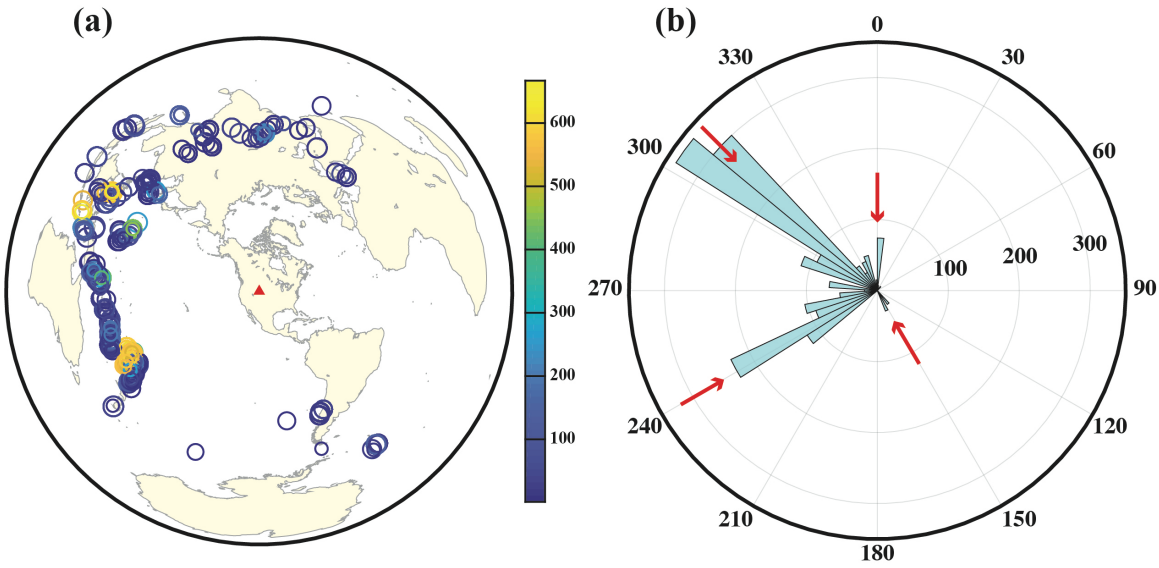


**Figure 3.3: (a)** Geographic distribution of events used in this study. Size of circles are scaled according to the magnitude of earthquakes, while color corresponds to depth of the event. The red triangle is located roughly in the center of the Wyoming Craton (at station TB010). **(b)** Polar histogram of the backazimuthal distribution of events used in this study. Note that the vast majority of events used come from the more westerly backazimuths. Red arrows indicate center of bins displayed in **Figure 3.9**.

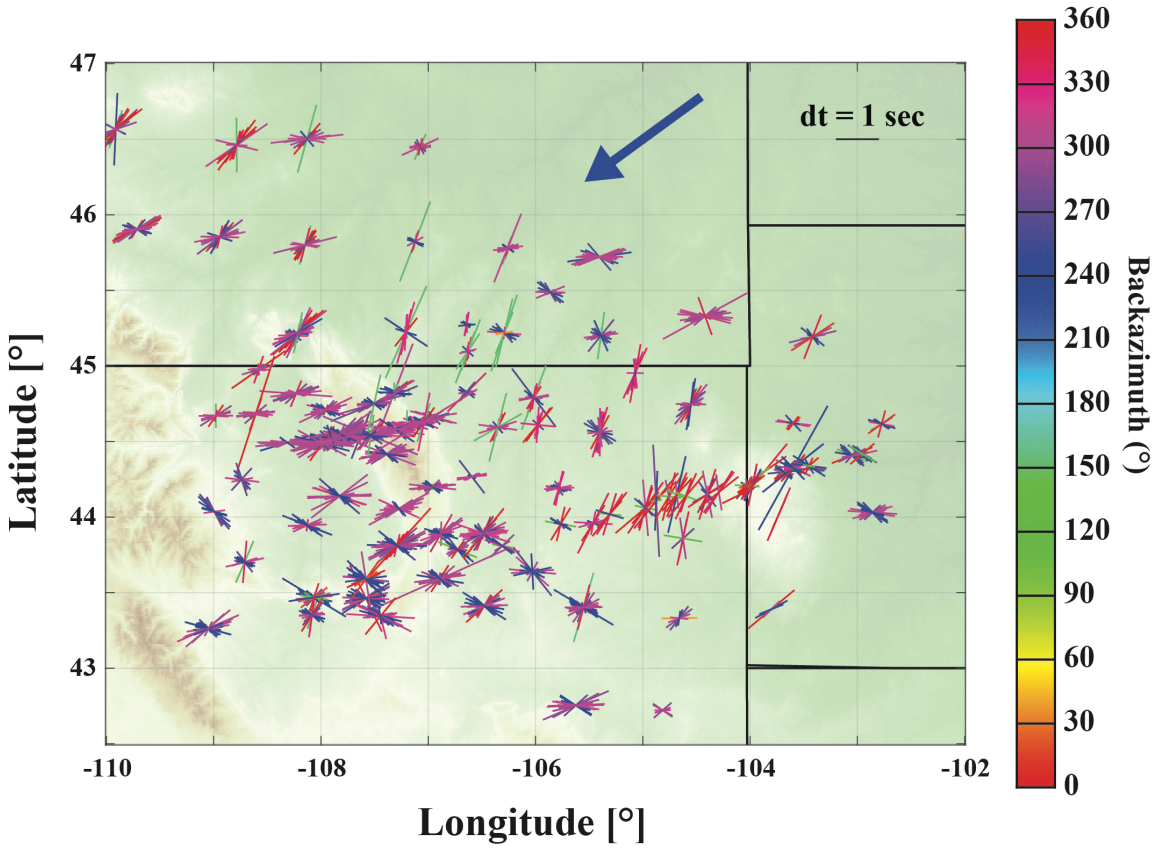


**Figure 3.4:** Map of splitting parameters by backazimuth. Orientation of bars is the fast direction, length the delay time, and color the backazimuth. An example split with a fast direction of 90° and a delay time of 1 second is shown in the upper left corner. The large blue arrow is APM for this region.

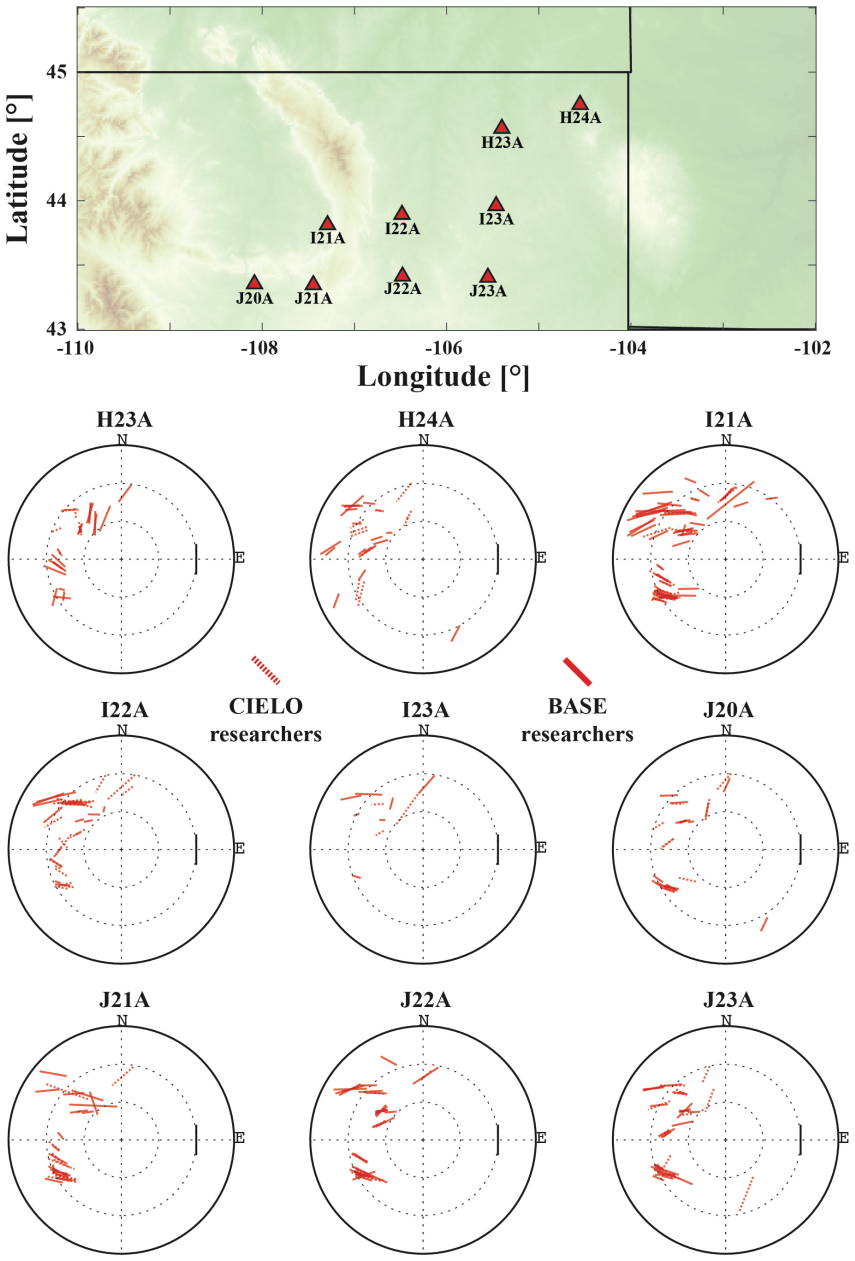


**Figure 3.5:** Comparison of splits calculated at TA stations by both research groups. Length of the bars is the delay time, and the orientation is the fast direction. Splits are plotted at their backazimuth (around the circle) and inclination (from the center, starting at 0° and moving out at 5° increments). Solid lines were calculated by BASE researchers, while dashed lines were calculated by CIELO researchers. Black line at 90° backazimuth and 10° inclination is an example split with a fast direction of 0° and a delay time of 1 second.

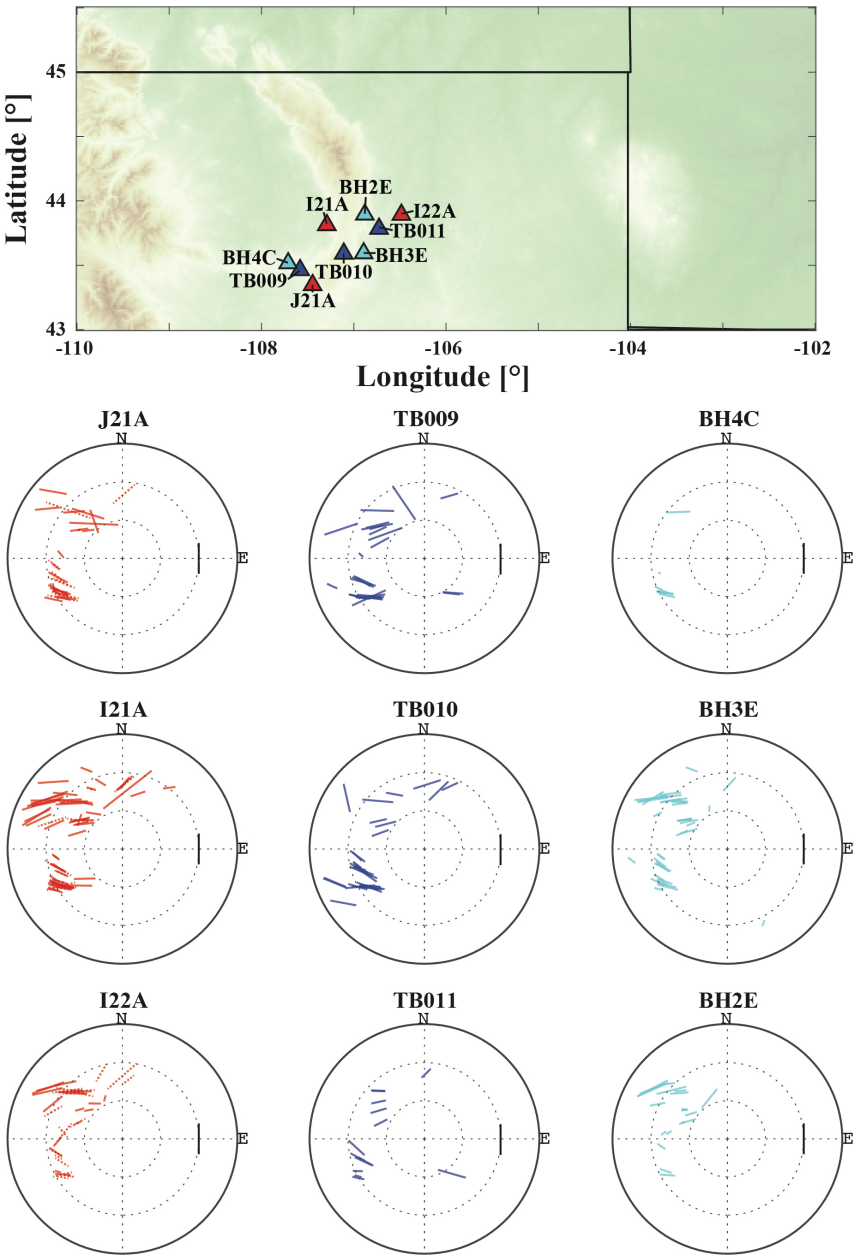


**Figure 3.6:** Comparison of splits at stations in geographic proximity from BASE, CIELO, and TA deployments. Stereoplots same as in ta_comp. For the left column (TA stations), solid lines were calculated by BASE researchers, while dashed lines were calculated by CIELO researchers. The middle column are CIELO splits, and the right column are BASE splits.

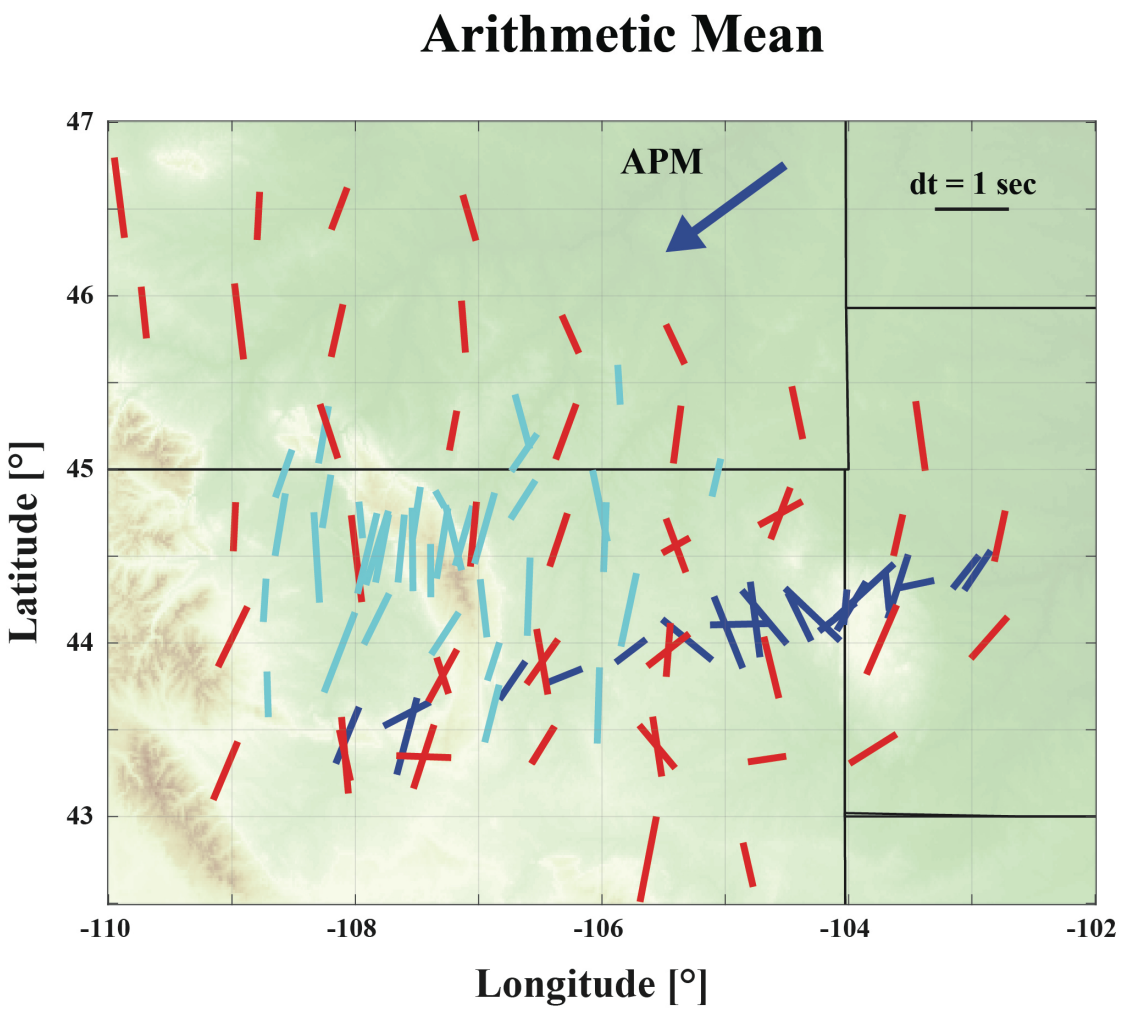


**Figure 3.7:** Average splitting parameters for all stations. Cyan splits are BASE stations, blue splits from CIELO, and red splits from TA. Several TA stations had splits calculated by both teams of researchers: where there are differences in the average fast direction, it is most likely due to splits from different backazimuths, rather than differences in methodology between groups (see **Figure 3.5** and **Figure 3.6**).

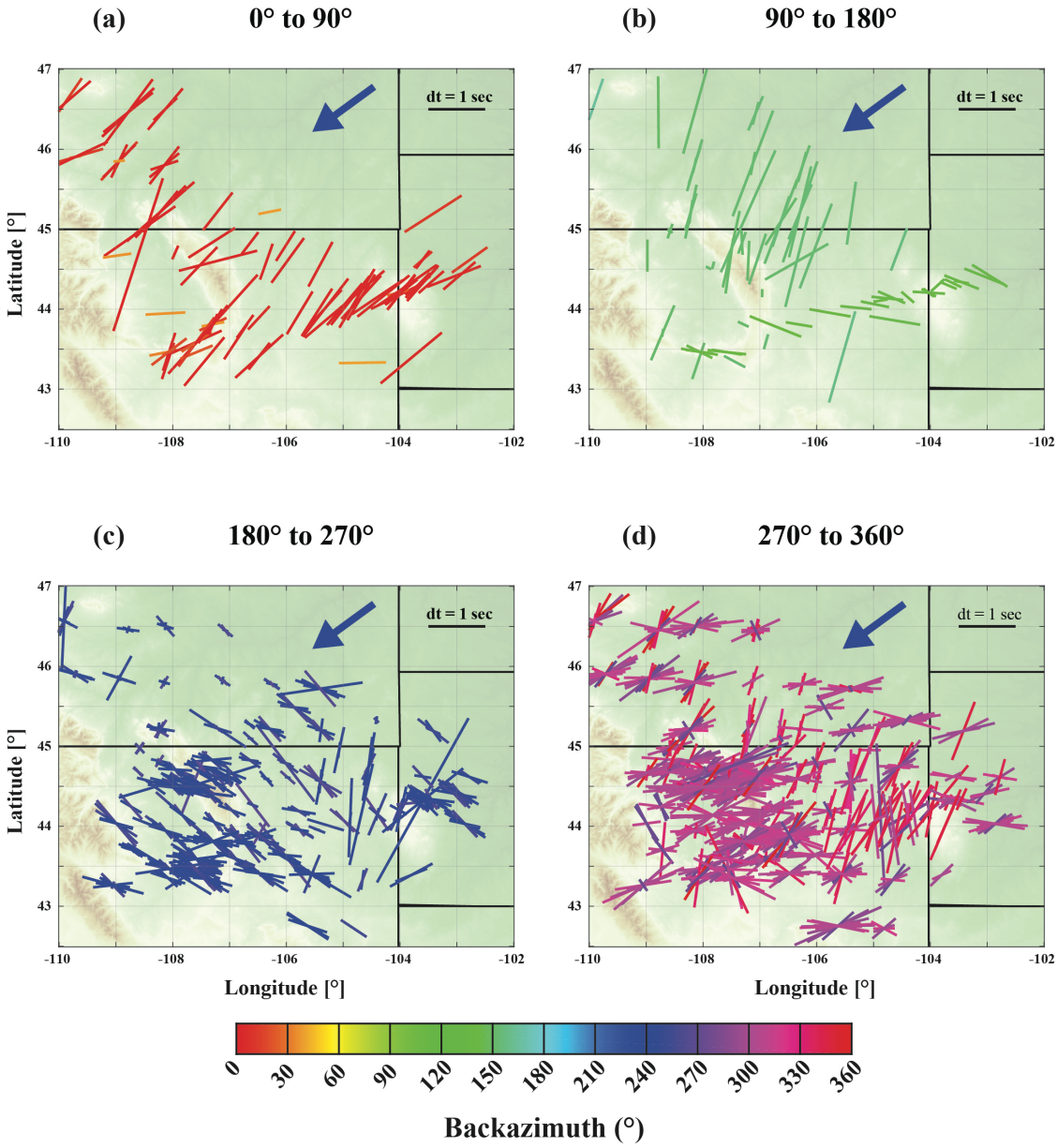


**Figure 3.8:** Splits plotted in 90° backazimuthal bins. Most splits come from the more westerly backazimuths (180° to 360°). An example split with a fast direction of 90° and a delay time of 1 second is plotted in the upper left corner.

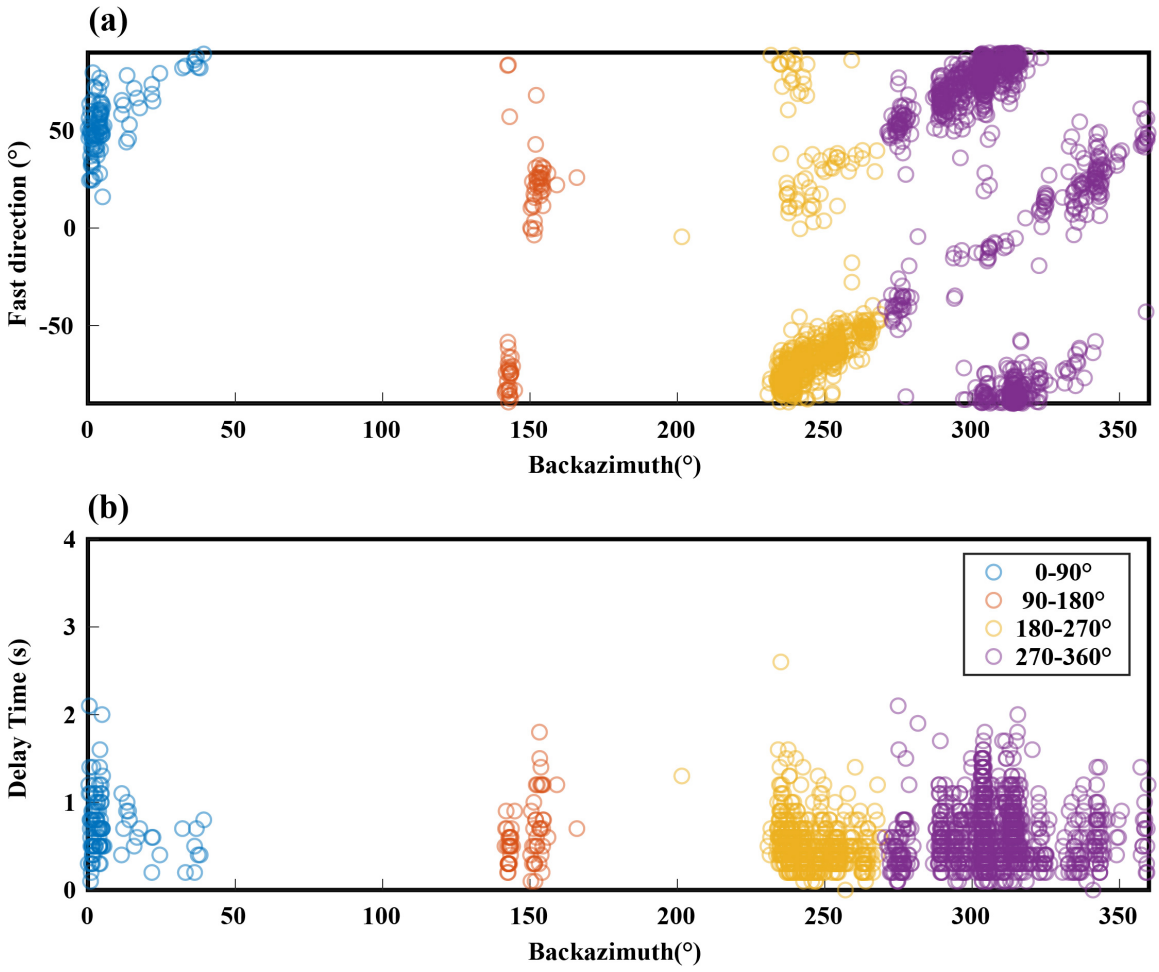


**Figure 3.9: (a)** Fast direction for all non-null splits against backazimuth. **(b)** Delay time for all non-null splits against backazimuth. Both are color-coded by bins shown in **Figure 3.8.**

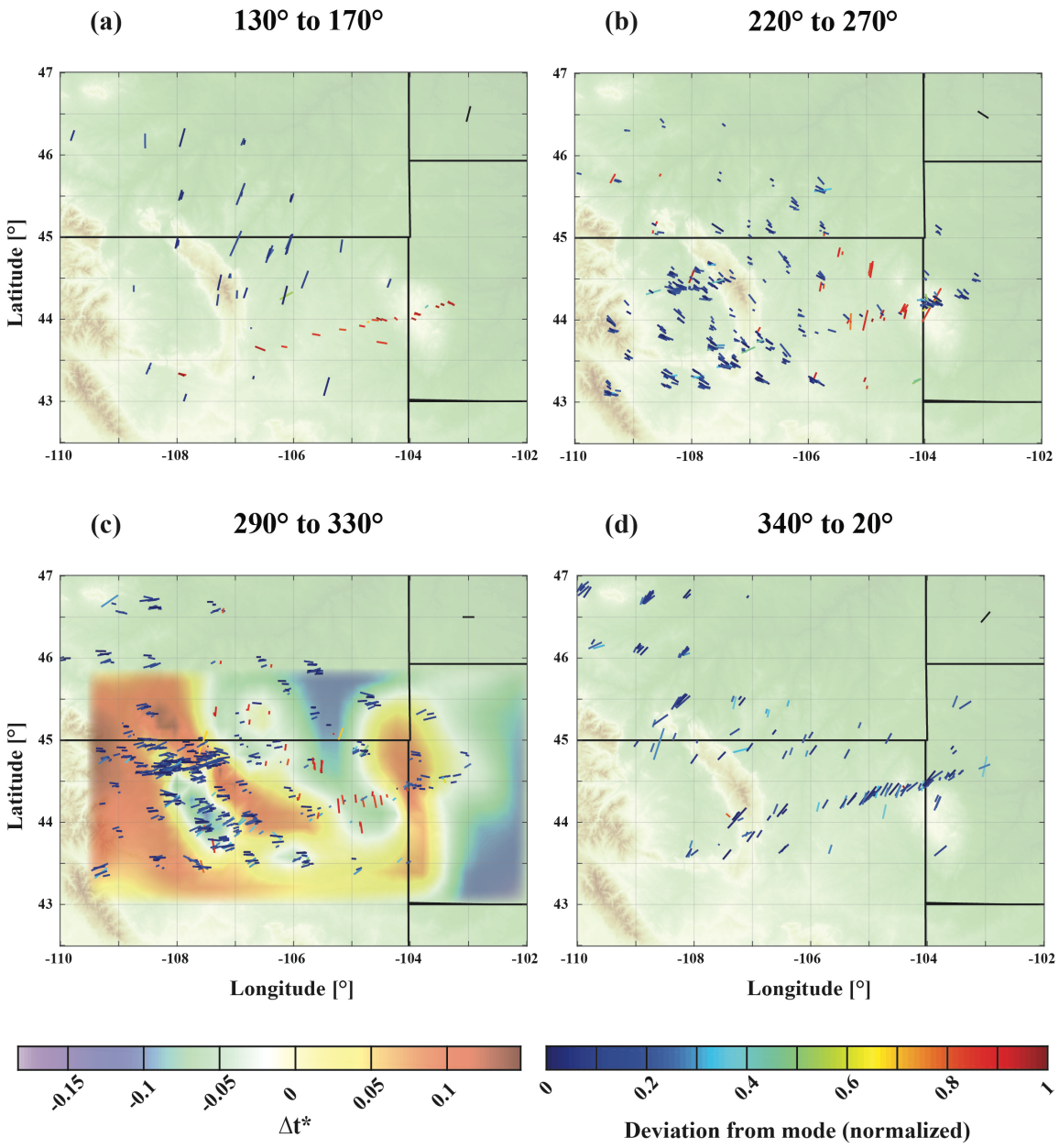


**Figure 10:** Splits plotted in the four backazimuthal bins with the most splits (see **Figure 3**). Splits are plotted at the piercing point at 150 km depth to separate splits and show geographic dependence. Color of splits corresponds to the deviation between the modal fast direction of each bin and the fast direction for individual splits. In panel (c) we plot our splits against the attenuation model of Zhu et al. (2021).

## References


Allmendinger, R. W., Brewer, J. A., Brown, L. D., Kaufman, S., Oliver, J. E., & Houston, R. S. (1982). COCORP profiling across the Rocky Mountain Front in southern Wyoming, Part 2: Precambrian basement structure and its influence on Laramide deformation. *Geological Society of America Bulletin*, *93*(12), 1253-1263.

Anderson, M. L., Porter, R. C., Yeck, W. L., Sheehan, A. F., Beck, S. L., & Gilbert, H. J. (2014, December). Contrasting lithospheres: does one size fit all for the structure of mantle under foreland arches?. In *AGU Fall Meeting Abstracts* (Vol. 2014, pp. T23A-4639).

Bader, J. W. (2019). Structural inheritance and the role of basement anisotropies in the Laramide structural and tectonic evolution of the North American Cordilleran foreland, Wyoming. *Lithosphere*, *11*(1), 129-148.

Bedle, H., Cooper, C. M., & Frost, C. D. (2021a). Nature versus Nurture: Preservation and destruction of Archean cratons. *Tectonics*, *40*(9), e2021TC006714.

Bedle, H., Lou, X., & Van der Lee, S. (2021b). Continental Tectonics Inferred From High-Resolution Imaging of the Mantle Beneath the United States, Through the Combination of USArray Data Types. *Geochemistry, Geophysics, Geosystems*, *22*(10), e2021GC009674.

Bedrosian, P. A., & Finn, C. A. When Wyoming became Superior: Oblique Convergence along the Southern Trans-Hudson Orogen. *Geophysical Research Letters*, e2021GL092970.

Becker, T. W., Lebedev, S., & Long, M. D. (2012). On the relationship between azimuthal anisotropy from shear wave splitting and surface wave tomography. *Journal of Geophysical Research: Solid Earth*, *117*(B1).

Boerner, D. E., Craven, J. A., Kurtz, R. D., Ross, G. M., & Jones, F. W. (1998). The Great Falls Tectonic Zone: suture or intracontinental shear zone?. *Canadian Journal of Earth Sciences*, *35*(2), 175-183.

Bowman, J. R., & Ando, M. (1987). Shear-wave splitting in the upper-mantle wedge above the Tonga subduction zone. *Geophysical Journal International*, *88*(1), 25-41.

Burdick, S., van der Hilst, R. D., Vernon, F. L., Martynov, V., Cox, T., Eakins, J., ... & Pavlis, G. L. (2012). Model update March 2011: Upper mantle heterogeneity beneath North America from traveltime tomography with global and USArray Transportable Array data. *Seismological Research Letters*, *83*(1), 23-28.

Camfield, P. A., & Gough, D. I. (1977). A possible Proterozoic plate boundary in North America. *Canadian Journal of Earth Sciences*, *14*(6), 1229-1238.

Carlson, R. W., Irving, A. J., Schulze, D. J., & Hearn Jr, B. C. (2004). Timing of Precambrian melt depletion and Phanerozoic refertilization events in the lithospheric mantle of the Wyoming Craton and adjacent Central Plains Orogen. *Lithos*, *77*(1-4), 453-472.

Chamberlain, K. R., Bauer, R. L., Frost, B. R., & Frost, C. D. (2002). Dakotan Orogen: Continuation of Trans-Hudson Orogen or younger, separate suturing of Wyoming and Superior cratons. In *Geological Association of Canada–Mineralogical Association of Canada, Abstracts* (Vol. 27, p. 18).

Chamberlain, K. R., Frost, C. D., & Frost, B. R. (2003). Early Archean to Mesoproterozoic evolution of the Wyoming Province: Archean origins to modern lithospheric architecture. *Canadian Journal of Earth Sciences*, *40*(10), 1357-1374.

Chamberlain, K. R., Kilian, T. M., Evans, D. A., Bleeker, W., & Cousens, B. L. (2017). Wyoming on the run—Toward final Paleoproterozoic assembly of Laurentia: REPLY. *Geology*, *45*(4), e412-e412.

Chevrot, S. (2000). Multichannel analysis of shear wave splitting. *Journal of Geophysical Research: Solid Earth*, *105*(B9), 21579-21590.

Coney, P. J., & Reynolds, S. J. (1977). Cordilleran benioff zones. *Nature*, *270*(5636), 403-406.

Cooper, C. M., Lenardic, A., & Moresi, L. (2004). The thermal structure of stable continental lithosphere within a dynamic mantle. *Earth and Planetary Science Letters*, *222*(3-4), 807-817.

Crosswhite, J. A., & Humphreys, E. D. (2003). Imaging the mountainless root of the 1.8 Ga Cheyenne belt suture and clues to its tectonic stability. *Geology*, *31*(8), 669-672.

Dahl, P. S., Hark, J. S., FreiI, R., Ghosh, A. K., Whitehouse, M. J., & Wooden, J. L. (2010, April). More Evidence that the Black Hills Domain was originally part of the Archean Wyoming Craton: occurrences of 3.8-2.6 Ga detrital zircons in 2.5-1.9 Ga metasedimentary rocks. In *Geological Society of America Abstracts with Programs,* (Vol. 42, No. 3, p. 46).

Dahl, P. S., Holm, D. K., Gardner, E. T., Hubacher, F. A., & Foland, K. A. (1999). New constraints on the timing of Early Proterozoic tectonism in the Black Hills (South Dakota), with implications for docking of the Wyoming province with Laurentia. *Geological Society of America Bulletin*, *111*(9), 1335-1349.

Dave, R., & Li, A. (2016). Destruction of the Wyoming craton: Seismic evidence and geodynamic processes. *Geology*, *44*(11), 883-886.

Deng, J., Long, M. D., Creasy, N., Wagner, L., Beck, S., Zandt, G., ... & Minaya, E. (2017). Lowermost mantle anisotropy near the eastern edge of the Pacific LLSVP: constraints from SKS–SKKS splitting intensity measurements. *Geophysical Journal International*, *210*(2), 774-786.

Duebendorfer, E. M., & Houston, R. S. (1987). Proterozoic accretionary tectonics at the southern margin of the Archean Wyoming craton. *Geological Society of America Bulletin*, *98*(5), 554-568.

Eakin, C. M., & Long, M. D. (2013). Complex anisotropy beneath the Peruvian flat slab from frequency-dependent, multiple-phase shear wave splitting analysis. *Journal of Geophysical Research: Solid Earth*, *118*(9), 4794-4813.

Egan, S. S., & Urquhart, J. M. (1993). Numerical modelling of lithosphere shortening: application to the Laramide erogenic province, western USA. *Tectonophysics*, *221*(3-4), 385-411.

Elkins-Tanton, L. T. (2007). Continental magmatism, volatile recycling, and a heterogeneous mantle caused by lithospheric gravitational instabilities. *Journal of Geophysical Research: Solid Earth*, *112*(B3).

Erslev, E. A., & Rogers, J. L. (1993). Basement-cover geometry of Laramide fault-propagation folds.

Ford, H. A., Bezada, M. J., Byrnes, J. S., Birkey, A., & Zhu, Z. (2021). The CIELO Seismic Experiment. *Seismological Research Letters*.

Ford, H. A., Long, M. D., & Wirth, E. A. (2016). Midlithospheric discontinuities and complex anisotropic layering in the mantle lithosphere beneath the Wyoming and Superior Provinces. *Journal of Geophysical Research: Solid Earth*, *121*(9), 6675-6697.

Fouch, M. J., & Rondenay, S. (2006). Seismic anisotropy beneath stable continental interiors. *Physics of the Earth and Planetary Interiors*, *158*(2-4), 292-320.

Frost, C. D., & Fanning, C. M. (2006). Archean geochronological framework of the Bighorn Mountains, Wyoming. *Canadian Journal of Earth Sciences*, *43*(10), 1399-1418.

Gorman, A. R., Clowes, R. M., Ellis, R. M., Henstock, T. J., Spence, G. D., Keller, G. R., ... & Miller, K. C. (2002). Deep Probe: imaging the roots of western North America. *Canadian Journal of Earth Sciences*, *39*(3), 375-398.

Gripp, A. E., & Gordon, R. G. (2002). Young tracks of hotspots and current plate velocities. *Geophysical Journal International*, *150*(2), 321-361.

Hrncir, J. A., & Karlstrom, K. E. Origins of the Black Hills Terrane in the Eastern Wyoming Craton.

Hrncir, J., Karlstrom, K., & Dahl, P. (2017). Wyoming on the run—Toward final Paleoproterozoic assembly of Laurentia: COMMENT. *Geology*, *45*(4), e411-e411.

Hongsresawat, S., Panning, M. P., Russo, R. M., Foster, D. A., Monteiller, V., & Chevrot, S. (2015). USArray shear wave splitting shows seismic anisotropy from both lithosphere and asthenosphere. *Geology*, *43*(8), 667-670.

Huang, Z., Gou, T., & Wang, L. (2021). P and S wave tomography of east-central China: insight into past and present mantle dynamics. *Tectonophysics*, *809*, 228859.

Humphreys, E. D., Schmandt, B., Bezada, M. J., & Perry-Houts, J. (2015). Recent craton growth by slab stacking beneath Wyoming. *Earth and Planetary Science Letters*, *429*, 170-180.

Kaneshima, S. (1990). Origin of crustal anisotropy: Shear wave splitting studies in Japan. *Journal of Geophysical Research: Solid Earth*, *95*(B7), 11121-11133.

Karlstrom, K. E., & Houston, R. S. (1984). The Cheyenne belt: Analysis of a Proterozoic suture in southern Wyoming. *Precambrian Research*, *25*(4), 415-446.

Kilian, T. M., Chamberlain, K. R., Evans, D. A., Bleeker, W., & Cousens, B. L. (2016). Wyoming on the run—Toward final Paleoproterozoic assembly of Laurentia. *Geology*, *44*(10), 863-866.

Kusky, T. M., Windley, B. F., Wang, L., Wang, Z., Li, X., & Zhu, P. (2014). Flat slab subduction, trench suction, and craton destruction: Comparison of the North China, Wyoming, and Brazilian cratons. *Tectonophysics*, *630*, 208-221.

Lei, J. (2012). Upper-mantle tomography and dynamics beneath the North China Craton. *Journal of Geophysical Research: Solid Earth*, *117*(B6).

Levin, V., Menke, W., & Park, J. (1999). Shear wave splitting in the Appalachians and the Urals: a case for multilayered anisotropy. *Journal of Geophysical Research: Solid Earth*, *104*(B8), 17975-17993.

Livaccari, R. F., Burke, K., & Şengör, A. M. C. (1981). Was the Laramide orogeny related to subduction of an oceanic plateau?. *Nature*, *289*(5795), 276-278.

Lopes, E., Long, M. D., Karabinos, P., & Aragon, J. C. (2020). SKS splitting and upper mantle anisotropy beneath the southern New England Appalachians: Constraints from the dense SEISConn array. *Geochemistry, Geophysics, Geosystems*, *21*(12), e2020GC009401.

Lutz, K. A., Long, M. D., Creasy, N., & Deng, J. (2020). Seismic anisotropy in the lowermost mantle beneath North America from SKS-SKKS splitting intensity discrepancies. *Physics of the Earth and Planetary Interiors*, *305*, 106504.

McCombs, J. A., Dahl, P. S., & Hamilton, M. A. (2004). U–Pb ages of Neoarchean granitoids from the Black Hills, South Dakota, USA: implications for crustal evolution in the Archean Wyoming province.

McQueen, H. W. S., & Beaumont, C. (1989). Mechanical models of tilted block basins. *Origin and Evolution of Sedimentary Basins and Their Energy and Mineral Resources, Geophys. Monogr*, *48*, 65-71.

Mueller, P. A., & Frost, C. D. (2006). The Wyoming Province: a distinctive Archean craton in Laurentian North America. *Canadian Journal of Earth Sciences*, *43*(10), 1391-1397.

Obrebski, M., Allen, R. M., Pollitz, F., & Hung, S. H. (2011). Lithosphere–asthenosphere interaction beneath the western United States from the joint inversion of body-wave traveltimes and surface-wave phase velocities. Geophysical Journal International, 185(2), 1003-1021.Precambrian Research, 130(1-4), 161-184.

O'Rourke, C. T., Sheehan, A. F., Erslev, E. A., & Anderson, M. L. (2016). Small-magnitude earthquakes in north-central Wyoming recorded during the Bighorn Arch Seismic Experiment. *Bulletin of the Seismological Society of America*, *106*(1), 281-288.

Peterson, J. R. (1993). *Observations and modeling of seismic background noise* (No. 93-322). US Geological Survey.

Pollack, H. N. (1986). Cratonization and thermal evolution of the mantle. *Earth and Planetary Science Letters*, *80*(1-2), 175-182.

Saleeby, J. (2003). Segmentation of the Laramide slab—Evidence from the southern Sierra Nevada region. *Geological Society of America Bulletin*, *115*(6), 655-668.

Savage, M. K. (1999). Seismic anisotropy and mantle deformation: what have we learned from shear wave splitting?. *Reviews of Geophysics*, *37*(1), 65-106.

Scheevel, J. R. (1983). Horizontal compression and a mechanical interpretation of Rocky Mountain Foreland Deformation.

Schmandt, B., & Humphreys, E. (2010). Complex subduction and small-scale convection revealed by body-wave tomography of the western United States upper mantle. *Earth and Planetary Science Letters*, *297*(3-4), 435-445.

Schmandt, B., & Lin, F. C. (2014). P and S wave tomography of the mantle beneath the United States. *Geophysical Research Letters*, *41*(18), 6342-6349.

Schulte-Pelkum, V., & Mahan, K. H. (2014). A method for mapping crustal deformation and anisotropy with receiver functions and first results from USArray. *Earth and Planetary Science Letters*, *402*, 221-233.

Sheehan, A. (2011, September). Imaging the Roots of the Rocky Mountains: The EarthScope Bighorn Project. In *2011 SEG Annual Meeting*. OnePetro.

Shen, W., & Ritzwoller, M. H. (2016). Crustal and uppermost mantle structure beneath the United States. *Journal of Geophysical Research: Solid Earth*, *121*(6), 4306-4342.

Silver, P. G., & Chan, W. W. (1991). Shear wave splitting and subcontinental mantle deformation. *Journal of Geophysical Research: Solid Earth*, *96*(B10), 16429-16454.

Simmons, N. A., Forte, A. M., Boschi, L., & Grand, S. P. (2010). GyPSuM: A joint tomographic model of mantle density and seismic wave speeds. *Journal of Geophysical Research: Solid Earth*, *115*(B12).

Spasojevic, S., Liu, L., & Gurnis, M. (2009). Adjoint models of mantle convection with seismic, plate motion, and stratigraphic constraints: North America since the Late Cretaceous. *Geochemistry, Geophysics, Geosystems*, *10*(5).

Thayer, D. C. (2011). *Constraining Lithosphere and Mantle Structure in the Bighorn Mountains: Analysis of Frequency Dependence in Shear Wave Splitting* (Doctoral dissertation, Colorado College.).

Tikoff, B., & Maxson, J. (2001). Lithospheric buckling of the Laramide foreland during Late Cretaceous and Paleogene, western United States. *Rocky Mountain Geology*, *36*(1), 13-35.

Tikoff, B., Siddoway, C., Sokoutis, D., & Willingshofer, E. (2022). The lithospheric folding model applied to the Bighorn uplift during the Laramide orogeny. In *Tectonic Evolution of the Sevier-Laramide Hinterland, Thrust Belt, and Foreland, and Postorogenic Slab Rollback (180–20 Ma)*. Geological Society of America.

Waite, G. P., Schutt, D. L., & Smith, R. B. (2005). Models of lithosphere and asthenosphere anisotropic structure of the Yellowstone hot spot from shear wave splitting. *Journal of Geophysical Research: Solid Earth*, *110*(B11).

Walker, A. M., & Wookey, J. (2012). MSAT—A new toolkit for the analysis of elastic and seismic anisotropy. *Computers & Geosciences*, *49*, 81-90.

West, J. D., Fouch, M. J., Roth, J. B., & Elkins-Tanton, L. T. (2009). Vertical mantle flow associated with a lithospheric drip beneath the Great Basin. *Nature Geoscience*, *2*(6), 439-444.

Worthington, L. L., Miller, K. C., Erslev, E. A., Anderson, M. L., Chamberlain, K. R., Sheehan, A. F., ... & Siddoway, C. S. (2015). Crustal structure of the Bighorn Mountains region: Precambrian influence on Laramide shortening and uplift in north-central Wyoming. *Tectonics*, *35*(1), 208-236.

Wüstefeld, A., Bokelmann, G., Zaroli, C., & Barruol, G. (2008). SplitLab: A shear-wave splitting environment in Matlab. *Computers & Geosciences*, *34*(5), 515-528.

Yang, B. B., Liu, K. H., Dahm, H. H., & Gao, S. S. (2016). A uniform database of teleseismic shear-wave splitting measurements for the western and central United States: December 2014 update. *Seismological Research Letters*, *87*(2A), 295-300.

Yeck, W. L., Sheehan, A. F., Anderson, M. L., Erslev, E. A., Miller, K. C., & Siddoway, C. S. (2014). Structure of the Bighorn Mountain region, Wyoming, from teleseismic receiver function analysis: Implications for the kinematics of Laramide shortening. *Journal of Geophysical Research: Solid Earth*, *119*(9), 7028-7042.

Yuan, H., & Romanowicz, B. (2010). Depth dependent azimuthal anisotropy in the western US upper mantle. *Earth and Planetary Science Letters*, *300*(3-4), 385-394.

Zandt, G., & Humphreys, E. (2008). Toroidal mantle flow through the western US slab window. *Geology*, *36*(4), 295-298.

Zhao, L., Allen, R. M., Zheng, T., & Zhu, R. (2012). High-resolution body wave tomography models of the upper mantle beneath eastern China and the adjacent areas. *Geochemistry, Geophysics, Geosystems*, *13*(6).

Zhou, Q., Hu, J., Liu, L., Chaparro, T., Stegman, D. R., & Faccenda, M. (2018). Western US seismic anisotropy revealing complex mantle dynamics. *Earth and Planetary Science Letters*, *500*, 156-167.

Zhu, Z., Bezada, M. J., Byrnes, J. S., & Ford, H. A. (2021). Evidence for Stress Localization Caused by Lithospheric Heterogeneity from Seismic Attenuation. *Geochemistry, Geophysics, Geosystems*, *22*(11), e2021GC009987.

Zhu, R. X., Yang, J. H., & Wu, F. Y. (2012). Timing of destruction of the North China Craton. *Lithos*, *149*, 51-60.

**Estimates of subsurface rheology changes following the 2019 Ridgecrest sequence**

Andrew Birkey[1], Heather A. Ford[1], and Joseph S. Byrnes[2,3]

[1]Department of Earth and Planetary Sciences, University of California – Riverside, Riverside, CA

[2]Department of Earth & Environmental Sciences, University of Minnesota, Twin Cities, Minneapolis, MN

[3]School of Earth and Sustainability, Northern Arizona University, Flagstaff, AZ

**Abstract**

Large earthquakes can induce rheological changes within the shallow subsurface. To measure this effect, we examine 20 permanent seismic stations in the region around the 2019 $M_w$ 6.4 Searles Valley and $M_w$ 7.1 Ridgecrest earthquakes in eastern California. Changes in rheology are approximated through velocity changes calculated using passive image interferometry. For most stations analyzed, there are minimal changes in velocity that recover in the hours to days following the two events, suggesting an elastic response. At two of the stations, there is a sustained decrease in velocity. For these stations, we infer a plastic rheology instead.

## 1. Introduction

On July 4$^{th}$, 2019 a $M_w$ 6.4 earthquake occurred in the Mojave desert of California on left-lateral, northeast-striking faults north of the Garlock Fault. The following day (July 5$^{th}$, 2019) a larger $M_w$ 7.1 earthquake ruptured a right-lateral, southeast-striking fault roughly orthogonal to the first. This sequence has been widely examined using a number of techniques because of the large number of instruments that were already deployed in the region, and the proximity to a number of seismological institutions capable of rapidly deploying more instruments (e.g. Cortez et al., 2020; Kendrick et al., 2019; Li et al., 2020; Lomax, 2020; Lozos and Harris, 2020; Ponti et al., 2020).

In this study, we use a method known as Passive Image Interferometry (PII; Sens-Schönfelder and Wegler, 2006; Wegler and Sens-Schönfelder, 2007) to examine changes

in shallow subsurface velocity following these two earthquakes. We employ single-station cross-correlation, wherein signals are cross-correlated between different components of a three-component seismometer. This method builds on previous work involving ambient seismic noise (e.g. Shapiro and Campillo, 2004; Shapiro et al., 2005) and is an intermediate approach to XYZ, between performing a cross-correlation between two stations where one station acts as a virtual source for the other, and auto-correlating the signal at one station with itself. Early work utilizing a similar method examined changes in seismic velocity following the 2004 Mid-Niigata earthquake (Wegler et al., 2009) and the 2008 Wenchuan earthquake (Zhao et al., 2012). Single-station cross-correlation was first used to examine coseismic velocity decreases for the 2008 Iwate-Miyagi Nairiku earthquake (Hobiger et al., 2014). Passive image interferometry has been used to monitor geothermal fields (Okamoto et al., 2021) and volcanoes (De Plaen et al., 2016, 2019; Sens-Schönfelder and Wegler, 2006), measure seasonal variability in seismic velocity on Earth (Feng et al., 2021) and Mars (Compaire et al., 2022), estimate crustal thickness (Becker and Knapmeyer-Endrun, 2019), and observe velocity changes following earthquakes (Gassenmeier et al., 2016; Richter et al., 2014; Viens et al., 2018; Wegler and Sens-Schönfelder, 2007). Additionally, this method has been used to examine the Ridgecrest sequence (Boschelli et al., 2021)—there are slight methodological differences between that study and this one, and we report different results.

*1.1 Earthquakes and velocity changes*

The technique used in this study (single-station cross-correlation) is analogous to receiver function analysis, in that it is sensitive to conversions from P-waves to S-waves at reflectors below individual stations (Hobiger et al., 2018). Receiver functions (whether Ps or Sp) are most sensitive to changes in $V_S$—this implies that velocity changes observed from single-station cross-correlation also represent changes in $V_S$ rather than $V_P$. We will briefly lay out seismic velocity sensitivity to various parameters.

Rubinstein and Beroza (2004) lay out a number of potential mechanisms to explain coseismic velocity changes following large earthquakes. First is static stress change: in the case of decreased static stress, velocities should increase due to the closing of cracks; increased static stress will cause velocities to decrease due to the opening of cracks. Second, dynamic stress (estimated through peak ground acceleration or peak ground velocity) can influence velocity for similar reasons: large amounts of ground shaking could open new and enlarge existing cracks. Third is lithology, though this is strongly related to site specific effects such as dynamic stress. Finally, hydrology may play a role in velocity changes: opening of new cracks will increase both porosity and permeability, while decreasing the shear modulus—combined, these factors act to decrease the velocity. We will examine each of these in turn in **Section 4.3**.

*1.2 Tectonic Setting*

While most of the motion between the North American and Pacific plates occurs on the San Andreas fault, roughly 20% of the plate motion occurs much further to the east in a region known as the Walker Lane-Eastern California Shear Zone (WL-ECSZ; Faulds and Henry, 2008). The 2019 Ridgecrest sequence occurred on faults in this region. Whereas the San Andreas system consists of broadly interconnected dextral faults, the WL-ECSZ is composed of a more complex set of shorter dextral faults. With transform motion in this region beginning only 12 Ma (Atwater, 1970), this is a much less mature fault zone than the San Andreas (Faulds et al., 2005). Prior to the 2019 Ridgecrest sequence, there were several larger-magnitude earthquakes such as the 1872 Owens Valley earthquake and the 1986 Chalfant Valley earthquake.

## 2. Data and Methods

We obtained data from 20 Southern California Seismic Network (CI) stations, ranging from 5.57 km (CLC) to 154 km (TIN) from the epicenter. Data were requested from 06-20-2019 to 08-01-2019 every four hours, with a five-minute window. We show the stations used in this study in **Figure 1**. We test both 1.0-20.0 and 10.0-30.0 Hz frequency ranges because single-station cross correlations are most sensitive to frequencies above 0.5 Hz (Hobiger et al., 2014) and because different frequency ranges are sensitive to different depth ranges (Hobiger et al., 2014; Viens et al., 2014). In particular, our primary frequency range (1.0-20.0 Hz) is sensitive to the top ~100 m of the subsurface.

The methodology below is similar to that laid out in Viens et al. (2018). Once seismic traces are downloaded, background trends in the data are removed and they are one-bit normalized (achieved by setting the amplitude to either positive or negative one, which reduces the influence of earthquakes). Data are then windowed into five-minute segments. Single-station cross-correlations are then calculated using the following from Viens et al. (2018) for vertical (denoted by z) against horizontal (denoted by i) components:

$$SC_{z,i}(t) = \langle F^{-1}\left(\frac{\hat{v}_i(\omega)\hat{v}_z^*(\omega)}{\{|\hat{v}_z(\omega)|\}^2}\right)\rangle$$

In this case, $\hat{v}_z^*(\omega)$ is the Fourier transform of the five-minute vertical trace, and $\hat{v}_i(\omega)$ is the trace from the north or east component (both are calculated). The denominator is smoothed with a 20-point moving average to stabilize it (denoted by the curly braces).

Once the single-station cross-correlation is calculated, amplitudes are normalized and the cross-correlation is smoothed in time. A reference trace is then calculated by averaging all traces before the $M_w$ 7.1 earthquake. The time shift between individual single-station cross correlations and the reference trace is calculated using the stretching factor method from Sens-Schönfelder and Wegler (2006). These time shifts are assumed to be due to changes in velocity.

Assuming a homogeneous change in the medium, the two can be related via a stretching factor as:

$$\varepsilon = \frac{dv}{v} = -\frac{dt}{t}$$

Where ε is the stretching factor, *dt/t* is the time shift from the reference trace, and *dv/v* is the change in velocity (the variable of interest). The velocity change (*dv/v*) for all independent cross correlations are then averaged, which has been shown to stabilize the signal of the velocity change (Hobiger et al., 2014).

## 3. Results

### *3.1 Velocity changes*

We show all velocity changes in **Table 1**, examples of velocity change time series from stations with clear co-seismic velocity change in **Figure 2**, and examples of velocity change time series from stations with smaller (less than an absolute value of 0.1%) or no co-seismic velocity changes in **Figure 3**. To estimate changes in velocity due to the earthquakes, we limit our search to a 12-hour window before and a 12-hour window after each event; only instances where the change is greater than 0.1% are reported. We then find the largest change in velocity within this window. At 14 stations, we identify a decrease in velocity following one or both events: five stations (LRL, MPM, SLA, TOW2, and WCS2) had a decrease in velocity only after the $M_w$ 6.4 event, four (CCC, CLC, WBS, and WRC2) had a decrease only after the $M_w$ 7.1 event, and five (DAW, DTP, ISA, SRT,

and WBM) had a decrease after both events—all but station WBM also saw a recovery in velocities between the two events. While Boschelli et al. (2021) only report decreases in velocity following the 7.1, we also estimate velocity increases at nine stations. Four stations (CLC, CWC, WBS, and WRC2) had a velocity increase after the 6.4 only, while five stations (LRL, MPM, SLA, TOW2, and WCS2) had an increase after the 7.1 only; there were no stations where the velocity increased after both events. Five of the stations used had no significant changes in velocity after either event, and all of these stations were more than 100 km from the epicenter. The largest decrease in velocity was 1.17% at MPM, while the largest increase was 1.42% at CLC (both changes occurred after the 6.4 rather than the 7.1). The furthest station with a noticeable increase was CWC at 86.1 km from the epicenter, while the closest was CLC at 5.57 km.

While we limited our initial estimation of velocity change to 12-hour windows before and after the event, we note that there were several stations where there was a persistent change in velocity after the $M_w$ 7.1 event that was not captured in these windows. In these instances, we examine the change in velocity from the sample immediately before the $M_w$ 7.1 event to the lowest measured velocity value. These stations include DAW (velocity decrease from 16-52 hours after), DTP (28-40 hours after), ISA (52 hours after onward), SLA (16 hours after onward), SRT (48-84 hours after), WBS (36 hours onward), and WCS2 (20 hours onward). The largest of these changes was at ISA, where we observe a drop in velocity of 0.81%. However, while SLA had a relatively modest drop of 0.15% from immediately before the $M_w$ 7.1 event, velocity changes began 24 hours before the $M_w$

6.4 event; when measured from that point to the lowest point in velocity (at 36 hours after the $M_w$ 7.1 event), the drop in velocity is 0.98%.

*3.2 Long-term recovery*

Changes in velocity generally appear to be not permanent at the stations in this study. We classify long-term changes in velocity according to four categories: (1) stations where no recovery in velocity is observed following the earthquakes; (2) stations where a velocity change is observed after the earthquakes but is then followed by a near immediate recovery in velocity; (3) stations with a change in velocity after the earthquakes followed by a long-term recovery in velocity (days to weeks after the event); and (4) stations where the velocity signal is continuous or shows a constant increase over the whole timeframe. Stations SLA and WCS2 fall into the first category. Six stations (CCC, CLC, LRL, WBM, WRC2, and WBS) fall into the second category. Stations DAW, MPM, and SRT are in the third category. Finally, stations CWC, GRA, and TOW2 fall into the final category. Beyond these four categories, there are other stations where the velocity signal is inconsistent or exhibits complex changes with time that are not associated with the earthquakes (such as DSC, DTP, and ISA). Distance from the epicenter of the $M_w$ 7.1 event does not appear to be the controlling factor in whether there is a long- or short-term recovery in velocity change; for instance, CLC is the closest station to the epicenter and has a recovery in velocity change within 12 hours, but other close stations (e.g. SRT) recover over the days following. Other close stations (e.g. TOW2) have a continuous increase in velocity over the 28 days following the earthquake. For SLA and WCS2, we calculated velocity change

over a longer time period (60 days before and 120 days after the $M_w$ 7.1 event) to test for the potential of a recovery in velocity change over an even longer period—in both cases there was no observed long-term recovery. However, there are minor differences in the velocity changes calculated for each station, as this is reliant on the reference trace calculated over the entire time span examined (see **Figure 4**).

*3.3 Correlation change*

In addition to changes in velocity, we also observed changes in both the average correlation coefficient for all cross-component correlations as well as changes at individual cross-component correlations. A high correlation coefficient implies that waveforms are similar in shape even if time separated, and can thus be explained solely by velocity changes; a lower correlation coefficient suggests that waveforms are dissimilar and thus may require a structural change. There are marked changes in the correlation coefficient at DTP, SLA, SRT, WBM, WBS, and WCS2. At SLA, WBM, WBS, and WCS2, the average correlation coefficient is close to 1.0 before the $M_w$ 6.4 event but decreases afterwards (to ~0.6 for SLA, WBM, and WCS2, but ~0.8 for WBS). All four also saw a clear decrease in the average correlation coefficient after the $M_w$ 7.1 event: for WCS2 it dropped to ~0.5, for SLA and WBM it dropped to ~0.4, and for SRT it dropped to 0. At DTP there was also a drop in average correlation coefficients to 0 following the $M_w$ 6.4 event. Interestingly, the two stations closest to the epicenter of the $M_w$ 7.1 event (CLC and TOW2) saw very minimal changes in their average correlation coefficient.

Cross-component correlations for all stations saw some change following the $M_w$ 7.1 event. In **Figure 5**, we show the autocorrelation and cross-correlation of all components for a sample of four stations (the remainder are shown in Figure S2). We classify these as being more coherent after the $M_w$ 7.1 event (i.e., patterns are more apparent), less coherent after the $M_w$ 7.1 event (i.e., patterns are less apparent), or time shifted (i.e., no change in coherency, but a clear shift in the timing). Nine stations became more coherent following the event, two stations became less coherent, and nine stations were time shifted. All stations with more coherency after the $M_w$ 7.1 event were less than 60 km from its epicenter. Of the two stations with less coherency, DSC was 153.0 km and SLA was 32.1 km from the epicenter. Stations with only time shifted cross-component correlations ranged from 32.2 km to 155.0 km from the epicenter (with five stations more than 100 km away; these stations did not have any change in velocity greater than 0.1% following either event). The most noticeable change was at MPM, where there was very little coherency before the $M_w$ 7.1 event, followed by very clear patterns with strong positive and negative correlation values after.

## 4. Discussion

### *4.1 Comparison to previous studies*

Of the 20 stations used in this study, 15 were also used by Boschelli et al. (2021) in their analysis of the Ridgecrest earthquake. They report velocity decreases at four of the stations in common (CCC, CLC, SRT, and WRC2). We also observe velocity drops at all four stations, though at CLC we observe a much smaller velocity change; at SRT we observe

drops at both the $M_w$ 6.4 event and the $M_w$ 7.1 event, while Boschelli et al. (2021) only report one at the $M_w$ 7.1 event. At three stations (DSC, HEC, and SHO) both this study and Boschelli et al. (2021) report no velocity changes; it should be noted that these are all more than 100 km away, which may imply that the upper threshold for observable velocity changes is below this distance. Of the remaining eight stations, Boschelli et al. (2021) report no change in velocity following the $M_w$ 7.1 event, yet we do observe changes. For instance, at ISA we see a velocity drop associated with both events, at MPM we see a velocity drop following the $M_w$ 6.4 event but a velocity increase following the $M_w$ 7.1 event. In general, we see much larger changes in velocity following the $M_w$ 6.4 event (more than 1.0% in some cases), a result that disagrees with Boschelli et al. (2021), who report no changes following that event. Additionally, we report a velocity increase at many of the stations used in this study, which is not reported by Boschelli et al. (2021)—though at some stations shown in that study such as TOW2 and WBS there does appear to be an increase in velocity following the $M_w$ 7.1 event.

Differences between the two studies may be due to filtering: both utilize the same high-pass filter of 1.0 Hz, but Boschelli et al. (2021) does not report a low-pass filter (we use a low-pass of 20.0 Hz). As shown in **Section 4.2**, choice of frequency bands does seem to have some effect on the observed velocity changes because different bands are sensitive to different depths. Additionally, Boschelli et al. (2021) resampled their data to 20 Hz, while we retain the original sampling rate of 100 Hz. Cutoff criteria for observed velocity changes

are also different between the two studies, with Boschelli et al. (2021) only reporting decreases of more than 0.4%, while we report those with 0.1% change or more.

Lu and Ben-Zion (2021) performed a joint analysis of converted waves and station autocorrelations to estimate changes in velocity following the Ridgecrest sequence. Five of the stations used in that study (CCC, SRT, TOW2, WCS2, and WRC2) were also used in this study. Lu and Ben-Zion (2021) reported a large coseismic velocity drop following the $M_w$ 7.1 event at WCS2 (~8.0%) and WRC2 (~7.0%). While we do observe velocity decreases at both stations, the magnitude of the drop is much smaller in this study than the previous one: a 0.58% decrease following the $M_w$ 6.4 event at WCS2 and a 0.66% decrease following the $M_w$ 7.1 event at WRC2. At station SRT, Lu and Ben-Zion (2021) showed a modest coseismic velocity drop (~2.0%) followed by an overcorrection in the recovery of velocity change: we do observe a drop following the earthquake, but the recovery we identify is interrupted by further velocity drops. At CCC and TOW2, both studies show a slight change in velocity following the $M_w$ 7.1 earthquake followed by rapid recovery. In general, the magnitude of velocity change shown in Lu and Ben-Zion (2021) is much larger than those that we observe: for instance, at WRC2 they reported a 7% decrease while we report only a ~0.7% decrease.

One of the key differences between this study and Lu and Ben-Zion (2021) is the way in which changes in velocity were determined. While we use all independent correlations (both auto and cross-correlations), Lu and Ben-Zion (2021) only utilized autocorrelations.

Previous studies have shown that averaging over all independent correlations stabilizes the velocity change (Hobiger et al., 2014). Furthermore, there are differences in filtering: we use a passband from 1-20 Hz, while they use a passband from 8-12 Hz to filter out contributions from low frequency surface waves. Finally, the time period over which data are analyzed is different: we used data starting 14 days before the $M_w$ 7.1 and 28 days after, whereas Lu and Ben-Zion (2021) analyze data from 10 days before and 20 days after. As shown below, the selection of time period over which to calculate the velocity change has an effect on the final outcome.

*4.2 Frequency dependence*

Previous studies examining single-station cross correlations have used a number of frequency bands, though Hobiger et al. (2014) note that the method appears to work best at frequencies above 0.5 Hz. In this section, we discuss the effect that filtering has on our results. For all stations, we filtered the data in two passbands: 1-20 Hz (similar to Boschelli et al., 2021) and 10-30 Hz. We show comparative results for SLA and WCS2 in **Figure 6**, and results for all stations filtered from 10-30 Hz in **Figure S3**. In general, stations where no change in velocity was observed (greater than 100 km from the $M_w$ 7.1 epicenter), filtering had little effect on the overall variation in velocities seen over the period analyzed. Stations closer to the epicenter were more influenced by filtering, with those at the higher passband having somewhat more stable behavior over time (e.g., CLC, DAW, and WBS) and several stations even exhibiting more pronounced changes in velocity following the events (e.g., CLC, DTP, LRL, and WCS2). At the two stations where the velocity decrease

was most visually evident (SLA and WCS2), filtering did not change the overall trend of the data, though there were slight changes in the value of velocity decrease—at WCS2, for instance, the increase in velocity immediately following the $M_w$ 7.1 earthquake went from 0.3874% to 0.7783% (see **Figure 6**). At most stations there was no change in the stability of the velocity change over time, but the individual values were often different.

*4.3 Explanations for velocity changes*

For both the Ridgecrest $M_w$ 6.4 and the $M_w$ 7.1 events, there is little relationship between the distance from the epicenter of the $M_w$ 7.1 event to the station and changes in velocity (see **Figure 7**). Following the $M_w$ 6.4, fourteen of the stations had some change in velocity, with ten having a velocity decrease; fifteen stations had some change in velocity following the $M_w$ 7.1 event, also with ten stations having a velocity decrease. While there was no decay in velocity change following the $M_w$ 6.4 event, there was a slight decay following the $M_w$ 7.1 event, with stations more than 50 km from the epicenter experiencing smaller changes in velocity. Rubinstein and Beroza (2004) posit several explanations for postseismic velocity changes following larger magnitude earthquakes (lithology, static stress changes, dynamic stress changes, and hydrology). We use Jennings et al. (1977) to determine local geology. We display the velocity change and local geology for all stations in **Figure 9**. The largest change in velocity following the $M_w$ 6.4 event was an increase of 1.42% at CLC (situated on Mesozoic granite), though the largest decrease in velocity (1.17%) was at station MPM on Quaternary alluvium. After the $M_w$ 7.1 event, the largest change was at CCC (0.90%) on Quaternary alluvium, though the largest increase in

velocity (0.76%) was at MPM also on Quaternary alluvium. Velocity increases and decreases following both events occurred at stations with varying geology. We thus infer that there is no correlation between the two.

Changes in static stress may also have some effect on observe velocity changes, with increased mean stress correlating to increased velocities and vice versa (Rubinstein and Beroza, 2004). At some stations this may be a plausible explanation for observed velocity changes. For instance, at SRT and ISA there are decreases in both shear and normal stresses (Wang et al., 2020) with corresponding velocity decreases. However, at the station where we observe the largest velocity drop following the $M_w$ 7.1 event (i.e. CCC), Wang et al. (2020) report shear and normal stress increases. Furthermore, at many of the stations used in this study, we find a velocity increase following one event and a velocity decrease following the other. At such stations, we do not infer an obvious relationship between velocity change and static stress change. No studies have examined stress changes specifically due to the $M_w$ 6.4 event, so we cannot determine whether the reverse velocity changes we observe at some sites (such as CLC, MPM, SLA, WBS, WCS2, and WRC2) are due to variations in static stress following one event.

Similar to changes in static stress, changes in dynamic stress may have some influence on near-surface velocity changes (Rubinstein and Beroza, 2004). To test this, we calculated the peak dynamic strain following Hill et al. (1993) and van der Elst and Brodsky (2010). This also allows us to directly compare our results to Boschelli et al. (2021), who performed

the same analysis. To estimate peak dynamic strain, we divide peak ground velocity (PGV) by seismic wave velocity –estimated through Vs30 (Taira et al., 2015; Wald and Allen, 2007). In **Figure 8**, we show results for both the $M_w$ 6.4 and 7.1 events. While Boschelli et al. (2021) reported a clear correlation between peak dynamic strain and velocity changes (higher peak dynamic strain means higher velocity changes), we do not observe a clear relationship between the two. For instance, following the $M_w$ 6.4 event we calculate roughly the same decrease in velocity for MPM and SRT, yet SRT has significantly more peak dynamic strain than MPM; similarly, following the $M_w$ 7.1 event, WBM and SRT have roughly the same velocity change with SRT again having a significantly larger peak dynamic strain. The only clear relationship we observe is that some of the stations with no perceptible change following the $M_w$ 7.1 event (i.e. DSC, HEC, and TIN) have very low peak dynamic strain. But even this relationship is complicated by other stations with similarly low peak dynamic strain and observable velocity changes (ISA, for example). We also examine the relationship between velocity change and peak ground acceleration (PGA); Boschelli et al. (2021) note that while they observe a general trend between the two, there is complex behavior. We also observe an inconsistent relationship between velocity change and PGA. For example, following the $M_w$ 7.1 event there was a large amount of shaking at station CLC (56.91 %g), but it had a small velocity decrease (0.19%); yet at station CCC there was more modest shaking (35.00 %g) yet a much larger velocity decrease (0.90%).

Hydrologic changes may contribute to velocity changes. For instance, experiments have shown that increasing water content for soils, granites, and basalts (comparable to the lithology seen at various stations in this study) decreases velocity (Dong and Lu, 2016; Juneja and Endait, 2017; Zaima and Katayama, 2018). Large precipitation events (greater than ~five mm/hr) could increase saturation of soils, leading to velocity decreases as seen following the 2011 Tohoku-Ōki earthquake (Viens et al., 2018). Meteorological data for our area indicate that during the one-and-a-half-month period of this study there is only a small amount of precipitation—0.30 and 0.15 inches in June and July, respectively (NOAA, 2019). We can therefore rule out the possibility that any of the observed velocity changes that occur post-seismically can be related to precipitation. Structural changes (i.e. changes in porosity or permeability) in the subsurface could also change the amount of water present in the subsurface. Liquefaction was reported near the $M_w$ 7.1 rupture, particularly near stations CLC, SRT, TOW2, and WRC2; stations to the north and west of the main rupture also have moderate to high liquefaction susceptibility (Zimmaro et al., 2020). Stations CLC, SRT, and WRC2 all experienced velocity decreases following the $M_w$ 7.1 event, suggesting that liquefaction near those stations may be the result of increased porosity and permeability in the subsurface. Station TOW2, however, had a velocity increase; this is somewhat more difficult to explain through hydrologic effects. Importantly, many laboratory studies of the effects of water on shear velocities (i.e. those listed above) assume an elastic rheology, in which increases in porosity would decrease velocity. However, poroelastic media have been shown theoretically to have velocity increases with increased porosity (Son and Kang, 2012).

While specific causes of change in velocity are not clear in this case, sites where there was a recovery in velocity likely exhibit an elastic rheology, whereas at two stations (SLA and WCS2) there is no observed recovery over the time period exmained. This would argue for a plastic rheology. Both stations have different local geologic conditions (SLA is on Tertiary volcanic flows, while WCS2 is on Mesozoic granite). However, both did experience a decrease in normal stress following the $M_w$ 7.1 event (Wang et al., 2020). In the case of SLA, this lack of recovery may be due to the opening of mircocracks, as has been observed previously (Lyakhovsky et al., 1997; Ostrovsky and Johnson, 2001). Because WCS2 is on weaker lithology, this change may instead be due to the rearrangement of grains or cracks (e.g. Nakata and Snieder, 2011; Rubinstein and Berzoa, 2004).

## 5. Conclusion

Using passive image interferometry, we analyzed velocity changes following the 2019 $M_w$ 6.4 and $M_w$ 7.1 Ridgecrest earthquakes. At most stations, we observe only minimal velocity changes that recover quickly, suggesting viscoelastic rheology within the shallow subsurface. At two of the stations analyzed, there is a sustained reduction in subsurface velocities over the time period analyzed, suggesting plastic rheology.

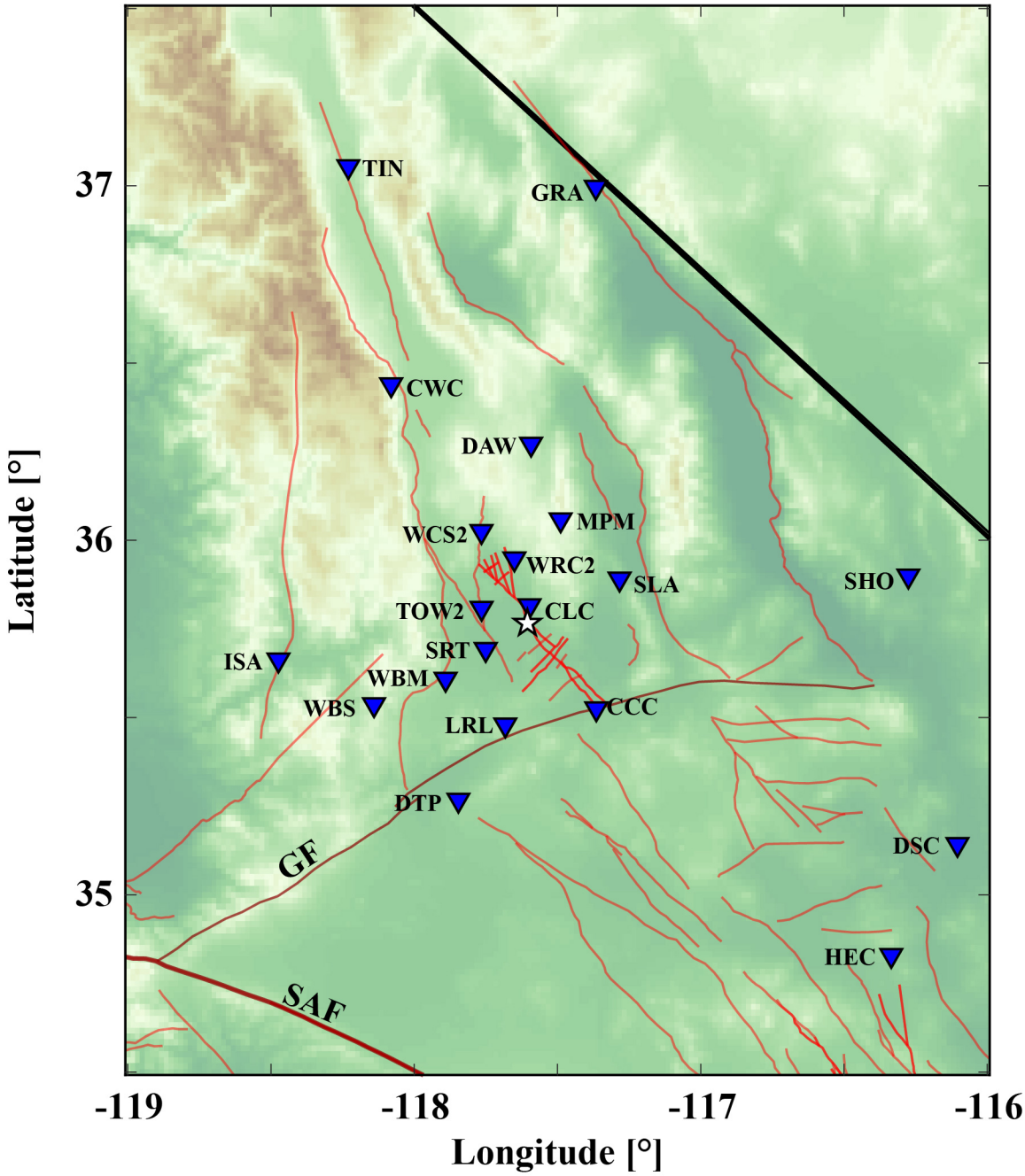


**Figure 4.1:** Map of stations used in this study. White star shows location of the Mw 7.1 Ridgecrest earthquake. Red lines are faults, with the San Andreas Fault (SAF) and the Garlock Fault (GF) labelled.

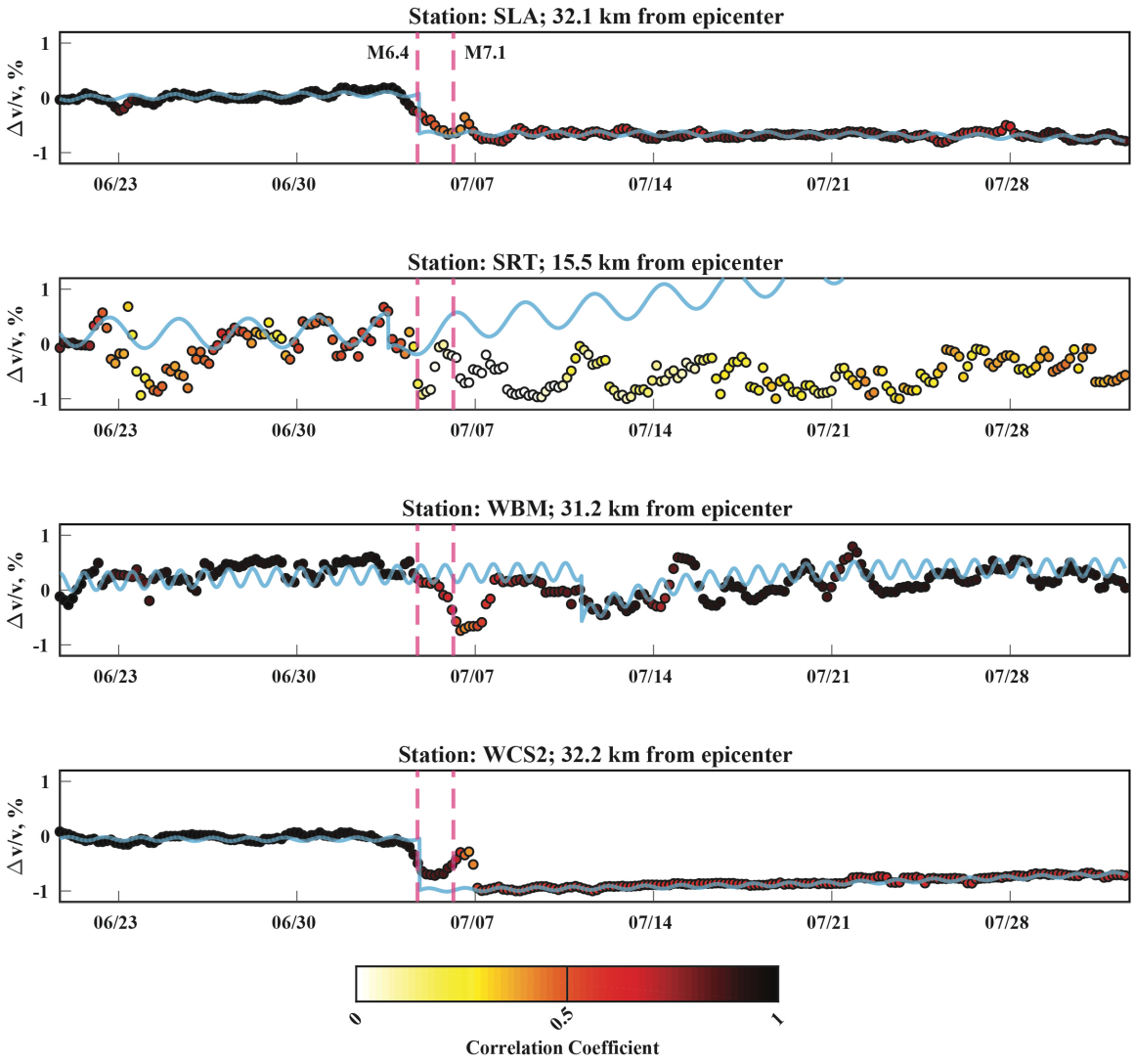


**Figure 4.2:** Change in velocity (dv/v) plotted against time for four stations with coseismic variations. Color of dots shows the average correlation coefficient for all independent cross-correlations. Distance is from the Mw 7.1 epicenter. Blue cyan line shows a Gibbs sampled fit to the data.

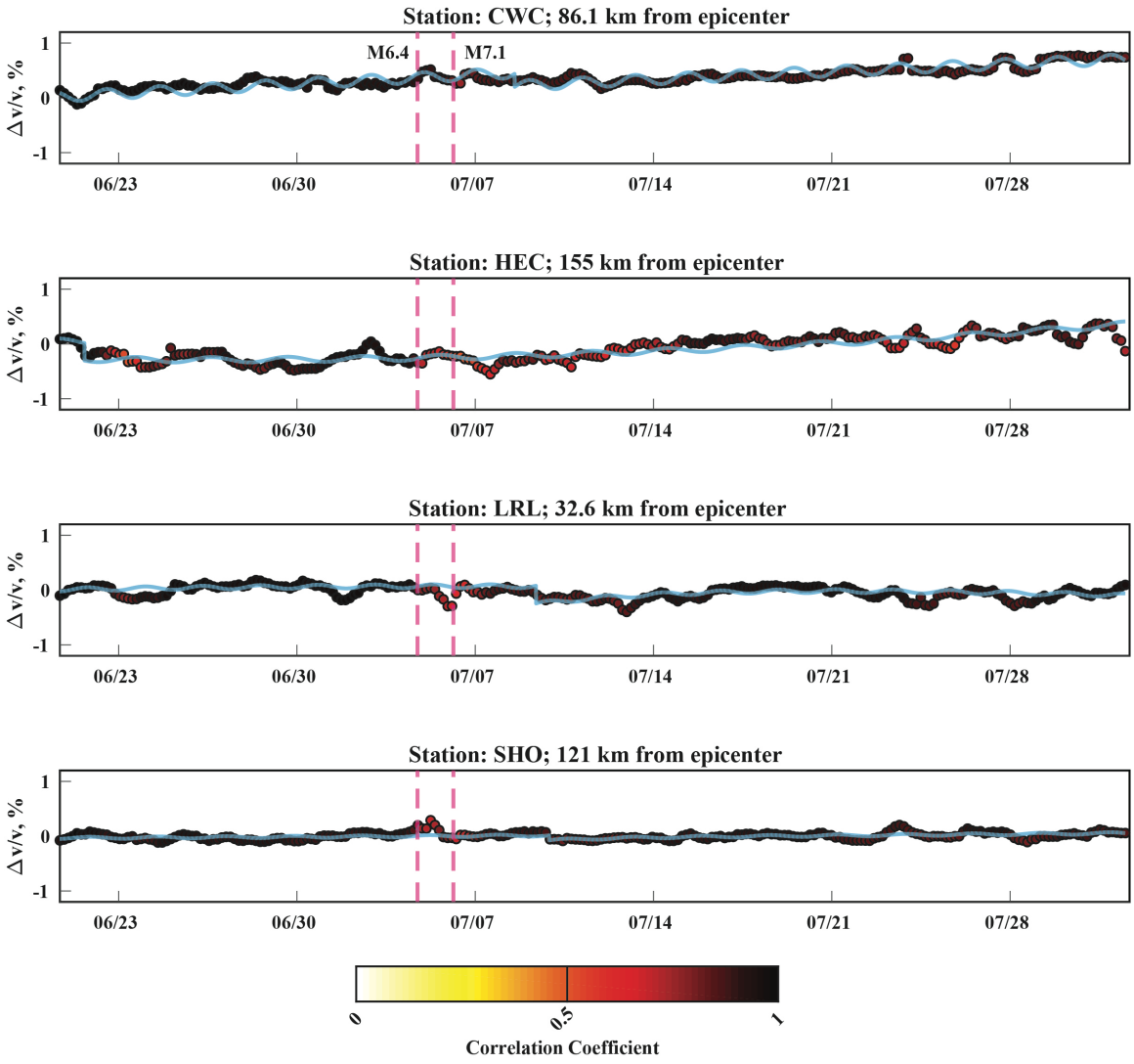


**Figure 4.3:** Change in velocity (dv/v) plotted against time for four stations without coseismic variations. All else is the same as in **Figure 4.2**.

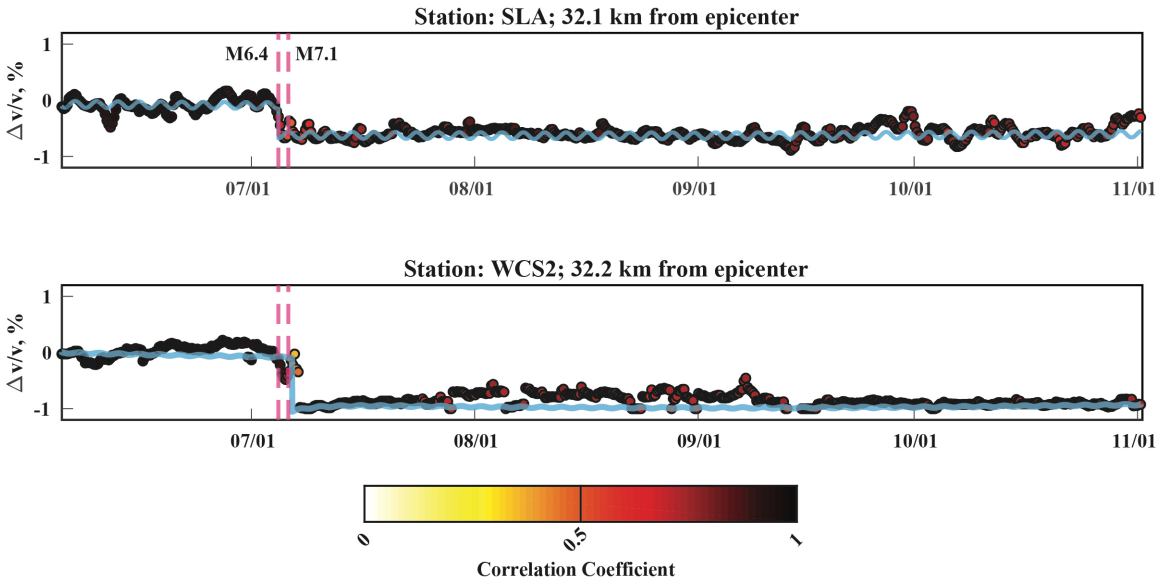


**Figure 4.4:** Change in velocity (dv/v) plotted against time over a longer period (60 days before and 120 days after the Mw 7.1). All else is the same as in **Figure 4.2**.

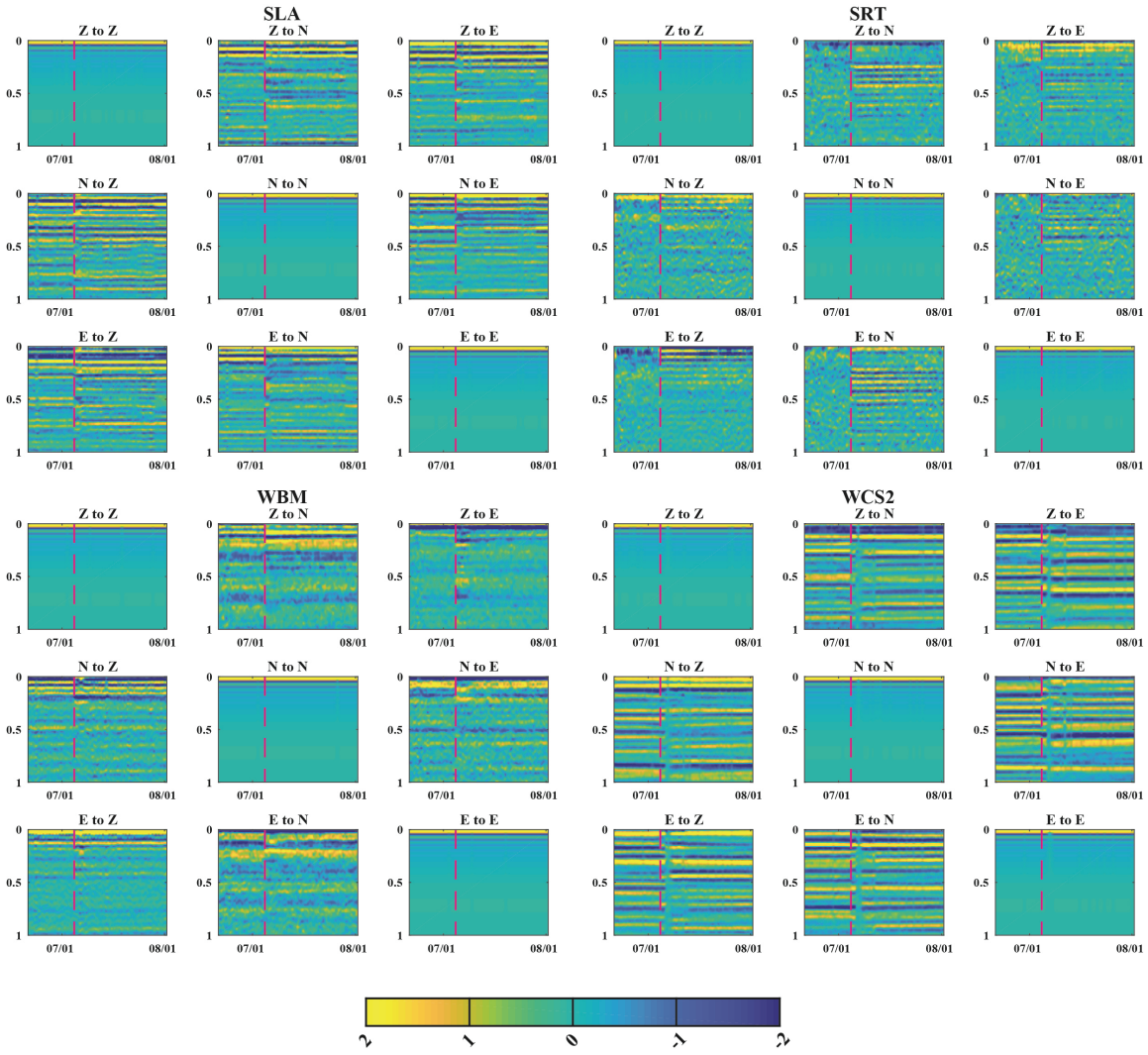


**Figure 4.5:** Daily cross-correlations for the four stations shown in **Figure 4.2**. Only positive times are shown on the y-axis.

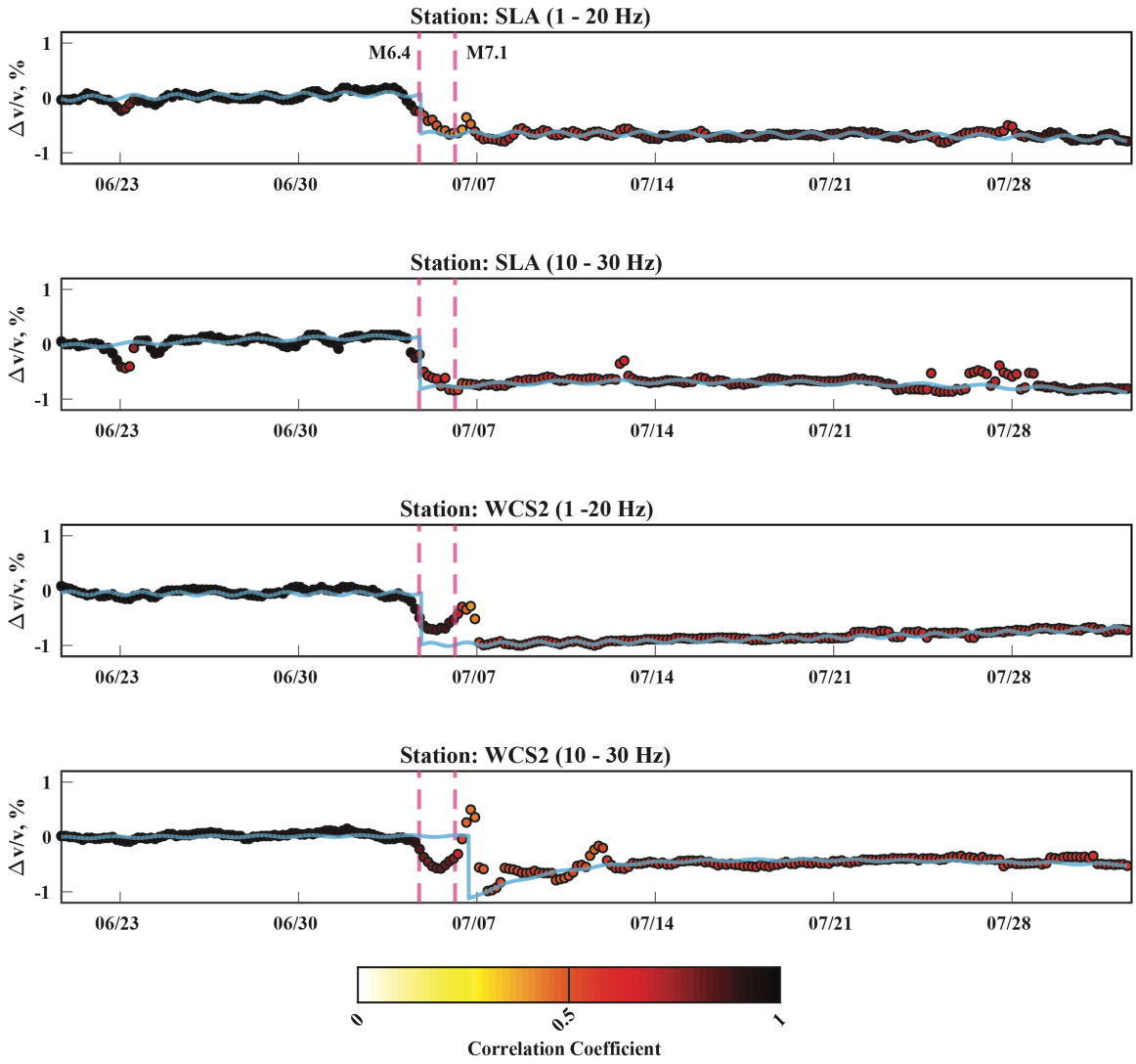


**Figure 4.6:** Change in velocity (dv/v) plotted against time for the two stations shown in **Figure 4.4** at two different frequency bands. All else is the same as in **Figure 4.2**.

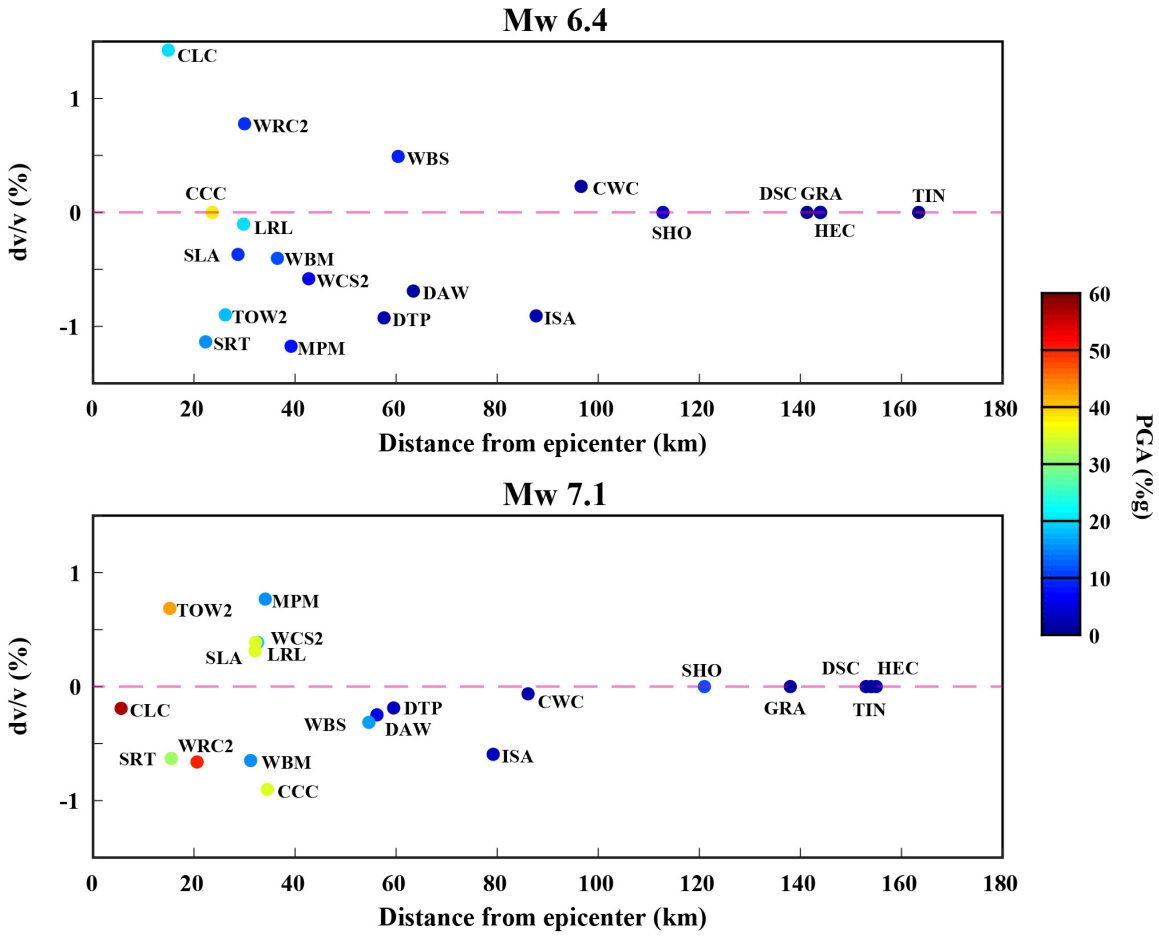


**Figure 4.7:** Change in velocity (dv/v) for all stations plotted against the distance to the respective epicenter. Stations are color-coded according to the peak-ground acceleration (PGA) at the site.

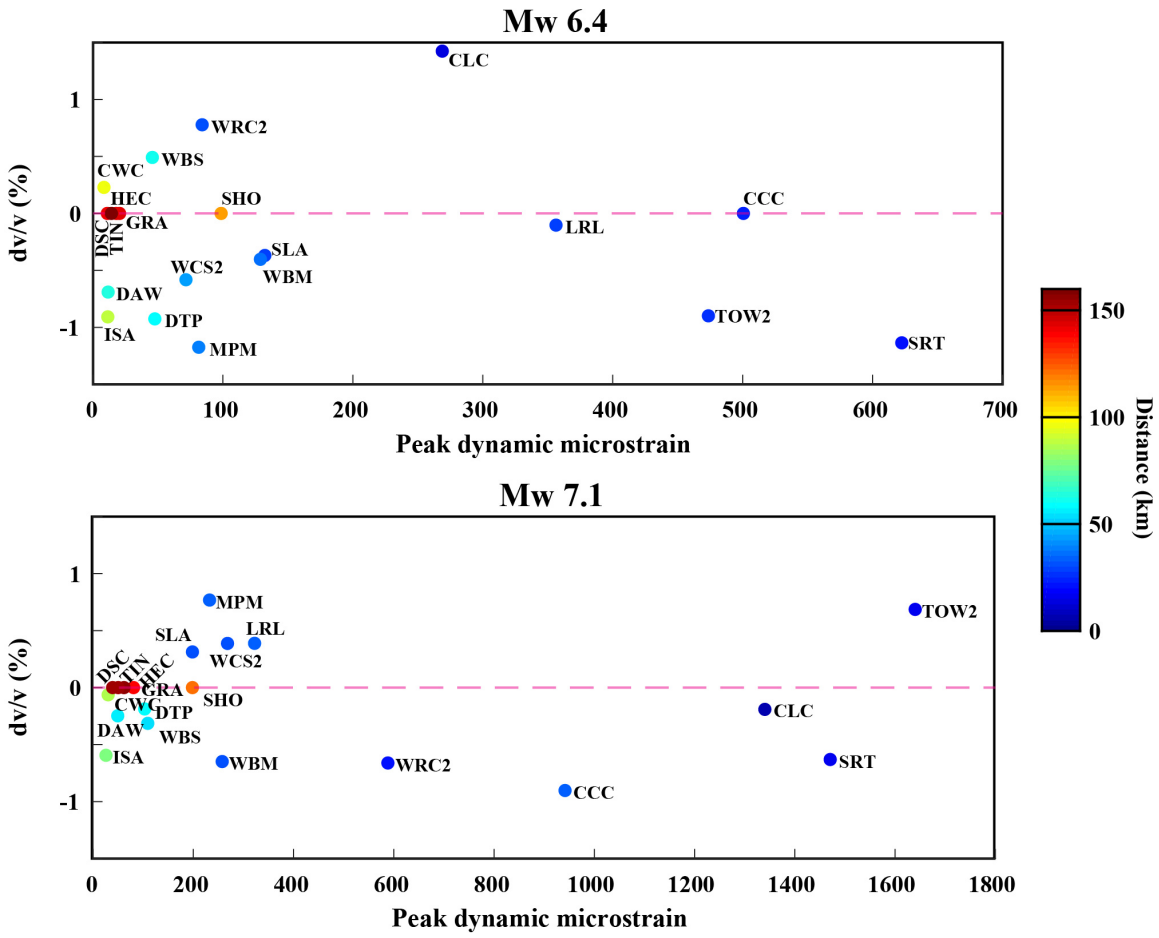


**Figure 4.8:** Change in velocity (dv/v) for all stations plotted against the peak dynamic microstrain at each site (defined as the peak ground velocity divided by Vs30 at the site). Stations are color-coded according to their distance from the respective epicenters.

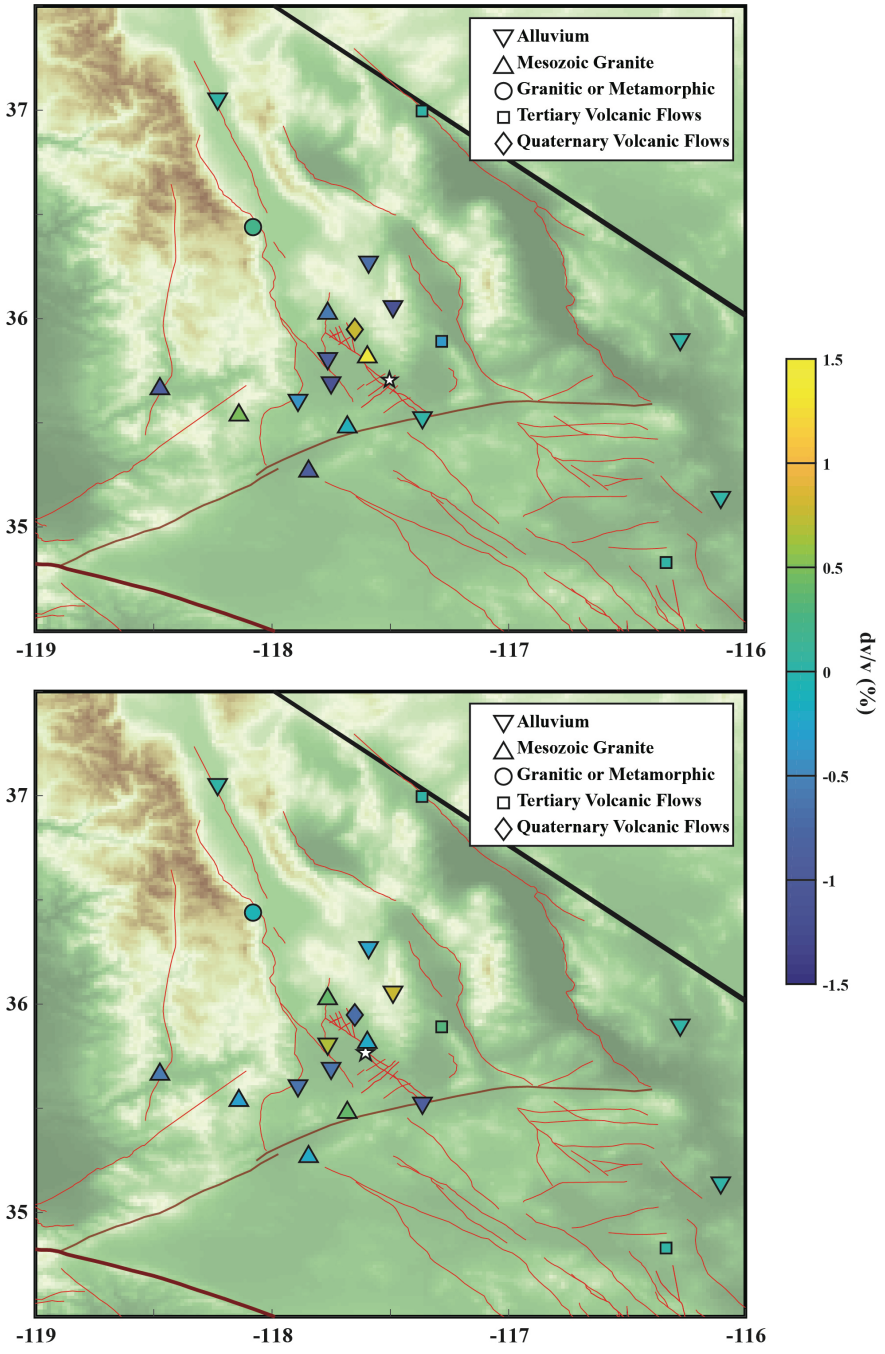


**Figure 4.9:** Change in velocity (dv/v) for all stations. White star shows the location of the Mw 6.4 (top panel) and the Mw 7.1 (bottom panel) respectively. Rock types are from Jennings et al. (1977).

| Network | Station | Distance from Mw 6.4 (km) | Distance from Mw 7.1 (km) | Mw 6.4 dv/v change (%) | Mw 7.1 dv/v change (%) | Mw 6.4 Microstrain | Mw 6.4 PGA (%g) | Mw 7.1 Microstrain | Mw 7.1 PGA (%g) |
|---|---|---|---|---|---|---|---|---|---|
| CI | CCC | 23.6 | 34.5 | -- | -0.90 | 500.56 | 38.17 | 941.62 | 35.00 |
| CI | CLC | 14.9 | 5.57 | 1.42 | -0.19 | 268.82 | 20.00 | 1340.14 | 56.91 |
| CI | CWC | 96.6 | 86.1 | 0.23 | -0.06 | 8.44 | 1.26 | 30.22 | 2.03 |
| CI | DAW | 63.4 | 56.2 | -0.69 | -0.25 | 11.65 | 1.39 | 49.42 | 5.76 |
| CI | DSC | 141.3 | 153 | -- | -- | 11.05 | 0.89 | 39.15 | 1.70 |
| CI | DTP | 57.6 | 59.5 | -0.93 | -0.19 | 47.60 | 2.34 | 103.14 | 3.42 |
| CI | GRA | 144.0 | 138 | -- | -- | 17.91 | 0.62 | 80.95 | 1.36 |
| CI | HEC | 143.9 | 155 | -- | -- | 20.46 | 1.99 | 61.83 | 3.33 |
| CI | ISA | 87.7 | 79.2 | -0.91 | -- | 11.41 | 1.96 | 25.92 | 3.17 |
| CI | LRL | 29.8 | 32.6 | -0.10 | 0.39 | 356.35 | 19.71 | 322.34 | 19.5 |
| CI | MPM | 39.2 | 34.1 | -1.17 | 0.77 | 81.40 | 7.50 | 232.56 | 15.00 |
| CI | SHO | 112.8 | 121 | -- | -- | 98.64 | 4.16 | 198.37 | 11.85 |
| CI | SLA | 28.7 | 32.1 | -0.37 | 0.31 | 132.28 | 10.00 | 198.41 | 35.00 |
| CI | SRT | 22.3 | 15.5 | -1.14 | -0.63 | 622.46 | 15.77 | 1470.53 | 31.12 |
| CI | TIN | 163.4 | 154 | -- | -- | 14.17 | 0.52 | 50.33 | 1.05 |
| CI | TOW2 | 26.2 | 15.2 | -0.90 | 0.69 | 473.64 | 17.86 | 1640.00 | 42.87 |
| CI | WBM | 36.5 | 31.2 | -0.40 | -0.65 | 128.87 | 12.00 | 257.73 | 15.00 |
| CI | WBS | 60.4 | 54.6 | 0.49 | -0.31 | 45.70 | 9.12 | 109.28 | 16.46 |
| CI | WCS2 | 42.7 | 32.2 | -0.58 | 0.39 | 71.56 | 6.00 | 268.34 | 35.00 |
| CI | WRC2 | 30.0 | 20.6 | 0.78 | -0.66 | 84.03 | 10.00 | 588.24 | 50.00 |

**Table 4.1:** Relevant parameters for all stations. Microstrain demonstrates the peak dynamic strain (defined as the peak ground velocity divided by Vs30). Peak ground velocity and peak ground acceleration were obtained from the USGS ShakeMap for each earthquake. Vs30 values were obtained from the USGS Vs30 Map viewer app.

| Station | Mw 6.4 dv/v change (%) | Mw 7.1 dv/v change (%) | Stress Change | Rock Type |
|---|---|---|---|---|
| CCC | -- | -0.90 | S/N increase | Alluvium |
| CLC | 1.42 | -0.19 | Unclear | Mesozoic granite |
| CWC | 0.23 | -0.06 | S increase; no change in N | Granitic or metamorphic |
| DAW | -0.69 | -0.25 | S decrease; N increase | Alluvium |
| DSC | -- | -- | No change | Alluvium |
| DTP | -0.93 | -0.19 | No change in S; N increase | Mesozoic granite |
| GRA | -- | -- | S decrease; N increase | Tertiary volcanic flows |
| HEC | -- | -- | No change | Tertiary volcanic flows |
| ISA | -0.91 | -0.59 | S/N decrease | Mesozoic granite |
| LRL | -0.10 | 0.39 | S decrease; N increase | Mesozoic granite |
| MPM | -1.17 | 0.77 | S decrease; N increase | Alluvium |
| SHO | -- | -- | S/N decrease | Alluvium |
| SLA | -0.37 | 0.31 | S increase; N decrease | Tertiary volcanic flows |
| SRT | -1.14 | -0.63 | S/N decrease | Alluvium |
| TIN | -- | -- | No change | Alluvium |
| TOW2 | -0.90 | 0.69 | S/N decrease | Alluvium |
| WBM | -0.40 | -0.65 | S increase; N decrease | Alluvium |
| WBS | 0.49 | -0.31 | S increase; N decrease | Mesozoic granite |
| WCS2 | -0.58 | 0.39 | S increase; N decrease | Mesozoic granite |
| WRC2 | 0.78 | -0.66 | S decrease; N increase | Quaternary volcanic flow |

**Table 4.2:** Other parameters examined for each station. Stress change was obtained from Wang et al. (2020). Rock type was determined from Jennings et al. (1977).

## References


Atwater, T. (1970). Implications of plate tectonics for the Cenozoic tectonic evolution of western North America. *Geological Society of America Bulletin*, *81*(12), 3513-3536.

Becker, G., & Knapmeyer-Endrun, B. (2019). Crustal thickness from horizontal component seismic noise auto-and cross-correlations for stations in Central and Eastern Europe. *Geophysical Journal International*, *218*(1), 429-445.

Boschelli, J., Moschetti, M. P., & Sens-Schönfelder, C. (2021). Temporal seismic velocity variations: recovery following from the 2019 Mw 7.1 Ridgecrest, California earthquake. *Journal of Geophysical Research: Solid Earth*, *126*(4), e2020JB021465.

Compaire, N., Margerin, L., Monnereau, M., Garcia, R. F., Lange, L., Calvet, M., ... & Banerdt, W. B. (2022). Seasonal variations of subsurface seismic velocities monitored by the SEIS-InSight seismometer on Mars. *Geophysical Journal International*, *229*(2), 776-799.

Cortez, J. T., Oglesby, D. D., Kyriakopoulos, C., Wu, B., Chaudhuri, K., Ghosh, A., & Douilly, R. (2021). On the rupture propagation of the 2019 M6. 4 Searles Valley, California, earthquake, and the lack of immediate triggering of the M7. 1 Ridgecrest earthquake. *Geophysical Research Letters*, *48*(4), e2020GL090659.

De Plaen, R. S., Cannata, A., Cannavo, F., Caudron, C., Lecocq, T., & Francis, O. (2019). Temporal changes of seismic velocity caused by volcanic activity at Mt. Etna revealed by the autocorrelation of ambient seismic noise. *Frontiers in Earth Science*, 251.

De Plaen, R. S., Lecocq, T., Caudron, C., Ferrazzini, V., & Francis, O. (2016). Single-station monitoring of volcanoes using seismic ambient noise. *Geophysical Research Letters*, *43*(16), 8511-8518.

Dong, Y., & Lu, N. (2016). Dependencies of shear wave velocity and shear modulus of soil on saturation. *Journal of Engineering Mechanics*, *142*(11), 04016083.

Faulds, J. E., Henry, C. D., & Hinz, N. H. (2005). Kinematics of the northern Walker Lane: An incipient transform fault along the Pacific–North American plate boundary. *Geology*, *33*(6), 505-508.

Faulds, J. E., Henry, C. D. (2008). Tectonic influences on the spatial and temporal evolution of the Walker Lane: An incipient transform fault along the evolving Pacific–North American plate boundary. *Ores and orogenesis: Circum-Pacific tectonics, geologic evolution, and ore deposits: Arizona Geological Society Digest*, *22*, 437-470.

Feng, K. F., Huang, H. H., Hsu, Y. J., & Wu, Y. M. (2021). Controls on Seasonal Variations of Crustal Seismic Velocity in Taiwan Using Single-Station Cross-Component Analysis of Ambient Noise Interferometry. *Journal of Geophysical Research: Solid Earth*, *126*(11), e2021JB022650.

Gassenmeier, M., Sens-Schönfelder, C., Eulenfeld, T., Bartsch, M., Victor, P., Tilmann, F., & Korn, M. (2016). Field observations of seismic velocity changes caused by shaking-induced damage and healing due to mesoscopic nonlinearity. *Geophysical Journal International*, *204*(3), 1490-1502.

Hobiger, M., Wegler, U., Shiomi, K., & Nakahara, H. (2014). Single-station cross-correlation analysis of ambient seismic noise: application to stations in the surroundings of the 2008 Iwate-Miyagi Nairiku earthquake. *Geophysical Journal International*, *198*(1), 90-109.

Jennings, C.W., Strand, R.G., and Rogers, T.H., 1977, Geologic map of California: California Division of Mines and Geology, scale 1:750,000.

Juneja, A., & Endait, M. (2017). Laboratory measurement of elastic waves in Basalt rock. *Measurement*, *103*, 217-226.

Kendrick, K. J., Akciz, S. O., Angster, S. J., Avouac, J., Bachhuber, J. L., Bennett, S. E., ... & Oskin, M. E. (2019, September). Geologic observations of surface fault rupture associated with the Ridgecrest M6. 4 and M7. 1 earthquake sequence by the Ridgecrest Rupture Mapping Group. In *Poster Presentation at 2019 SCEC Annual Meeting* (pp. 7-11).

Li, S., Chen, G., Tao, T., He, P., Ding, K., Zou, R., ... & Wang, Q. (2020). The 2019 M w 6.4 and M w 7.1 Ridgecrest earthquake sequence in eastern California: Rupture on a conjugate fault structure revealed by GPS and InSAR measurements. *Geophysical Journal International*, *221*(3), 1651-1666.

Lomax, A. (2020). Absolute location of 2019 Ridgecrest seismicity reveals a shallow M w 7.1 hypocenter, migrating and pulsing M w 7.1 foreshocks, and duplex M w 6.4 ruptures. *Bulletin of the Seismological Society of America*, *110*(4), 1845-1858.

Lozos, J. C., & Harris, R. A. (2020). Dynamic rupture simulations of the M6. 4 and M7. 1 July 2019 Ridgecrest, California, earthquakes. *Geophysical Research Letters*, *47*(7), e2019GL086020.

Lu, Y., & Ben-Zion, Y. (2022). Regional seismic velocity changes following the 2019 M w 7.1 Ridgecrest, California earthquake from autocorrelations and P/S converted waves. *Geophysical Journal International*, *228*(1), 620-630.

Lyakhovsky, V., Reches, Z. E., Weinberger, R., & Scott, T. E. (1997). Non-linear elastic behaviour of damaged rocks. *Geophysical Journal International*, *130*(1), 157-166.

Nakata, N., & Snieder, R. (2011). Near-surface weakening in Japan after the 2011 Tohoku-Oki earthquake. *Geophysical Research Letters*, *38*(17).

NOAA (2019). Monthly Precipitation Summary Water Year 2019. https://www.cnrfc.noaa.gov/monthly_precip_2019.php

Okamoto, K., Asanuma, H., & Nimiya, H. (2021). Fluid activity detection in geothermal areas using a single seismic station by monitoring horizontal-to-vertical spectral ratios. *Scientific reports*, *11*(1), 1-9.

Ostrovsky, L. A., & Johnson, P. A. (2001). Dynamic nonlinear elasticity in geomaterials. *La Rivista del Nuovo Cimento*, *24*(7), 1-46.

Ponti, D. J., Blair, J. L., Rosa, C. M., Thomas, K., Pickering, A. J., Akciz, S., ... & Zinke, R. (2020). Documentation of surface fault rupture and ground-deformation features produced by the 4 and 5 July 2019 Mw 6.4 and Mw 7.1 Ridgecrest earthquake sequence. *Seismological Research Letters*, *91*(5), 2942-2959.

Richter, T., Sens-Schönfelder, C., Kind, R., & Asch, G. (2014). Comprehensive observation and modeling of earthquake and temperature-related seismic velocity changes in northern Chile with passive image interferometry. *Journal of Geophysical Research: Solid Earth*, *119*(6), 4747-4765.

Rubinstein, J. L., & Beroza, G. C. (2004). Evidence for widespread nonlinear strong ground motion in the Mw 6.9 Loma Prieta earthquake. *Bulletin of the Seismological Society of America*, *94*(5), 1595-1608.

Rychert, C. A., Rondenay, S., & Fischer, K. M. (2007). P-to-S and S-to-P imaging of a sharp lithosphere-asthenosphere boundary beneath eastern North America. *Journal of Geophysical Research: Solid Earth*, *112*(B8).

Sens-Schönfelder, C., & Wegler, U. (2006). Passive image interferometry and seasonal variations of seismic velocities at Merapi Volcano, Indonesia. *Geophysical research letters*, *33*(21).

Shapiro, N. M., & Campillo, M. (2004). Emergence of broadband Rayleigh waves from correlations of the ambient seismic noise. *Geophysical Research Letters*, *31*(7).

Shapiro, N. M., Campillo, M., Stehly, L., & Ritzwoller, M. H. (2005). High-resolution surface-wave tomography from ambient seismic noise. *Science*, *307*(5715), 1615-1618.

Son, M. S., & Kang, Y. J. (2012). Shear wave propagation in a layered poroelastic structure. *Wave Motion*, *49*(4), 490-500.

Taira, T. A., Brenguier, F., & Kong, Q. (2015). Ambient noise-based monitoring of seismic velocity changes associated with the 2014 Mw 6.0 South Napa earthquake. *Geophysical Research Letters*, *42*(17), 6997-7004.

Viens, L., Denolle, M. A., Hirata, N., & Nakagawa, S. (2018). Complex near-surface rheology inferred from the response of greater Tokyo to strong ground motions. *Journal of Geophysical Research: Solid Earth*, *123*(7), 5710-5729.

Wald, D. J., & Allen, T. I. (2007). Topographic slope as a proxy for seismic site conditions and amplification. *Bulletin of the Seismological Society of America*, *97*(5), 1379-1395.

Wang, K., Dreger, D. S., Tinti, E., Bürgmann, R., & Taira, T. A. (2020). Rupture process of the 2019 Ridgecrest, California M w 6.4 foreshock and M w 7.1 earthquake constrained by seismic and geodetic data. *Bulletin of the Seismological Society of America*, *110*(4), 1603-1626.

Wegler, U., Nakahara, H., Sens-Schönfelder, C., Korn, M., & Shiomi, K. (2009). Sudden drop of seismic velocity after the 2004 Mw 6.6 mid-Niigata earthquake, Japan, observed with Passive Image Interferometry. *Journal of Geophysical Research: Solid Earth*, *114*(B6).

Wegler, U., & Sens-Schönfelder, C. (2007). Fault zone monitoring with passive image interferometry. *Geophysical Journal International*, *168*(3), 1029-1033.

Zaima, K., & Katayama, I. (2018). Evolution of elastic wave velocities and amplitudes during triaxial deformation of Aji granite under dry and water-saturated conditions. *Journal of Geophysical Research: Solid Earth*, *123*(11), 9601-9614.

Zhao, P. P., Chen, J. H., Campillo, M., Liu, Q. Y., Li, Y., Li, S. C., ... & Qi, S. H. (2012). Crustal velocity changes associated with the Wenchuan M8. 0 earthquake by auto-correlation function analysis of seismic ambient noise. *Chinese Journal of Geophysics*, *55*(1), 137-145.

Zimmaro, P., Nweke, C. C., Hernandez, J. L., Hudson, K. S., Hudson, M. B., Ahdi, S. K., ... & Stewart, J. P. (2020). Liquefaction and related ground failure from July 2019 Ridgecrest earthquake sequence. *Bulletin of the Seismological Society of America*, *110*(4), 1549-1566.

**Conclusion**

Throughout the body of this work, we present evidence for complex seismic structure within the Earth's interior. While this is not a novel finding, it is becoming increasingly important to our understanding of the Earth's evolution, current structure, and dynamics to thoroughly examine its interior on multiple depth and areal scales. Below, we briefly summarize our findings in each chapter and highlight key outstanding questions.

In Chapter 1 we present clear evidence that the Australian lithosphere is seismically layered. Receiver function analysis of converted Sp phases indicate that there are sharp seismic discontinuities above the tomographically predicted lithosphere-asthenosphere boundary within cratonic Australia. These mid-lithospheric discontinuities seem to be a ubiquitous feature of cratonic lithosphere. Additionally, we observe a sharp, shallow negative phase on receiver functions that we can interpret as the lithosphere-asthenosphere boundary along the Phanerozoic eastern coast of the continent. However, it is not yet clear precisely what causes the aforementioned mid-lithospheric discontinuities. While we favor hydrous minerals, their presence in the mid-lithosphere still lacks a thorough explanation.

Chapter 2 proceeds with a further discussion of the seismic complexity of the Australian lithosphere. We present shear wave splitting and anisotropic Ps receiver functions. Shear wave splitting fast directions and delay times are inconsistent across the continent; while some averaged fast directions can be explained through plate motion alone, the smoothing out of significant backazimuthal dependence obscures robust results that argue for complex

seismic anisotropy. While modelling has shown that seismic anisotropy can induce clear, periodic variations on the transverse component of backazimuthally-binned Ps receiver functions, we do not observe such systematic changes. Rather, we suggest that the variations observed must occur over a broader depth range. Initial comparisons between other models of seismic anisotropy and both sets of results have been presented here, but further analysis is required. Basic forward modelling cannot replicate the complexity of shear wave splitting results. Further modelling may elucidate the exact nature of seismic anisotropy within the Australian lithosphere, particularly if shear wave splitting and Ps receiver functions can be jointly inverted. One key problem that must be addressed is the nature and presence of seismic anisotropy within the lowermost mantle.

We scale our analysis from a continent to a single craton in Chapter 3. As with shear wave splitting in Australia, the Wyoming Craton has complex splitting results. Averaged fast directions and delay times do indicate some geographic dependence, with consistency between results to the west of the Bighorn Mountains and east of the Black Hills; within the Powder River Basin splitting results are far more variable. However, we observe backazimuthal dependence, arguing for layered seismic anisotropy or a non-horizontal axis of symmetry. When paired with other analysis (such as an examination of modal fast directions within a given backazimuthal bin), shear wave splitting results in the Powder River Basin clearly deviate from others in the region. The region of anomalous splitting agrees well with attenuation modelling. While we present evidence of a change in shear wave splitting within the Powder River Basin, multiple explanations for the cause still

exist. We again stress that seismic anisotropy within the lowermost mantle could severely affect our understanding of our results.

Finally, we scale down even further to a regional examination of velocity and rheology changes within the top hundred meters of the subsurface in the area around the 2019 Ridgecrest earthquake. A lack of long-term changes in velocity perturbations at most stations suggests an elastic response. Two stations maintain a decreased velocity perturbation, which implies a plastic response. While we test a number of possible mechanisms to explain these changes, no single explanation seems best suited to our results. A further examination of hydrologic effects is needed.

**Appendix A:** Supplementary Material for Chapter 1

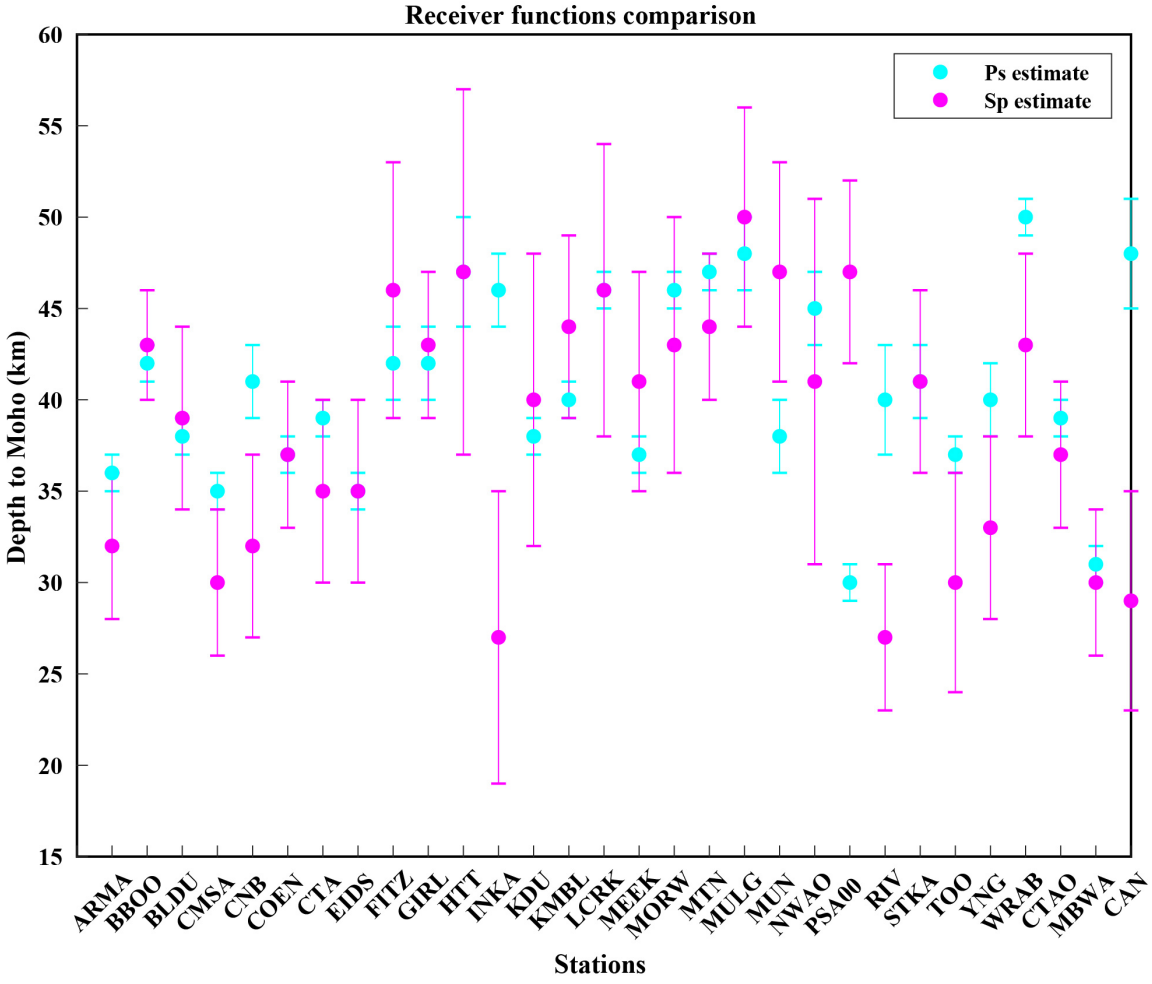


**Figure S1.1:** Comparison between Moho estimates from Ps and Sp receiver functions for all stations presented in this study.

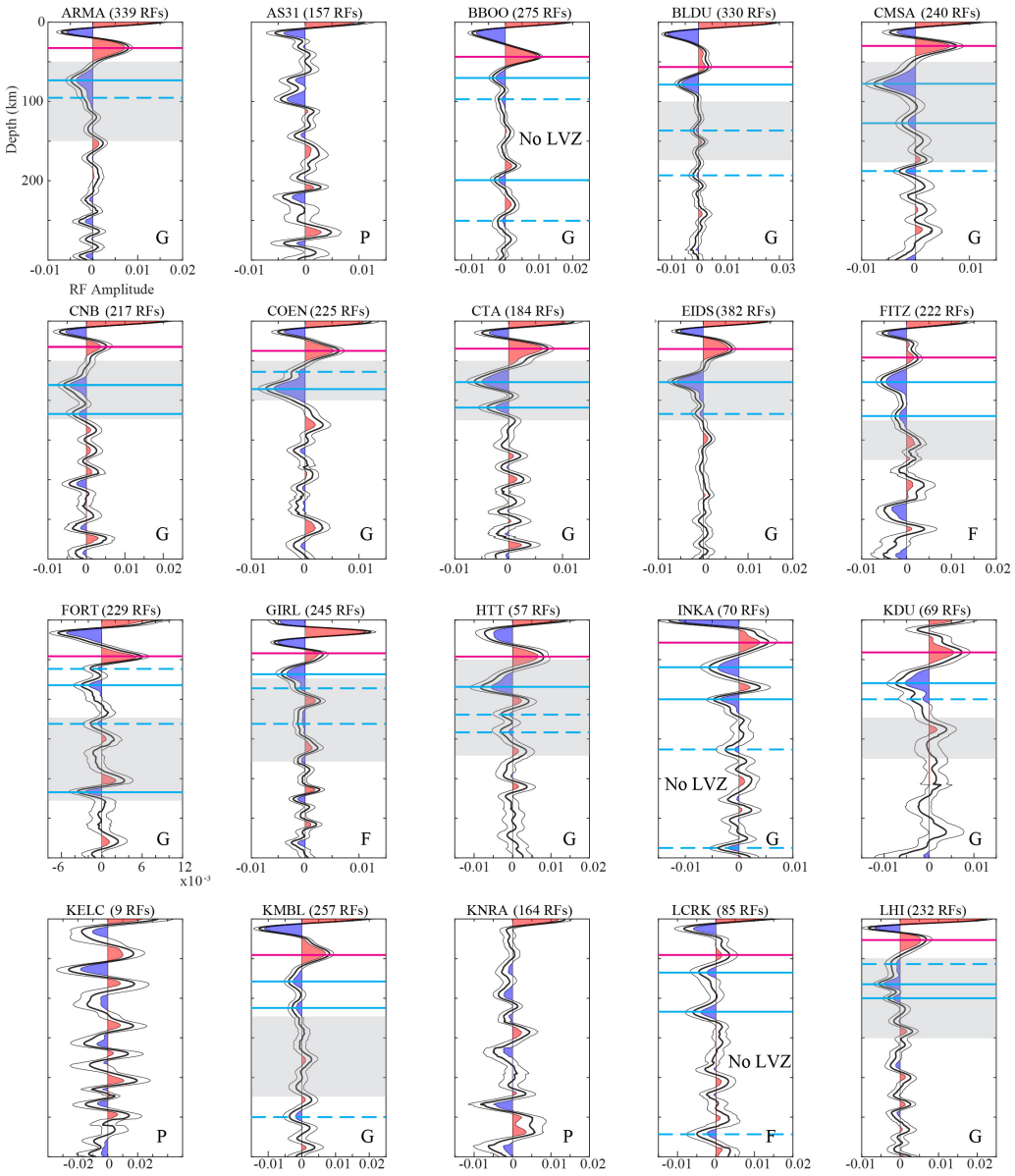
ARMA (339 RFs)
AS31 (157 RFs)
BBOO (275 RFs)
BLDU (330 RFs)
CMSA (240 RFs)
CNB (217 RFs)
COEN (225 RFs)
CTA (184 RFs)
EIDS (382 RFs)
FITZ (222 RFs)
FORT (229 RFs)
GIRL (245 RFs)
HTT (57 RFs)
INKA (70 RFs)
KDU (69 RFs)
KELC (9 RFs)
KMBL (257 RFs)
KNRA (164 RFs)
LCRK (85 RFs)
LHI (232 RFs)
Depth (km)
RF Amplitude
No LVZ
G
P
F
x10⁻³

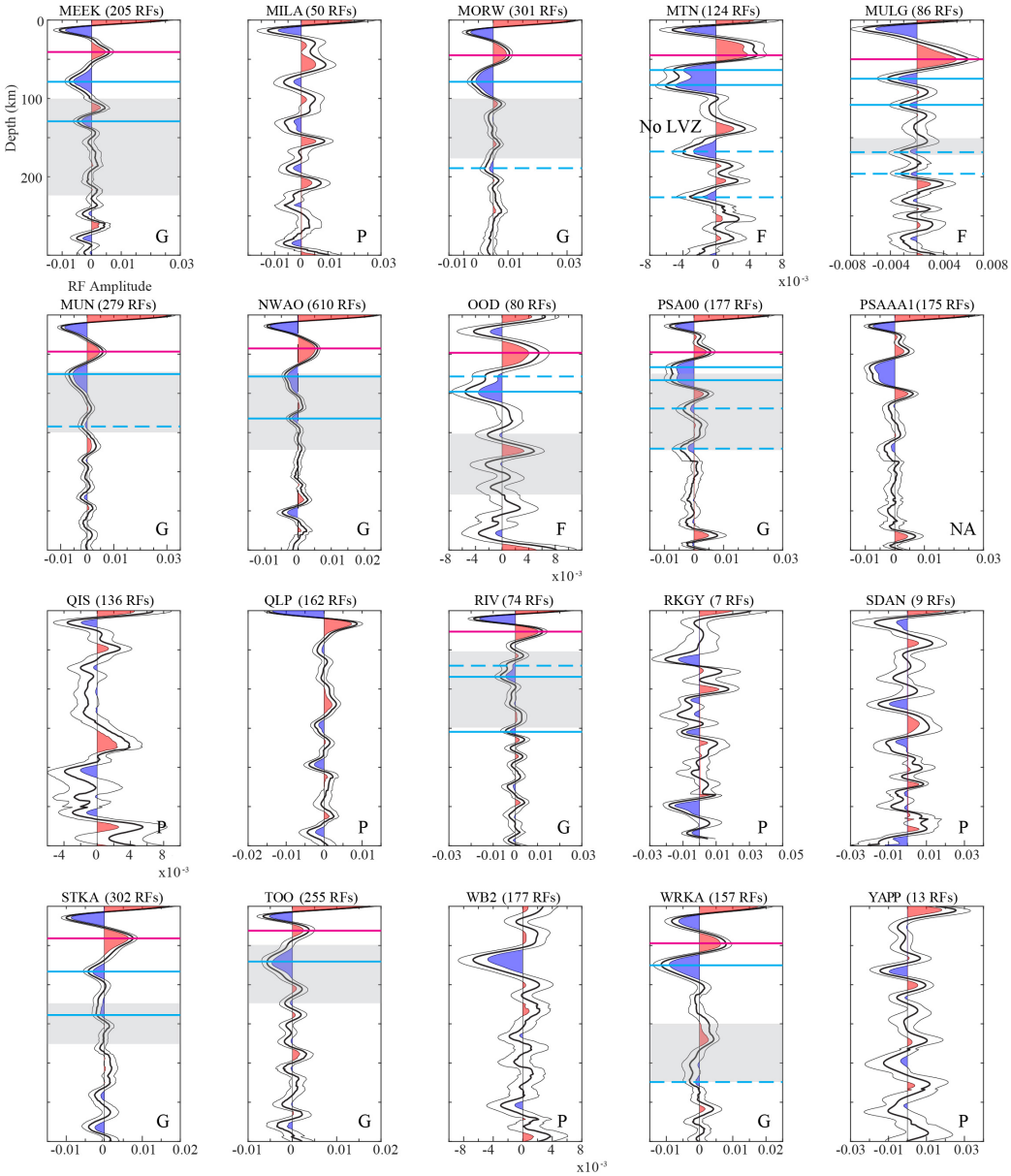
MEEK (205 RFs)
MILA (50 RFs)
MORW (301 RFs)
MTN (124 RFs)
MULG (86 RFs)
Depth (km)
No LVZ
RF Amplitude
MUN (279 RFs)
NWAO (610 RFs)
OOD (80 RFs)
PSA00 (177 RFs)
PSAAA1 (175 RFs)
QIS (136 RFs)
QLP (162 RFs)
RIV (74 RFs)
RKGY (7 RFs)
SDAN (9 RFs)
STKA (302 RFs)
TOO (255 RFs)
WB2 (177 RFs)
WRKA (157 RFs)
YAPP (13 RFs)

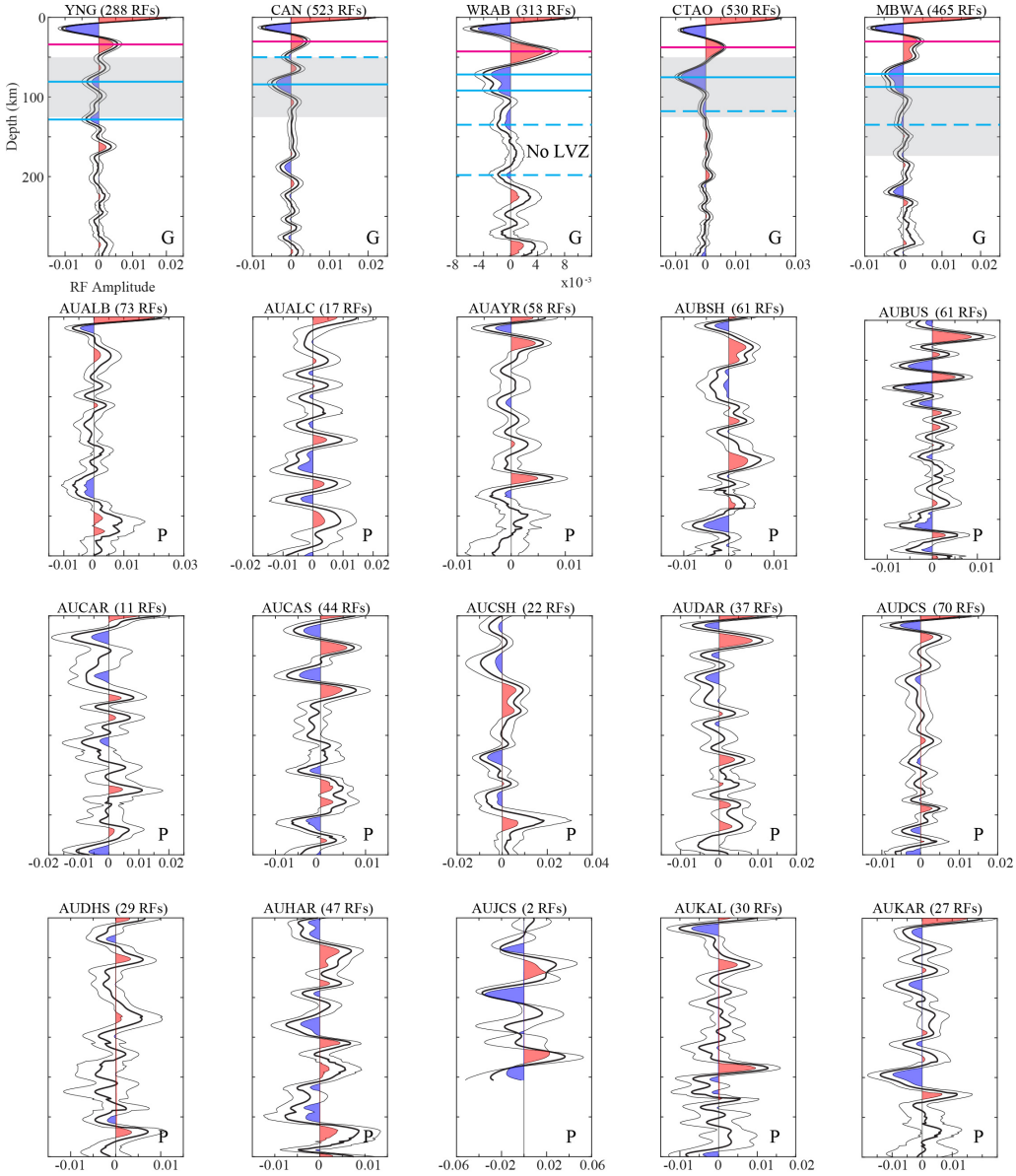
YNG (288 RFs)
CAN (523 RFs)
WRAB (313 RFs)
CTAO (530 RFs)
MBWA (465 RFs)
Depth (km)
No LVZ
RF Amplitude
AUALB (73 RFs)
AUALC (17 RFs)
AUAYR (58 RFs)
AUBSH (61 RFs)
AUBUS (61 RFs)
AUCAR (11 RFs)
AUCAS (44 RFs)
AUCSH (22 RFs)
AUDAR (37 RFs)
AUDCS (70 RFs)
AUDHS (29 RFs)
AUHAR (47 RFs)
AUJCS (2 RFs)
AUKAL (30 RFs)
AUKAR (27 RFs)

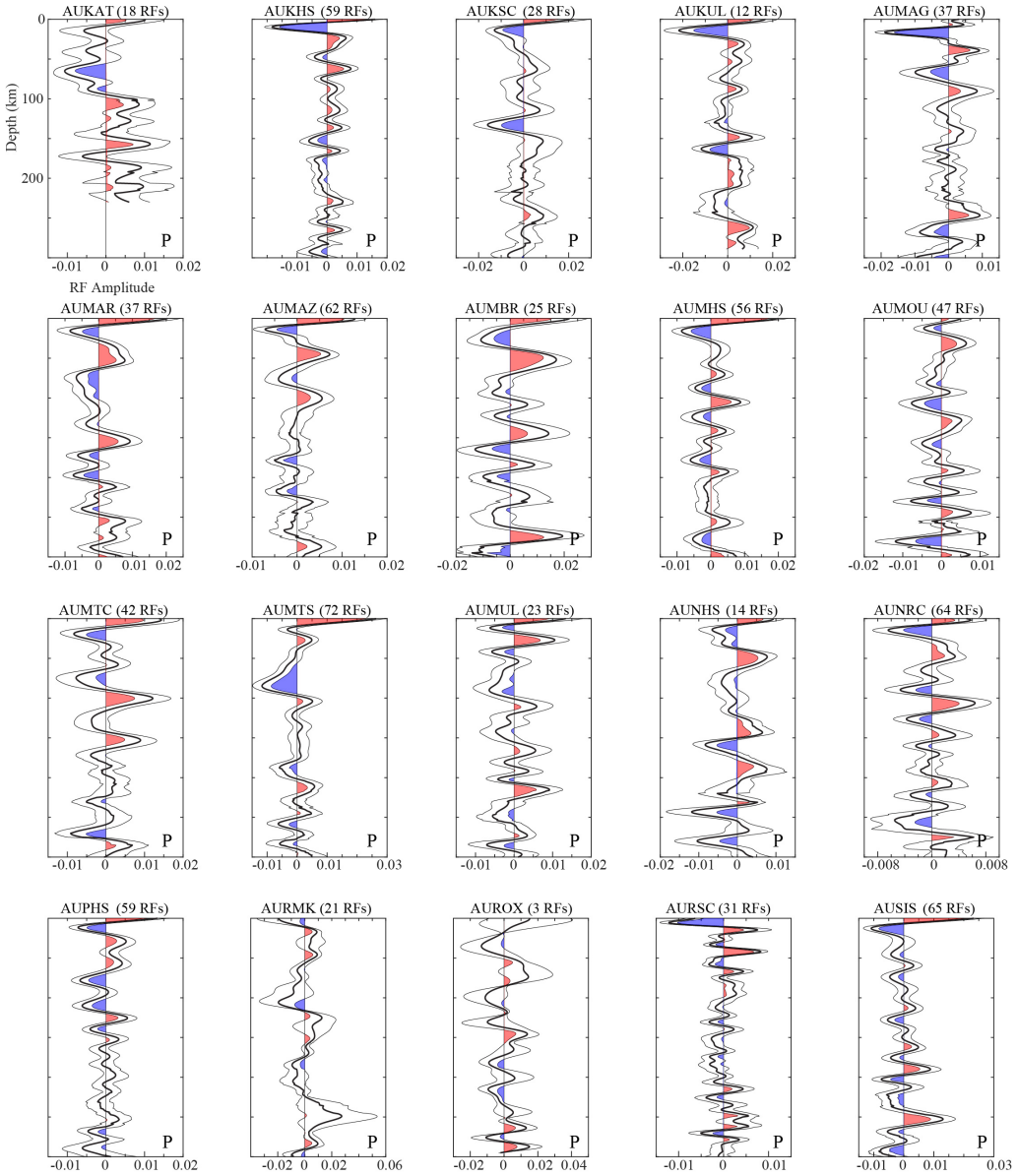
AUKAT (18 RFs)
AUKHS (59 RFs)
AUKSC (28 RFs)
AUKUL (12 RFs)
AUMAG (37 RFs)
AUMAR (37 RFs)
AUMAZ (62 RFs)
AUMBR (25 RFs)
AUMHS (56 RFs)
AUMOU (47 RFs)
AUMTC (42 RFs)
AUMTS (72 RFs)
AUMUL (23 RFs)
AUNHS (14 RFs)
AUNRC (64 RFs)
AUPHS (59 RFs)
AURMK (21 RFs)
AUROX (3 RFs)
AURSC (31 RFs)
AUSIS (65 RFs)
Depth (km)
RF Amplitude
P

**Figure S1.2 (previous pages):** Single station stacked receiver functions for all stations used in this study. Solid magenta lines are our estimate for the Moho. Solid cyan lines are at primary and secondary phase depths. Dashed cyan lines are at smaller amplitude phases. Gray boxes are the depth range of the negative velocity gradient from AuSREM profiles. Receiver functions are labelled as good (G), fair (F), or poor (P).

**Appendix B:** Supplementary Material for Chapter 2

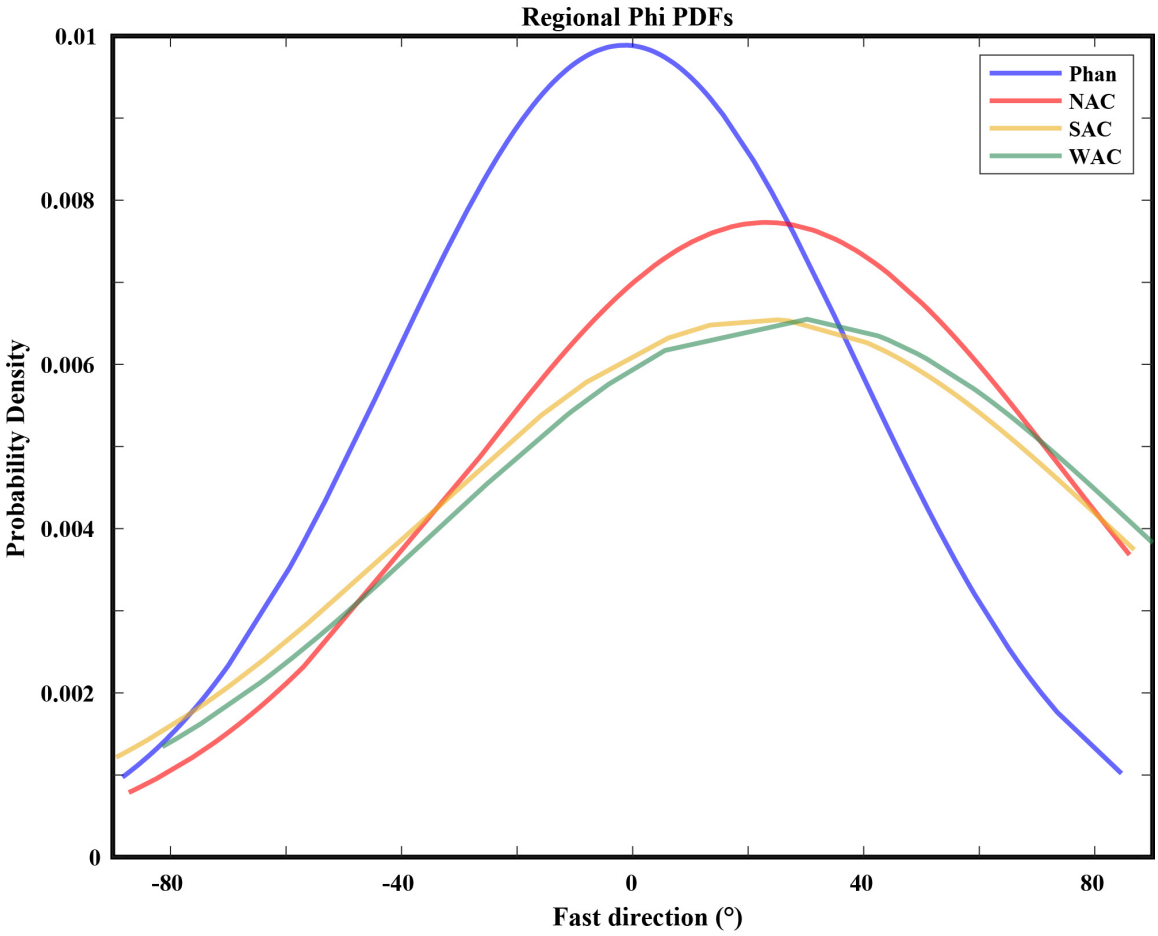


**Figure S2.1:** Probability density function of shear wave splitting delay times for each region in this study.

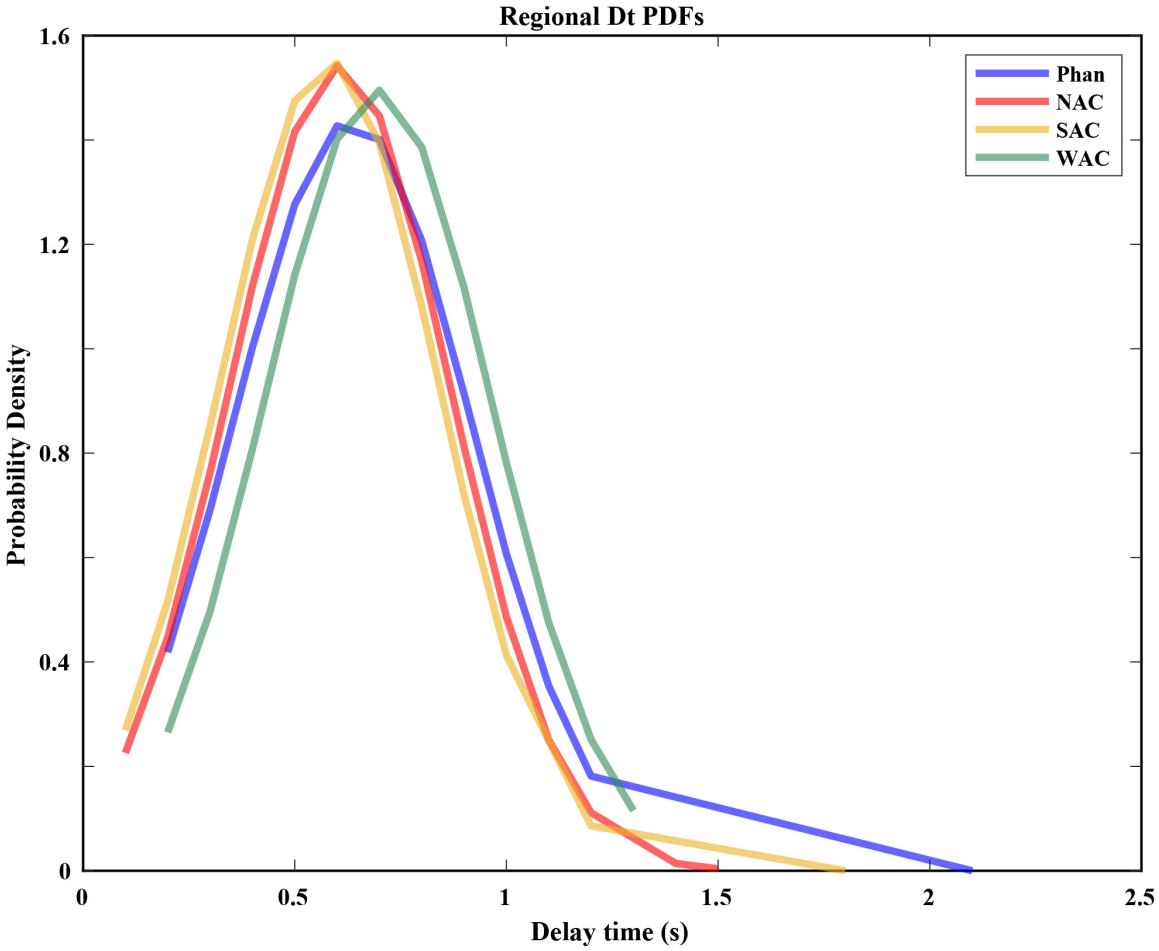


**Figure S2.2:** Probability density function of shear wave splitting fast directions (phi) for each region in this study.

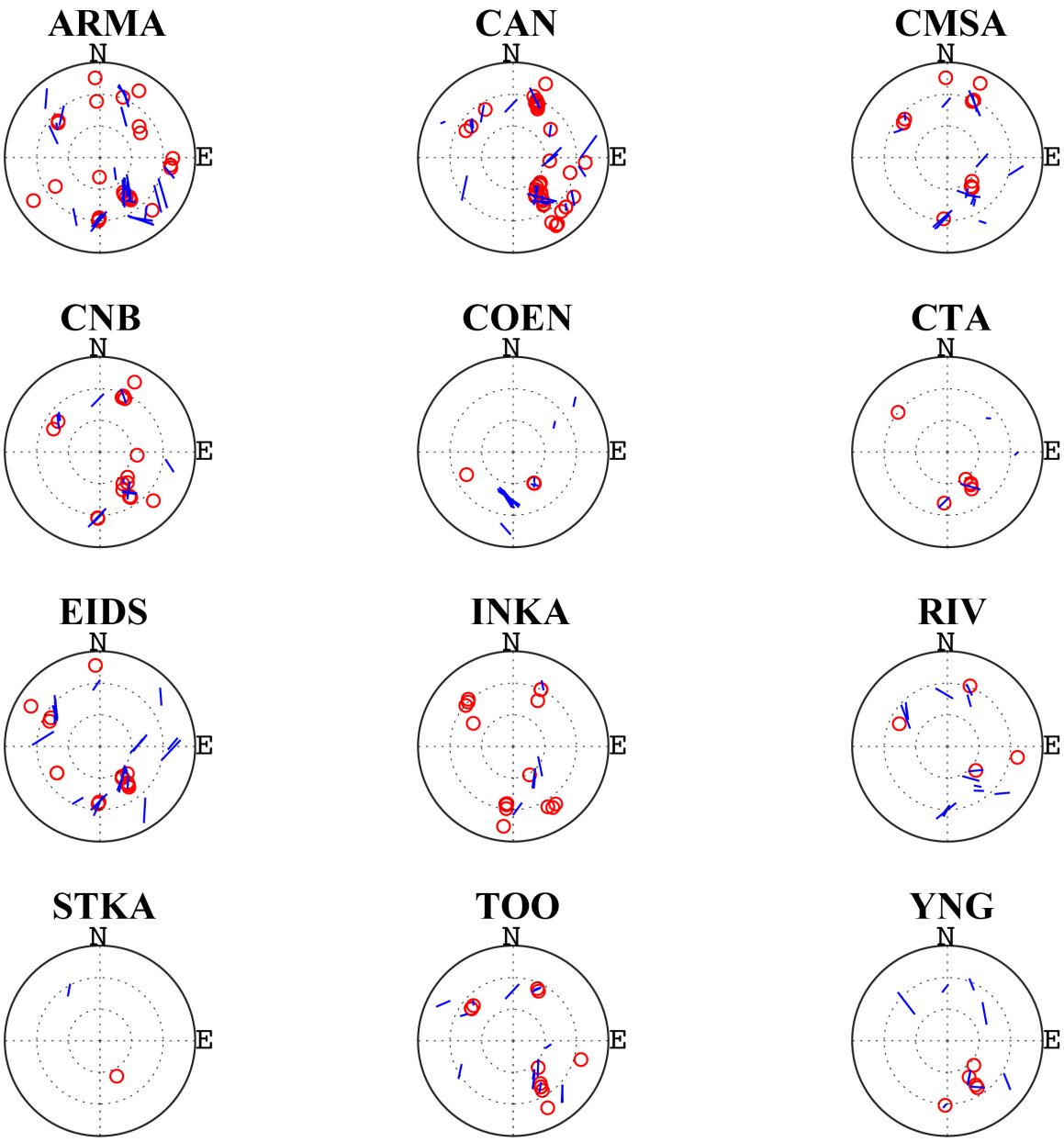


**Figure S2.3:** Stereoplots of shear wave splitting results (blue lines) and nulls (red lines) for Phanerozoic Australia. Backazimuth of events is along the circumference, while the inclination of the ray is plotted from 0° at the center to 15° at the edge.

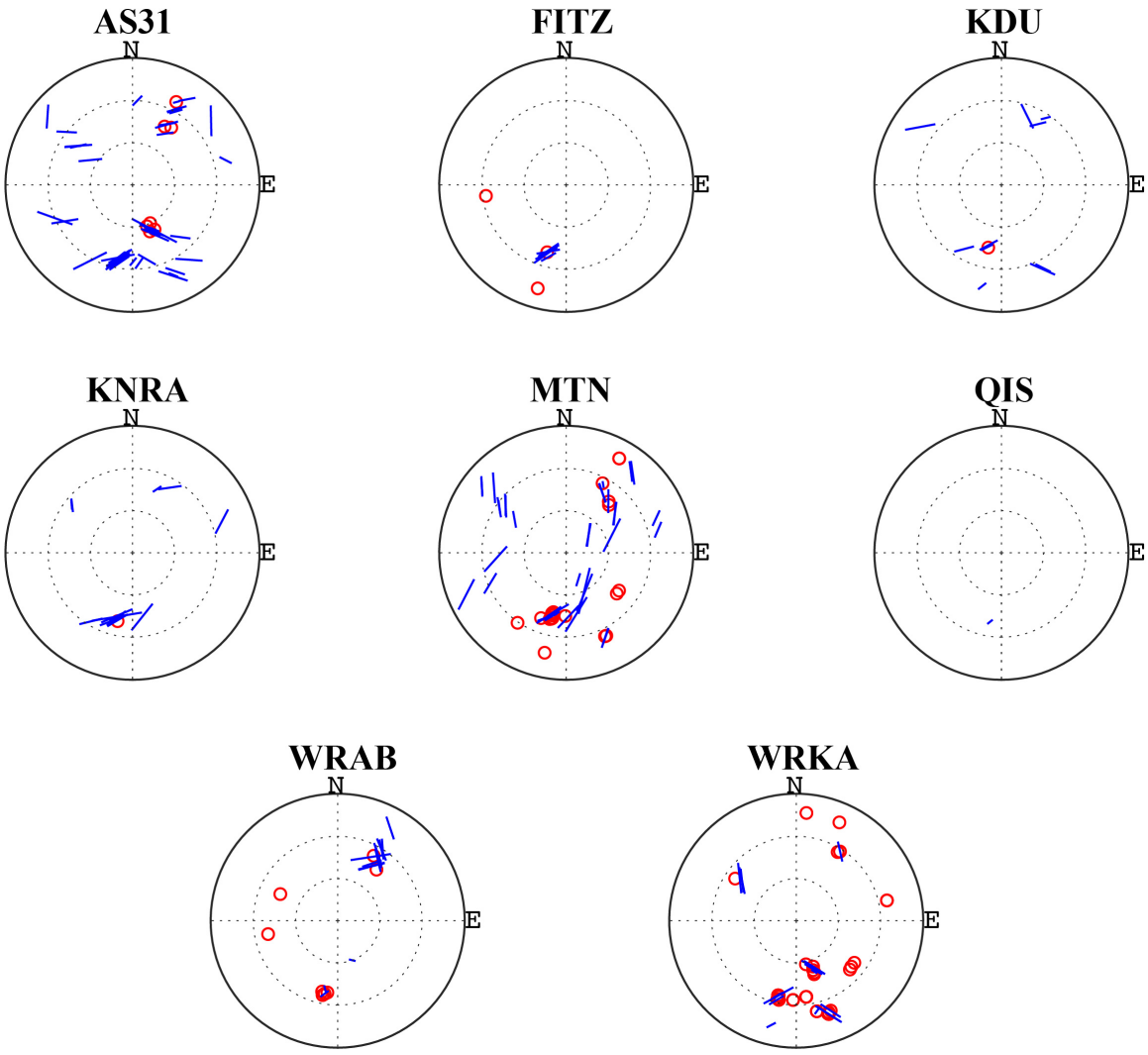


**Figure S2.4:** Stereoplots of shear wave splitting results (blue lines) and nulls (red lines) for the North Australian Craton (NAC). Backazimuth of events is along the circumference, while the inclination of the ray is plotted from 0° at the center to 15° at the edge.

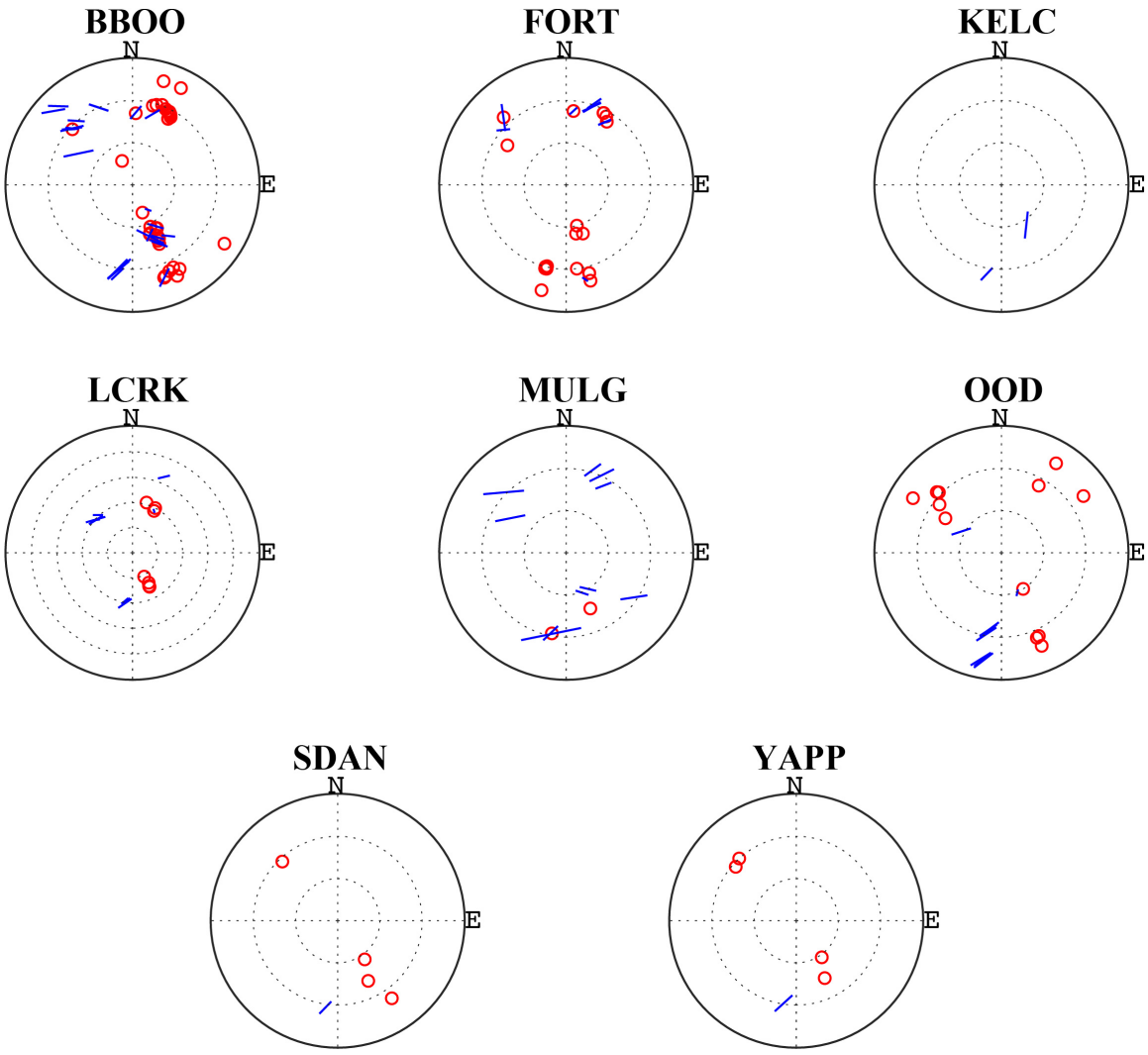


**Figure S2.5:** Stereoplots of shear wave splitting results (blue lines) and nulls (red lines) for the South Australian Craton (SAC). Backazimuth of events is along the circumference, while the inclination of the ray is plotted from 0° at the center to 15° at the edge.

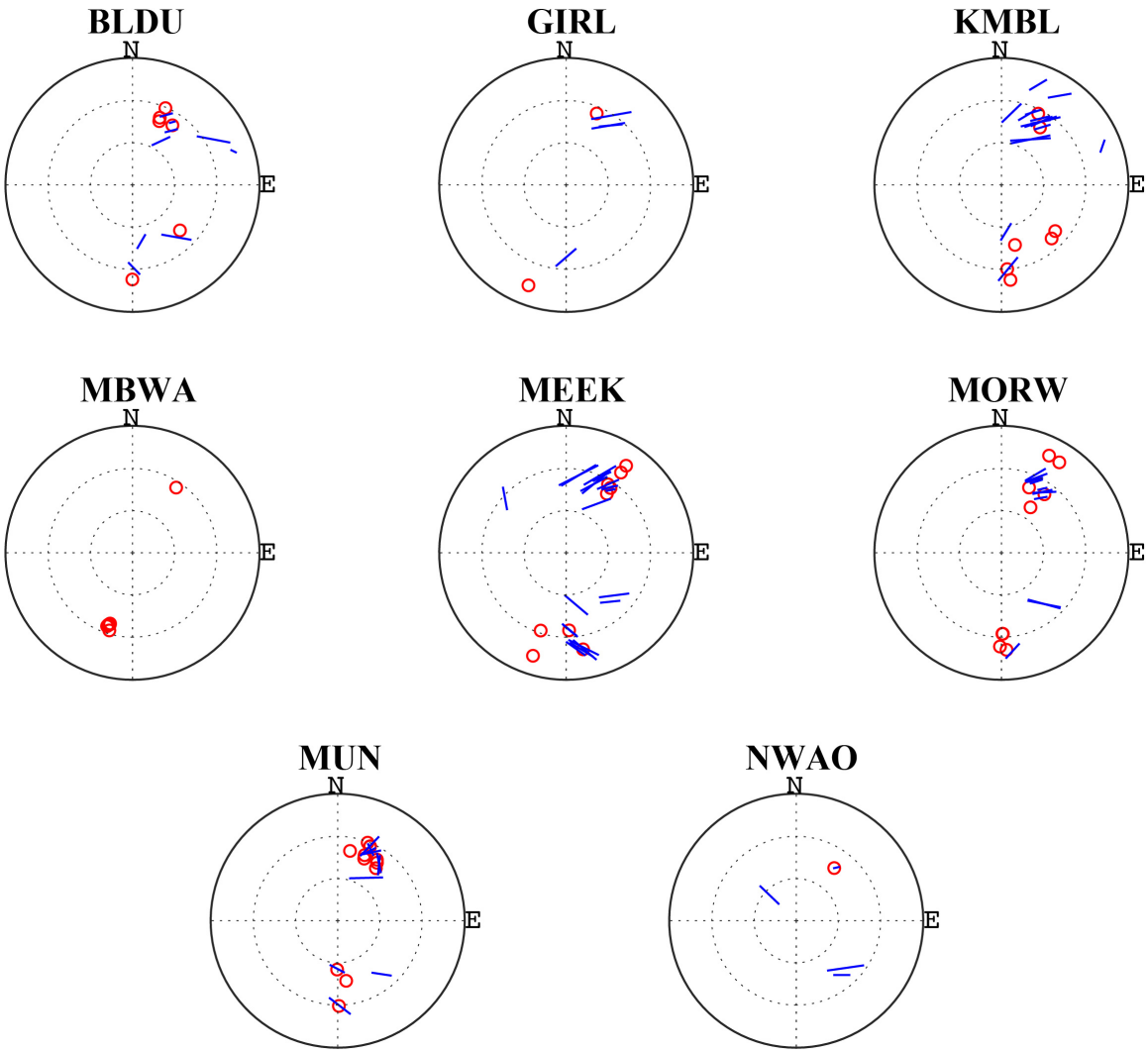


**Figure S2.6:** Stereoplots of shear wave splitting results (blue lines) and nulls (red lines) for the West Australian Craton (WAC). Backazimuth of events is along the circumference, while the inclination of the ray is plotted from 0° at the center to 15° at the edge.

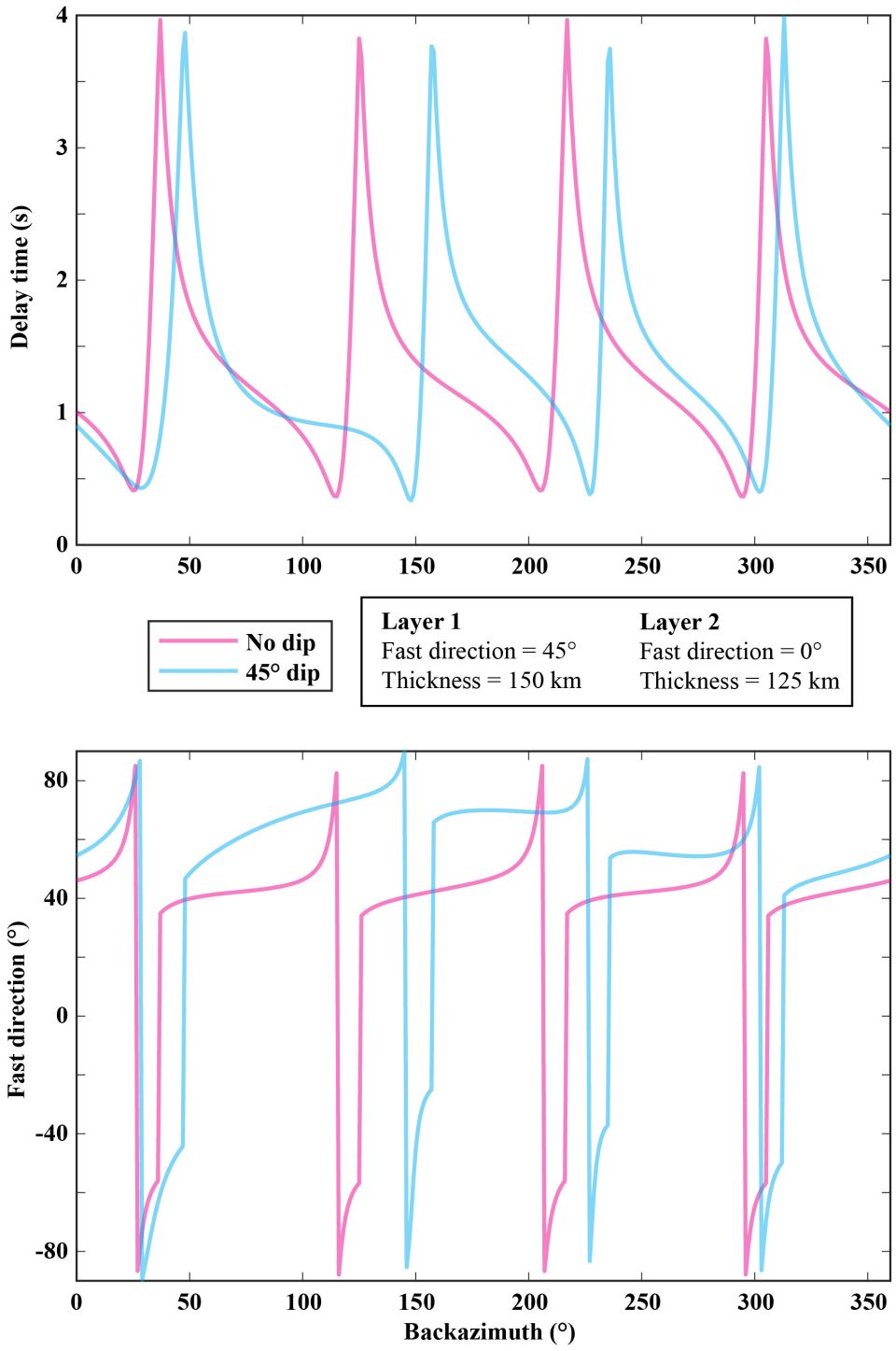


**Figure S2.7:** Effective splitting parameters for two two-layer models, calculated in MSAT (Walker and Wookey, 2012).

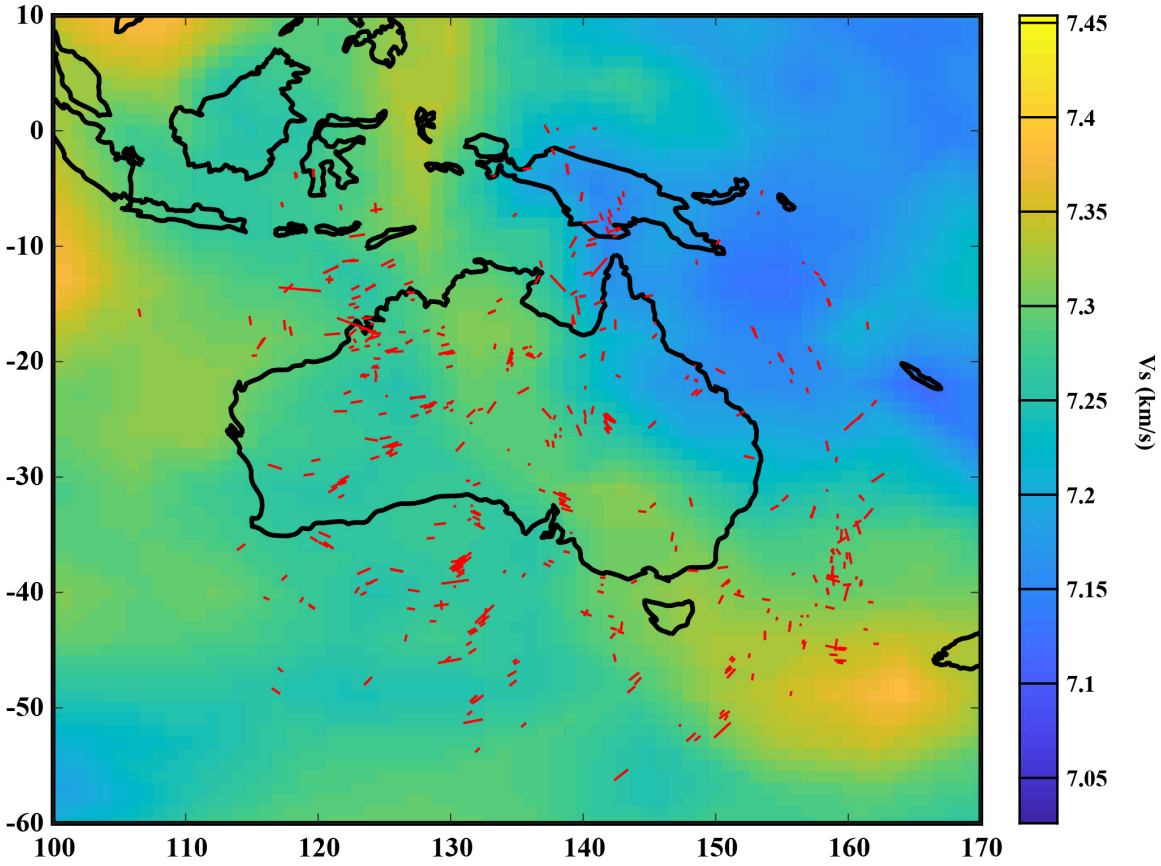


**Figure S2.8:** All non-null splits plotted at 2700 km depth against the 2700 km depth slice from the 3D2018_08Sv model (Debayle et al., 2016).

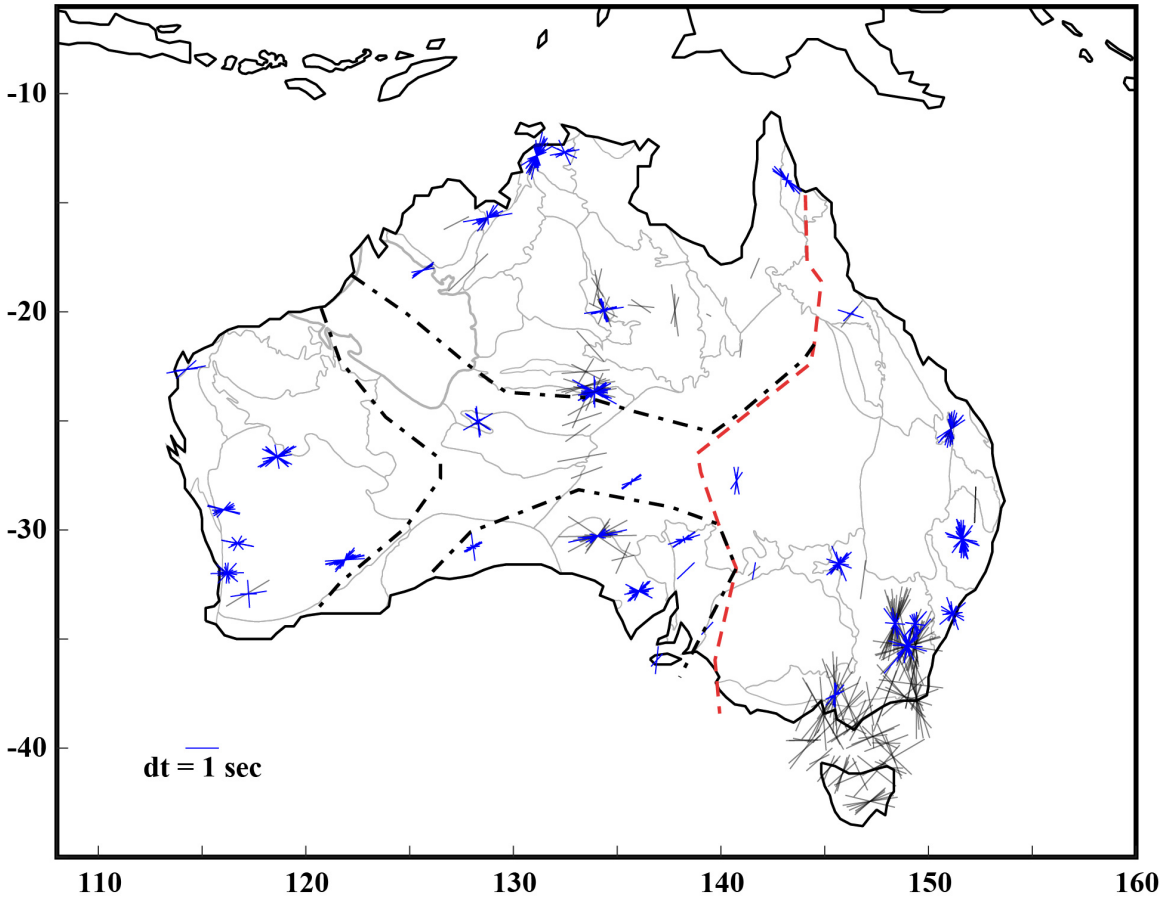


**Figure S2.9:** All non-null splits calculated for this study (blue lines) as well as splits from previously published studies (gray lines). An example split with a fast direction of 90° and a delay time of 1 second is shown in the lower left.

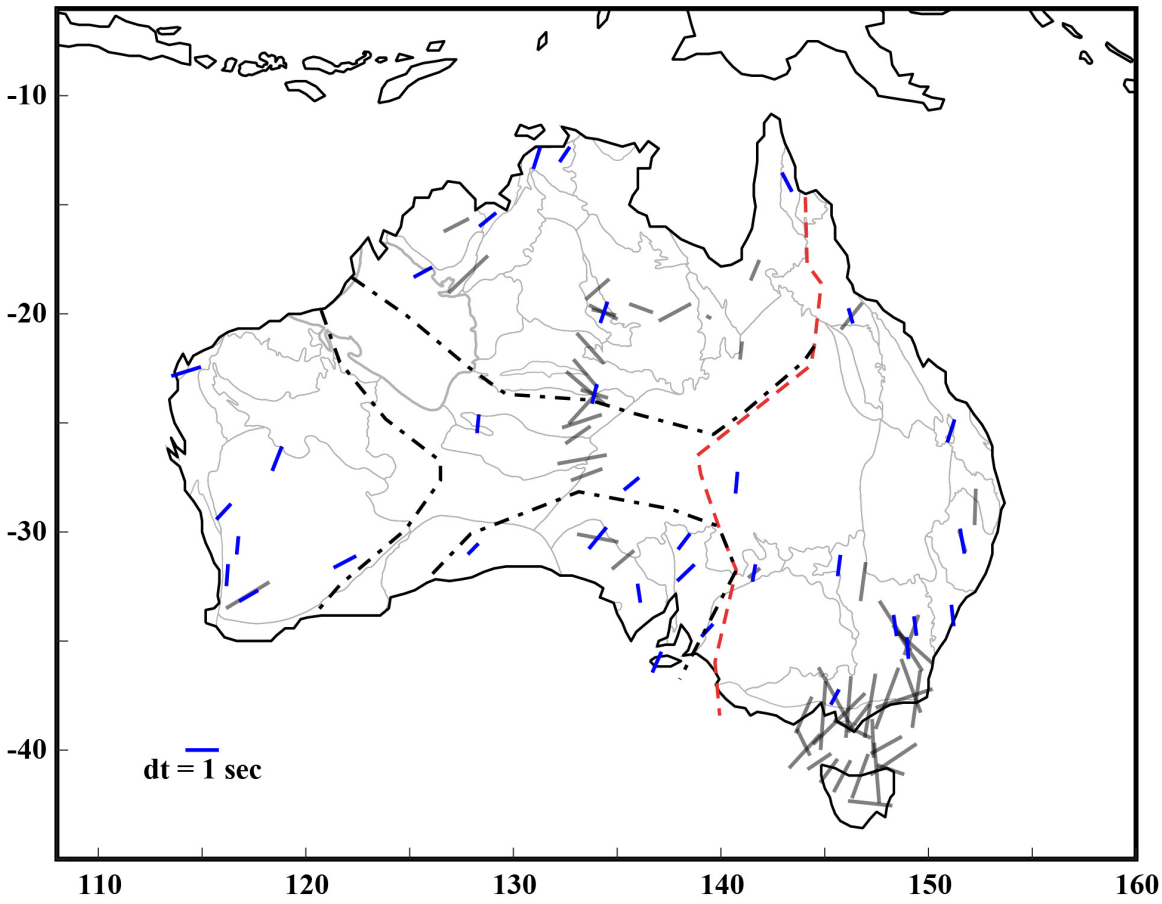


**Figure S2.10:** Average splitting parameters calculated for this study (blue lines) as well as average splitting parameters from previously published studies (gray lines). An example split with a fast direction of 90° and a delay time of 1 second is shown in the lower left.

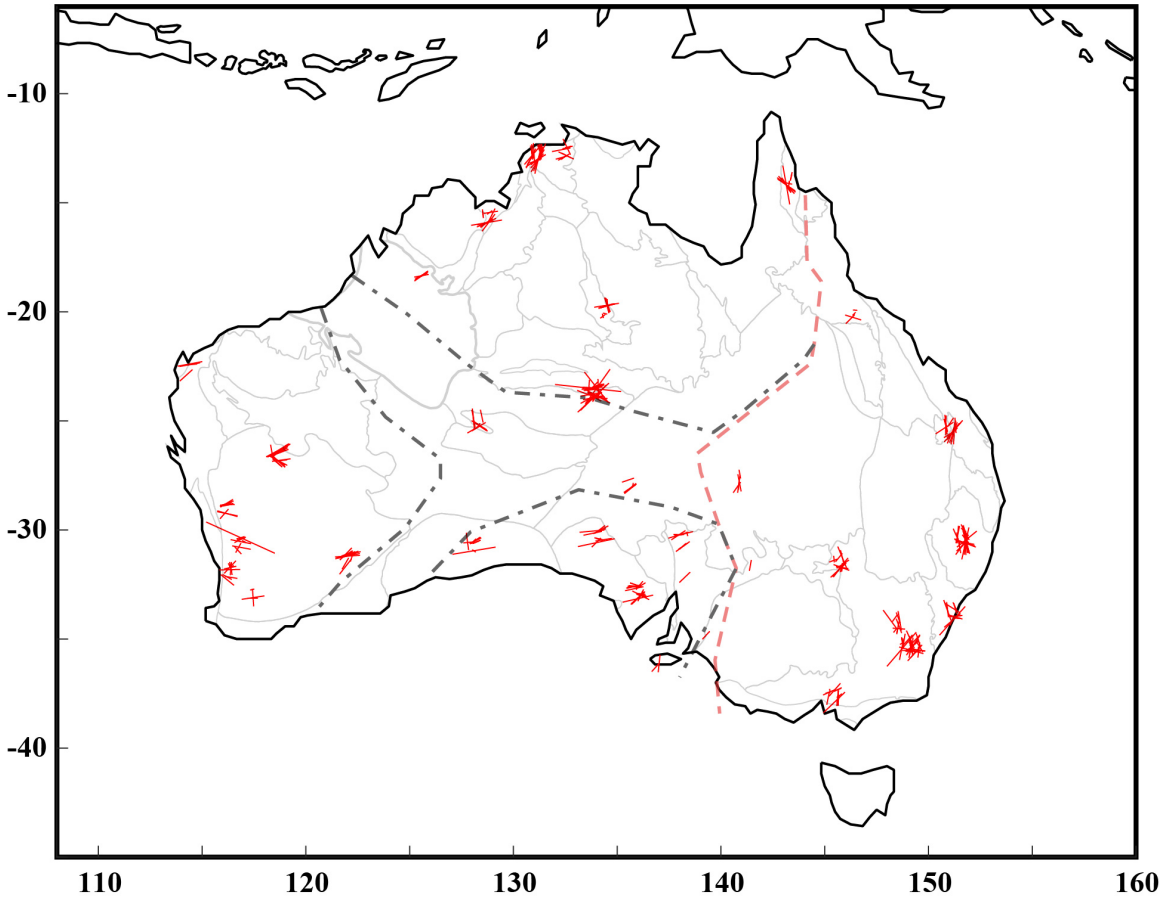


**Figure S2.11:** Shear wave splitting results projected along their raypaths to 150 km depth.

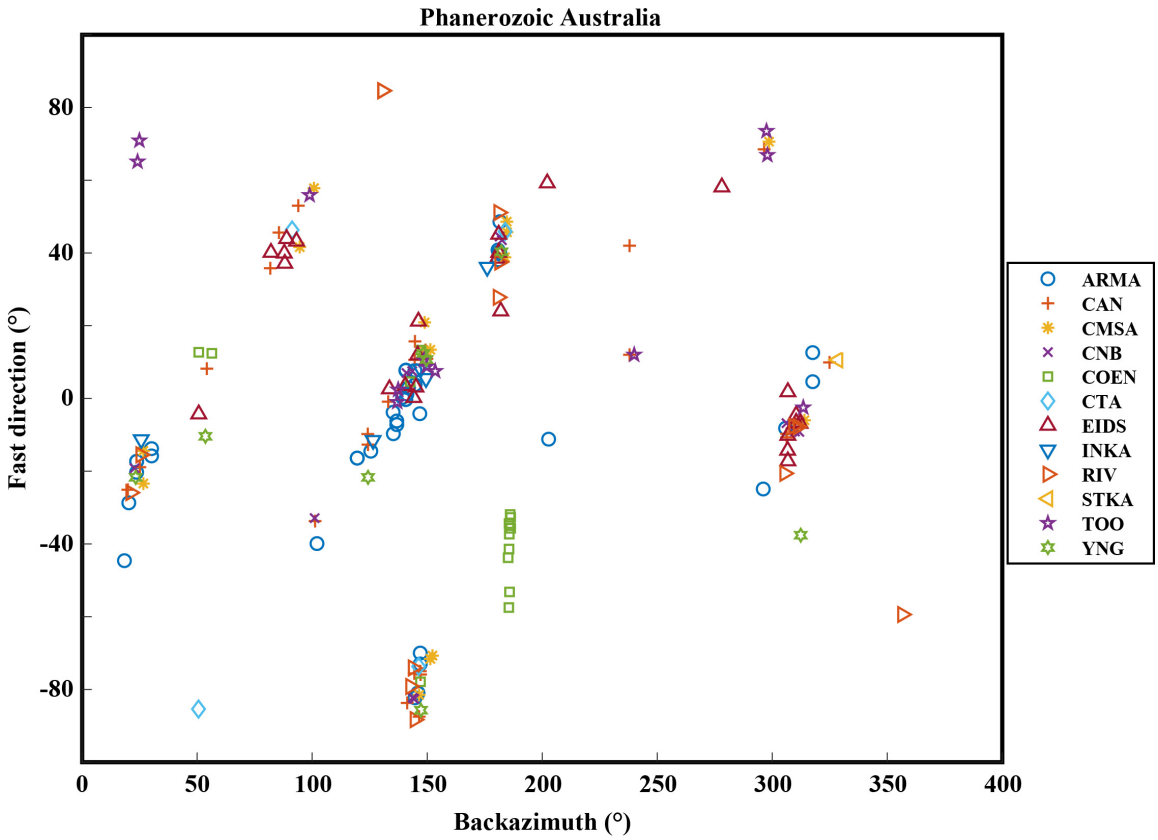


**Figure S2.12:** Scatter plot of shear wave splitting fast direction against backazimuth for all stations in Phanerozoic Australia.

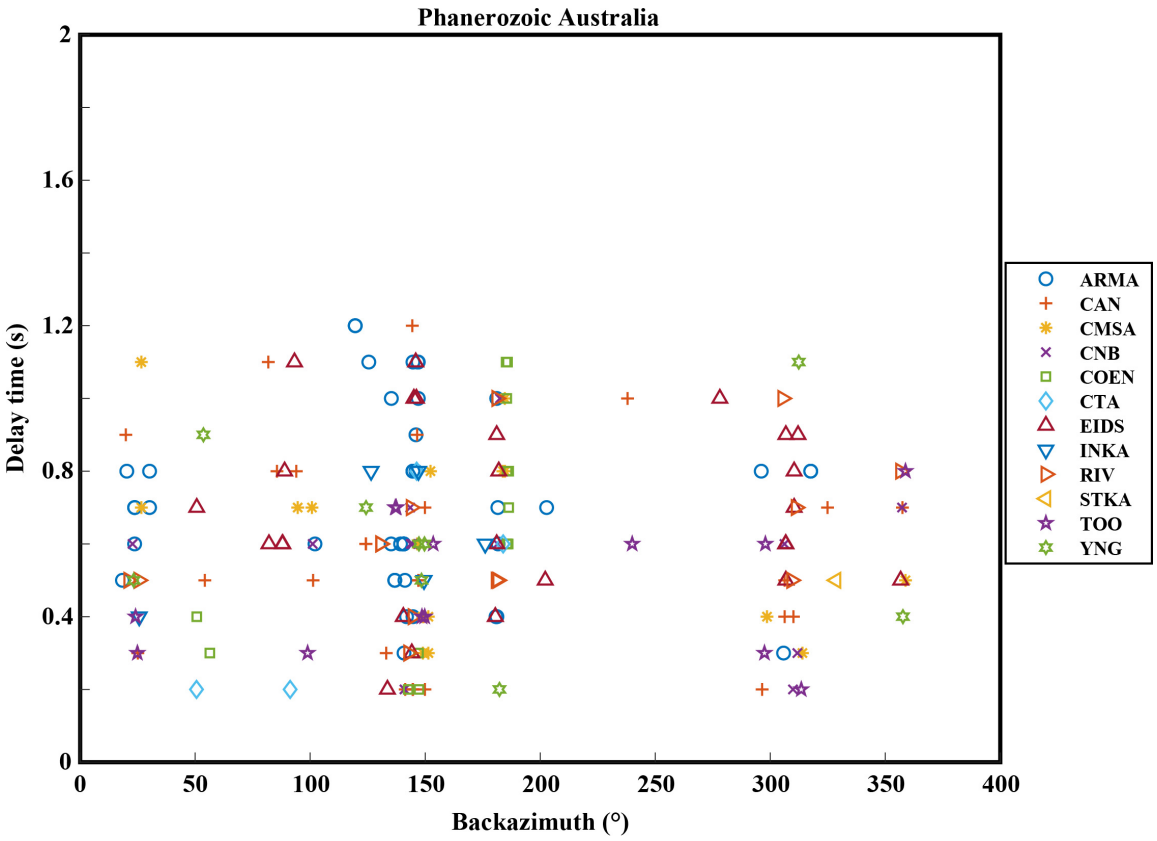


**Figure S2.13:** Scatter plot of shear wave splitting delay time against backazimuth for all stations in Phanerozoic Australia.

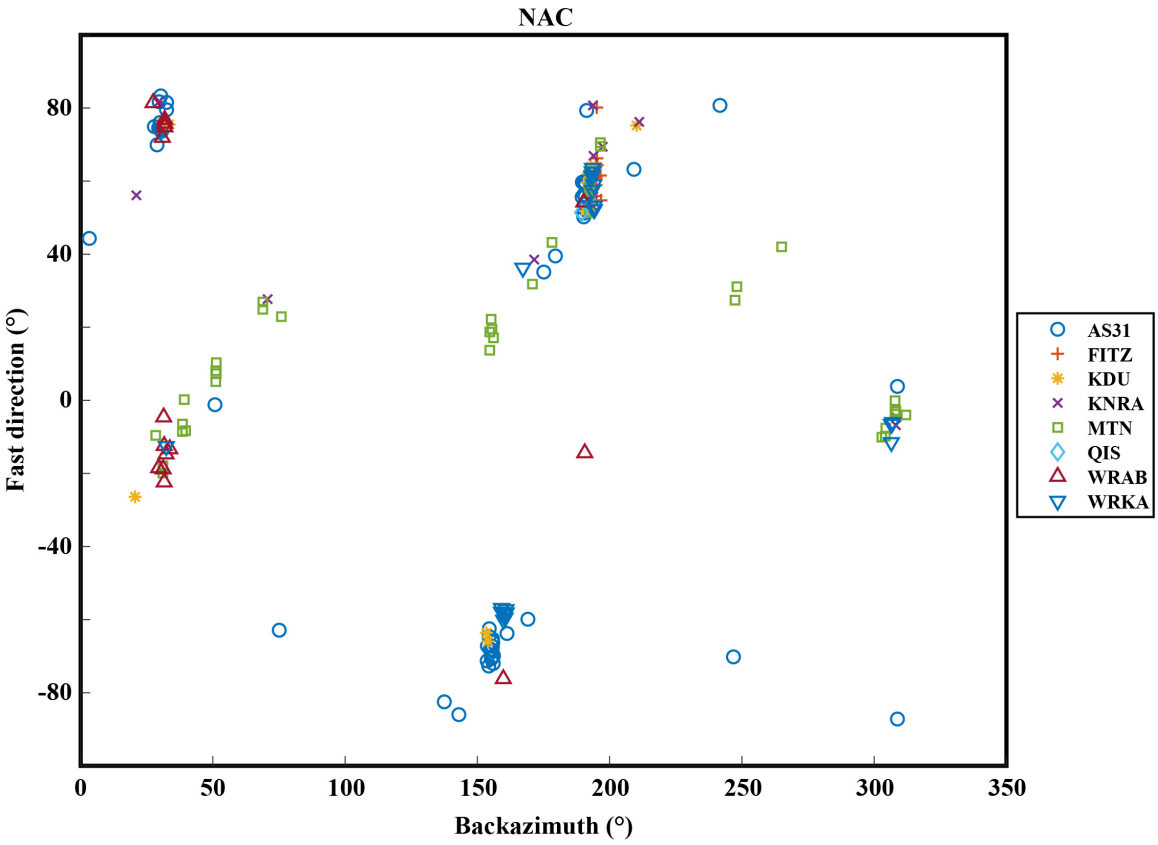


**Figure S2.14:** Scatter plot of shear wave splitting fast direction against backazimuth for all stations in the North Australian Craton (NAC).

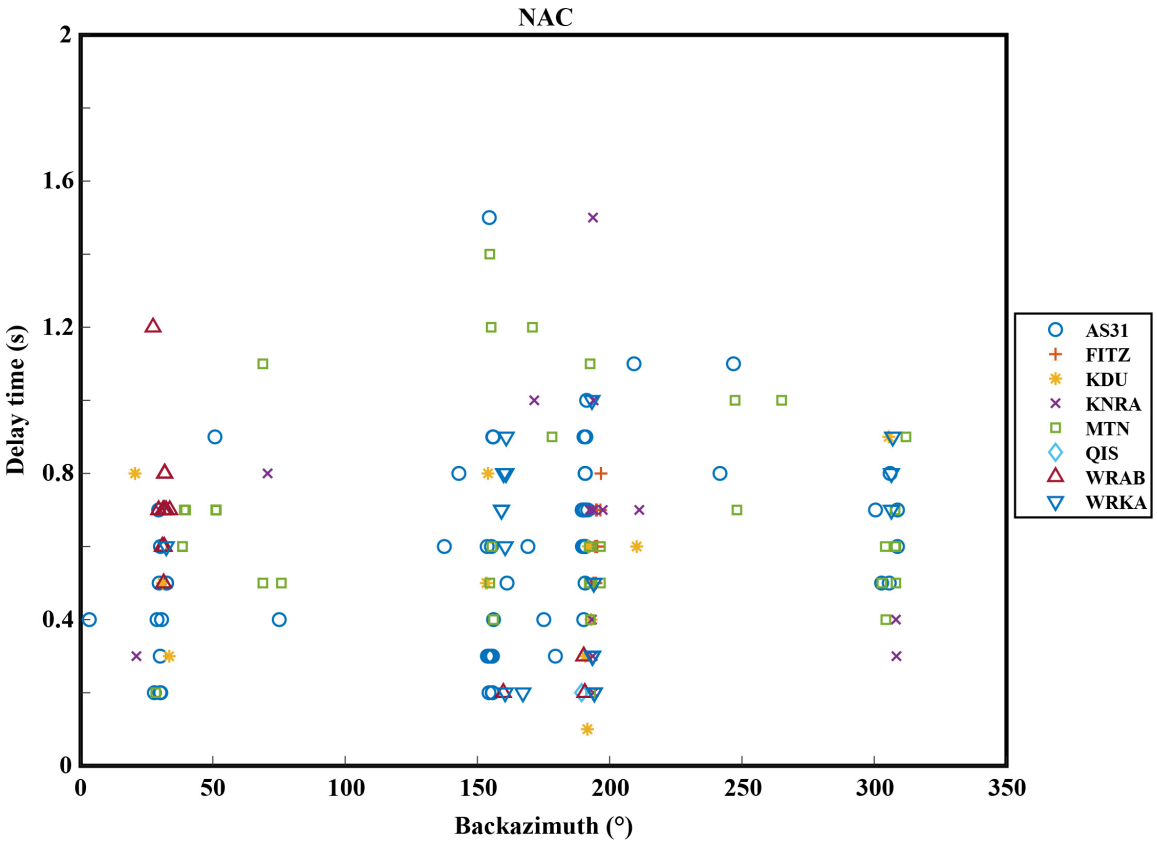


**Figure S2.15:** Scatter plot of shear wave splitting delay time against backazimuth for all stations in in the North Australian Craton (NAC).

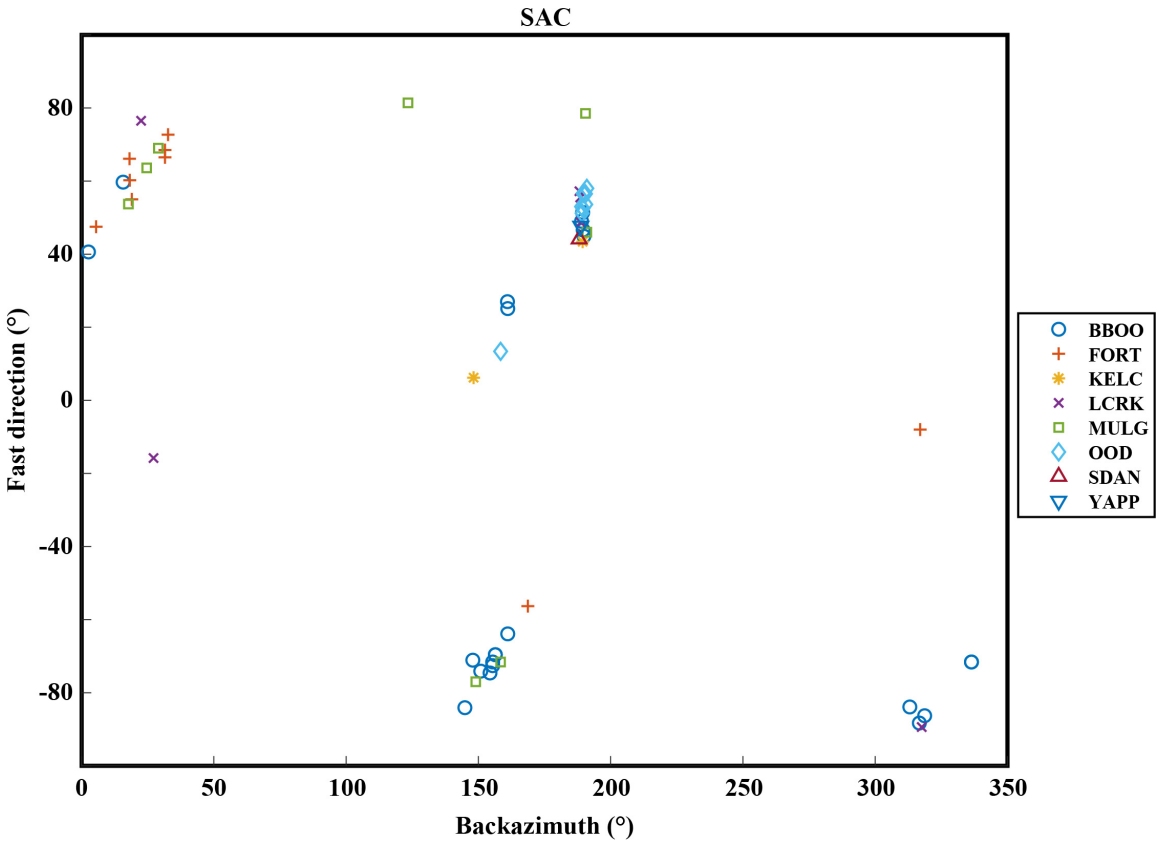


**Figure S2.16:** Scatter plot of shear wave splitting fast direction against backazimuth for all stations in the South Australian Craton (SAC).

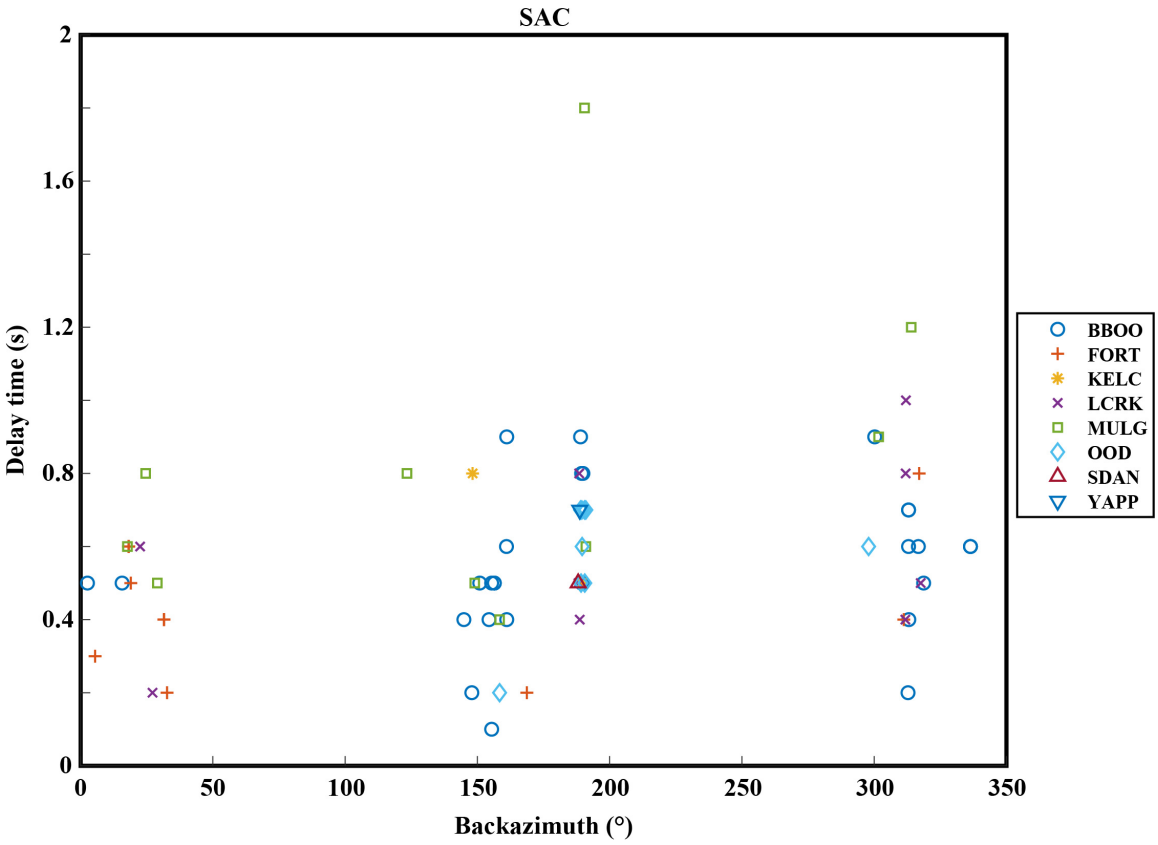


**Figure S2.17:** Scatter plot of shear wave splitting delay time against backazimuth for all stations in in the South Australian Craton (SAC).

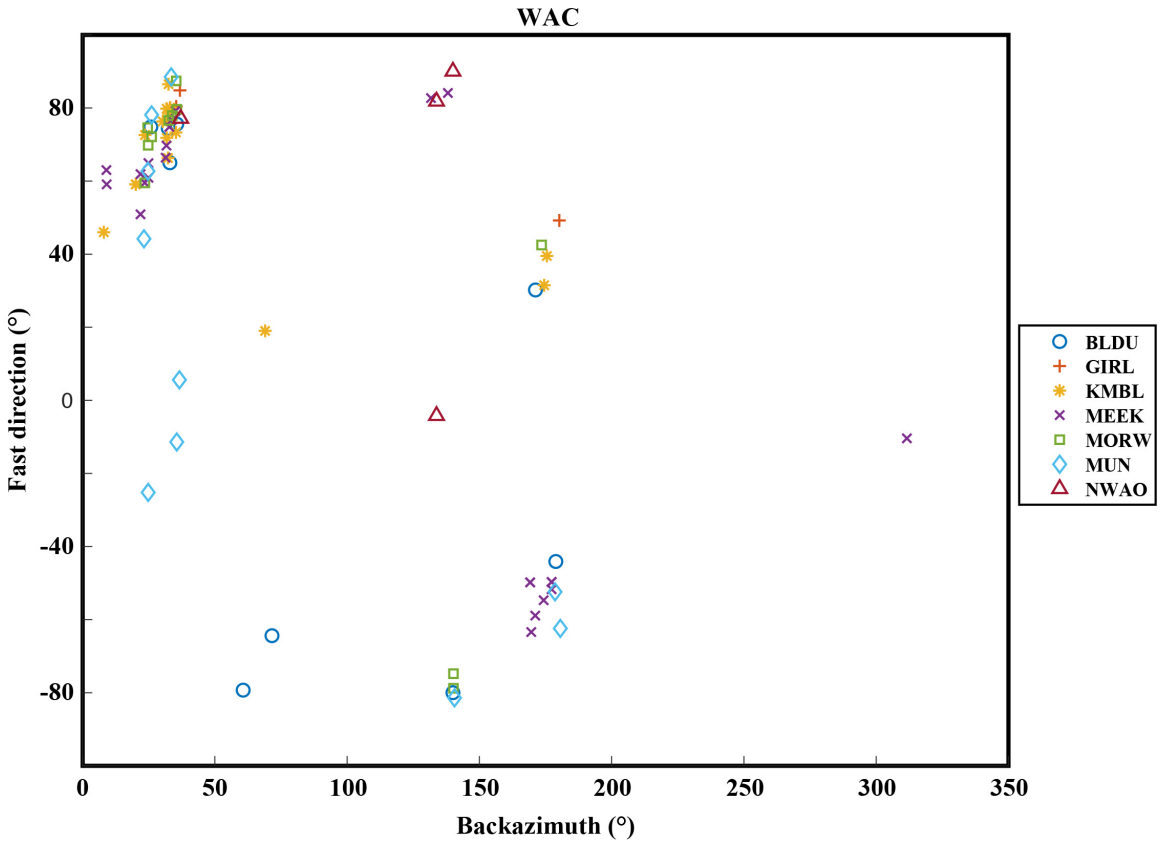


**Figure S2.18:** Scatter plot of shear wave splitting fast direction against backazimuth for all stations in the West Australian Craton (WAC).

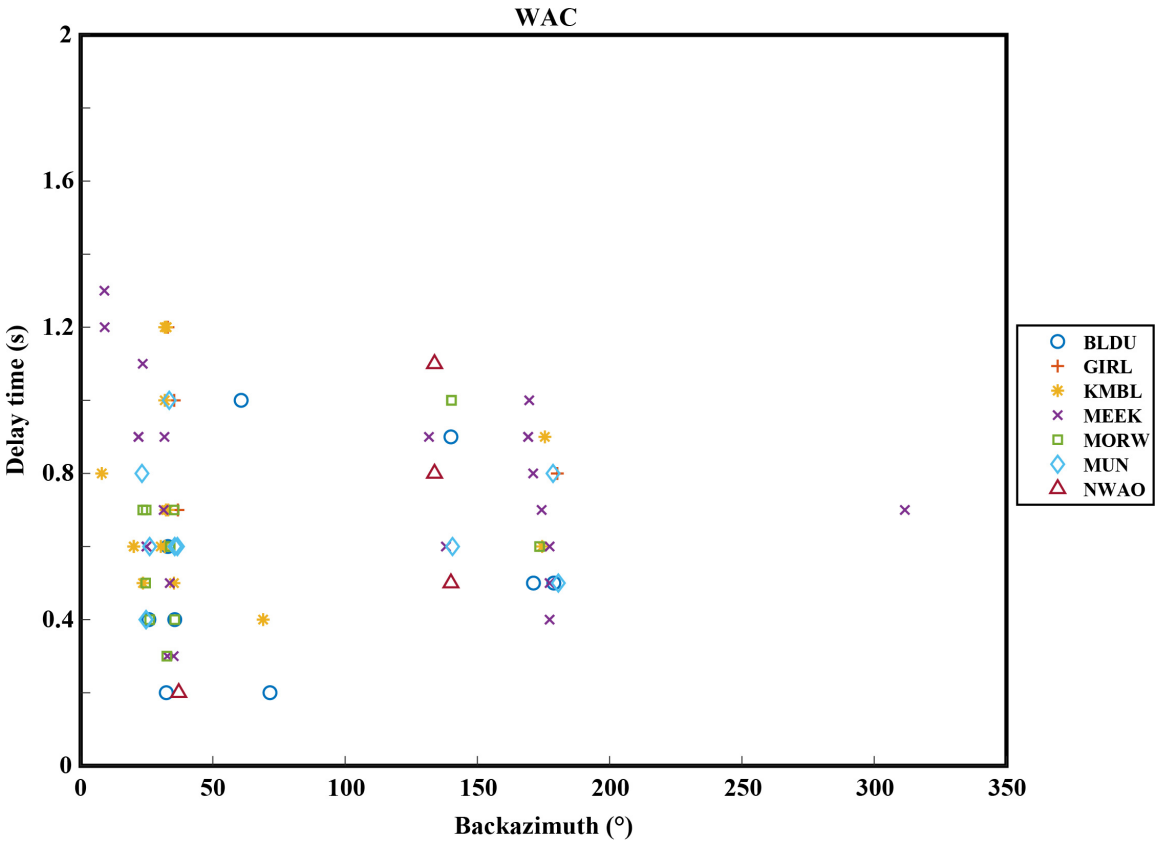


**Figure S2.19:** Scatter plot of shear wave splitting delay time against backazimuth for all stations in in the West Australian Craton (WAC).

**Appendix C:** Supplementary Material for Chapter 3

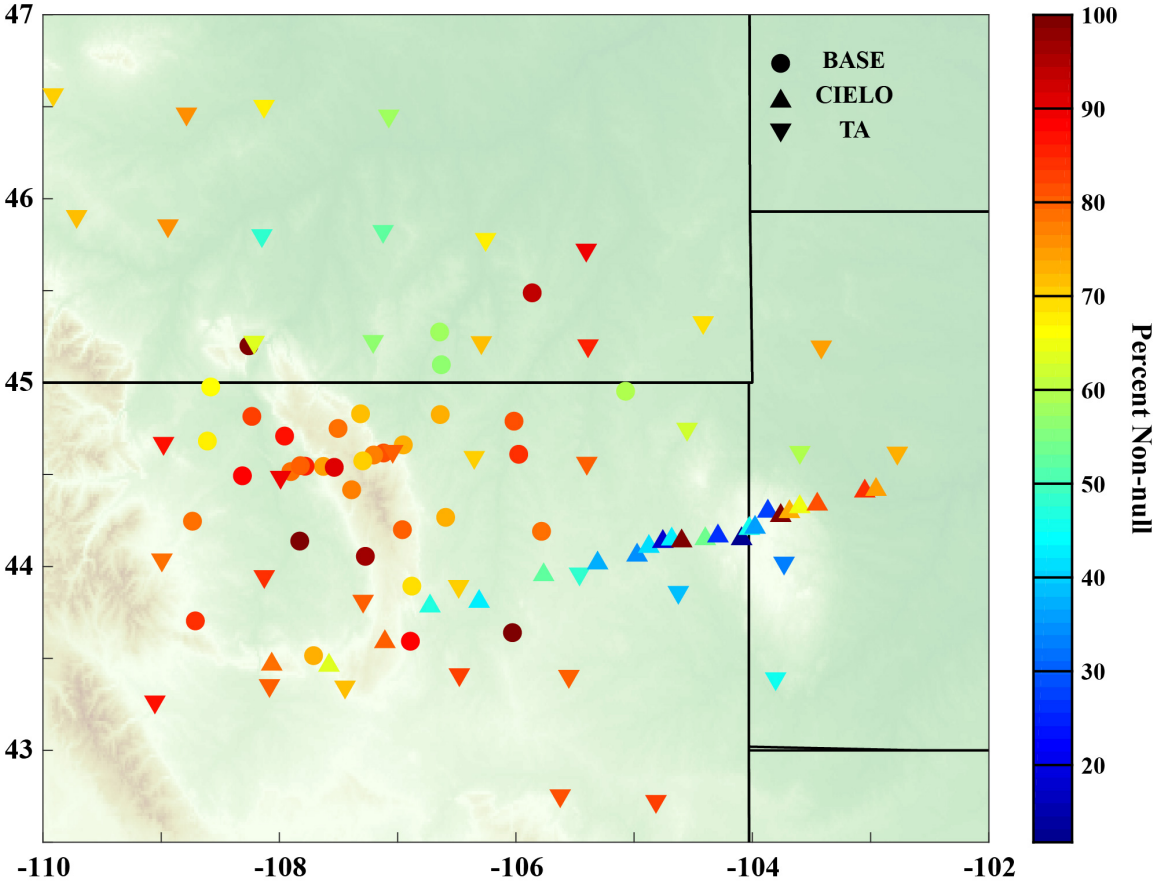


**Figure S3.1:** Percentage of non-null splits per station. Circles are BASE stations, triangles are CIELO stations, and inverted triangles are TA stations.

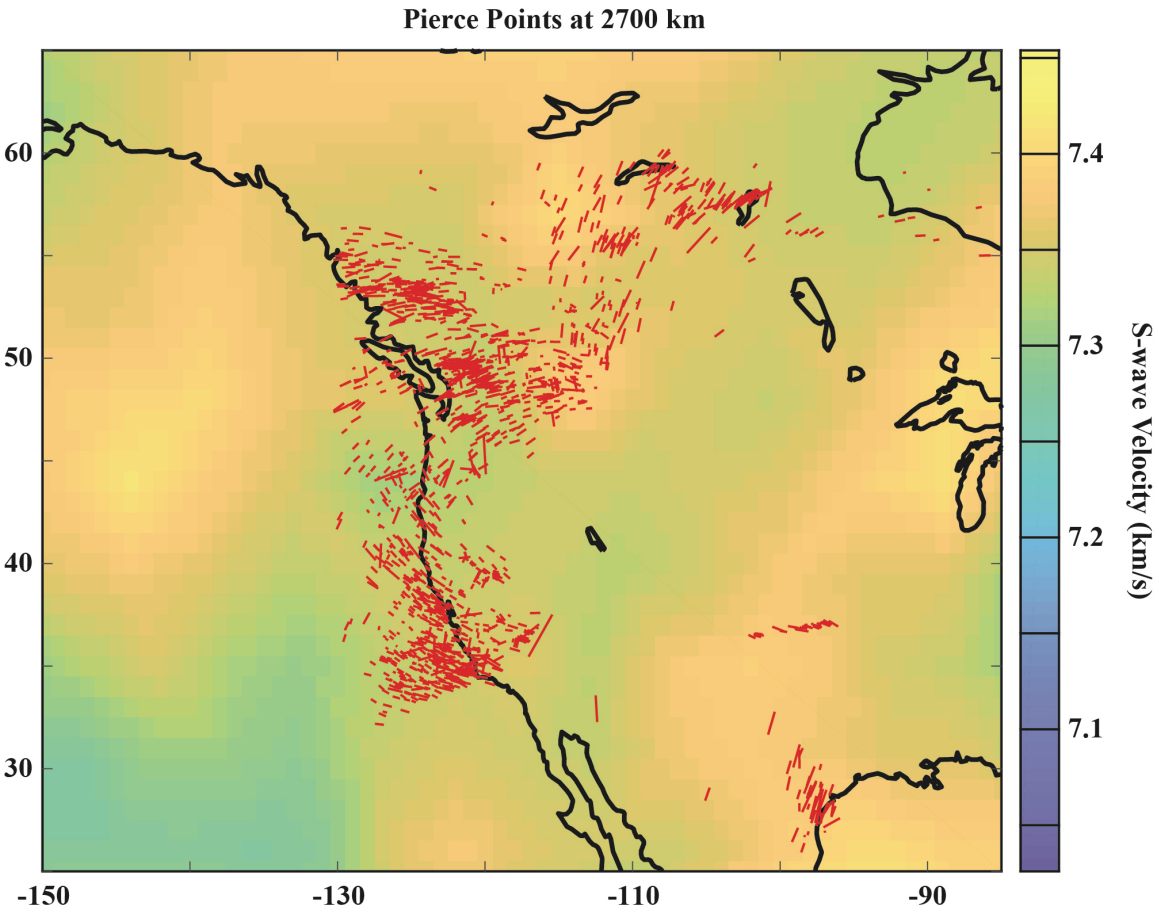


**Figure S3.2:** Non-null splits plotted at their piercing points for 2700 km depth (i.e. within the D" layer). Splits are plotted over the 2700 km depth slice from the GyPSuM tomography model (Simmons et al., 2010).

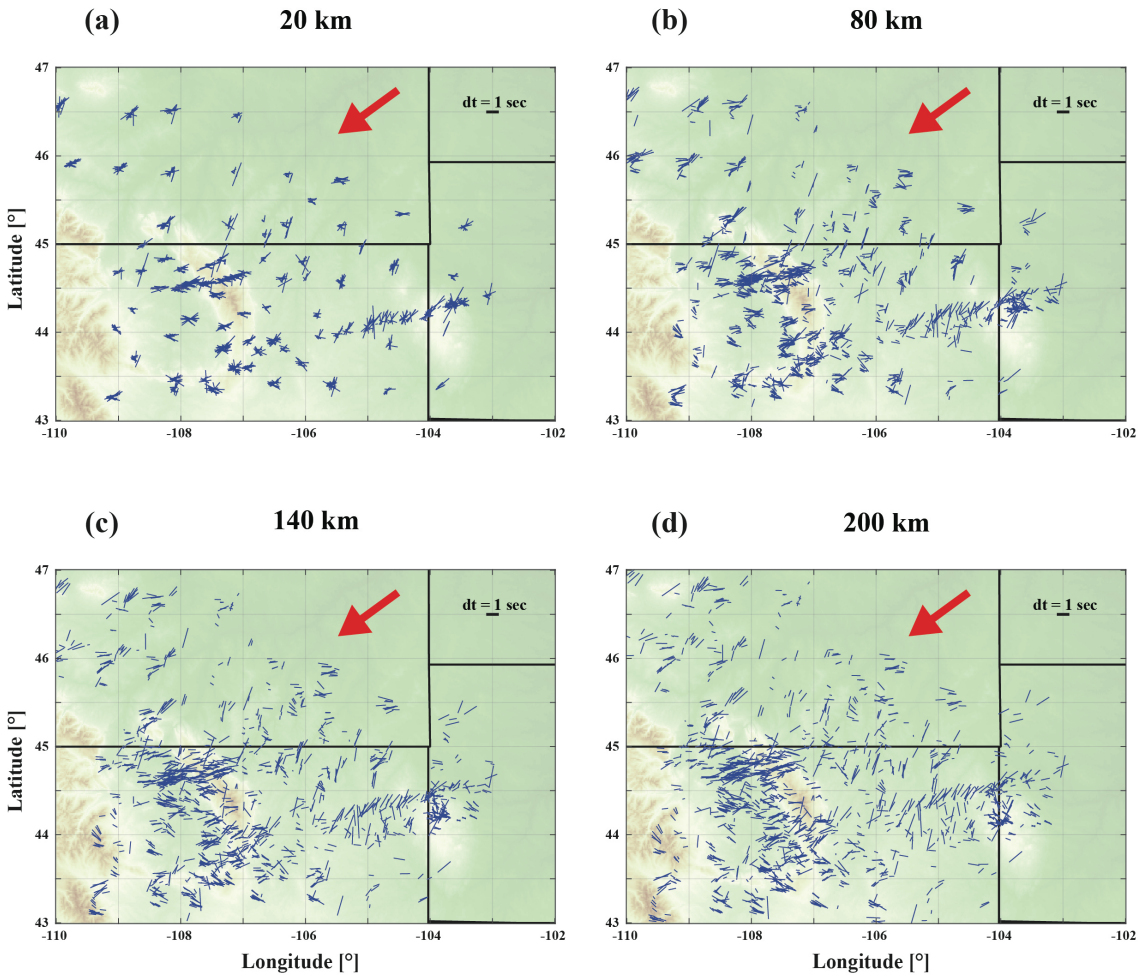


**Figure S3.3:** Piercing point of all splits at four different depths (20, 80, 140, and 200 km). An example split with a fast direction of 90° and 1 second delay time is plotted in the upper left corner. The large red arrow is the apparent plate motion in this region.

**Appendix D:** Supplementary Material for Chapter 4

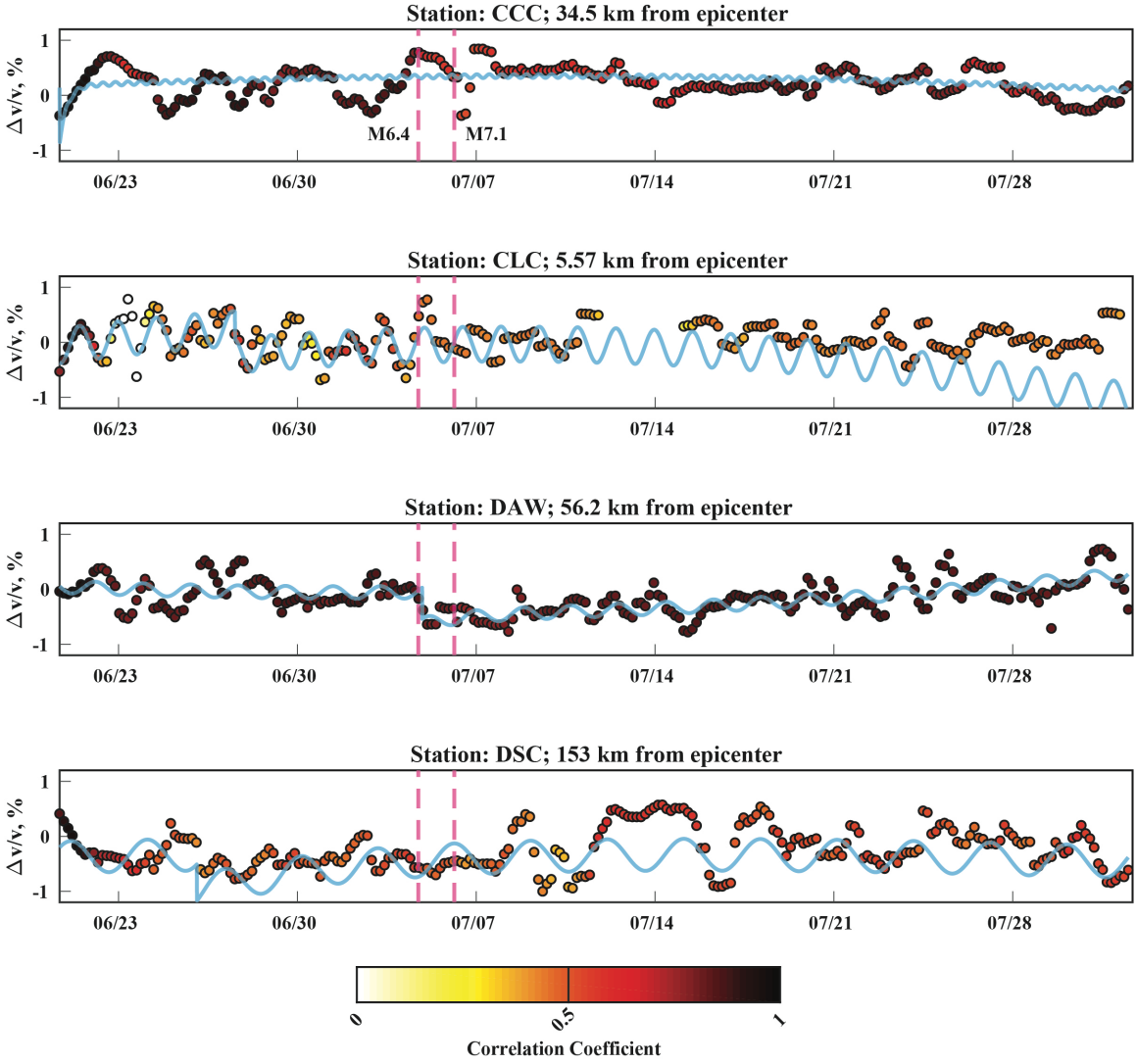

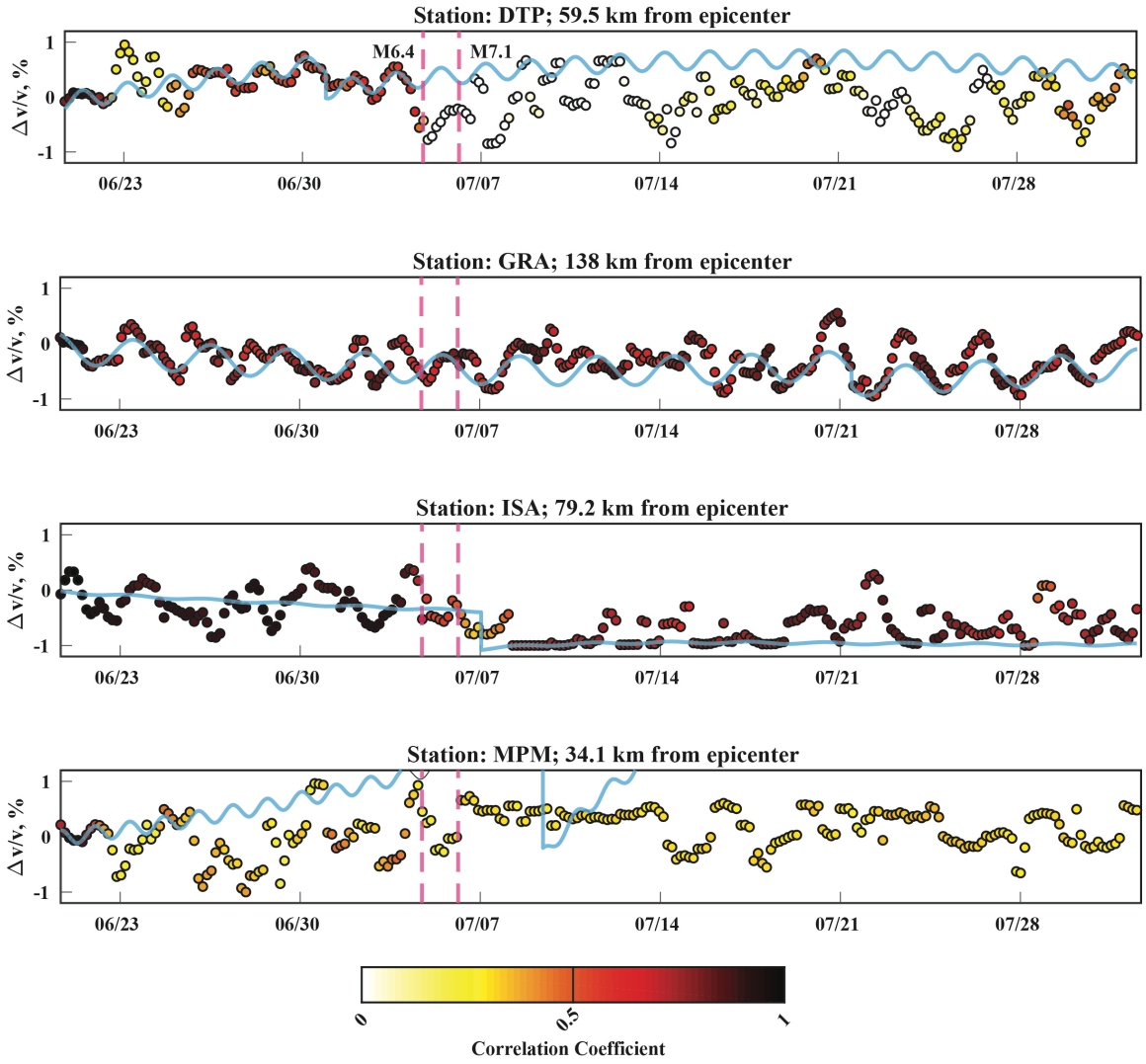
Station: DTP; 59.5 km from epicenter
M6.4
M7.1
Δv/v, %
1
0
-1
06/23
06/30
07/07
07/14
07/21
07/28
Station: GRA; 138 km from epicenter
Station: ISA; 79.2 km from epicenter
Station: MPM; 34.1 km from epicenter
0
0.5
1
Correlation Coefficient

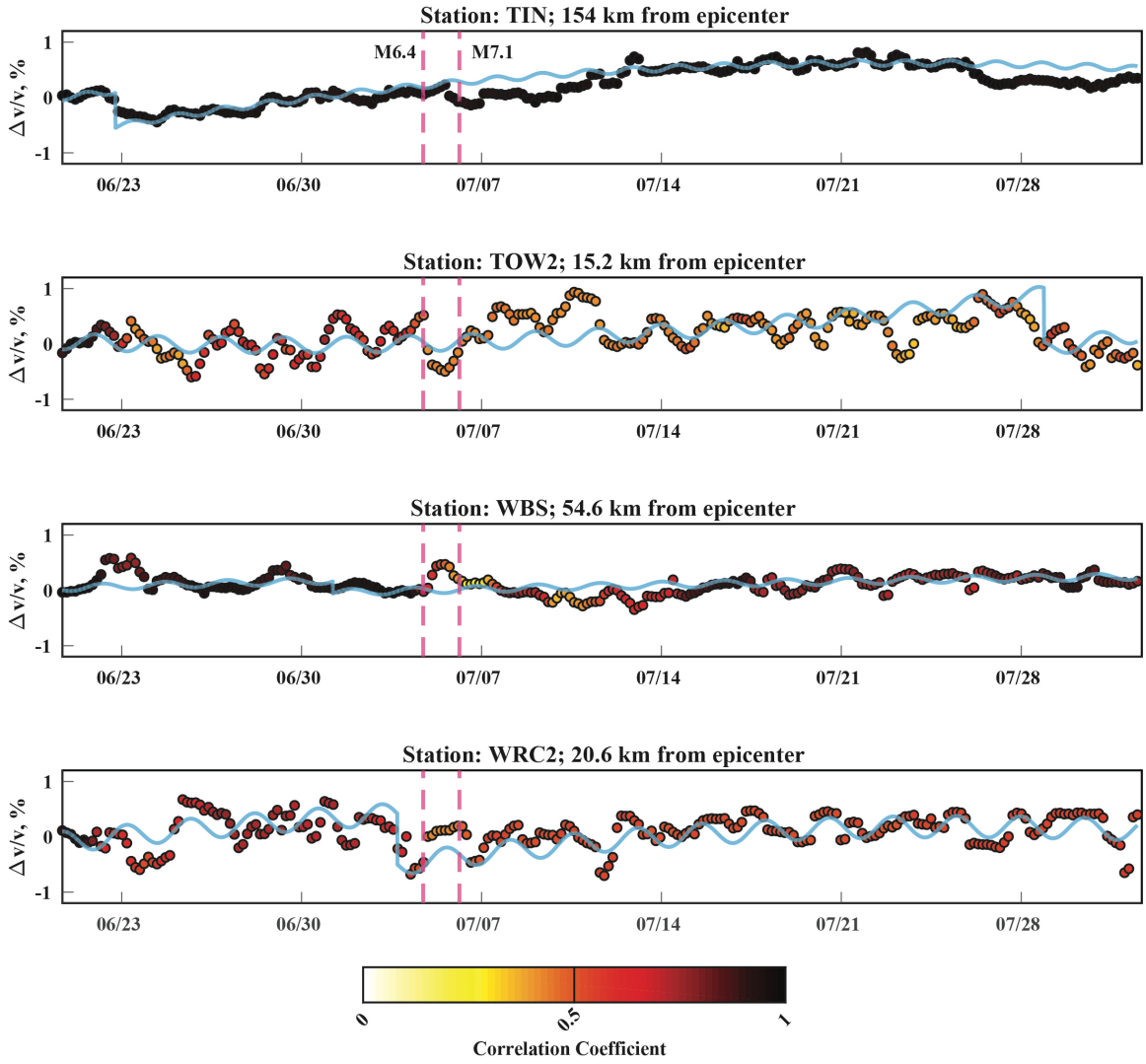


**Figure S4.1:** Change in velocity (dv/v) plotted against time for all stations not shown in **Figures 4.2** and **4.3**.

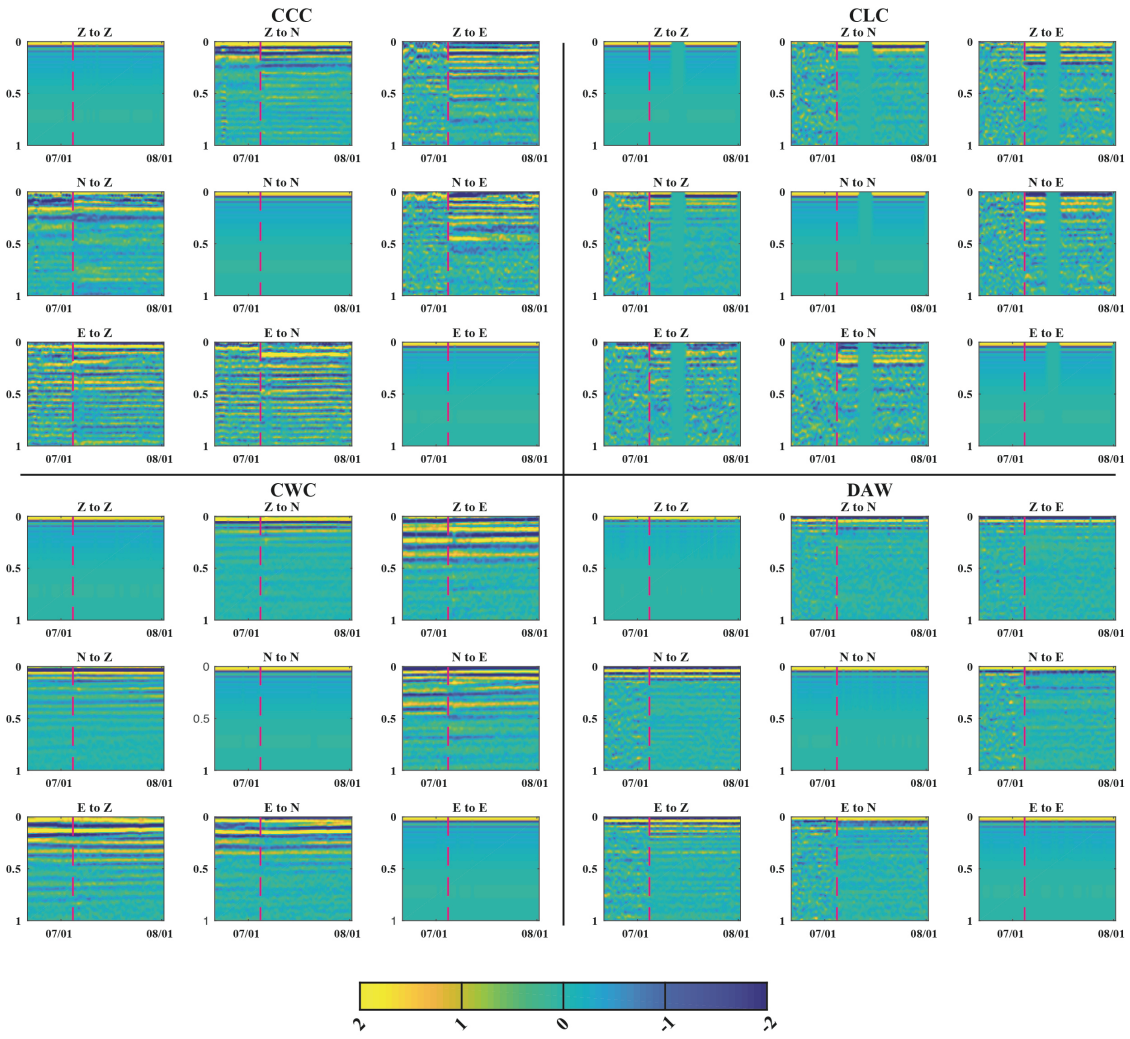
CCC
CLC
CWC
DAW
Z to Z
Z to N
Z to E
N to Z
N to N
N to E
E to Z
E to N
E to E
0
0.5
1
07/01
08/01
2
1
0
-1
-2

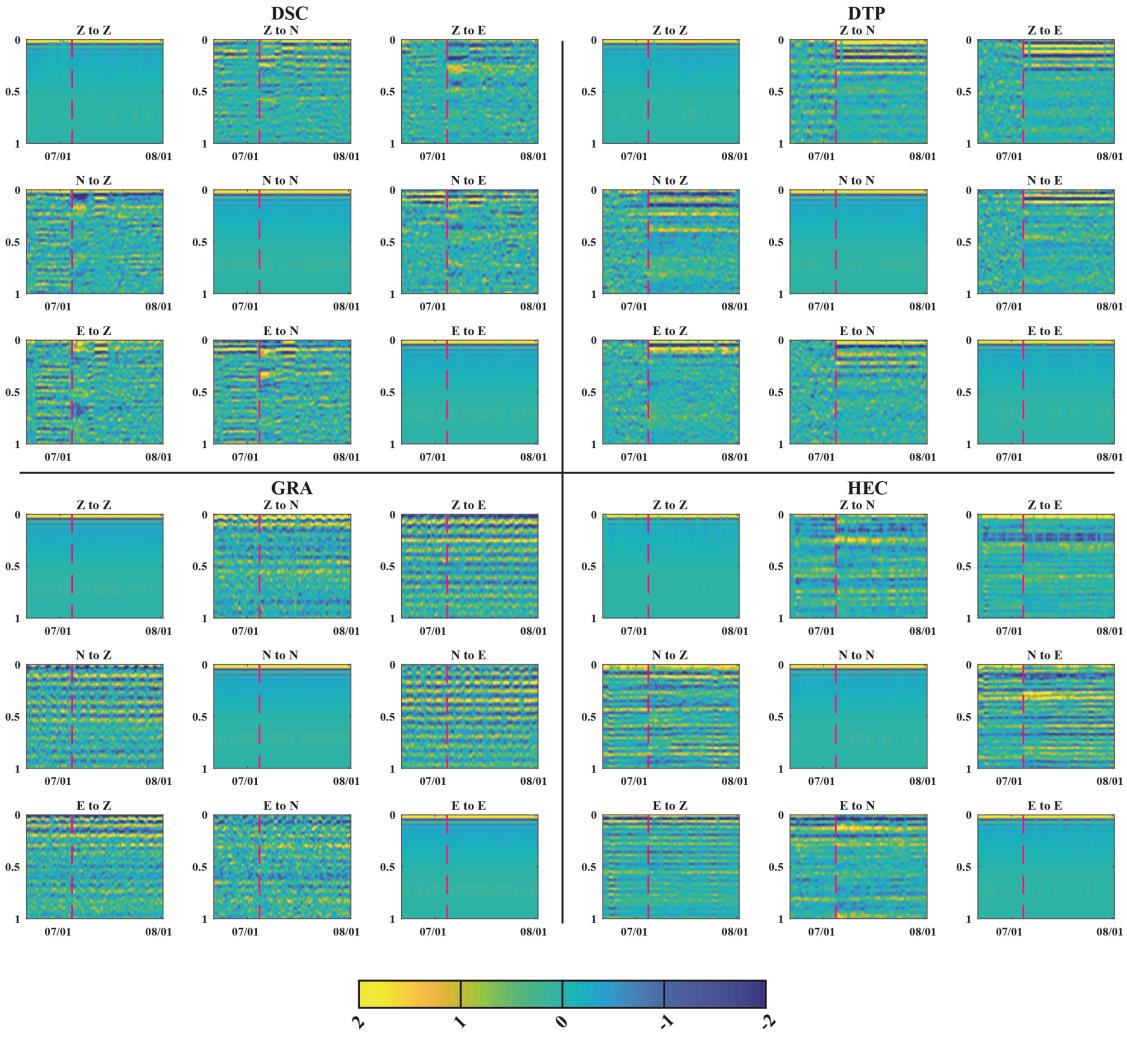
DSC
DTP
GRA
HEC
Z to Z
Z to N
Z to E
N to Z
N to N
N to E
E to Z
E to N
E to E
0
0.5
1
07/01
08/01
2
1
0
-1
-2

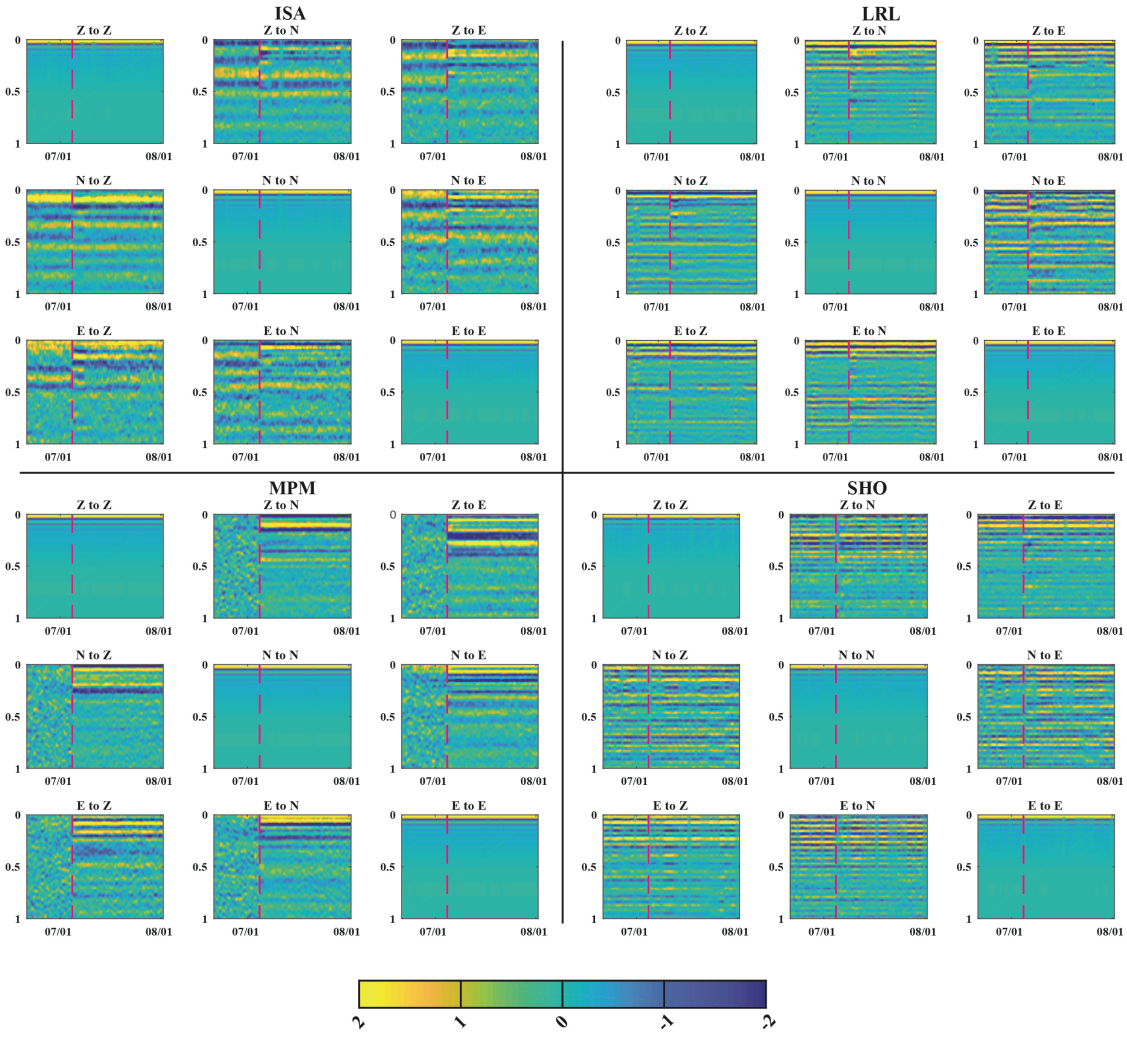
ISA
LRL
MPM
SHO
Z to Z
Z to N
Z to E
N to Z
N to N
N to E
E to Z
E to N
E to E
0
0.5
1
07/01
08/01
2
1
0
-1
-2

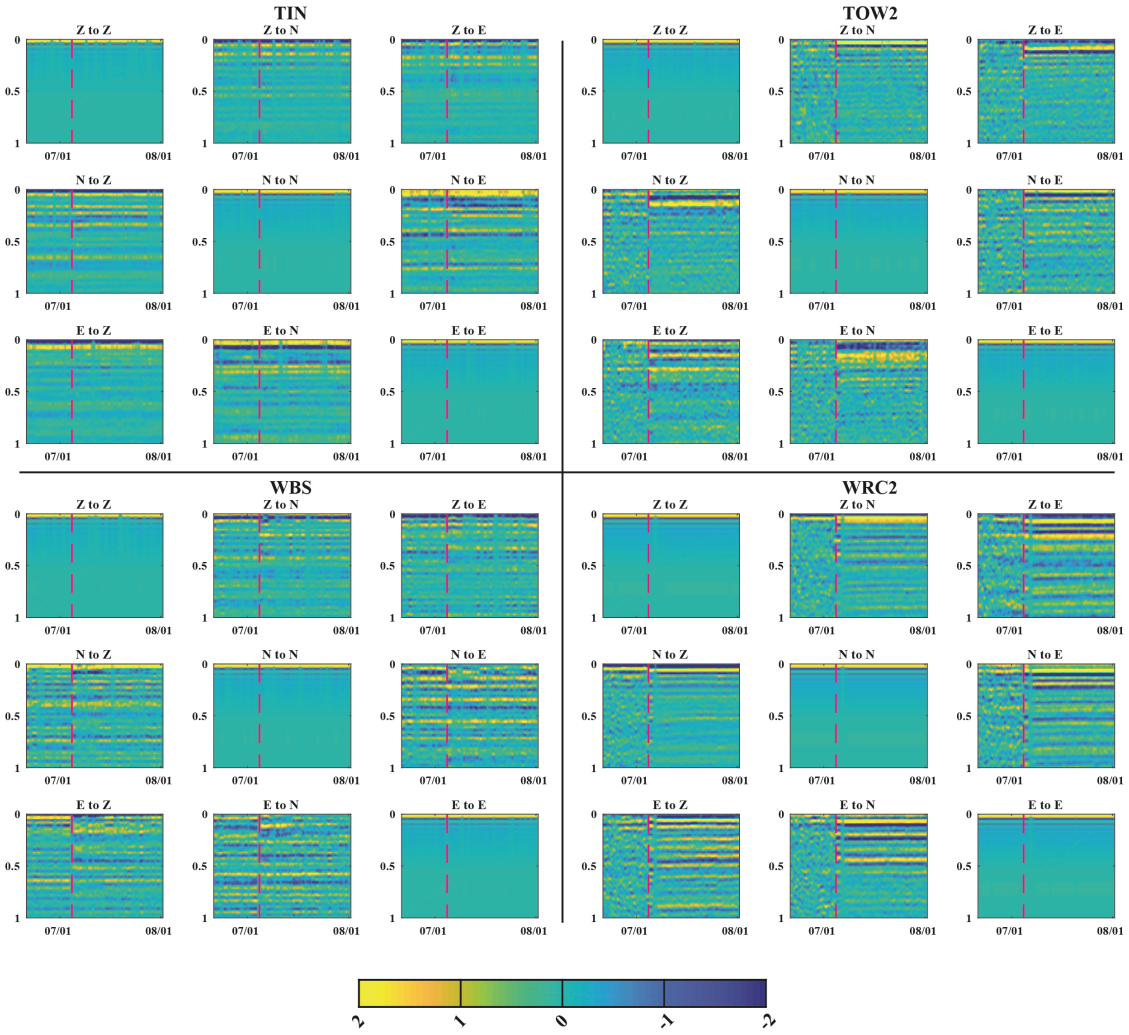
TIN
Z to Z
Z to N
Z to E
N to Z
N to N
N to E
E to Z
E to N
E to E
TOW2
WBS
WRC2
0
0.5
1
07/01
08/01
2
1
0
-1
-2

**Figure S4.2 (previous pages):** Daily cross-correlations for all stations not shown in **Figure 4.5**.

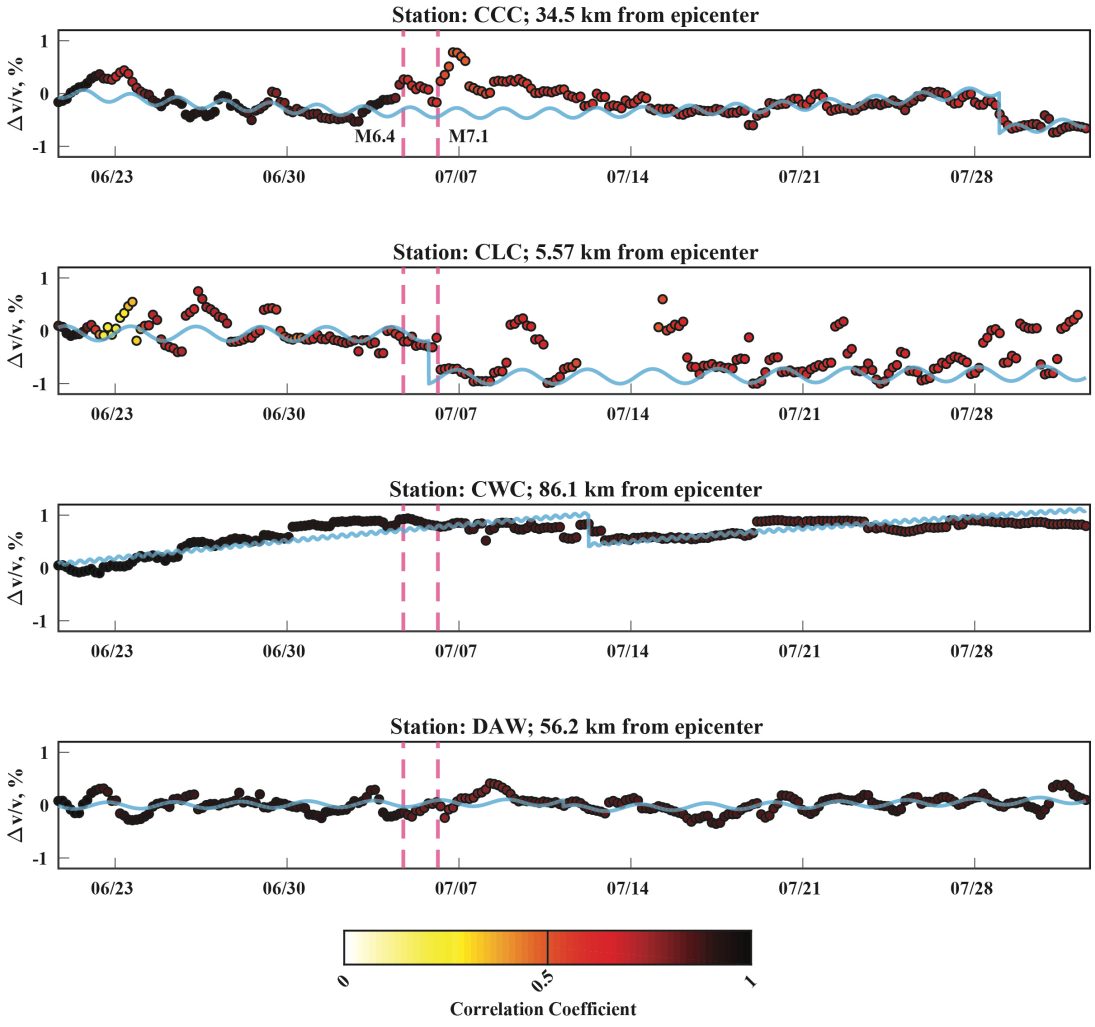
Station: CCC; 34.5 km from epicenter
Δv/v, %
1
0
-1
M6.4
M7.1
06/23
06/30
07/07
07/14
07/21
07/28
Station: CLC; 5.57 km from epicenter
Δv/v, %
1
0
-1
06/23
06/30
07/07
07/14
07/21
07/28
Station: CWC; 86.1 km from epicenter
Δv/v, %
1
0
-1
06/23
06/30
07/07
07/14
07/21
07/28
Station: DAW; 56.2 km from epicenter
Δv/v, %
1
0
-1
06/23
06/30
07/07
07/14
07/21
07/28
0
0.5
1
Correlation Coefficient

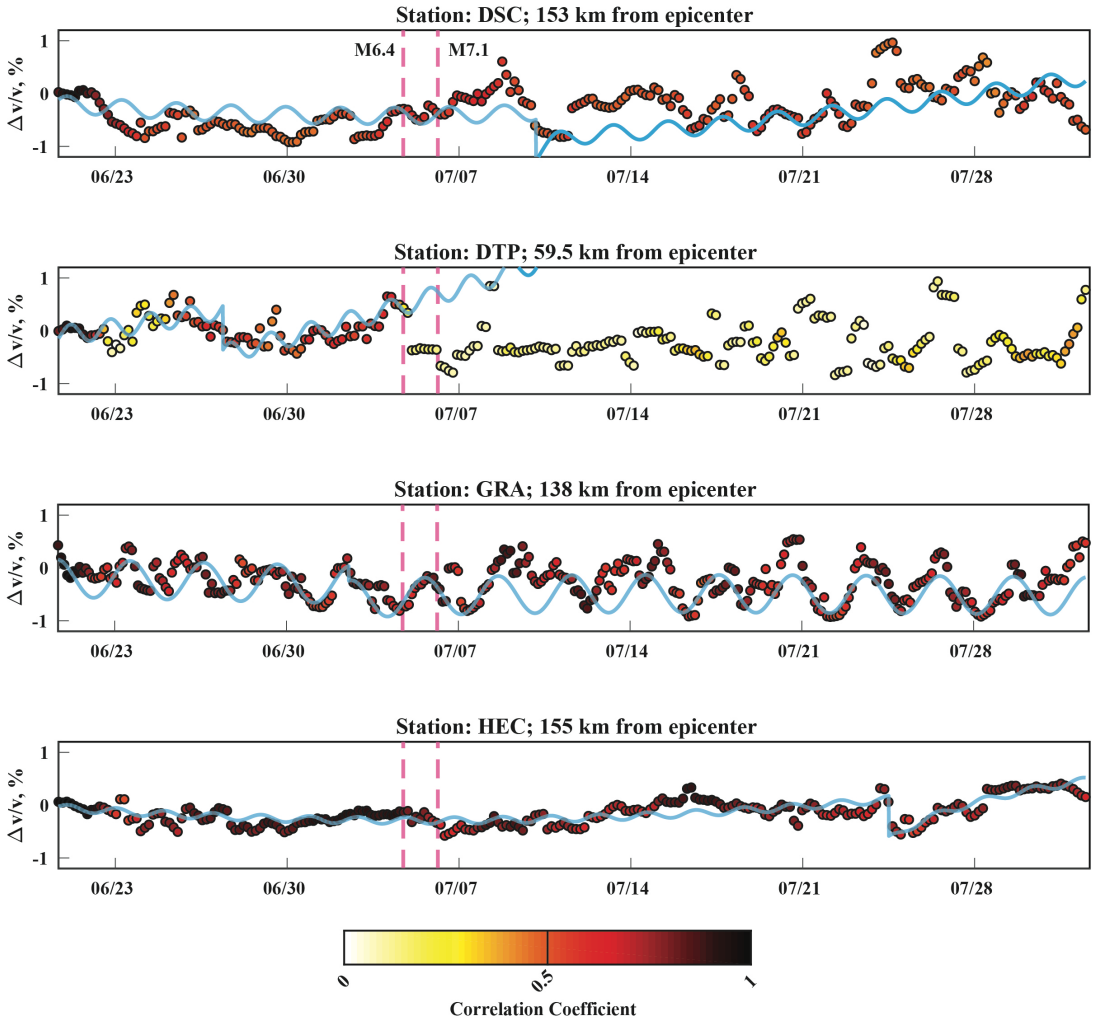
Station: DSC; 153 km from epicenter
M6.4
M7.1
Δv/v, %
1
0
-1
06/23
06/30
07/07
07/14
07/21
07/28
Station: DTP; 59.5 km from epicenter
Station: GRA; 138 km from epicenter
Station: HEC; 155 km from epicenter
0
0.5
1
Correlation Coefficient

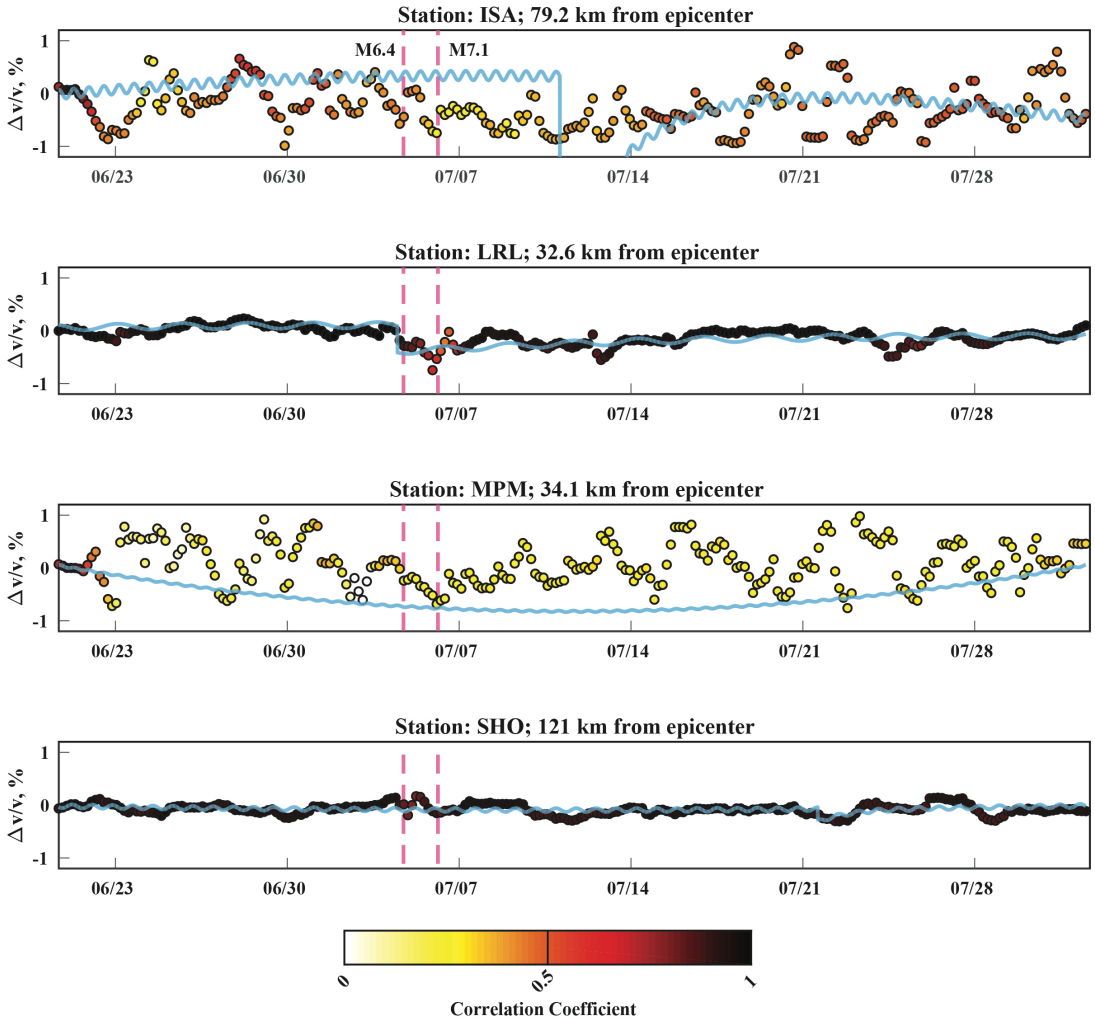
Station: ISA; 79.2 km from epicenter
M6.4
M7.1
Δv/v, %
1
0
-1
06/23
06/30
07/07
07/14
07/21
07/28
Station: LRL; 32.6 km from epicenter
Station: MPM; 34.1 km from epicenter
Station: SHO; 121 km from epicenter
0
0.5
1
Correlation Coefficient

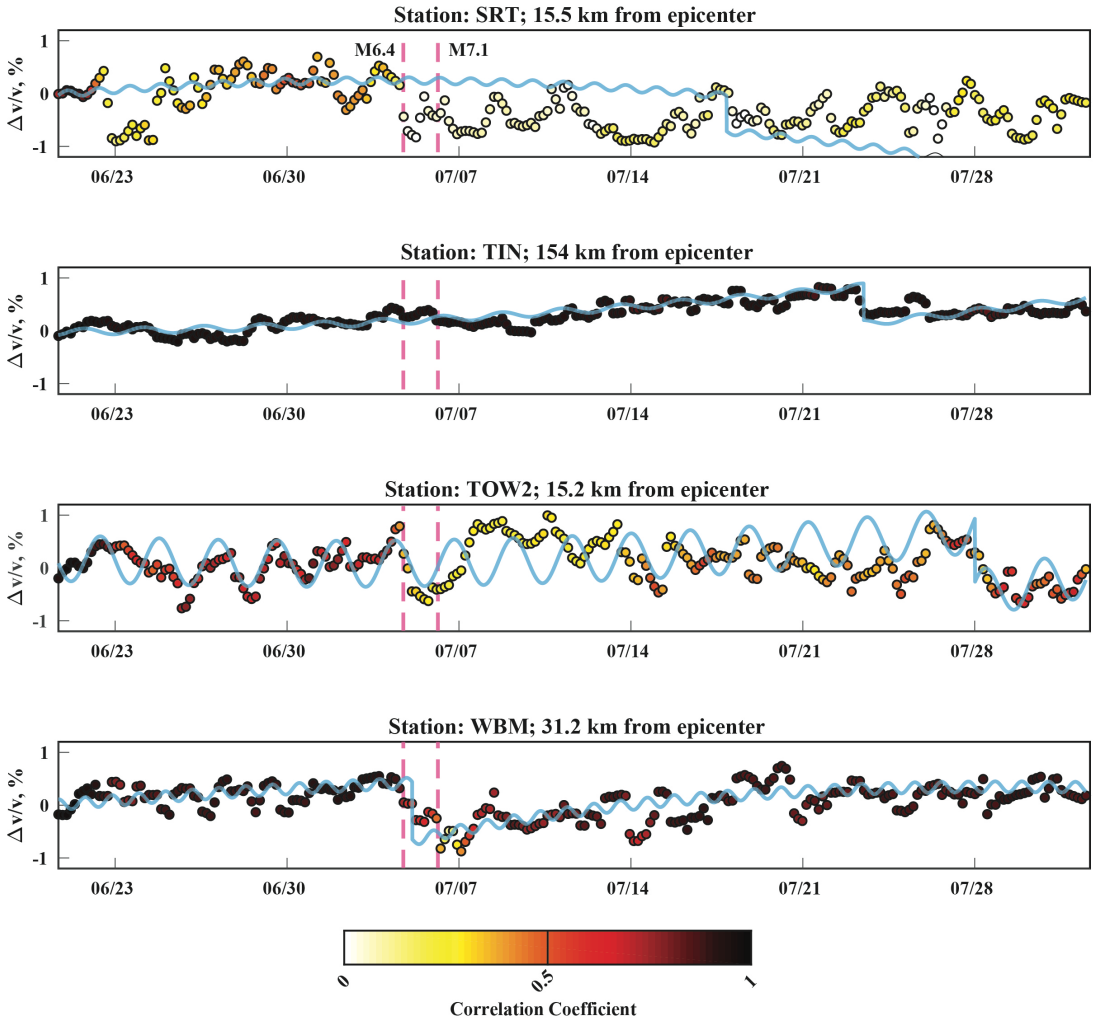
Station: SRT; 15.5 km from epicenter
M6.4
M7.1
Δv/v, %
1
0
-1
06/23
06/30
07/07
07/14
07/21
07/28
Station: TIN; 154 km from epicenter
Station: TOW2; 15.2 km from epicenter
Station: WBM; 31.2 km from epicenter
0
0.5
1
Correlation Coefficient

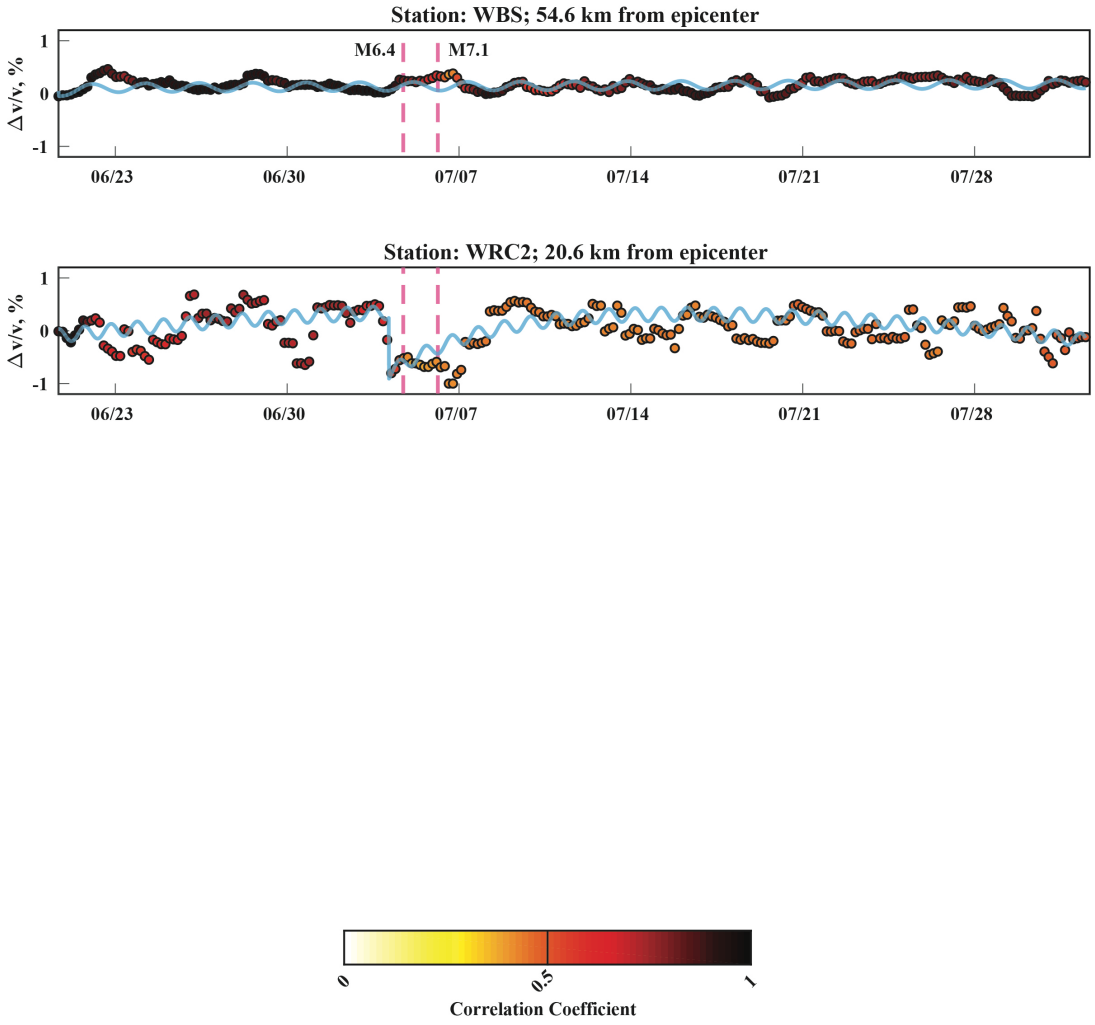


**Figure S4.3:** Change in velocity (dv/v) plotted against time and filtered from 10-30 Hz. All else is the same as in **Figure 4.2**.